INFLUENCE OF POLYMER SURFACES ON BACTERIAL BIOFILM FORMATION

Olutoba Sanni, MPharm(Hons)

Thesis submitted to the University of Nottingham for the degree of

Doctor of Philosophy

September 2019

Abstract

High throughput materials discovery screens have revealed polymers that reduce bacterial surface colonization which have progressed to ongoing clinical trials [Hook *et al*. Nature Biotech 2012]. These novel poly(meth)acrylate coatings reduced biofilm formation by *Pseudomonas aeruginosa, Staphylococcus aureus* and *Escherichia coli* in laboratory cultures *in vitro* and *in vivo* in a mouse foreign body infection model. These coatings are known to function by preventing biofilm formation; however, why the bacterial cells respond in this way to these polymers has yet to be elucidated. This knowledge gap leaves us unable to undertake rational design of novel materials to prevent bacteria attachment. In this thesis, we focus on understanding the influence of the polymer surface on attachment of bacteria and subsequent biofilm formation.

Using ToF-SIMS and XPS, we carry out careful surface chemical analysis of adsorbates on two polymers known to exhibit drastically different biofilm formation in a standard biofilm promoting culture media: protein-free, amino acid containing bacterial RPMI. Amino acid adsorption is identified to correlate with polymer resisting biofilm formation. The amino acid adsorption process for these two polymers was modelled and two key descriptive parameters: adsorbent capacity and on/off rate of nutrients on polymer surfaces were obtained.

To move the study from a small set of samples to a greater number from which to derive a structure-function relationship, we developed a high throughput surface characterisation approach. A cheap ninhydrin staining technique, which allows to quantify by fluorescence amount of adsorbed amino acids from standard RPMI onto surfaces of individual polymers in a microarray in high throughput manner was adapted. The amount of adsorbed amino acid on individual polymers together with ion fragments obtained from ToF-SIMS were used to develop a linear regression model and identify key fragments that promoted nutrient adsorption

using a total of 141 polymers chosen on the basis of possessing carbon, hydrogen and oxygen atoms.

To guide synthesis of novel anti-biofilm materials beyond the original monomer library, a simple predictive composite parameter termed *alpha* [Sanni *et al.* Adv Healthc Mater, 2015] that takes into consideration contributions from the partition coefficient (*logP*) and the number of rotatable bonds (*nRotB*) for hydrocarbon acrylate pendant groups was validated experimentally. We report the predictions of new monomers from the *alpha* QSAR model were successfully validated by the synthesis of new monomers, which were polymerized to create coatings found to be resistant to biofilm formation by six different bacteria pathogens: *Pseudomonas aeruginosa, Proteus mirabilis, Enterococcus faecalis, Klebsiella pneumoniae, Escherichia coli and Staphylococcus aureus*.

Potential biological degradation of novel anti-biofilm material has been postulated as a possible mode of action for these materials through release of bactericidal compounds. Here we used a quick-acting esterase enzyme (PLE) to verify that the mechanistic mode of action for novel anti-biofilm material was not due to enzymatic release of bacteriostatic/bactericidal compounds.

Acknowledgements

My journey through the PhD maze in search of the treasured “unknown” has oftentimes left me clueless and in such state I remain until this day. My numerous “faultless” and “flawless” plans for a great discovery vortexed me into the never-ending loop of “trying again,” from which I came out thanks to the invaluable assistance from a firm network of supporters.

I am forever grateful to my supervisors Morgan Alexander, Paul Williams, Derek Irvine and Martyn Davies for giving me the opportunity to carry out a research project under their close supervision and scientific guidance. Their depth of knowledge, foresight, work ethic and scientific rigor is something I deeply cherish and personally emulate. The funds to support this project provided by the Wellcome Trust, EPSRC and University of Nottingham is greatly appreciated.

It is a heart-felt thank you to a friend Dr. Laurence Burroughs for his patience and guidance with chemical synthesis, printing of polymer microarray and countless many more, what if he was not there?! Thanks to Dr. E. P. Magennis for helping me find my footing in the lab and to Dr. Andrew Hook for scientific guidance. Dr. J. F. Durben, Dr. M. Romero and Dr. M. Fletcher have been instrumental in helping me with microbiological experiments and guidance. I forever cherish the fruitful collaboration with Dr. A. A. Dundas, from office colleagues to co-authors. Special thanks to Dr. A. Blok for his unending kindness in providing me with an infinite number of arrays.

I recognize and appreciate the technical assistance from Paul Cooling, Amy, Elizabeth Steer (SEM), Emily Smith (XPS), Nichola Starr (ToF-SIMS), Long (XPS), Craig Stopiello (XPS), Grazziela Figueroa (Predictions), Tahseen (Predictions) and Valentina Cuzzucoli (GPC).

Kayleigh, Anjola and Marco were brilliant project students that provided the much-needed assistance with routine but essential laboratory procedures: dip-coating and silanisation. I kept mental sanity thanks to my “special” D20 office colleagues Gordon, Dipak, Ryan, Smiley Bhanu, Valentina, TJ, Stephen, Sunil, Robert, Mike, Paola, Matilde, Nikar, Adam, Akmal and Jatin. A sincere thank you to Alessandro M. Carabelli for sticking close as a friend or bacteria in our journey through the PhD maze and for being a trailblazer. It is my humble confession that in difficult and dire moments of utter confusion I drew strength from his resilience.

A big thank you to the other Sanni(s): Fatai, Christiana, Doyin, Dupe and Iyanu for being there and “understanding” my PhD. My dearest friends, Ruky, Victor, Trisha and Debo have been an immense source of encouragement through this 4 years and I am forever grateful to them. A final thank you to the RHN charity for the opportunity to serve the community in Nottingham.

List of Publications

1. *Sanni, O., et al., Bacterial attachment to polymeric materials correlates with molecular flexibility and hydrophilicity. Adv Healthc Mater, 2015. 4(5): p. 695-701*
2. *Mikulskis, P., Sanni O., et al., Prediction of Broad-Spectrum Pathogen Attachment to Coating Materials for Biomedical Devices. ACS Applied Materials & Interfaces, 2018. 10(1): p. 139-149*
3. *Sanni, O., Dundas, A.A., et al., Validating a Predictive Structure–Property Relationship by Discovery of Novel Polymers which Reduce Bacterial Biofilm Formation. Advanced Materials, 2019. 31(49): p. 1903513.*

Table of Contents

List of Figures

List of Abbreviations

Chapter 1 – Introduction

Biofilms are a major form of microbial life in which bacteria form dense surface-associated communities, typically enclosed in a matrix of self-produced exopolymeric substances (EPS). Bacteria within biofilms are up to 1,000 times more tolerant to antibiotics, disinfectants, mechanical removal, and other stresses, and this tolerance heavily impedes antimicrobial treatment [1].

Bacterial biofilm is increasingly recognised as a serious, worldwide public health concern. Surveys such as that conducted by Lord O'Neill (2016) estimated that the global financial impact of no action could lead to the loss of 10 million lives a year by 2050 and cost £ 69 trillion annually [2]. In contrast, the combined gross domestic product of G7 countries is forecasted to be just under £ 50 trillion by 2050 [3]. This imbalance threatens to drag the world back into the Dark Ages just a few decades following Fleming's Nobel Prize recognition for revolutionary penicillin antibacterial treatment in 1945 [4].

This chapter provides a review of bacteria-surface interaction, starting with an overview of various economic sectors affected by bacterial biofilms including a discussion of why bacteria colonise surfaces and the advantages derived. The chapter progresses following a detailed description of bacterial cell wall, to consider the life-cycle of bacteria on surfaces. In addition, we explore the communication systems that exist between bacteria cells, the influence of substrate properties, including morphological, chemical and physicochemical properties on bacterial biofilm development. Finally, an overview of current anti-fouling and anti-biofilm strategies is presented.

1.1 The Biofilm Challenge Across Various Sectors

Bacteria constitute the most successful form of life on earth when considering the extent of habitats colonised and a central understanding in microbiology is that majority of bacteria in the biosphere live in communities that are associated with surfaces [5-7]. Across many industries including refineries, steel mills, food, petrochemical and power plants, the availability of surfaces in essential systems such as the heat exchangers, water reservoir and cooling pipelines contribute to the extensive growth of biofilms [8]. This observation is also consistent for frequently used water-connected domestic appliances such as showerheads, automated coffee and washing machines [9, 10]. In the aquatic habitat, bacteria have been detected on sand grains, soil particles, stones, algae and plastic debris [11-13]. Surfaces immersed in the sea including aquaculture cages, fishnets, petroleum pipelines, sensors and ship hulls have all been a harbour base for bacteria [14]. The presence of bacterial biofilms together with barnacles and algae on marine ship hulls accounts for 40% increased friction with up to 45% corresponding effect on fuel consumption and augmented release of greenhouse gases. The latter outcome is considered a totally undesired effect and poses significant threat to the post-2020 actions outlined in the Paris Agreement. The resulting consequences from delays and maintenance of ship hulls is estimated to cost the transportation and environmental sector in the United States alone $ 150 billion per year [15-17].

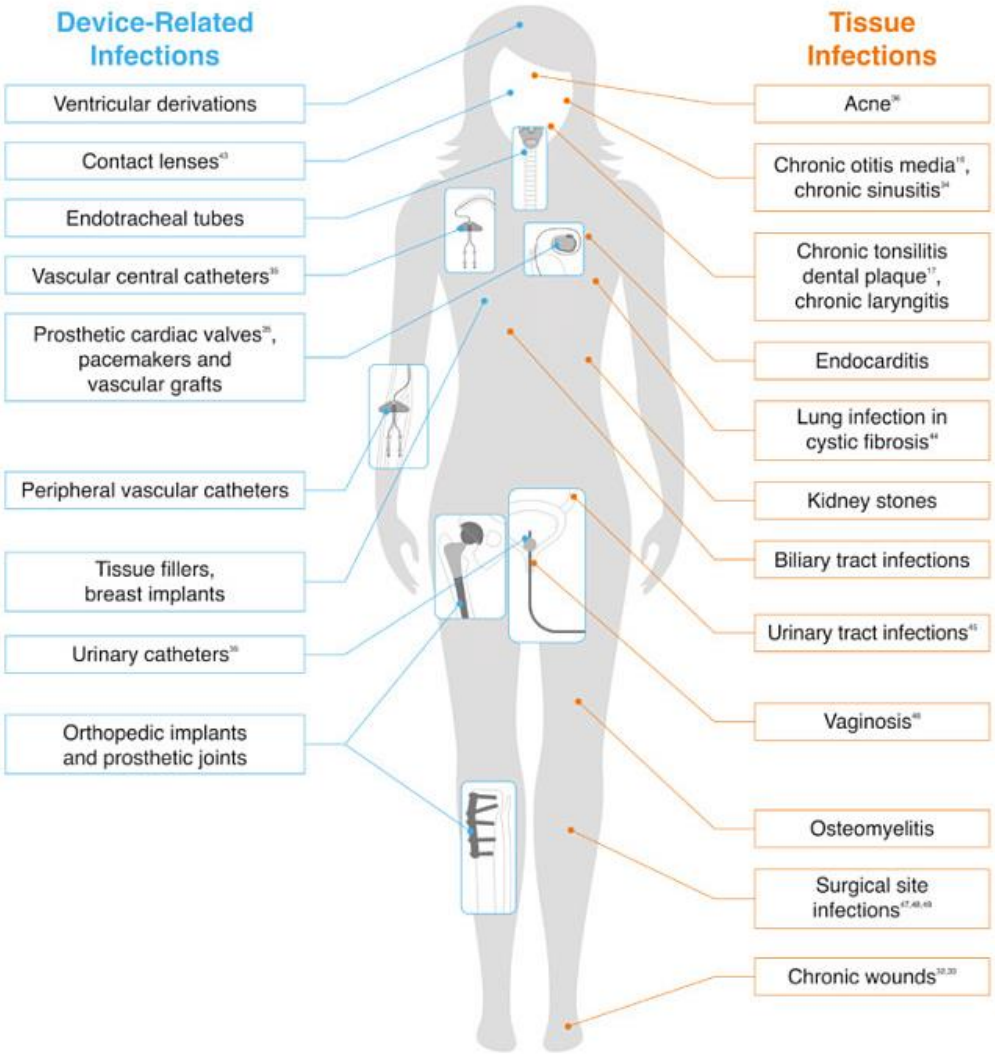

Figure 1. Summary of clinically relevant biofilm-associated diseases. Image adapted from U. Romling [18].

In both developed and underdeveloped countries, the spectrum of biofilm disease from a medical perspective is wide, encompassing the clinical problems of persistent infections of medical devices and soft tissues, see Figure 1 [18]. In a typical biotic environment, bacteria preferentially colonise mouth surfaces (teeth, tongue, gingival and hard palate) over saliva [19, 20]. For example dental plaque is the most common dental disease in the US and is the primary cause of tooth loss through young adulthood [21]. The acid destruction of dental hard tissues by acid-producing bacteria in plaque such as *Streptococcus mutans* leads to formation of painful dental caries [22].

An increased level of complication is introduced with the growing use of biomedical devices such as catheters, prostheses, contact lenses, heart valves, etc. that present abiotic surfaces for

bacteria to colonise. Statistics for device-related infections have estimated infection rate at 2% for breast implants, 2% for joint prostheses, 4% for heart valves, 4% for pacemakers and defibrillators and about 40% for ventricular-assisted devices [23, 24]. One in ten of hospitalized patients can acquire healthcare associated infections (HAI) or nosocomial infections caused by antibiotic resistant bacteria. A quarter of these cases manifest as central line-associated bloodstream infections, catheter-associated urinary tract infections (CAUTI), surgical site infections and ventilator-associate pneumonia [25]. Prevalence reaches up to 30% in intensive care units making it the sixth leading cause of death in western-industrialized countries [26].

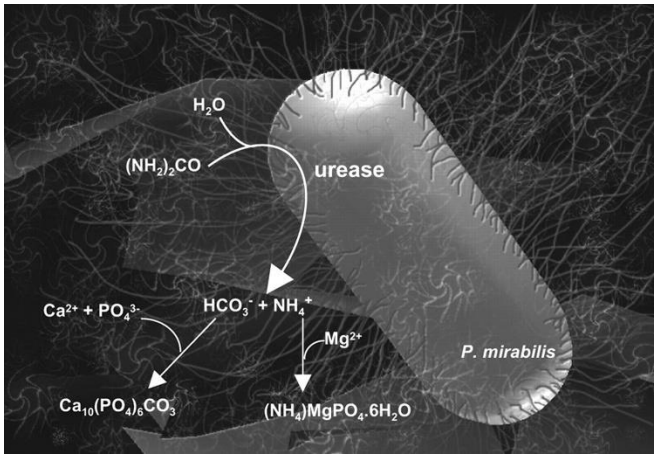

Figure 2. Role of urease in *Proteus mirabilis* infection. Infection induced stones are formed due to the presence of ammonia and carbon dioxide released during the hydrolysis of urea catalysed by urease. Ammonia and carbon dioxide form struvite [$(NH_4)MgPO_4.6H_2O$] and carbonate apatite [$Ca_{10}(PO_4)_6CO_3$], respectively. Image adapted from C. Follmer [27].

The increased statistics associated with urinary tract infection is also due to the ability of bacteria to colonise biomedical surfaces utilising a physiological compound such as urea with a mean normal concentration of ca. 16 g/L in normal urine [28]. A class of ureolytic (urea-hydrolysing) bacteria such as *Proteus mirabilis*, *Klebsiella* and *Staphylococcus aureus* produce urease, an enzyme that breaks down urea generating ammonium and carbon dioxide thus alkalizing urine pH to reported values of pH 9.1 [29]. The changes in urine chemistry tend to promote precipitation of magnesium, calcium, ammonium and phosphate crystals referred to as struvite ($(NH_4)MgPO_4 \cdot 6H_2O$) or carbonate apatite ($Ca_{10}(PO_4)_6CO_3$), see Figure 2 [30]. The formed crystals also referred to as stones may become secondarily infected and promote biofilm site deposition resulting in formation of crystalline biofilm [31]. Indeed, there is an association

between urinary infection, biofilm formation and encrustation of biomaterials in approximately 50% of all long-term catheterized patients [32].

A group of antibiotic resistant bacteria known to cause 62% of nosocomial infections have been identified – *Enterococcus faecium, Staphylococcus aureus, Klebsiella pneumonia, Acinetobacter baumanni, Pseudomonas aeruginosa* and *Enterobacter* species altogether termed "the ESKAPE bugs" by Rice; are especially known for developing and disseminating antimicrobial resistance. Learning to control these pathogens for the desired outcome of safer hospitals requires the full understanding of bacteria-surface interactions and subsequent biofilm formation [33, 34]. To understand the interaction between bacteria and surfaces, it is fundamental to take into consideration the surface structures present on bacteria cells.

1.2 Structure of Bacterial Cell Wall

Most bacteria have a cell envelope that maintains cell shape, protects against osmotic lysis and unpredictable hostile environment [35, 36]. Bacteria have historically been divided into two classes or groupings based upon the interactions of their cell envelope with iodine and crystal violet dye (the so called "Gram stain") [37]. Those bacteria which were stained dark were denoted as Gram-positive (e.g. *S. aureus*) or if they stained a lighter pink colour the bacteria were classed as Gram-negative (e.g. *P. aeruginosa*). The difference in the staining of these bacteria reflected a substantial variance between the structures of their cell walls [38]. Both Gram-negative and Gram-positive cell envelopes contain peptidoglycan units patterned in a complex multi-layered manner. Peptidoglycan is a repeating *N*-acetylglucosamine (NAG)-*N*-acetylmuramic disaccharide (NAM) having a pentapeptide attached to the D-lactyl moiety of each NAM (see Figure 3b). This pentapeptide stem participates in an interglycan cross-linking reaction, thus creating the cell wall polymer [39]. The thick cell wall of the Gram-positives are responsible for their differences in Gram staining.

1.2.1 Gram-positive Bacteria

On the basis of morphological criteria three distinct cellular compartments can be distinguished in Gram-positive bacteria: the cytosol, a single cytoplasmic membrane, and the surrounding cell wall which serves as an attachment site for proteins (e.g. adhesins and Protein A in *S. aureus*) that interact with the bacterial environment [40]. Wall associated proteins attach by virtue of covalent or non-covalent interactions with the peptidoglycan wall or secondary wall polymers such as teichoic acids [41].

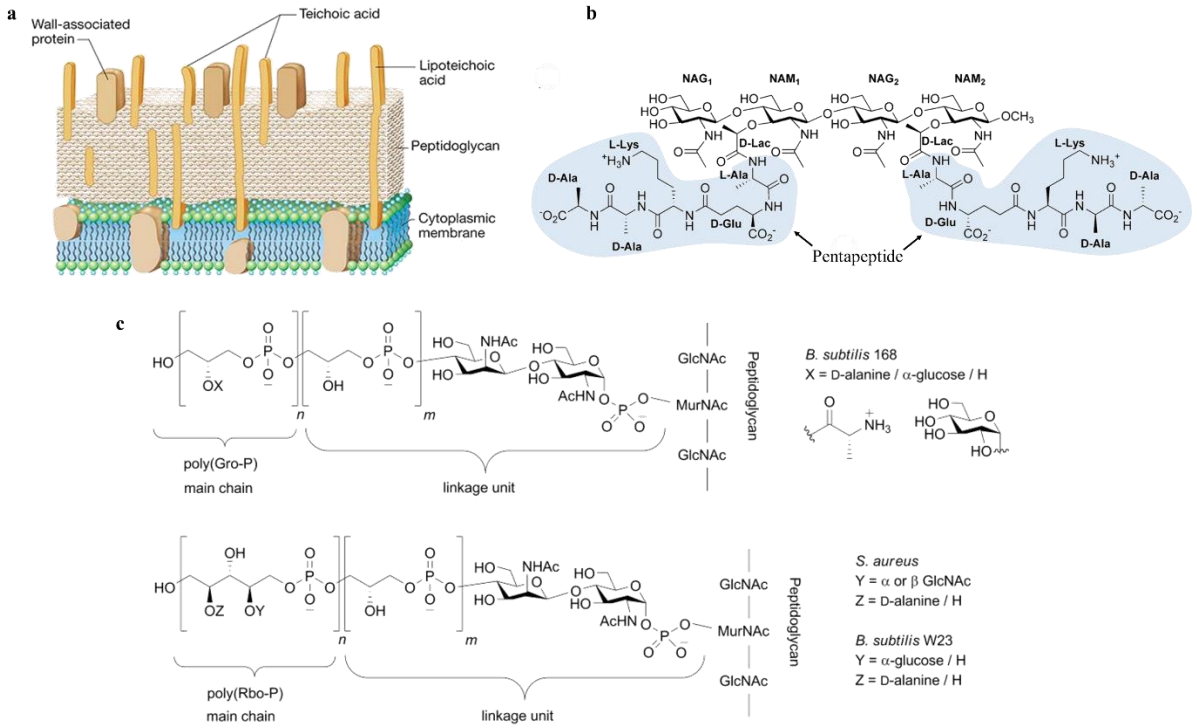

Figure 3. **(a)** Diagram showing cell wall of Gram-positive bacteria with associated protein and teichoic acid. **(b)** Structure of peptidoglycan composed of *N*-acetylglucosamine-*N*-acetylmuramic disaccharide. Coloured in blue is pentapeptide attached to the D-lactyl moiety of each *N*-acetylmuramic. **(c)** Generic chemical structure for teichoic acid. Image readapted from A. Tankeshwar [42].

There are two types of teichoic acids: lipoteichoic acid, which are anchored to the plasma membrane and extend from the cell surface into the peptidoglycan layer; and the wall teichoic acids which are covalently attached to the peptidoglycan and extend through and beyond the cell wall, see Figure 3a, [43]. The wall teichoic acid are highly abundant modifications that constitute up to 60% of gram-positive cell wall. The wall teichoic acid can be divided into two components: a disaccharide linkage unit and a main chain polymer composed of phosphodiester

linked polyol repeat unit. The highly conserved disaccharide linkage unit is composed of *N*-acetylmannosamine and *N*-acetylglucosamine-1-phosphate, with one to two glycerol 3-phosphate units attached to the C4 oxygen of *N*-acetylmannosamine, see Figure 3c, [44]. The main chain varies among organisms and it is usually made up of glycerol or ribitol phosphate repeats. For example *Bacillus subtillis*, the Gram-positive model organism, makes poly(glycerol phosphates) or poly(ribitol phosphate) wall teichoic acids depending on the strain, while *S. aureus* strains primarily make poly(ribitol phosphate) wall teichoic acids [43]. Additional structural diversity on polyol chain arises from presence or absence of D-alanine esters or a variety of mono or oligosaccharides, commonly glucose or NAG, which play an important role in surface colonisation, more specifically for cell signalling and communication between bacteria cells [45, 46].

The cell surface of most Gram-positive bacteria has a moderately negative net charge at neutral pH, which is probably due to the fact that the teichoic acids contain fewer positively charged D-alanine residues than negatively charged phosphate groups [47]. The lack of D-alanine esters affects the pattern and abundance of surface-bound proteins which in turn influences the hydrophobicity and net charge of the bacterial cell envelope and the interaction with substrate surfaces [48]. It has been reported that during biofilm growth of *E. faecalis*, there is a significant change in peptidoglycan modifications, including reduction in amino acid substitutions of the peptide sidechain as well as modifications that indicate the activity of amidases and deacetylases [49, 50]. It is however also true that the direct interaction of Gram-positive bacteria and surfaces is dependent on van der Waals forces, which are generally attractive, and interionic forces, which can be either attractive or repulsive. Therefore, even if bacteria and surfaces are charged alike, van der Waals forces can overcome repulsion and lead to adhesion [51].

1.2.2 Gram-negative Bacteria

The cell walls of Gram-negative bacteria have an outer membrane situated above a thin peptidoglycan layer. Sandwiched between the outer membrane and the plasma membrane, a concentrated gel-like matrix (the periplasm) is found, see Figure 4A, [52]. In contrast to Gram-positive organisms, Gran-negative do not contain teichoic acids in their thin peptidoglycan layer, but rather possess proteins, phospholipids, and lipopolysaccharides (LPSs) in the outer membrane which separates the external environment from the periplasm [53].

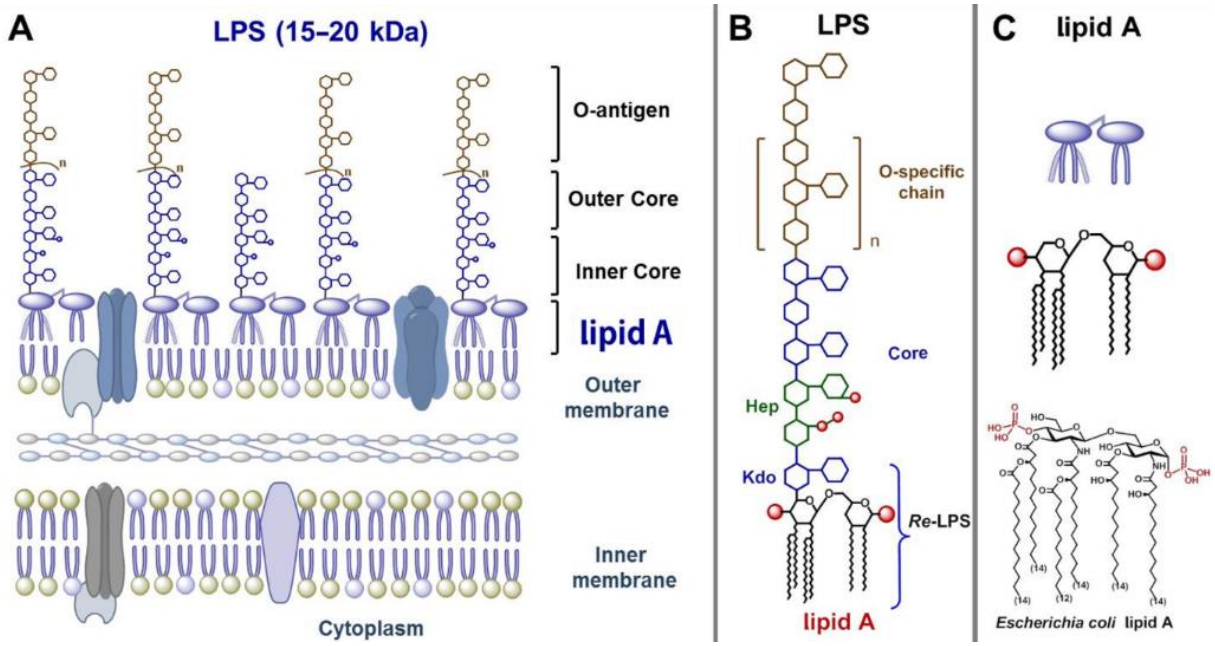

Figure 4. **(A)** Gram-negative bacterial membrane with LPS as major component of the outer membrane. **(B)** structural constituents of LPS: lipid A, inner/outer core and O-specific chain. **(C)** Structure of lipid A. Image adapted from [54]

Lipopolysaccharide is often described as a molecule with three domains (Figure 4B). The first domain is called lipid A: it contains a phosphorylated disaccharide backbone, to which are attached several fatty acid chains that anchor LPS into the outer membrane. The lipid A is attached to a nine or ten-sugar, branched and phosphorylated oligosaccharide known as the core. A proportion of the LPS molecules on the surface of any given cell has only these two domains. Such molecules are sometimes referred to as lipid A-core. The third LPS domain consists of a repetitive carbohydrate polymer, which is covalently attached to the core, and can be referred to as the O antigen, O polysaccharide or O chain [55]. LPS has been shown to be

essential in most Gram-negative organisms due to its role in membrane integrity and key factor in immune stimulation via its detection by host pattern recognition receptors [56]. It is highly antigenic and also responsible for the activation of the innate immunity cascade.

The O-polysaccharide chain of LPS has been found to be an important determinant of non-specific surface properties, and studies have demonstrated that loss of the O-polysaccharide chain can dramatically alter the overall surface charge and hydrophobic character of the Gram-negative cell surface [57]. Specifically, *Walker et al.* investigated the importance of the distribution of charged functional groups on the LPS and the outer membrane by utilizing three *E. coli* K12 strains with well-characterized LPS molecule. Their results showed that, for strains lacking O-chain and with exposed charged phosphate groups on core domain, adhesion was dominated by electrostatic interactions. However, for the bacterial strain with the full LPS molecule, the uncharged O-antigen portion of the LPS shielded charged functional groups, which resulted in significantly reduced electrostatic interactions [58]. The variation in relative expression of LPS domains maybe a mechanism by which bacteria alter their overall surface characteristics in such a way as to influence adhesion and favour survival [57].

In a comparative analysis of LPS from *P. aeruginosa* in planktonic and biofilm state, Ciornei *et al.* revealed a number of important structural modifications in LPS caused by the switch between these two life-styles. They observed reversible modifications affected both the polysaccharide moiety and the lipid A part of the LPS molecules. *P. aeruginosa* in biofilm showed an almost complete loss of O-polysaccharide and its lipid A moiety had quantitatively less hydroxylations on fatty acid chains [59]. Modification of LPS in biofilm state have also been reported for *E. coli* where increased palmitoylation of fatty acid moiety was seen and for *Pr. mirabilis,* an extension of core oligosaccharide chain was observed [60, 61].

Such findings reiterate the centrality of these changes both in Gram-negative and Gram-positive to adaption and survival in different environmental conditions.

1.3 Steps in Bacteria Surface Colonisation

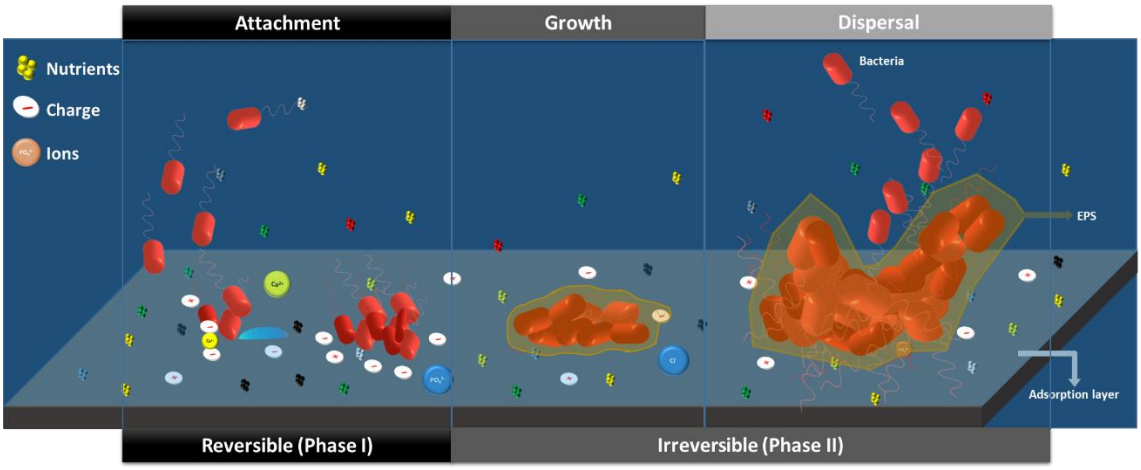

Figure 5. Summary of initial interaction of planktonic free-floating bacteria with pristine surface. Micro and macronutrients adsorbed from aqueous environment on pristine surface form the *ad layer*. Initial physicochemical interactions between bacteria and *ad layer* determines formation of a reversible attachment. Progression to a molecular and cellular phase that involves secretion of extracellular polymer substance to encapsulate growing bacteria leads to irreversible attachment on surface and formation of mature biofilms, from which daughter cells emerge to colonise new surfaces.

Surface association appears to be an ancient, universal and fundamental survival mechanism that confers microorganisms with critical advantages, including greater access to nutritional resources, enhanced organism interactions, reproduction, protection, greater environmental stability and pathogenicity [62, 63]. It is generally accepted that the formation of microbial biofilms on surfaces is a multi-step process involving in its very early stages the complex interplay of factors such as surface charge, surface topography, flow rate, temperature, nutrient abundance and adsorption layer etc. Garrett *et al.* divided this phenomenon into three stages of adsorption, attachment and colonisation by organism. Characklis *et al*. went further to describe an eight-step detailed process that took into consideration formation of adsorption layer, reversible and irreversible adhesion of bacteria, and eventual dispersion of cells [24, 64]. However characterised, the majority of researchers agree with several steps leading to biofilm formation and here we have adopted a variant of the two-step mechanism proposed by Marshall *et al.* (see Figure 5) which originally included an initial, instantaneous and reversible physical

phase (Phase I) and a time-dependent, irreversible molecular and cellular phase (Phase II) [65, 66]. In addition, here we briefly explore the formation of a conditioning layer preceding these two phases.

1.3.1 Surface Conditioning Layer

The exact sequence of events capturing the initial stages of bacteria interaction with a biomedical surface (e.g., catheter, stent, hip joint replacement) are yet to be fully established and are complex, but may however be theorised from first principles of surface chemistry, simplified to predict the adsorption of organic biomolecules such as proteins will concentrate at certain areas on surfaces [67]. In a typical biotic environment, for example the human blood tissue, with over 150 proteins at varying concentrations, with unique rates of diffusion and affinity for surface, the exposure of a native surface triggers what Gristina termed "a race to the surface," between Angstrom-sized proteins and micron-sized cells [68]. From diffusion theory, it is deducible that the race from the region of high concentration to the surface is predictably in favour of organic matter smaller than 0.01 – 0.1 µm. Transport of such small molecules is relatively rapid when compared to transport of larger sized cells (e.g., bacteria is 0.5 – 10 µm) and it has been reported that adsorption of proteins occur almost instantaneously. [69].

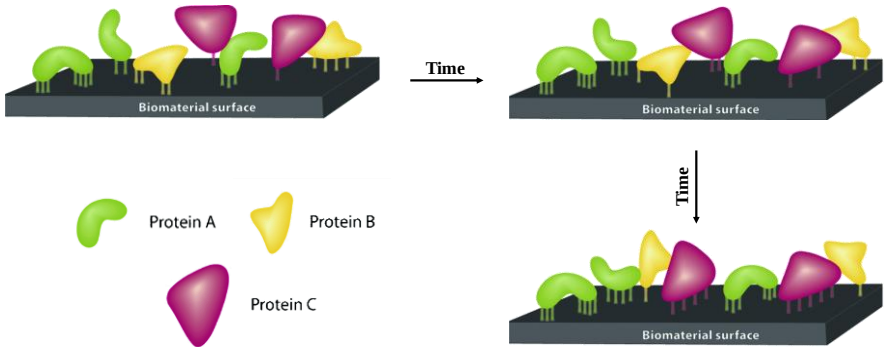

Figure 6. Schematic of the sequential adsorption of proteins as described by the Vroman effect. Initially, many protein molecules in various conformations are adsorbed onto the biomaterial surface. On the left portion of all three frames are two proteins A (green) in different conformations, which change over time. In the centre of the figure, different proteins B (yellow) with multiple bonds are replaced over time by a larger, higher-affinity protein C (red) that arrived later on the substrate surface. Image adapted from D. R. Schmidt [69].

In a multicomponent solution composed of proteins with various dimensions and regions, i.e., hydrophilic/hydrophobic, charged/uncharged, a competition for the surface between proteins

also ensues. The adsorption behaviour is often a result of an overlap of transport, adsorption, and repulsion processes. Smaller proteins diffuse faster than larger ones and are the dominating species in the early adsorption stage. Larger proteins, however, typically bind stronger to the surface because of a larger contact area and can even repel other pre-adsorbed proteins during spreading on the surface (see Figure 6) [70]. At hydrophilic interfaces, proteins predominantly expose hydrophilic residue-containing regions toward the surface, and on hydrophobic surfaces, proteins direct their hydrophobic regions to the surface. Analogously, proteins adsorbing at positively or negatively charged interfaces tend to expose the oppositely charged regions to the surface [71]. Proteins adsorbed on a material surface replace each other over time in a process called the Vroman effect (see Figure 6). The bonds or interactions formed between a protein and a material surface can be broken and reformed randomly over and over [69].

The outcome of this event is the formation of an adsorbed layer of organic molecules on biomedical surface also called the *ad layer*, which serves to mask the surface properties and also provide a local concentration of nutrients due to increased surface area to nutrient ratio, thought to be particularly useful for cell growth and reproduction in a nutrient deprived environment [72]. It is also true that, the protein surface density, conformation and distribution in the conditioning layer directs cell responses such as proliferation, matrix reorganization, differentiation and also affects the initial stages of cell-surface interactions and adhesion [73, 74].

The mechanisms of protein adsorption in relation to surface wettability have been extensively studied. Surface wettability generally referred to as hydrophobicity/hydrophilicity is an important parameter shown to have profound effect on biological response, one of which is the broadly studied protein adhesion to surfaces [75]. According to Vogler, the study of wettability from the perspective of water structure and reactivity at surfaces can help identify correlations

and clarify the disputed contrast in protein adsorption and subsequent biological response of hydrophobic/hydrophilic materials [76].

1.3.1.1 The Influence of Surface Wettability on Protein and Cell Adhesion

The relationship of protein adsorption to wettability of self-assembled monolayers terminated systematically with increasing chains of polyethylene glycol have since been studied by *Prime et al*. Their results demonstrated that for a given hydrophilic component, resistance to protein adsorption increased with hydrophilicity and that homologous hydrophilic groups had similar properties of resistance to protein adsorption [77, 78]. In line with this view, Chapman *et al*. screened more than 50 homogenous self-assembled monolayer surfaces made using alkanethiols, each presenting with a different functional group. They established that surfaces possessing functional groups with four molecular characteristics resisted the adsorption of proteins, namely: (i) they contain a polar functional groups, (ii) they incorporate hydrogen bond accepting groups, (iii) they do not contain hydrogen bond donating groups and (iv) they have no net charge [79]. With regards to this perspective, low-fouling surfaces terminated with ethylene glycol groups are well studied with clear understanding of their mechanistic mode of action based on thermodynamic considerations used to generically define antifouling surfaces [80].

$$\Delta G_{ads} = \Delta H_{ads} - T\Delta S_{ads}$$

Equation 1. Gibbs free energy

The free energy of the adsorption (ΔG_{ads}) process given by Equation 1, contains an enthalpic component (ΔH_{ads}), which describes the strength of interactions between the fouling agent, solvent and surface, and an entropic component (ΔS_{ads}), which denotes the conformational changes in the system. Irrespectively of the exact mechanism of the adsorption process, it will only occur if the Gibbs energy decreases at constant temperature and pressure [81]. If the

interaction between the fouling agent and surface is strong, adsorption occurs due to the contribution from the enthalpy gained (ΔH_{ads}).

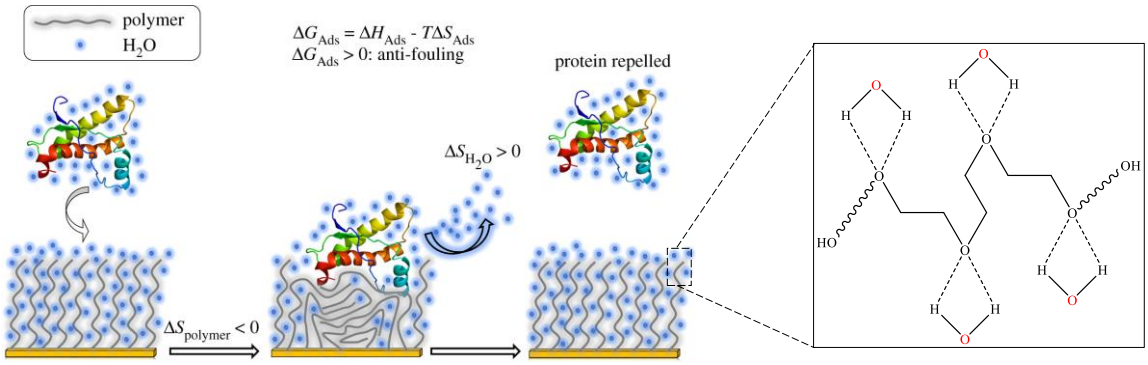

Figure 7. Protein repellency mechanism for a hydrophilic, brush-like grafted polymer. Protein adsorption onto grafted PEG results in the release of the hydration barrier from both the polymer and the protein. This process increases the entropy for water, but is outweighed by a decrease in conformational entropy for the polymer. The net result is entropically unfavourable for protein adsorption. Enthalpy of adsorption for the protein–polymer interaction can either be favourable or unfavourable depending on the paired species. Scheme on right hand side shows the interaction of water via hydrogen bonds with polyethylene glycol. Image readapted from A. Halvey [82].

Jeon *et al*. were one of the first groups to study and propose a theory for the antifouling characteristics of grafted PEG. Working with a simple model that considered attraction due to van der Waals to be tiny and hydrophobic interactions with hydrophilic PEG to be negligible, the group found that as a protein approaches a substrate, the PEG chains are compressed, leading to a decrease in conformational entropy (entropically unfavourable since the conformational dynamics of the polymer chains are restricted), translating to compressive elastic forces. Water molecules attracted to the hydrophilic PEG are displaced to the bulk as a result of this compression (with corresponding enthalpic penalty from bond breaking), leading to a thermodynamically unfavourable osmotic barrier, see Figure 7. The coupling of both forces act as a net repulsive force to the incoming proteins [83-86].

Chapman *et al*. in their classification of surfaces resistant to proteins based on molecular characteristics following a systematic search concluded that their principles may not be sufficient to design surfaces inert to adhesion of bacterial and mammalian cells. Nonetheless, compelling evidence to suggest the interaction of water with surfaces is a determinant factor for inertness was obvious [80]. In line with this, *Luk et al*. reported that SAMs of

alkanethiolates terminated with mannitol that is rich in hydrogen bond donors were inert to protein adsorption and cell attachment, but still proposed a similar mechanism describing mannitol terminated monolayers served as templates on which an ordered solvent structure that prevents the approach and adsorption of proteins to the surface can occur [87, 88].

The question of whether adsorption of proteins, bacteria, and mammalian cells to materials occurs only within the framework proposed by Whitesides *et al.* remains a subject of legitimate speculation [80]. For example, Hook *et al*. showed that in contrast to the SAM studies, when a broader range of chemistries (576) were employed as polymers, there was no correlation between wettability and attachment of *P. aeruginosa*, *S. aureus* and *E. coli* [89]. In his review, Rosenhahn concluded such results would depend on both, biofouling species and the chemical composition of the substrates tested [90]. Similar opinions were also reported by Alexander and Williams, where they described bacteria response to a diverse range of synthetic culture media to be a complex phenomenon where the cell type, its phenotype, the media composition, culture conditions (static or dynamic) and the range of surface chemistries under consideration needed to be considered along with other variables [91].

1.3.2 Reversible Phase One Attachment

Historical attempts by colloidal scientists to model initial phase of bacteria attachment to surfaces have oftentimes considered bacteria as particulates with very little consideration of its chemosensory abilities. One common conclusion was that bacteria were transported to the surfaces by physical long range interactions (distances > 150 nm) and upon closer contact, short-range interactions become more important (distance < 3 nm) [92]. This was temporarily backed up with the theory by Derjaugin, Landau, Verwey, and Overbeek (DLVO) that considered interplay between attractive van der Waals forces and generally repulsive electrostatic forces when they described initial bacteria adhesion as a function of separation distance between the cell and surface [93, 94]. The simplified approach to a complex scenario

brought about the extended version of DLVO theory proposed by Jucker *et al*. to include hydrophobic and hydrophilic interactions for a more robust model, but biological changes in attaching bacteria affect adhesion to such an extent that predicting this process is virtually impossible based on a physicochemical model alone [95, 96].

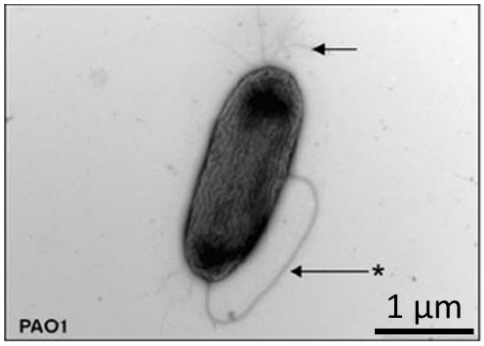

Figure 8. Transmission electron microscope detection of assembled flagella on the cell surface of *Pseudomonas aeruginosa* O1 (PAO1) wild-type. Fully assembled flagella indicated by the arrows with asterisks and assembled pili with normal arrow [97].

Bacteria are capable of sensing and moving across a surface, besides sessile aggregation: swimming, twitching, gliding and sliding are frequently observed movements of bacteria on surfaces [98]. These movements are made possible due to presence of extracellular organelles or specific structural appendages such as flagellum and pilus whose molecular components are well conserved amongst phylogenetically distant species and particularly well understood in *P. aeruginosa* species, long appreciated by investigators for biofilm formation (see Figure 8) [99, 100]. *P. aeruginosa* is multi-piliated with type IV pili (TFP) and monotrichous, i.e., possessing a single polar flagellum both commonly reported to be involved in promoting surface attached behaviours via surface sensing [101]. The flagellum operates as a rotor and generates force via the hydrodynamic drag opposing its rotation, whilst TFP operate as linear actuator that pull the bacterium along a surface [102].

Sometimes, bacteria can become highly motile and migrate over the substrate surface in a process known as swarming, operationally defined as rapid multicellular movement of bacteria across a surface powered by rotating flagella [98]. These surface movements are believed to play pivotal roles in microbial surface sensing, colonization and spreading across the substrate

[103]. In fact, it has been visualised that surface-bound pili of *Caulobacter crescentus* face resistance on retracting in order to trigger synthesis of adhesive attachment organelles called holdfast, a process believed to be mediated by increased production of cyclic diguanylate monophosphate (c-di-GMP) secondary messenger near the surface after sensing [104, 105].

The ultimate decision for bacteria to stick to a surface or not after surface sensing is also influenced by a combination of intrinsic surface features, e.g., surface topography/roughness, surface stiffness, surface wettability, surface charge and surface chemistry[106].

1.3.2.1 The Influence of Surface Roughness and Stiffness on Bacterial Adhesion

Studies from Busscher *et al*. revealed that when surface roughness of voice prosthesis made from silicone was modified from 46 nm to 8 nm, it reduced *in vitro* biofilm formation (corrected for surface area) of *Staphylococcal* species and resulted in prolonged clinical lifetime of silicone rubber voice prostheses in laryngectomised patients [107]. Similar findings in the field of oral science showed that increased roughness (0.1 – 1.2 μm) of resin composite cement resulted in higher biofilm formation by *Streptococcus mutans* [108]. One of three possible explanations for this is that bacteria preferentially attach to irregularities similar in diameter to their size [109]. Secondly, based on DVLO energy calculations, repulsive interaction energy barrier between a particle and rough surface is much lower than corresponding smooth surface [110]. Lastly, increased attachment of bacteria to rough surfaces may also be attributed to protection against shear stress conferred by irregularities [111]. However, a different study reported that engineered poly(dimethyl siloxane) (PDMS) square and circular topographies with nanometre scale vertical roughness (21 - 117 nm) effectively inhibited adhesion and colonisation by *Staphylococcal* species and demonstrated they preferentially attached to areas of maximum surface [112].

The effect of material stiffness measured by atomic force microscope on attachment of *E. coli* to PDMS surfaces was studied by tracking motility of cells on the surface. Results suggested that *E. coli* cells do not prefer stiff PDMS (2.6 MPa) surfaces for attachment since the cells were more motile on these surfaces than on soft PDMS (0.1 MPa). It is reported that *E. coli* uses extracellular appendages to sense substrate stiffness and if favourable, cells reduce motility and start biofilm growth [113]. Schiffman *et al*. obtained different results when they studied the attachment of *E. coli* and *S. aureus* to polymerised polyethylene glycol dimethacrylate and agar of varying stiffnesses with Young's moduli in range 0.044 – 6.5 MPa. They concluded that more *E. coli* and *S. aureus* cells adhered to stiffer hydrogels and that this relationship occurred independently of chemistry studied [114]. However, the lack of a standard control for determining low and high bacteria attachment makes reported results relative and not easy to extrapolate to a wider range of materials. Despite the lack of a general consensus on the minimum level of roughness or stiffness needed to correlate bacterial adhesion, studies have shown they both have a role to play in bacteria decision making [115, 116].

1.3.2.2 The Influence of Surface Charge on Bacterial Adhesion

Numerous attempts to understand bacterial adhesion from principles of electrostatic interactions have been made, but there has been no success in finding trends or general correlations. It is commonly reported that most bacteria have a net negative surface charge (estimated via surface zeta potential) and will preferentially interact with positively charged surfaces, whilst being repelled by negatively charged ones [5, 35]. A different explanation takes into consideration the hydration layer on charged surfaces acting as an exclusion zone that pose as an energetically insurmountable barrier for bacteria to displace [117]. Using *P. aeruginosa* as a model bacterium, Ramstedt *et al.* illustrated that negatively charged polymer surfaces of 3-sulphopropylmethacrylate and [(2-methacryloyloxy)ethyl]dimethyl(3-sulphoproyl)ammonium hydroxide strongly reduced its attachment and motility when compared to glass and poly(methyl methacrylate). They generalised for gram negative bacteria based on findings from

P. aeruginosa that the increased production of exopolysaccharides when in contact with charged surfaces allowed bacteria modify their surface thus influencing development of biofilm [118].

Employing a different approach of comparing attachment of amino and carboxyl functionalised polystyrene beads to attachment of *P. aeruginosa, S. aureus* and *E. Coli* on PDMS, Ren *et al*. concluded that zeta potential of beads/bacteria and hence electrostatic interaction is not the sole factor influencing bacteria adhesion. They reasoned the chemical composition of Gram-positive cell wall differed substantially from those of Gram-negative cells and could see the challenge of predicting adhesion from bacterial and substrate charges [119]. It is also true that the electric double layer becomes less important with increasing ionic strengths (> 100 mM), which is typical for aqueous environments encountered in biomedical applications and bacteria culture media (e.g. 153 mM in RPMI) [120, 121].

1.3.2.3 The Influence of Surface Chemistry on Bacterial Adhesion

In their work, Hook *et al.* studied the influence of surface chemistry on bacterial attachment to 576 different polymers. The attachment of *P. aeruginosa* and *S. aureus* correlated with material surface chemistry obtained through Time-of-Flight Secondary Ion Mass Spectrometry (ToF-SIMS), with R^2 of 0.68 and 0.76 respectively [89]. Secondary ions consistent with cyclic carbon groups (C_4H^-, C_6H^-), ester group (CHO_2^-), the tertiary butyl moiety ($C_4H_7^+$) and ions from aliphatic groups ($C_2H_3^+$, $C_2H_5^+$, $C_3H_7^+$) were correlated with lower bacterial attachment for both pathogens. Whilst ions from ethylene glycol groups ($C_2H_3O^+$, $C_2H_3O_2^-$), and hydroxyl containing fragments ($C_4H_5O_2^-$, $C_6H_{11}O_3^-$) correlated with higher bacterial attachment [89].

In a different study, ToF-SIMS was used to compare surface chemistries and bacterial attachment of defined chemical groups in copolymer pairs. The results showed that copolymers series with cyclic aliphatic chemistries were better at preventing attachment of *P. aeruginosa*

compared to cyclic aromatic chemistries and that *tert*-butyl bulky groups play a role in achieving resistance to bacterial attachment [122].

Parreira *et al.* also studied the effect of surface chemistries on *Helicobacter pylori* (*H. pylori*) nonspecific adhesions [123]. Self-assembled monolayers (SAMs) of alkanethiols on gold were used to obtain surfaces exposing different functional groups: OH, CH_3 and ethylene glycol (EG4). After a 24 h incubation in phosphate buffered medium, a correlation was observed between number of adhered bacteria per square area and functional group, with bacterial cells adhering preferentially to CH_3-SAMs while EG4-SAMs prevented *H. pylori* adhesion [123]. The full effect of surface chemistry on bacterial attachment is not yet fully understood. However, it is evident that it plays a central role in bacteria decision making to initiate surface contact.

1.4 Irreversible Phase Two Attachment

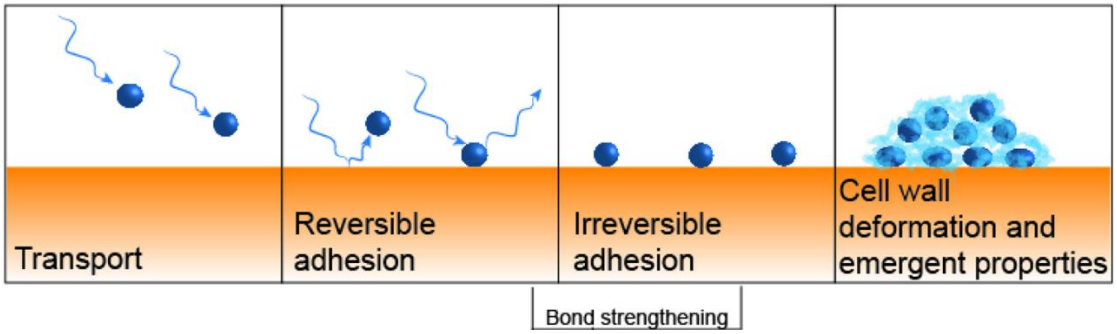

Figure 9. Schematic showing transition from reversible to irreversible adhesion through bond strengthening [124].

Once bacteria initiate surface contact, they transit to an irreversible phase (phase II) of attachment which involves securing and strengthening adhesion by generating a more permanent type of attachment achieved via interaction between the cell and the surface through the repositioning of the cell body which often involves small signalling molecules [106]. One such molecule is the cyclic diguanylate monophosphate (c-di-GMP) secondary messenger, known to play a key role in lifestyle changes of many bacteria, including transition from the motile to the sessile state, which aids in the establishment of multicellular biofilm communities.

Cyclic di-GMP has also been shown to regulate motility, virulence, the cell cycle, differentiation, and other processes. Most c-di-GMP-dependent signalling pathways control the ability of bacteria to interact with abiotic surfaces or with other bacterial and eukaryotic cells [125].

The first step in bond strengthening is the removal of interfacial water that enables closer approach of bacteria to substrate surface. A step followed by multiple tether coupling that in turn enhances the irreversibility of microbial adhesion. Repositioning of cell body (*P. aeruginosa* and *E. coli*) from initial polar adhesion mediated by flagella and pili to longitudinal position maximizes the contact area between bacterial cell and the surface. Cell wall deformation then occurs in bacteria that are in direct contact with substratum surface and it is due to the adhesion force felt by initially adhering bacteria as arising from the substratum surface, see Figure 9, [118, 124]. The characteristic result of adhesion is the production of extracellular polymeric substances known to be a biological process that contributes to strengthening bacterium-substratum adhesion strength.

1.4.1 Extracellular Polymeric Substance

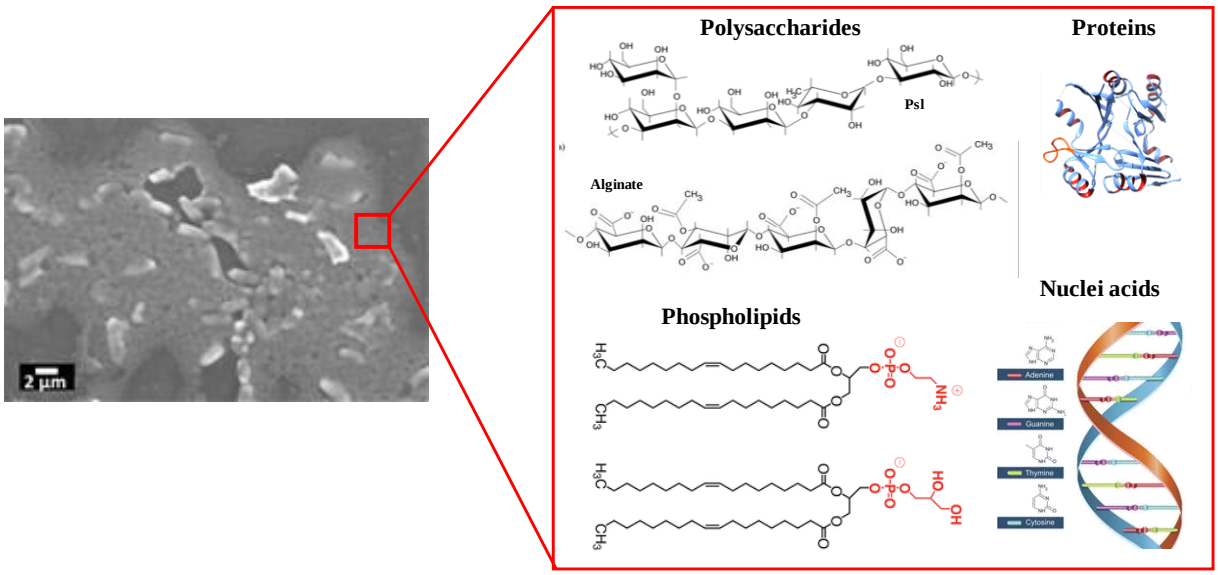

Figure 10. *P. aeruginosa* encapsulated in extracellular polymeric substances (EPS) [126, 127]. On the right hand side are shown major components of EPS: polysaccharides, proteins, phospholipids and nucleic acids.

Extracellular polymeric substances which are secreted by microorganisms during growth, consist of various organic compounds such as polysaccharides, proteins, nucleic acids and lipids, Figure 10 [128]. EPS and their composition may be the result of different processes: active secretion, shedding of cell surface material, cell lysis, and adsorption from the environment. Another mechanism of release of extracellular polymers is the spontaneous liberation of integral cellular components such as LPS, phospholipids, nuclei acids and enzymes from the bacterial cell membrane [129].

Across different bacteria species, the abundance of produced EPS components varies. For example, in experiments performed by Strathmann *et al*., EPS secreted by environmental *P. aeruginosa* mucoid strain SG81 was rich in uronic acid also identified as acetylated alginate and accounted for 87% of the total carbohydrate content in EPS [130]. In contrast, other non-mucoid strains of *P. aeruginosa* routinely used in labs such as PA14 or PAO1 have been shown to contain significantly reduced amount of alginate polysaccharides in their EPS, albeit abundant in glucose-rich Pel and mannose-rich Psl polysaccharides [131, 132].

The protein composition of *P. aeruginosa* biofilm matrix have also been studied by Toyofoku *et al.,* where they identified 178 different proteins, a category of which included exoenzymes such as proteases and amino peptidases involved in degradation of macromolecules and speculated to play a key role in nutrient provision during infection. Another category of identified proteins involved oxidative stress proteins (catalase and peroxidase) which are thought to serve as essential defence mechanism against peroxide producing phagocytic cells [133].

In biofilm systems, the chemical structures of EPS components often presenting with hydrogen bond donors/acceptors, negatively charged acetyl/phosphate groups and long hydrophobic chains are frequently responsible for binding cells and other particulate materials together

(cohesion) and to the substratum (adhesion) [134]. Both adhesion and cohesion are facilitated by weak physicochemical interactions such electrostatic interactions, hydrogen bonds, London dispersion forces and not covalent bonds. The individual binding force of any type of these interactions is relatively small compared to a covalent carbon-carbon bond. However, the total binding energies of weak interactions between EPS molecules multiply with the large number of binding sites available in the macromolecules and add up to bond values exceeding those of covalent carbon-carbon bonds [135].

The EPS protects bacteria, provides mechanical stability and confers at least 10 to 1,000 times more resistance to antibiotics or host immune cells compared to planktonic counterparts [136, 137]. Biofilm phenotype displays increased resistance characteristics and is often associated with treatment failure in implant-associated infections where *in vitro* minimum inhibitory and bactericidal concentrations do not correlate to *in vivo* antimicrobial treatment schedules. Resistance can be primarily due to secreted glycocalyx, altered growth rate also known as 'biofilm mode of growth' observed in biofilm bacteria or even transfer of genetic information via plasmids [13, 122, 138-141]. In addition, the negatively charged surface of EPS is able to interact with cationic antimicrobial agents to prevent their penetration into biofilm [142]. Von Eiff *et al*. have described the formation of biofilms as the most important feature for bacterial pathogenicity. Pathogens unable to colonise surfaces and produce biofilms are less pathogenic due to reduced adherence and increased vulnerability to phagocytosis by host immune defences when in their planktonic state [62, 143].

1.4.2 Communication Between Bacteria Cells

Cell-to-cell communication in bacteria is accomplished through the exchange of extracellular signalling molecules called autoinducers. This process, termed quorum sensing (QS), allows bacterial populations to coordinate gene expression [144]. QS was first described in the regulation of bioluminescence in *Vibrio fischeri* and *Vibrio harveyi*, and since then shown to

be a widespread mechanism of gene regulation in bacteria [145]. The uptake of QS signalling molecules has two consequences. First, they regulate a variety of behaviours such as the production and secretion of diverse exoproducts, which have various uses: virulence factors that damage the host, nutrient scavenging molecules, compounds for providing structure for growth in biofilms, and surfactants for facilitating movement, an example of which include Rhamnolipids. Second, the uptake of signal molecules also leads to an increase in production of the signal molecules (termed autoinduction). This often leads to positive feedback loop at high cell densities and to a marked increase in the cooperative production of exoproducts [146].

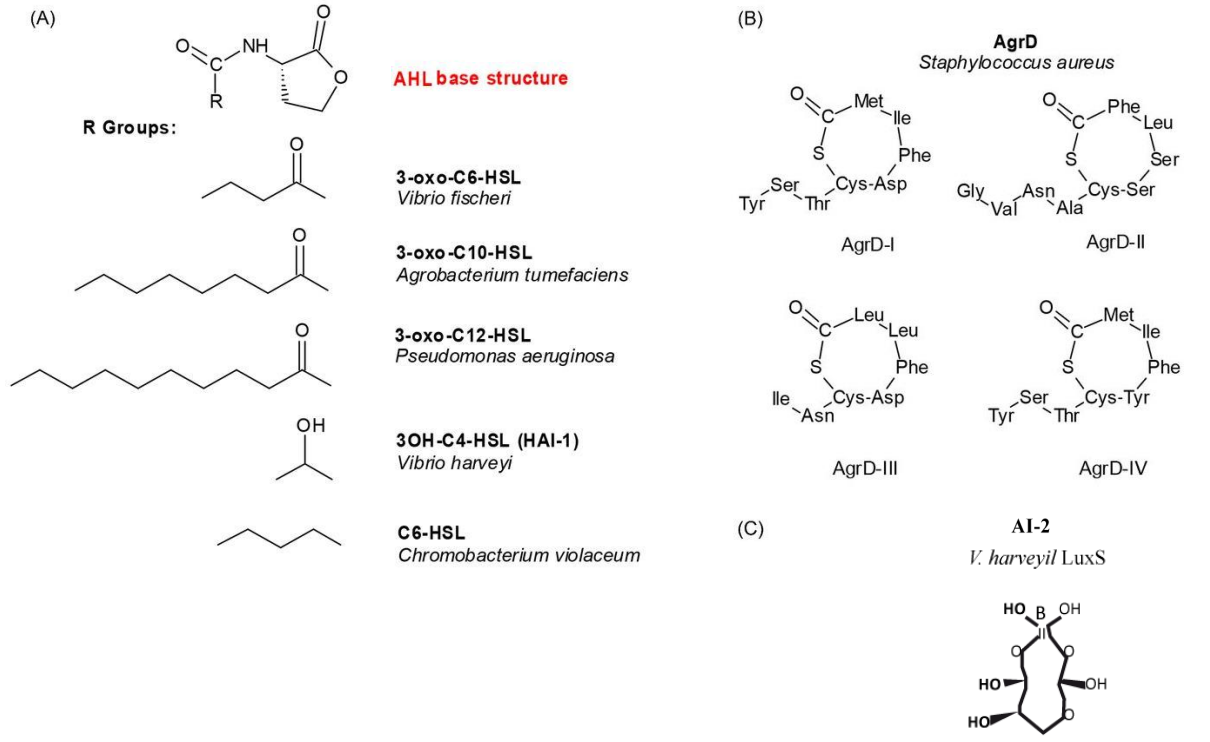

Figure 11. Structures of bacterial autoinducers **(a)** Acyl-homoserine lactones (AHLs) that are produced by various Gram-negative bacteria. Shown is the AHL base structure, plus various R groups that differ among species. **(B)** The four AgrD variants produced by *S. aureus* **(C)** AI-2 autoinducers produced by Vibrio species. Image readapted from L. A. Hawver [147].

There are three types of QS signal known to be used by bacteria. Gram-negative bacteria typically produce acylated homoserine lactone (AHLs), whereas Gram-positive bacteria use small peptides. The autoinducer-2 (AI-2) signalling molecule has been detected in both Gram-positive and Gram–negative bacteria and therefore thought to be a universal signalling molecule allowing bacteria to sense other bacterial populations, see Figure 11 [148]. Here we will

consider QS systems in well studied P. aeruginosa and S. aureus as examples to cover the two different classes of Gram-negative and Gram-positive bacteria respectively.

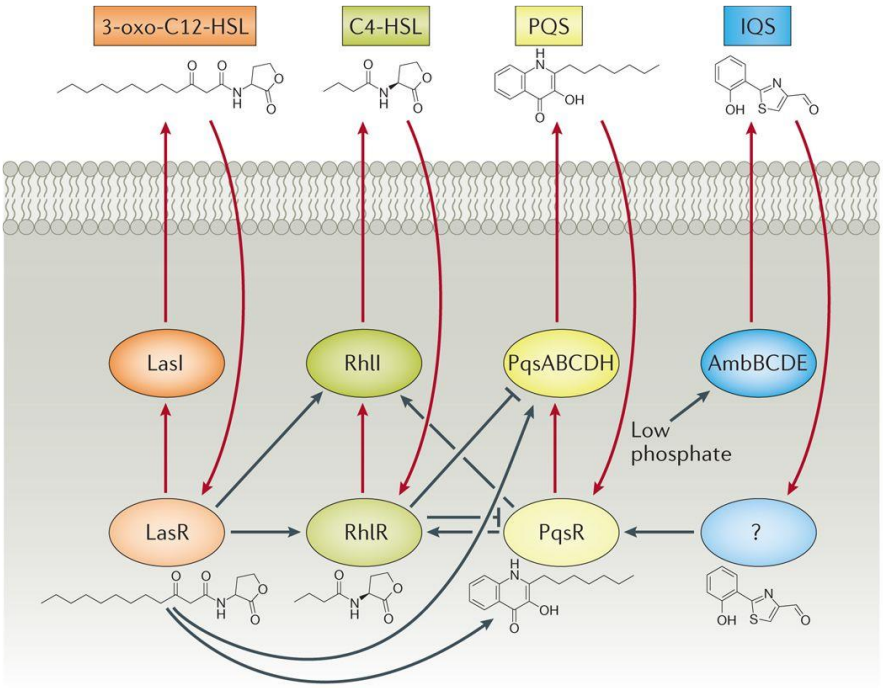

Figure 12. The four autoinducer synthases, LasI, RhlI, PqsABCDH and AmbBCDE, produce the autoinducers, 3-oxo-C12-homoserine lactone (HSL), C4-HSL, 2-heptyl-3-hydroxy-4-quinolone (PQS) and 2-(2-hydroxyphenyl)-thiazole-4-carbaldehyde (IQS), respectively. 3-oxo-C12-HSL, C4-HSL and PQS, are recognized by cytoplasmic transcription factors. The receptor for IQS is currently unknown. The production of the IQS signal is induced under phosphate starvation. The individual circuits are highly interconnected and involve autoinduction (red arrows). Image after *Kai et al.* [149].

The core of the *P. aeruginosa* QS system consists of the LasRI and RhlRI genes where LasR and RhlR are members of the LuxR family of transcriptional regulators that specifically bind to N-(3-oxododecanoyl)homoserine lactone (3-oxo-C12-HSL) and N-butanoylhomoserine lactone (C4-HSL) [150]. Together, the Las and Rhl systems have been shown to regulate between 1 and 4% of the genes carried by *P. aeruginosa*, demonstrating the global importance of these intercellular signalling systems [151]. The two other known pathways in *P. aeruginosa* are PqsR-controlled quinolone system and the IQS system that functions under phosphate-limiting conditions, see Figure 12.

The systems are organized in a hierarchy with LasR at the top of the cascade. LasR, in complex with 3-oxo-C12-HSL, activates a large regulon of downstream genes that includes the lasI synthase gene, which leads to autoinduction. The LasR–autoinducer complex also activates the

expression of RhlR and RhlI, which encode the second quorum sensing pathway, and the pqsR and pqsABCDH genes, which encode the PQS system. RhlR operates similarly to LasR, and when bound to C4-HSL, activates its own regulon that includes RhlI and thereby establishes the second autoinduction feed-forward loop. The PqsR–PQS complex feeds back to activate rhlRI, which connects the three signalling modules. In addition, RhlR inhibits the expression of pqsR and pqsABCD, and this loop is suggested to ensure the correct ratio of 3-oxo-C12-HSL to C4-HSL, which, in turn, dictates the activation of PQS, see Figure 12, [149].

A well-known example of virulent factor production by *P. aeruginosa* is that of Rhamnolipids which occurs through the RhlAB gene under QS control. Rhamnolipids also known as bio-surfactants are amphipathic glycolipids and able to influence multiple facets of *P. aeruginosa* biofilm formation, including: microcolony formation, detachment of cells from the biofilm and maintenance of open channels. The presence of open channels is thought to facilitate access to nutrients, oxygen and enable removal of waste [152].

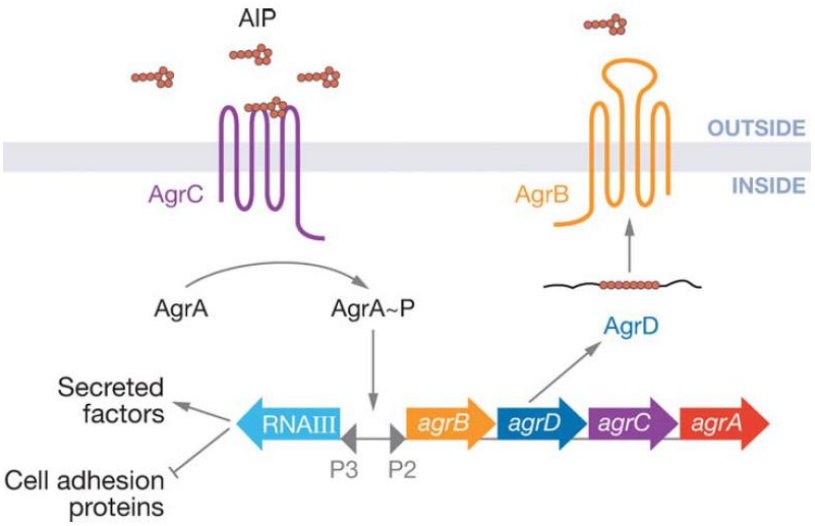

Figure 13. Using a two-component response regulatory system, *S. aureus* detects and responds to an extracellular peptide. Small red circles indicate the AIP. P2 and P3 designate the promoters for agrBDCA and RNAIII, respectively. Image after J. M. Yarwood [153].

S. aureus quorum sensing involves a system unrelated to the *P. aeruginosa* acyl-homoserine lactone system. The *S. aureus* quorum-sensing system is encoded by the accessory gene regulator (agr) locus [154].

From Figure 13, two primary transcripts, RNAII and RNAIII, are generated by the agr locus and originate from the P2 and P3 promoters, respectively. The P2 operon encodes four proteins that generate the agr-sensing mechanism. AgrB is a transmembrane protein that appears to be involved in processing of the agrD product into an octapeptide and secretion coupled with modification of the autoinducing peptide (AIP) signal. AgrA and AgrC form a two-component regulatory system in which the transmembrane component, AgrC (histidine kinase), binds the extracellular AIP and in turn modulates the activity of AgrA, the response regulator. AgrA activity then leads to greatly increased P2 and P3 transcription in the late-log phase of growth, when the concentration of the signal in the medium is high [155]. Most of the effects of QS on regulation of virulence in *S. aureus* are mediated through direct and indirect regulation by RNAIII also involved in secretion of cell adhesion proteins [156]. The QS system in *S. aureus* ultimately leads to the production and secretion of both AIP and a range of virulence factor including hemolysins α, β, δ, and γ, toxic shock syndrome toxin (TSST), enterotoxins, Panton-Valentine leukocidin (PVL), and exfoliatins A and B [157].

The multi-signal QS system in both Gram-negative and Gram-positive plays a key role in controlling virulence factor production, biofilm maturation, swarming motility and the expression of antibiotic efflux pumps while the QS signal molecules involved also contribute directly to the outcome of host–pathogen interactions at latter stages.

1.5 Current Strategies to Combat Biofilms with Focus on Urinary Catheters

Catheter associated urinary tract infection (CAUTI) is the commonest hospital-acquired infection, accounting for 40% of all nosocomial infections and over 100,000 admissions to hospital within the USA annually [158]. Total avoidance of urinary catheters is proposed to be the best way forward to prevent or reduce CAUTI, but not possible firstly for its widespread use with nearly a quarter of hospitalized patients receiving a urinary catheter and secondly due to greatly improved healthcare benefits derived for humans [159, 160]. Consequently,

contemporary solutions are based on current understanding of biofilm-formation mechanism, and can be divided into three major categories: (1) release of bactericidal agents; (2) contact-killing and (3) catheter surface modification for prevention of initial adherence [161].

1.5.1 Release of Bactericidal Agents

1.5.1.1 Silver as a Bactericidal Agent

The incorporation of bactericidal agents into medical devices was an approach that started in 2001 and has from onset involved the use of silver metal or alloy compounds intended to release silver ions to coat or impregnate silicone catheters for example, in Bard or Tyco catheters [162, 163]. It is no surprise that there are increased efforts directed towards maximising and controlling the silver ion (Ag^{+}) release from silver biomaterials, including metallic silver nanoparticles [164, 165].

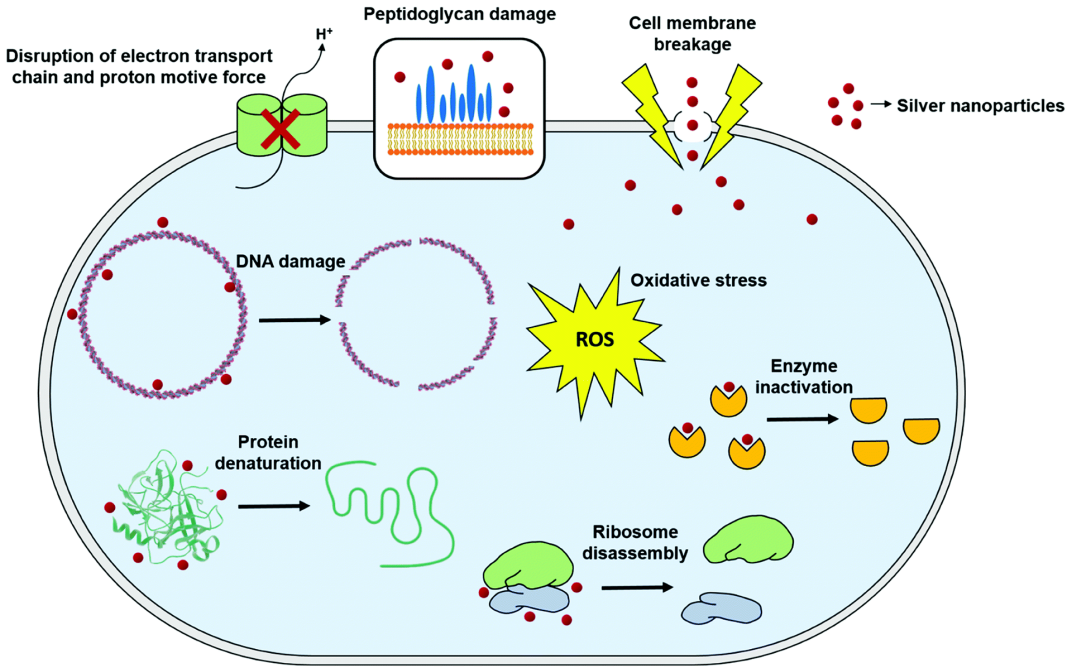

Figure 14. General mechanisms for antimicrobial mode of action of silver ions. Image after A. Roy [166].

Although the antibacterial mechanism of action for silver is still unclear, it is thought that silver ion (Ag^{+}) is the most potent and common form of silver for antimicrobial efficacy, whilst metallic silver (Ag^{0}) is most often shown not to be intrinsically antimicrobial. Theories proposed for Ag^{+} mechanism of action include protein denaturation (i.e. conformational

change), competitive inhibition of the functional groups of key enzymes, cell membrane dysfunction, cell division interruption, generation of reactive oxygen species and interaction with DNA base groups caused by silver ion (Figure 14) [167, 168].

Irrespective of the mechanism by which it functions, recent meta-analysis of collections of smaller trials have questioned the efficacy of expensive silver coated catheters as there were no statistical differences in CAUTI rates between patients using silver impregnated or non-silver impregnated urinary catheters [162, 169]. There have also been disappointing clinical results with this method, despite the reduced biofilm formation from pathogens such as *E.coli* and *Enterococcus* [170]. Silver nanoparticle-coated catheters are also thought to be genotoxic and cytotoxic on human cells at high doses as a result of damage to DNA and chromosomes from oxidative stress, which may ultimately induce mutagenicity [171].

1.5.1.2 Antibiotic Impregnation

Impregnating catheters with organic antibiotic molecules effective at low concentration is another route undertaken by manufactures and researchers. So far, nitrofurazone impregnated catheter has been the only approved and commercially available urinary catheter in this category, though not totally void of concerns with reports on its narrow spectrum of activity that excludes relevant clinical strains like *P. aeruginosa* [159, 172].

However, there has been an increased effort by researchers attempting to impregnate catheters with a combination of bioactives. One such example is highlighted in a work carried out by Bayston *et al*. where they impregnated urinary catheters with a combination of rifampicin, sparfloxacin and triclosan. Their results showed the antimicrobial catheters prevented colonization by common uropathogens: *Pr. mirabilis, S. aureus* and *E. coli* for 7 to 12 weeks *in vitro* compared with 1–3 days for other commercially available antimicrobial catheters currently used clinically [173].

In an attempt to develop novel and smart materials as candidate coating for urinary catheters. Colin *et al*. exploited pathogen-induced elevation of urine pH caused by urease enzyme activity as a trigger for "intelligent" antimicrobial release from novel hydrogel drug delivery systems of 2-hydroxyethyl methacrylate and vinyl-functionalized nalidixic acid derivatives. They showed that *in vitro* and at pH 10 representative of infected urine pH, there was up to a 96.5% reduction in adherence of ureolytic bacteria such *S. aureus* and *Pr. mirabilis* after a 24 hour incubation [29].

The dual combination of pathogens developing resistance coupled with selective pressure exerted by antibiotics may pose some limitations to their use as a permanent solution, particularly at the diminished rate at which antibiotics are entering the market [174, 175].

1.5.2 Contact Killing

There are some limitations and disadvantages from using release of biocidal agents; nonspecific leaching of bioactive, their narrow spectrum of action, emergence of resistant strains and difficulty in achieving sustained release amongst many other. To address these, researchers have turned attention to contact active materials, which generally employ surface grafted moieties that are lethal to various bacteria upon contact [176].

1.5.2.1 Quaternary Ammonium Compounds and Antimicrobial Peptides

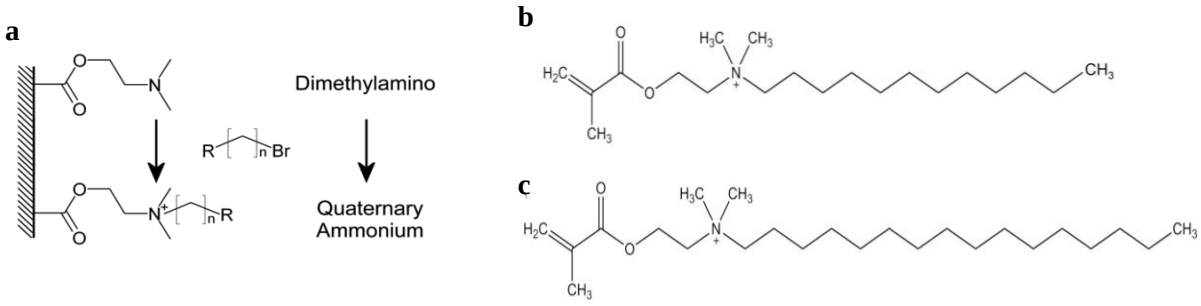

Figure 15. **(a)** Polymers containing tertiary amino groups, like poly(dimethylaminoethyl methacrylate), can for instance be quaternized by specific functional halides. The chemical structures of two quaternary ammonium monomers **(b)** Dimethylaminododecyl methacrylate and **(c)** Dimethylaminohexadecyl methacrylate.

Quaternary ammonium compounds (QACs) are not only used as disinfectants in hospitals, because of their ability to kill bacteria, but have also found application in contact killing surfaces, where they are used to functionalise polymer surfaces by grafting and are also regularly employed as surface modifying agents for medical devices [177]. QACs can easily be obtained from quaternization of tertiary amino groups by specific functional halides, see Figure 15A, [178]. The presence of positive charge on the surface due quaternary ammonium (Figure 15B-C) has been shown to have a negative effect on cell survival in general. The main antimicrobial activity of QACs is associated with their cationic, surfactant characteristics. Upon contact, the membranes of the microbes will become distorted, leaky and consequently the microbe will die [179]. This process is also known as membrane suctioning [180, 181].

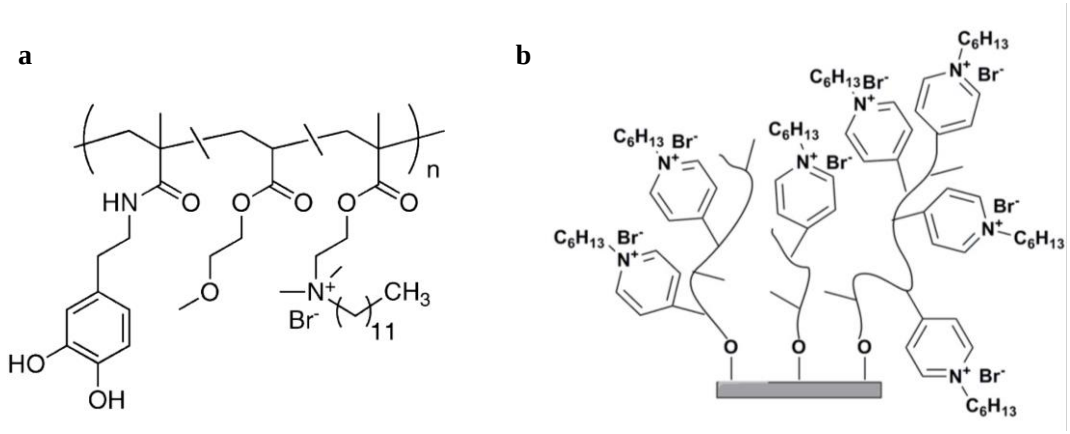

Figure 16. **(a)** Chemical formula for polymer composed of dopamine methacrylamide (DMA), methoxyethyl acrylate (MEA) and 2-(dimethylamino)ethyl methacrylate (DMAEMA). **(b)** Polymer with quaternary ammonium group derivatized from quaternization of 4-vinylpyridine groups with hexyl bromide. Image adapted from H. Han and L. Cen [182].

Han *et al*. showed that in comparison to uncoated glass slide, *S. aureus* and *E. coli* died upon contact when exposed to a glass slide coated with a copolymer composed of alkyl quaternary ammonium (DMAEMA), methoxyethyl (MEA) and catechol (DMA), see Figure 16A. The coating also prevented the accumulation of viable *E. coli, S. aureus,* and *Acinetobacter baumannii* for up to 96 hours. The inability of bacteria cells to remain adhered to these surfaces was considered advantageous for the surface to retain antimicrobial activity. [182]. In a different study by Cen *et al.*, polycationic chains introduced on the substrate surface via derivatisation of the pyridine groups by hexyl bromide (Figure 16B) showed the desired

antibacterial activity against *E. coli*. The bacteria killing efficiency was dependent on the surface pyridinium concentration [183]. They hypothesized the antimicrobial mechanism for long alkyl chain modified poly(vinyl pyridines) was dependent on immobilized cationic side chains of polymers interacting with negatively charged bacterial cell surfaces, and that the long alkyl chains with ammonium functionality inserted into the cell membranes, leading to the disruption of membrane integrity and cell death [182].

Antimicrobial peptides (AMP) grafted onto surface of medical devices are also an attractive alternative that act through contact killing mechanisms. Recently, an optimized surface active AMP, labelled with cysteine at the C-terminus was coated onto surface of polyurethane catheter. The surface coating prevented bacterial adhesion by up to 99.9 % for both Gram-positive and negative bacteria, and inhibited growth of planktonic bacterial by up to 70 % [184].

1.5.3 Antifouling Coatings

The principal goal of the antifouling strategy is to prevent initial adhesion of bacteria, thereby reducing biofilm development in a non-bactericidal manner. Hydrogel-coated devices have been used clinically for over two decades and constitute attractive materials for medical device coatings on the basis of their characteristic biocompatibility, resistance to non-specific macromolecular adhesion and similar degree of flexibility to body tissue [185].

1.5.3.1 Polyethylene Glycol

Polyethylene glycol (PEG) in its oligomeric or cross-linked hydrogel state is useful not only in its several pharmaceutical applications such as preparation of hydrophilic ointment base for incorporating a wide variety of therapeutic agents, but also well-known for its ability to resist protein adsorption because of its hydrophilicity, large excluded volume and unique coordination with surrounding water molecules in aqueous medium (section 1.3.1.1, Figure 7)

[186]. Nie *et al.* showed that surface modification by the immobilization of PEG improved antifouling property and biocompatibility of poly(acrylonitrile)-based polymer [187]. Dong *et al.* evaluated the antifouling ability of PEG-modified stainless steel surfaces and compared to unmodified stainless steel surface. Their result showed between 81-96% reduction in *Listeria monocytogenes* attachment and biofilm formation [188]. In some commercially available catheters such as Bardex®, the incorporation of silver alloy into PEG hydrogels coatings produce a dual antifouling and bactericidal effect. Although PEG has been successfully employed for antifouling purposes, it has several disadvantages including rapid autoxidation in the presence of oxygen and transition metal ions contained in most biologically relevant solutions [189]. *In vivo,* the hydroxyl groups of PEG can be oxidized enzymatically to aldehydes and acids, allowing proteins and cells to attach. The susceptibility of PEGs to oxidation damage reduces their utility for applications that require long-term material stability [190].

1.5.3.2 Poly(2-hydroxyethyl methacrylate)

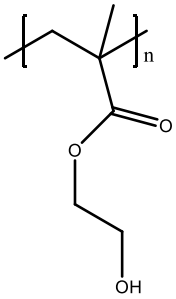

Figure 17. Chemical structure for poly(hydroxyethyl methacrylate)

The polymer of hydroxyethyl methacrylate (pHEMA) is one of the most versatile, widely studied and used synthetic hydrogel ever since the pioneering work by Wichterle and Lim in 1960 where HEMA was copolymerised with ethylene dimethacrylate to obtain adequate stability, swelling and mechanical properties [191, 192]. Poly(HEMA) is biocompatible and has been used in a variety of medical applications including dressings, drug delivery and contact lenses [193, 194]. The use of pHEMA in contact lenses is due to its intrinsic capacity to absorb water (up to 38%), which permits atmospheric oxygen dissolution when in contact with air.

Secondly, owing to the hydrophilic nature of pHEMA, tear film is easily extended to lenses and held in position due to its high surface tension [195].

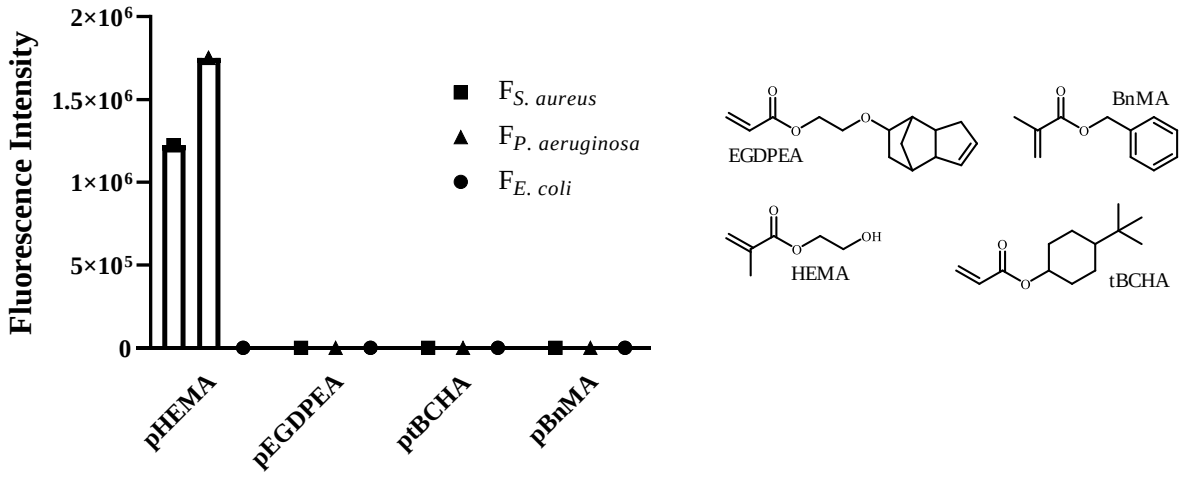

Figure 18. Attachment of *S. aureus*, *P. aeruginosa* and *Uropathogenic E. coli* measured via fluorescence on polymer surfaces made from monomers of hydroxyethyl methacrylate (HEMA), ethylene glycol dicyclopentenenyl ether acrylate (EGDPEA), *tert*-butyl cyclohexyl acrylate (tBCHA) and benzyl methacrylate (BnMA). Data from A. Hook *Adv. Materials 2013* [196].

In a similar way to ethylene glycol (Figure 7, section 1.3.1.1), the ability of pHEMA to interact with water molecules via hydrogen bonds, leads to the formation of a layer of tightly bound water molecules at its surface. The energy penalty accompanying the expulsion of this ordered layer by fouling agent often represent an insurmountable barrier [197]. This intrinsic mechanism of antifouling pHEMA has allowed its use as coating agent to control cell adhesion, cell growth and protein adsorption [198]. However, a consequence of this high water content is the significantly compromised ease of handling of the material, because of the reduced concentration of network chains in the swollen state. Hence, as bulk polymers, pHEMA lacks the mechanical strength and elasticity required for applications such as coating of urinary catheter [199]. In Figure 18 is data from Hook *et al*. comparing the performance of pHEMA to ethylene glycol dicyclopentenyl ether acrylate (EGDPEA), *tert*-butyl cyclohexyl acrylate (tBCHA) and benzyl methacrylate (BnMA) in preventing attachment from three different species: *P. aeruginosa*, *S. aureus* and *E. coli* after a 72 hour incubation in RPMI culture media [196]. The polymer from HEMA performed well against *E. coli*, but did not show similar resistance against *P. aeruginosa* and *S. aureus*. In contrast, the comparator surfaces, pEGDPEA,

ptBCHA and pBnMA, with better mechanical properties, all displayed broad resistance against the three bacterial species tested.

1.5.3.3 Zwitterionic Materials

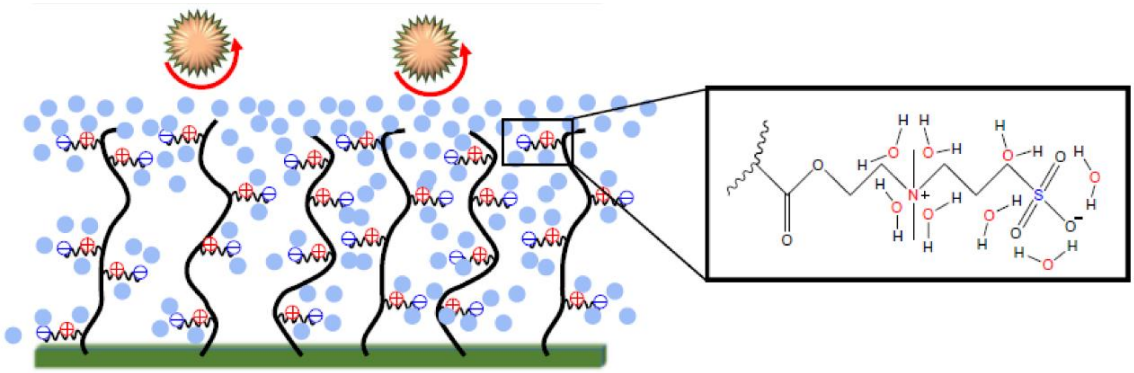

Figure 19. Schematic illustration for the formation of hydration shell. Each unit of the zwitterionic material is integrated with eight water molecules. Image adapted from Shahkaramipour [86].

Zwitterionic-based materials have both positively and negatively charged moieties, which are uniformly mixed such that they are electrostatically neutral Figure 19. They have received increasing attention because of their biocompatibility [200, 201]. Materials such as poly(2-methacryloyloxethyl phosphorylcholine) (polyMCP), poly(sulfobetaine methacrylate) (polySBMA), and poly(carboxybetaine methacrylate) (polyCBMA), have demonstrated their excellent bio-inert capacity and high stability in many complex media including undiluted human blood serum/plasma [117]. It has been proposed that zwitterions have the capability to tightly binding significant quantities of water and function by forming a hydration layer via electrostatic interactions, thus creating a repulsive barrier for organic molecules and making them excellent candidates as non-fouling materials, see Figure 19, [201]. Smith *et al*. noticed that the modified surface of a commercially available catheter with pSBMA effectively reduced protein, mammalian cell, and microbial attachment *in vitro* and *in vivo*. Adherence of a broad spectrum of microorganisms was reduced on both the external and the internal surfaces of pSBMA-modified catheters compared to unmodified catheters and 50% less inflammation coupled with fewer bacteria were associated with pSBMA-modified catheters [202].

1.5.3.4 Novel Materials

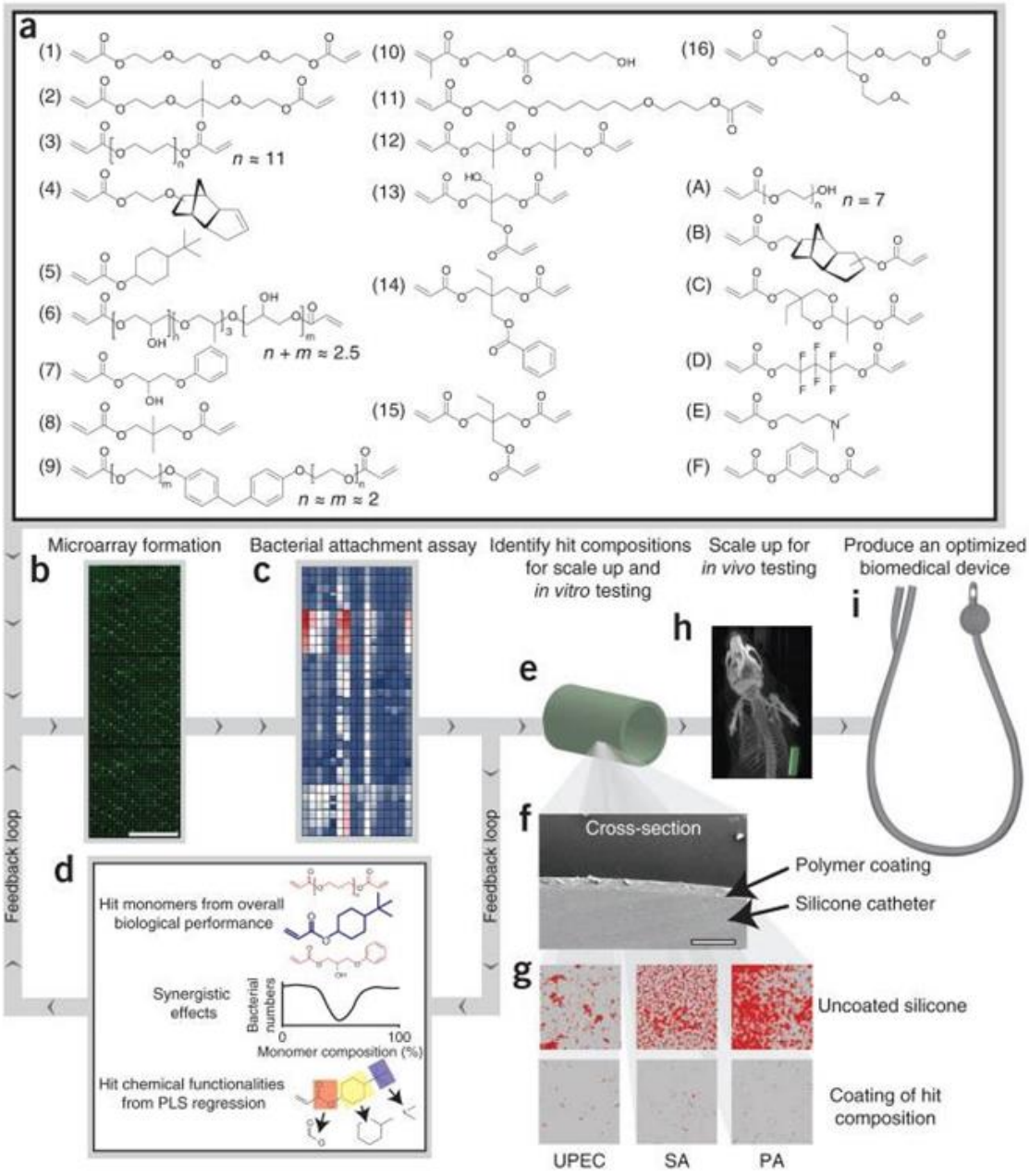

Figure 20. Schematic of the approach used to identify hit materials resistant to bacterial attachment and scale-up of hit materials. (**a**) The chemical structures of the monomers screened. (**b–f**) Outline of the strategy utilized for identifying hit material. (Image source [89])

In 2012, Hook *et al*. employed a high throughput microarray screening method to determine the attachment of selected bacterial species *(P. aeruginosa, S. aureus* and *E. coli*) to hundreds of structurally related polymeric materials comprising of ester and cyclic hydrocarbon moieties that substantially reduced their attachment. Coating silicone catheters with these 'hit' materials achieved up to 30-fold reduction in the surface area covered by bacteria compared with commercially available silver hydrogel coated catheter and also reduced bacteria attachment *in*

vivo, resulting in the granting of a CE mark for a urinary catheter device [89]. Building up from this, Hook *et al.* expanded their screening library to include most commercially available acrylates and meth(acrylates), studying the bacterial resistance of 116 materials. The findings were consistent with their previous results, materials with a combination of mildly hydrophilic ester groups and hydrophobic cyclic hydrocarbon groups reduced attachment of a broad spectrum of bacterial [196]. Unlike bactericidal silver or zwitterions that sterically hinder bacteria attachment, the mechanism of action by which this class of novel materials effectively prevent bacterial attachment still remains unknown and what is really clear is that these materials do not kill bacteria.

1.6 Aims and Objectives

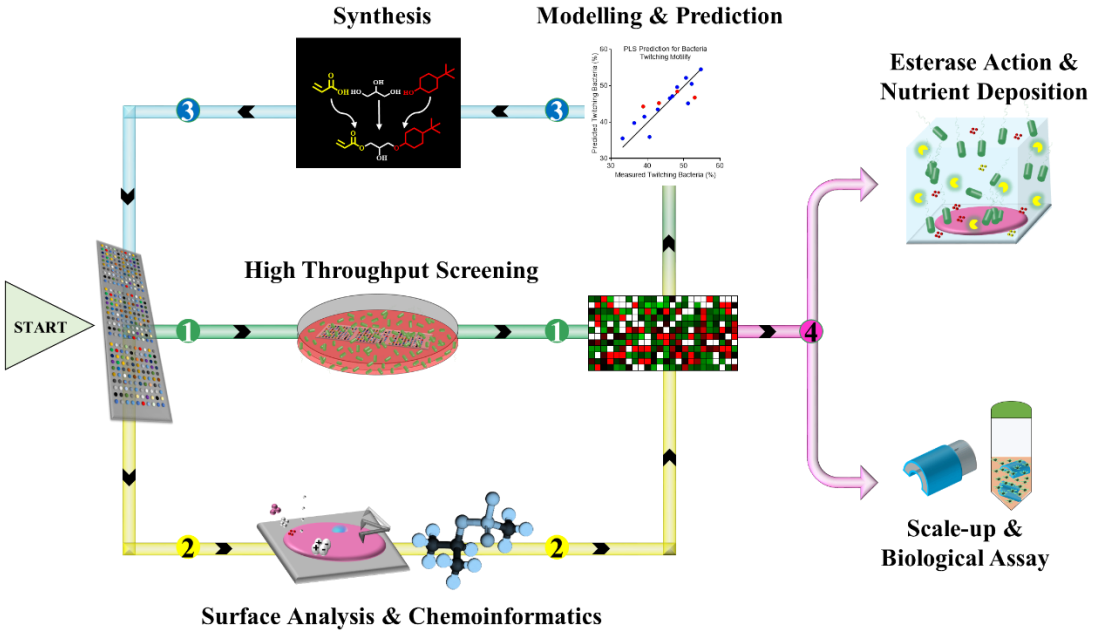

Figure 21. An overview of experimental approaches used to investigate action mechanism of novel anti-attachment materials in this thesis.

The aim of this thesis was to investigate the action mechanism of novel polymers that reduced attachment of *P. aeruginosa in vitro*. An overview of the various approaches employed is schematised in Figure 21, where hundreds of polymeric materials printed onto a glass slide are biologically screened against bacteria to assess their anti-attachment performance (green pathway). In parallel, polymer surfaces are characterised using surface analytical methods and

chemoinformatics (yellow pathway). Data generated from both yellow and green pathways are then combined to construct predictive models used to identify new chemistries for chemical synthesis and polymer library expansion (blue pathway). Interesting polymeric materials identified from microarray screens are scaled-up to either test new hypothesis on mode of action or coated on medical devices for further biological assays (pink pathway).

The objectives were as follows:

- Use high throughput surface characterisation to *experimentally* probe surface chemistry of all materials to identify key features most relevant to bacteria decision making.
- Identify effective *theoretically* derived molecular descriptors for polymer surface chemistry and correlate surface property of materials to biological response of *P. aeruginosa.*
- Validate existing predictive models by predicting, synthesizing and testing biological function of selected new monomers.
- Generate and test new mechanistic hypothesis for anti-attachment materials.

Chapter 2 - Materials and Methods

2.1 Materials

All commercially available materials used in this project were utilised as supplied by Sigma Aldrich or VWR. Various aspects of this project adopted a high throughput screening methodology which involved the use of hundreds of materials listed in Appendix E with IUPAC nomenclature and in-house acronyms. Where appropriate, chemical structures for materials of interest are revealed in result chapters. All solvents employed were ordered from Fisher Scientific UK and used as-received with exception of Toluene that was dried with molecular sieves when necessary for use in silanisation procedures reported in section 2.2.1. Names of chemicals used are directly reported in experimental section of each chapter.

2.2 High Throughput Microarray Screening

High Throughput Screening (HTS) is an approach to drug discovery that basically involves screening and assaying a large number of biological modulators and effectors against selected and specific targets, a technique embraced in non-discriminatory fashion by both industrial and academic scientists [203]. HTS has successfully revolutionised research in genomics, proteomics and beyond this, has also made tremendous impact in screening and discovery of novel biomaterials that allow for long term renewal of pluripotent stem cells, and also identification of novel biomaterials that resist bacterial attachment [89, 204].

Interesting progressions from HTS to high throughput surface characterisation (HTSC) using analytic methods such as ToF-SIMS, wettability measured by water contact angle, x-ray photoelectron spectroscopy, Raman and atomic force microscopy which reveal surface intrinsic properties of the top 2 nm mainly responsible for instructing biological response have become relevant. Data obtained from HTSC may be correlated to biological response from HTS with

the help of recent advances in chemometric analytical tools, a key step that has contributed to the transitioning of HTS from a random to a more predictive method [205].

Historically, HTS has strongly relied on the microarray platform that allowed the successful screening of microspots of DNA, protein or small organic compounds that can be probed with possible binding ligands. Together with advances in fluorescence-based techniques for detecting the incidence of interactions, we are now equipped with the possibility of simultaneous analysis of thousands of variables in a single experiment [206]. There are however essential rigorous methodologies involved in the fabrication and screening of microarrays, particularly materials microarray, these are namely: (a) substrate modification (b) microarray printing (c) high throughput surface characterisation (d) high throughput surface screening.

2.2.1 Substrate Modification

The success of a microarray fabrication process is largely dependent on having a substrate that minimises defects within the printed materials, ensures good adhesion or immobilization of printed material and prevents non-specific adsorption during bioassays [207]. Standard glass slides are not suitable candidates as substrates primarily due to the ease by which weakly interacting polymers peel off its surface and secondly for its high fouling reputation during bioassays [208]. To circumvent this, we adopted a method previously reported by Anderson *et al.* where surfaces of glass slides were modified with epoxy silane and uniformly coated with low fouling poly(hydroxyethyl methacrylate) (pHEMA) that promoted adhesion of materials onto its surface by allowing interpenetration of monomers and potentially becoming fixed in place upon polymerisation [209].

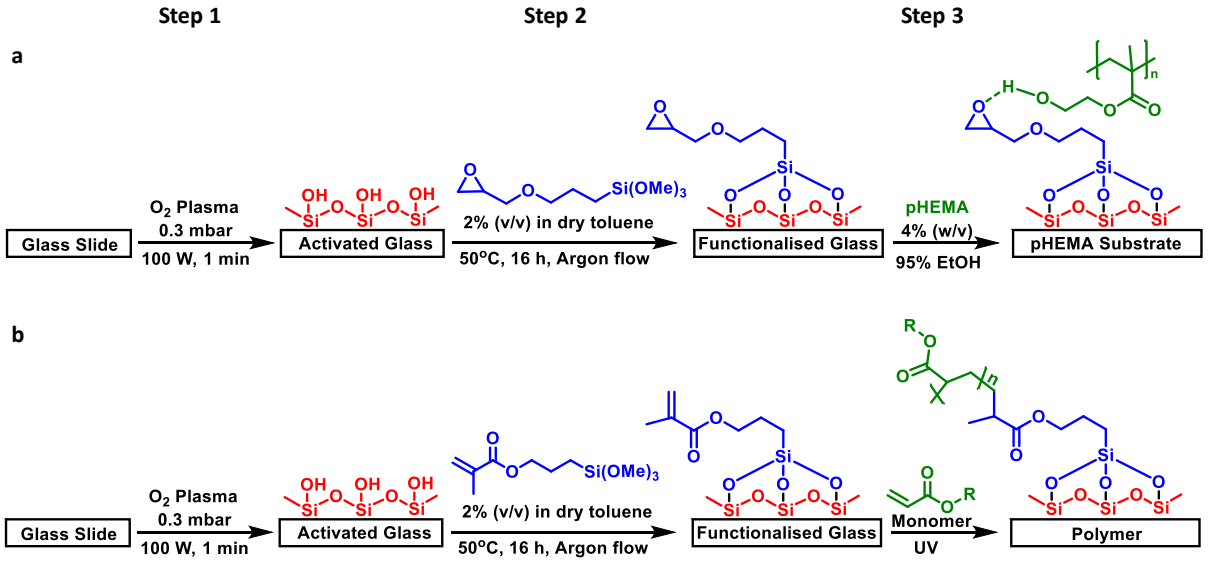

Figure 22. **(a)** Summary of substrate modification process for polymer microarray fabrication. Step 1 involves oxygen plasma cleaning of commercially available glass slide to expose surface hydroxyl groups, followed by silanisation of activated slides with 3-(Glycidyloxypropyl)trimethoxysilane in Toluene solvent for 16 hours at 50 °C. The last step is the coating of epoxy functionalised slides with 4% (w/v) solution of pHEMA in ethanol. **(b)** Summary for methacrylate silanisation of glass slides or coverslips. The modification process is similar to (a), differing for the silane used: 3-(trimethoxysilyl)propyl methacrylate. In step 3, a methacrylate or acrylate monomer with any pendant R group is photopolymerised onto modified surface. (Method used during the course of this project)

In this work, substrate modification was conducted in-house based on cost benefits comparisons with commercially accessible substrates. One fundamental guiding principle for this process (see Figure 22, step 1) is that surface activation can be achieved using O_2, N_2 or H_2 plasma gases to remove surface contaminating organic groups and creating new functional groups on the surface. Plasma is efficient enough to break weak surface bonds present in the organic substances and replace them with highly reactive hydroxyl groups to increase adhesion strength [210, 211]. Subsequently, the activated glass surface with exposed hydroxyl groups is able to covalently bond with methoxy groups from silane compound via a condensation reaction, which also explains why reaction is carried out under dry argon conditions to avoid competition from water associated hydroxyl groups in the air. The molecular interaction between the epoxide moiety (hydrogen bond acceptor) and the hydroxyl group in pHEMA (hydrogen bond donor) serves to promote adhesion of pHEMA onto silanised glass surface.

For methacrylate silanisation, a similar guiding principle to that reported above applies. However, the silane 3-(trimethoxysilyl)propyl methacrylate is used in place of the epoxy silane,

see Figure 21b. Upon exposure to UV light, the methacrylate functionality participates in the formation of a strong carbon-carbon covalent bond between polymer and substrate, which helps to prevent polymer detachment from substrate for experiments conducted in aqueous solution.

The coating of pHEMA onto functionalised glass slides can be easily achieved through manual dipping of slides into a solution of pHEMA in volatile solvent such as ethanol. Alternatively, a semi-automated way is possible with the use of dip-coater instrument. A key concern at this stage is the uniformity and reproducibility of thin coating layer, which is actually dependent on retraction speed from dip solution, albeit influenced by uncontrolled human variability in manual approach. There is a well-established relationship between retraction speed and coating thickness: thicker coatings are a product of greater retraction speeds, because the viscous coating solution is not allowed sufficient time to pull off and vice versa. Thus, to eliminate variability we used a robotic dip-coater unit (Holmarc, India) (Figure 23) in this project.

Figure 23 Automated dip coater used to dip coat glass slides with pHEMA solution.

The adhesion between epoxy functionalised slide and pHEMA is based on non-covalent interactions strong enough to hold coating on surface.

In a routine dip-coating cycle used here, 5 epoxy silanised glass slides were dipped at 9 mm/s into a 200 ml solution of 4% (w/v) pHEMA dissolved in 95% (v/v) ethanol in water for 2s. Slides were then retracted at 2 mm/s and allowed to dry at ambient conditions for 5 minutes.

This process was repeated three additional times after which slides were firstly dried overnight at ambient conditions and then dried in oven for 7 days.

2.2.2 Microarray Printing

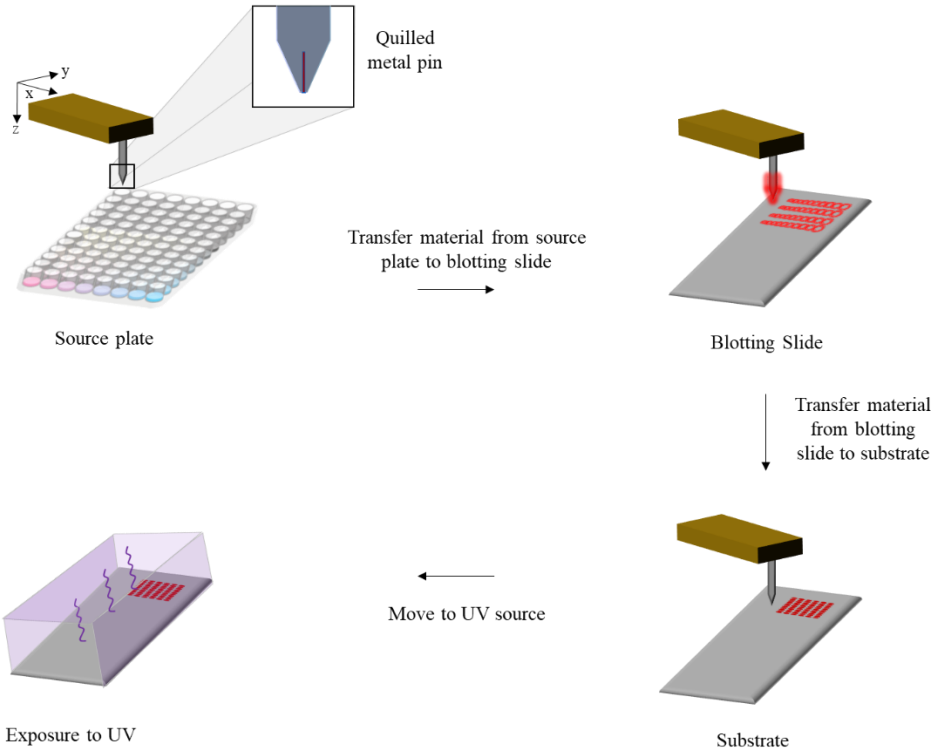

Figure 24. Schematic representation of key processes involved in printing of polymer microarray.

Polymer microarrays have been fabricated using a variety of patterning technologies categorized into two main methods “contact printing” and “non-contact printing.” Contact printing is a widely used technology, comprising methods such as contact pin printing and microstamping [212]. The contact printing often uses a steel metal pin to load the monomer “ink” and then deposit the “ink” onto a substrate by direct close contact, the pins are attached to a high-precision robotic arm capable of 3D movements, which facilitates the precise location of microarray spotting [205, 213]. Steel metal pins are chemically resistant, making it easy to wash off monomer “inks” with solvents between subsequent loading cycles.

Advantages of contact printing include the possibility of printing large numbers of polymer spots with a single uptake, defined loading volume, tightly defined spot diameter, no

mechanical differences between printing pins and durable over millions of printing cycles. Disadvantages include environmental control (e.g. humidity) required for optimal printing and high replacement cost of pins if robot crashes [214].

In this project, a routine microarray print was carried out using a XYZ3200 pin printing workstation on a Biodot® contact printer (CA, USA) and four 946MP6B slotted metal pins (Arrayit, USA) with a tip diameter of 220 µm which were used to transfer approximately 2 nL of pre-mixed monomer solution with photoinitiator from a chemically resistant polypropylene 384-well plate onto pHEMA coated substrate slides. The metal pins as well as printer pin head were cleaned with plasma for up to 1 hour prior to use, a necessary step to prevent pins getting stuck or blocked during print runs or transferring contaminants from previous runs. In order to obtain regular-sized spots with homogenous diameter, excess monomer solution adsorbed onto the exterior of steel pin was initially blotted multiple times onto a normal glass prior to printing on substrate, see Figure 24. It has also been previously reported that (meth)acrylates monomers have high photopolymerization rate and solubility in high boiling point organic solvents (e.g. DMF). In fact, light-assisted polymerizations of (meth)acrylates have been extensively used to prepare synthetic polymer microarrays and we have adopted same approach in this project [213].

The array fabrication run was designed using a macro on the Biodot software, the printing was done using four steel pins, organised such that four monomer solutions were printed in each printing loop followed by pin washing prior to printing the next four monomers. The basic components of each loop were (a) the quilled steel pins were filled with monomer solutions by dipping the pins into well plate at a set speed of 1-5 mm/s, remained in solution for 2.5 seconds and lifted out of the solution at 10 – 175 mm/s, (b) the filled pins were pre-printed 35 times on blank glass slides to remove excess monomer solution from the outside of the pins, (c) the monomer solutions were printed onto pHEMA coated slides by making pin contact on the

surface at a speed of 1 – 5 mm/s, (d) the pins were washed in the flow bath of DMF twice, before continuing with the next loop. The monomer solutions printed on the substrate slide were then irradiated with ultraviolet (UV) light (30 watt, λ = 365 nm) for 10 seconds between each print loop. After pin printing all the monomer solutions, the slides were further irradiated for 10 minutes using UV light. The printing was done in a sealed chamber with oxygen concentration below 2000ppm (to prevent free radical quenching by oxygen), at 30 – 35% relative humidity and at room temperature. The polymers were placed under vacuum (< 50 mTorr) for one week to remove DMF and any unpolymerised monomers.

2.3 Surface Characterisation and Multivariate Analysis

Characterising the surface of biomaterials is of paramount importance for the role and activity they play in instructing biological responses.

2.3.1 Time-of-Flight Secondary Ion Mass Spectrometry (ToF-SIMS)

ToF-SIMS is a qualitative technique used for the surface characterization analysis, providing information related to the molecular compounds, typically fragments of much larger organic macromolecules from the outermost surface of the sample. It is considered as a destructive technique due to the impact of the ion beam that destroys the first monolayers on the surface's sample.

The sputtering process central to the SIMS technique can be described as a collision cascade of particles in the sample being analysed (Figure 25). A focussed beam of primary ions from an ion gun source is rastered in a pulsatile manner onto the sample to set atoms in motion, both by direct collisions between the primary ions and the atoms in the sample or indirectly by collisions of atoms in the sample already in motion with other atoms in the sample (knock-on effects) [215]. Since the typical primary ions are in the KeV range, they are capable of breaking any

chemical bond, with intense fragmentation occurring near the site of impact thus producing atomic particles (also termed secondary ions) overall at site of impact. Desorption of molecular fragments also occurs at a distal site where propagated energy is only sufficient enough to overcome surface binding energy of molecular fragments. Most desorbed particles come off as neutrally charged with only a small proportion (10^{-6} – 10^{-1}) coming off as either negatively or positively charged that can be mass analysed.

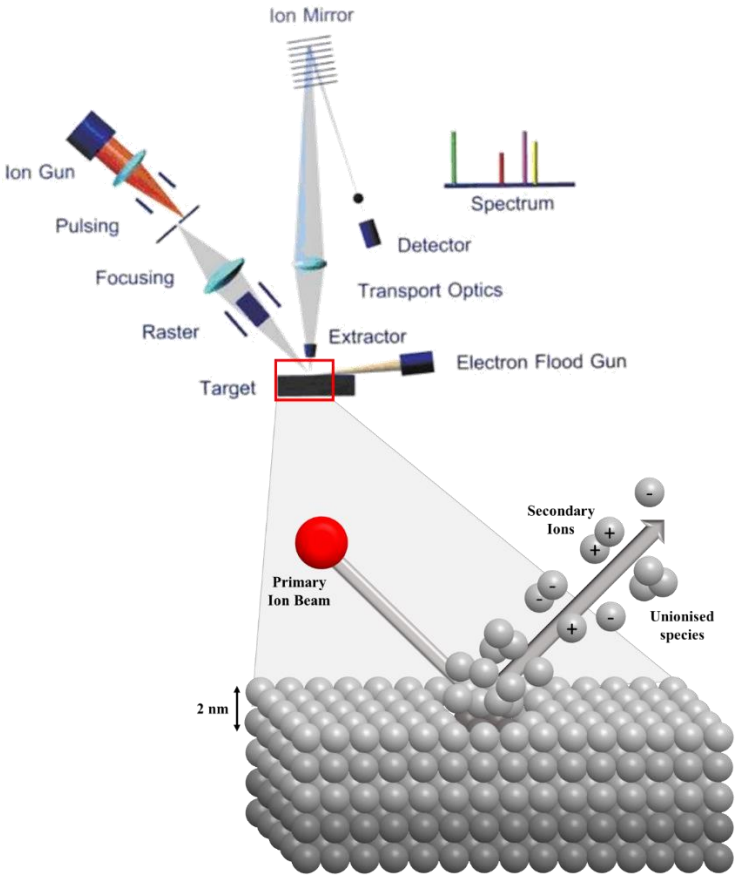

Figure 25. Diagram of time-of-flight secondary ion mass spectroscopy (ToF-SIMS). Schematic illustrates primary ion bombardment of first monolayer samples (1-2 nm depth) producing the ejection of secondary ions from the surface.

Depending on the ion dose, the technique can be very surface sensitive (1–2 nm) and with a finely focused primary ion beam, high lateral resolution of the order of a few tens of nanometers can be achieved. Ion dose is an important parameter that leads to two different modes of SIMS: "static" SIMS characterised by low primary ion dose (< 10^{13}/cm^2 with 10 pA – 5 nA), and "dynamic" SIMS characterised by high flux (μA), rapid erosion rates yielding elemental distribution or depth profiles [216].

Secondary ion yield does not generally provide a direct quantitative determination of analyte concentration in a sample, as the ionization efficiency of molecules in a heterogeneous sample is affected by neighbouring molecules. Molecules with high ionization efficiency suppress the ionization of other molecules with a lower ionization efficiency. This general and well-known phenomenon is called the matrix effect [217]. The matrix effect makes quantitative analysis with ToF-SIMS complicated.

Upon desorption, the secondary ions are extracted into an analyser by a high voltage potential and their mass is determined by measuring their time-of-flight from the sample to the detector. All secondary ions generated from one pulse are accelerated by passage through a fixed accelerating voltage before entering the flight path. The polarity of the fixed voltage determines whether positive or negative secondary ions are analysed. It follows that all the ions which enter the flight path with the same kinetic energy separate according to their mass, because lighter ions travel with greater velocity than ions with higher mass [218]. That is the velocity is inversely correlated to the mass of ion fragment. The relationship between kinetic energy, mass and velocity is shown in Equation 2 below:

$$E_k = \frac{1}{2}mV^2$$

Equation 2

Where E_k is the kinetic energy, m is the mass and V is the velocity of desorbed secondary ion. Ions with greater velocity will require a shorter time to arrive at detector. It is therefore possible to calculate the mass of detected fragments by rearranging Equation 2 to account for velocity as a relationship between displacement and time, thus giving rise to Equation 3 below:

$$t - t_0 = L\left(\frac{m}{2E_k}\right)^{1/2}$$

Equation 3

Where t_0 is the start time and t is the arrival time of an ion at the detector, L is the length of the flight path, m is the mass and E_k is the kinetic energy of an ion.

The function of the transport optic lens focusses the ion beam onto the detector in addition to the ion mirror that serves as a focussing element used to compensate the energy and angular variations of secondary ions that originate with the emission process. A common mode of action is through a retarding electric field in the middle of the flight path, whose end results is improved mass separation and consequently higher mass resolution.

If a sample is dielectric, it retains and accumulates charge on the surface under study and thus alters the trajectory of the secondary ions. This process generates measurement artefacts and lowers the efficiency of the secondary ion detection. Therefore, for the charge compensation an additional electron flood gun is used that irradiates the region under study by the electron flow with energy of about 20 eV. The gun is activated between the impulses of the primary ions, and the intensity of the sample irradiation is regulated by increasing or decreasing thermionic emission of electrons [219].

The lateral distribution of secondary ion emission, and therefore that of the surface constituents responsible for emission is measurable from a few microns down to 50 nm. This gives the possibility to construct an image for each secondary ion species or group of species showing the distribution on the surface. An area ranging from few microns to mm size can be imaged to obtain SIMS images that consist of a full mass spectrum per pixel of the image. Hence, SIMS image can be used retrospectively to visualize any ion in the spectrum.

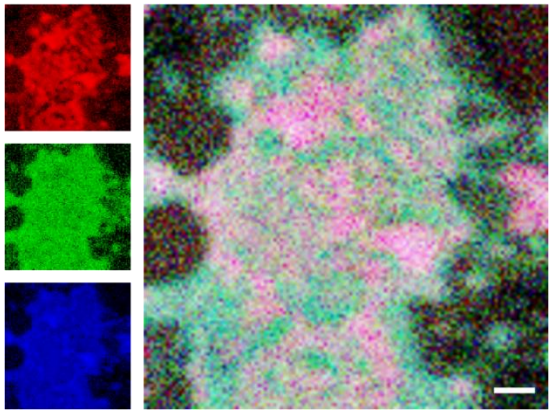

Figure 26. ToF-SIMS ion image for distribution of amino acids (isoleucine, aspartic acid and glutamic acid) secondary ions on polymer surface. Scale bar is 50 µm. Image acquired using ION TOF IV instrument and analysed using SurfaceLab 7 software.

The time of flight analyser has unique features that makes it an ideal analyser for static SIMS technique: (a) it allows for parallel detection of all ions thus permitting great sensitivity with a low ion dose such as used in static SIMS. (b) High mass range up to 10 kDa. (c) Excellent mass resolution and sensitivity. (d) Effective charge compensation for insulators provided by pulsed mode of primary ion source [216].

2.3.2 Water Contact Angle

Using water as a solvent, a solid surface can be easily wetted with high levels of adhesion in which case it is classified as hydrophilic or it can have low adhesion and water repellence and thus classified as hydrophobic. The scientific phenomenon that describes these interactions and governs the hydrophilicity and hydrophobicity of surfaces is called surface free energy. Understanding of surface free energy through meticulous measurements and analysis is a valuable asset that provides insight to surface properties. Water contact angle has been used in many studies to explain the behaviour of bacteria towards materials [91, 220].

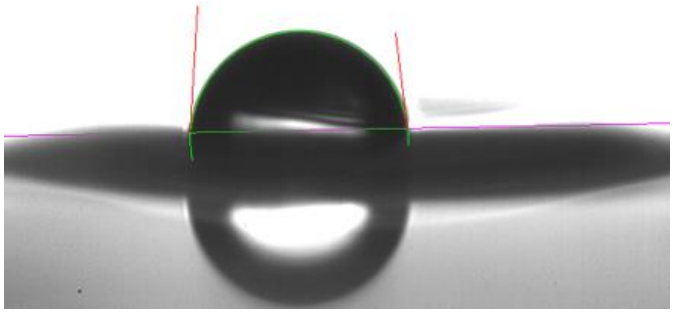

Figure 27. Measuring water contact angle on polymer microarray spots using a DSA100 instrument. Image showing the profile of 100 pL water droplet on micron spot together with circle fit.

To determine the surface free energy of micron sized polymer spots (≈ 400µm), the DSA100 (Kruss) instrument with a piezo dosing head unit was used to dispense 100 pL droplets of ultra-pure water (18.2 MΩ resistivity at 25 ˚C) onto the centre of each polymer spot. The motorised sample stage was used to navigate through all polymer spots on the microarray.

Sharp images were acquired by using a high speed, high resolution zoom camera to record the side profile of each back lit spot in an automated fashion. A second camera at the top ensured alignment of piezo-doser head with spot surface and provided a bird's eye view of the spot to ensure water droplet was deposited in the middle of each polymer spot, as shown in Figure 27. The video clips recorded for each polymer spot were analysed using DSA100 software (Kruss) by using a circle fitting method appropriate for small spots unaffected in shape by gravity.

2.3.3 X-ray Photoelectron Spectroscopy (XPS)

XPS is a non-destructive, surface sensitive method (top 1 to 10 nm of a surface) capable of quantitative elemental measurements (except hydrogen and helium). The XPS technique is used to get information about ionisation energy and it also provides information of the chemical bond nature that exist between elements. It is expensive and requires high vacuum [221]. The key components and the working mechanism of an XPS instrument are shown in Figure 28**.**

It works by irradiating a sample with an X-ray beam and then quantifying the kinetic energy and number of electrons that are ejected from material. XPS involves placing a sample in ultra-high vacuum (UHV) and irradiating the sample surface with photon of X-ray energy range (Magnesium K alpha (Mg Ka) = 1486.6eV and Aluminium K alpha (Al Ka) = 1253.6eV). An anode (usually made up of aluminium or magnesium) is bombarded with high energy electron from a heated filament to generate X-ray beam. The X-rays produced are commonly monochromated with a smaller energy range, improving the resolution of the technique [222].

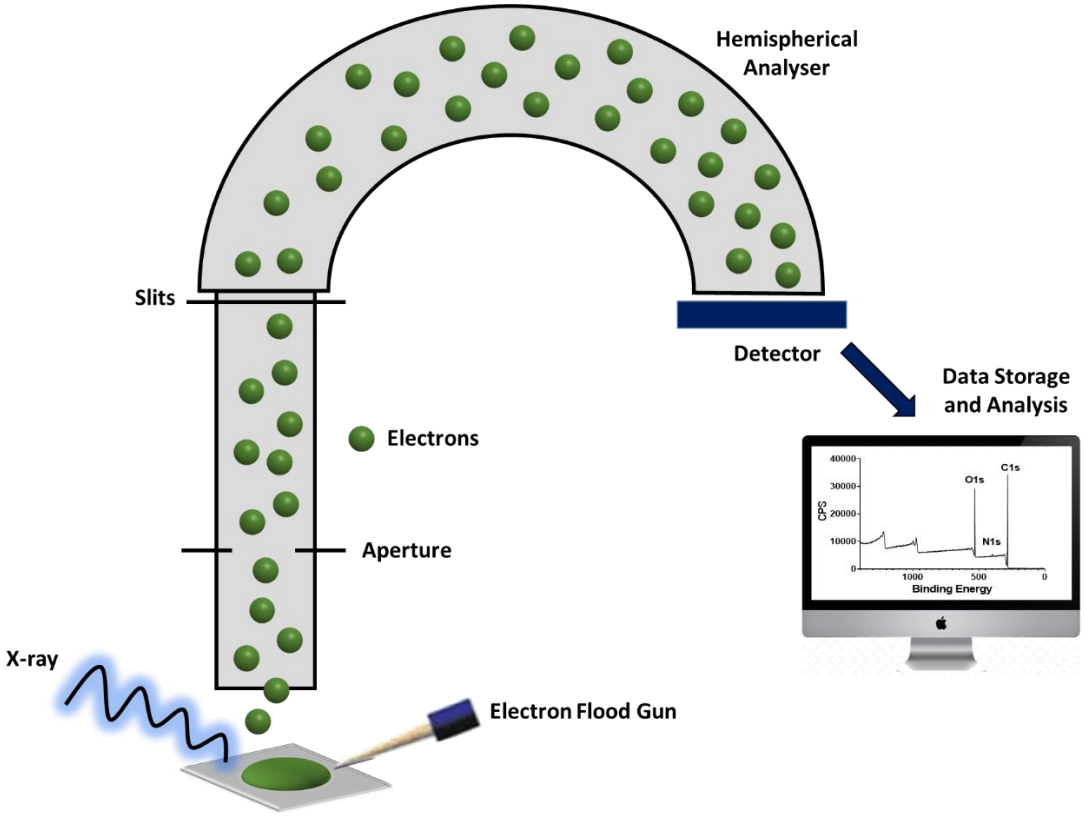

Figure 28. Schematic representation of mechanism of action of an XPS instrument showing key components of the instrument. Image adapted from Richard T. Haasch [223].

Following the irradiation of a surface, one of two undesired outcomes is X-ray passing through an atom with no interactions and a second is scattering of photons by electrons. A different scenario is set out when the incoming X-ray with enough energy is absorbed by an atom, leading to the ejection of inner shell electrons in a phenomenon known as the photoelectric effect [221]. Only a small amount of electrons ejected from an atom emerge from the surface without losing the energy through collisions on their way through the sample bulk. The probability of an electron reaching the surface without any energy loss reduces as the distance from the surface

increases. Due to this loss of electron energy, although X-rays can penetrate to a distance of microns in the sample bulk, only the electron from top 10 nm are detected by the detector. Because the energy of an X-ray with a particular wavelength is known, the ejected photoelectron has a kinetic energy that can be calculated from Einstein's equation:

$$E_B = h\nu - (E_K + \phi_{sp})$$

Equation 4. Einstein's equation

Where E_B is the binding energy of an electron, $h\nu$ is the energy of the X-ray source, E_k is the kinetic energy of the emitted electron measured by the detector and ϕ_{sp} is the work function of the spectrometer. Work function is defined as minimum energy needed to remove an electron from a solid to a point in the vacuum immediately outside the solid surface. The calculated binding energy is unique for each element and can be used to determine the composition of sample.

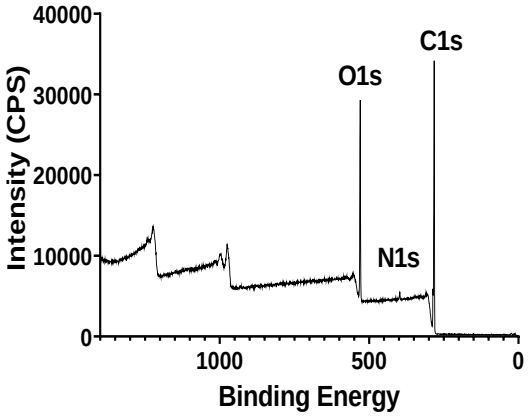

Figure 29. An example of a survey or broad XPS spectrum obtained from an oxygen and carbon containing polymer material.

In a typical XPS analysis, initially a survey XPS scan (broad spectrum) covering the entire binding energy range (usually 0 to 1000 eV) is carried out. This broad XPS spectrum Figure 29 shows binding energy of the electrons plotted against the electron intensity in counts per second (CPS). This allows a relative quantification of each atom on the surface by integrating the area under each peak on the spectrum.

As the case with ToF-SIMS, sample charging can also affect XPS spectra and causes a shift in binding energies of electrons. This is because the sample gains a net positive charge due to removal of negatively charged electrons from the surface. Hence, an electron flood gun is employed to minimise the charging of the surface. Charge correction of the spectrum must also be carried out before data analysis and shifting the data to C-C at 284.5 eV is the most commonly used protocol.

2.3.4 Partial Least Square Regression

Once data from high throughput surface characterisation of polymer microarray has been collected, the challenge is to develop the existing statistical data-handling approaches to relate this large amount of surface analytical information to other properties such bacteria attachment or adsorption of amino acids. The end goal is to develop quantitative structure-property relationships which aim to improve our understanding of the key causal factors underlying the properties of relevant and key polymers.

However, if the independent variable is composed of multiple observations such as spectral data from ToF-SIMS (i.e. it is multivariate in nature), it is necessary to use multivariate regression techniques to identify correlations. For example, Principal Component Analysis (PCA) and Partial Least Squares (PLS) Regression [224].

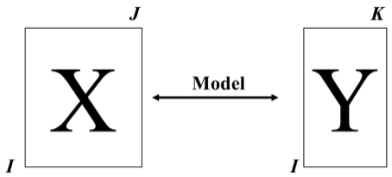

Figure 30. Basic schematic to represent relationship between multivariate dataset X with J variables related to univariate dataset Y.

The general regression problem involves a multivariate X matrix with many (that is J) variables and a Y block with K variables. However, PLS is a multivariate statistical method allowing models to be built that relate a set of multivariate data to a set of univariate data. PLS uses

factors to describe the variance in the dataset, thereby reducing the dimensionality of the data. Specifically, PLS finds factors (called latent variables) that describe variance in both the independent and dependent variables, i.e. to maximise the covariance described by the model. Covariance is measure of how closely the independent and dependent variables follow the same trends.

$$\mathbf{X = TP' + E}$$

$$\mathbf{Y = UQ' + F}$$

Equation 5. Equation for dimensionality reduction for datasets X and Y. Where T and U are scores, P and Q are variables, E and F are residuals.

To achieve this, PCA is performed independently on the X and Y matrices which allows them to be described by a smaller number of variables compared to number of original variables, see Equation 5. A PLS model is then developed in such a way that the first score in X (T_1) has maximum covariance with the first score in Y (U_1).

The difference between PLS and PCA is that, in PLS the loadings in X and Y are rotated from a PCA solution until arriving at a PLS solution where maximum covariance is obtained between scores, that is, Y can be predicted from X. So the model of PLS is structurally the same as PCA, but with the alteration of finding maximum covariance between X and Y scores.

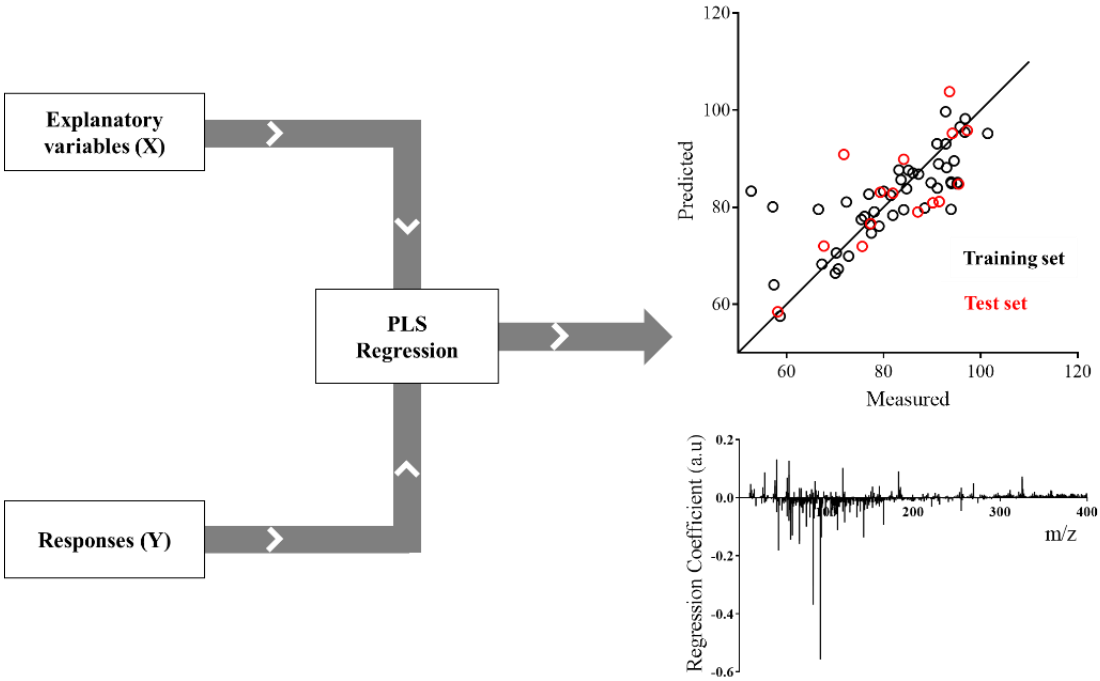

Figure 31. Basic schematic summarising PLS analysis; explanatory variables and responses are both simultaneously decomposed and PLS identifies variables which have a large degree of covariance. Using these variables a model is constructed and visualised with a measured vs predicted response plot. The regression coefficient is used to identify which of these variables capture said covariance.

The data used to build the PLS model is termed the training set. The predictive ability of a PLS model can be assessed using a test set of samples which have not been included in the training set. This is called validation. An alternative method is cross-validation which does not require a test set, only the original data in the training set. The most common form of cross-validation is the Leave One Out (LOO) method which involves leaving out of the training set one sample at a time, then repeating the PLS model. The error in the predictions of the samples left out can then be determined. LOO cross-validation is commonly used to determine the optimum number of factors used to build a PLS model, i.e. the number which generates a model that adequately describes the variance within the training set data, without including any variance due to noise in the data. Using too many latent variables inevitably leads to a model which over-fits the data.

Where stated in this project, PLS analysis was carried out using PLS Toolbox 5.2 software (Eigenvector). For cross-validation, the datasets were randomly split into a training group, between containing 75 - 80% of the samples, and a test set, containing the remaining 20 - 25%

of samples. Datasets were pre-processed by mean-centring, which calculates the mean of each column and subtracts this from the column. Another way of interpreting mean-centred data is that, after mean-centring, each row of the mean-centred data includes only how that row differs from the average sample in the original data matrix.

2.3.5 Surface Zeta Potential

Surface charge is one of the most frequently mentioned factors that are responsible for a range of biological effects [225]. Examining surface charge phenomena provides a deeper knowledge of interactions that occur during the events of surface fouling by microorganism [226].

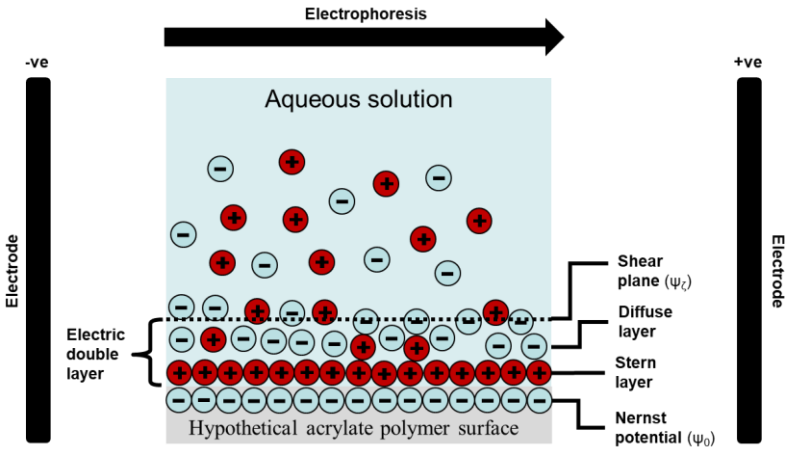

Figure 32. A representation showing the electric double layer on a negatively charged polymer surface. Immediately on top of the particle surface there is a strongly adhered immobile layer (Stern layer) comprising of ions of opposite charge i.e. positive ions in this case. Beyond Stern layer a diffuse layer develops consisting of both negative and positive charges.

The spatial distribution and concentration of dissolved solutes at the membrane-solution interface is structured, resulting in the formation of an electrical double layer (EDL). The first layer consisting predominantly of counter ions/molecules is termed the immobile Stern layer. Beyond this layer the electrostatic effects due to the surface charge on the particles decrease, resulting in a diffuse layer of mixed ions [225]. It is possible to induce electrophoresis by introducing an electric field to this structured system instigating charged particles to migrate towards the opposite electrode. A resultant electric potential known as Zeta (ζ) is generated at the imaginary shear plane within the diffuse layer interfacing with moving particles. As the

actual surface potential termed Nernst potential (ψ_0) is not readily measured, the quantifiable Zeta potential (ψ_ζ) parameter is a good estimate for polymer surface charge. In brief, the velocity of moving particles at shear plane, that is highly dependent on sample surface charge can be determine by electrophoretic light scattering, which is then used to deduce zeta potential through series of mathematical equations later explained in Equation 6, [227].

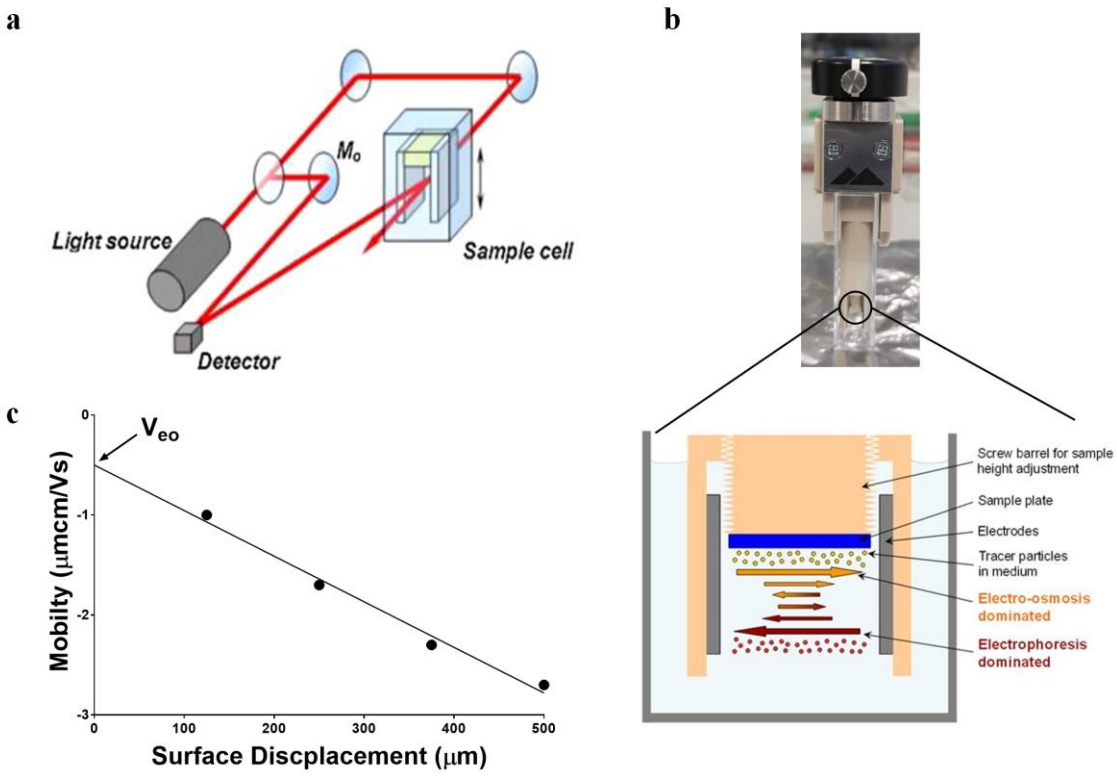

Figure 33. Schematic for determination of surface zeta potential by electrophoretic light scattering. (a) Zetasizer Nano optics. (b) Dip-cell arrangement and the flow-field mapping of the tracer particles. Net mobility results from the combination of electroosmosis (orange) and electrophoresis (red). (c) Exemplary plot of particle velocity against displacement from surface.

In electrophoretic light scattering, the mobile particles scatter an incident laser so causing a shift in frequency of scattered light compared to the original laser. The frequency shift is often termed Doppler shift and it is proportional to the speed of the particles. The instrumentation used for this technique is shown in Figure 33a. In short, the laser beam is split into two and while one beam is directed towards the sample the other one is used as reference beam. The scattered light from the sample is combined or optically mixed with the reference beam to determine the Doppler shift [228].

To quantify the surface zeta potential ($\psi\zeta$), we used a recently available and simple Uziguris (dip) cell arrangement that facilitates the probing of tracer particles motion dispersed in electrolyte alongside the test surface. As schematized in Figure 33b, on application of electric field, the tracer particles move under the influence of both the electroosmotic motion of the fluid dominant closer to sample surface and their own electrophoretic motion dominant farther away from sample [229].

The micrometric screw allows vertical movement of sample plate with respect to the detection optics. Consequently, measurements of tracer particle mobility at various displacements from sample surface generates a displacement-velocity calibration curve, whose y-intercept is the velocity of particle at shear plane. The relationship between tracer particle velocity and surface zeta potential is then given by the Smoluchowski equation (Equation 6).

$$\zeta = \frac{\eta \nu_{eo}}{\varepsilon E_x}$$

Equation 6. Where η is the viscosity of the medium, ε is the permittivity in vacuum, E_x is the dielectric constant of the medium and ν_{eo} is electrophoretic mobility of tracer particles at shear plane.

2.4 Thermal and Photopolymerisation

Polymerisation reactions are chemical processes in which monomeric precursors of low molecular weight are transformed into polymeric chains or macromolecules. UV radical polymerisation is a type of chain polymerisation where the chain growth and the successive incorporation of monomer start with the UV activation of an initiator.

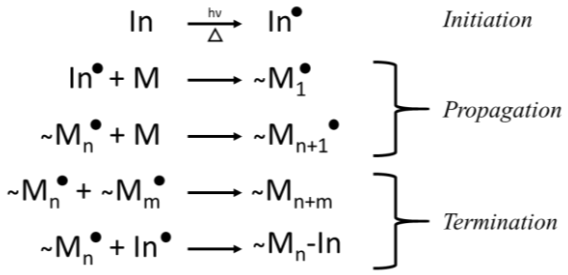

Figure 34. Stages in free radical polymerisation initiated by UV or heat. In and M denote initiator and monomer respectively; ~Mn • and Mn • are macroradicals.

Three essential steps are involved in this process, see Figure 34. The initiation step is the reaction which first generates the free radicals by homolytic fission. A lot of energy is required to break this bond, which is why UV light or heat is necessary. The propagation steps are reactions which are instigated by free radicals that regenerate replacement free radicals upon reacting, thus allowing reaction to continue unaided. The termination steps are reactions in which free radicals are used up and not regenerated which eventually stops the polymerisation reaction. The free radical polymerisation is uncontrolled and tends to produce branched-chain structures and polymers with broad molecular weights, i.e., polydispersed [230].

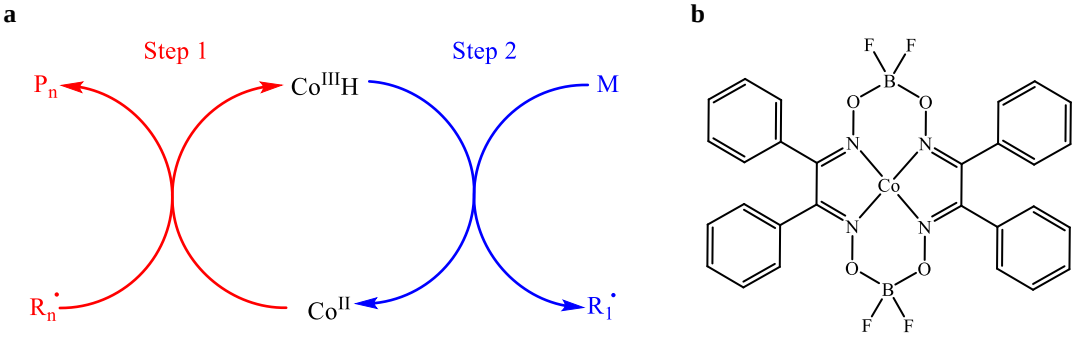

Figure 35. **(a)** Scheme for catalytic cycle for cobaloxime mediated catalytic chain transfer. **(b)** Chemical structure for Bis[(difluoroboryl) diphenylglyoximato]cobalt(II).

To obtain more controlled molecular weights during scale up for monomers of interest, thermal polymerisation was carried out with the addition of a catalytic chain transfer agent for vinyl polymers as patented by David Borman and Derek Irvine [231]. The most widely accepted mechanism for catalytic chain transfer polymerisation proposes a two-step process, see Figure 35a. Using Bis[(difluoroboryl) diphenylglyoximato]cobalt(II) (PhCoBF) as an example (Figure 35b), first, the active cobalt(II) complex abstracts a hydrogen atom from the propagation radical

(Rn), forming a cobalt(III)-hydride ($Co^{III}H$) complex (which is thought to be the rate limiting step) and a dead polymer chain (P_n) containing a vinyl end group (referred to as a macromonomer). In the second step, the $Co^{III}H$ complex reacts with a monomer molecule (M) resulting in the original active cobalt(II)complex and a monomer radical (R_1) capable of propagation [232, 233].

2.5 Details of Bacteria Strains Used in this Project

P. aeruginosa, S. aureus, K. pneumonia, Pr. mirabilis, *Uropathogenic E. coli* and *E. faecalis* were used in this project for two reasons: firstly, based on their clinical relevance and secondly to test both Gram-positive and Gram-negative bacteria species [234].

Bacterial strain	*Description*	*Origin*
P. aeruginosa	PAO1 Washington sub-line	Dr. J. Dubern's lab collection
S. aureus	SH1000 - mkat	Dr. J. Dubern's lab collection
K. pneumonia	NCIMP10104	Dr. J. Dubern's lab collection
Pr. mirabilis	Hauser 1885	Dr. J. Dubern's lab collection
Uropathogenic E. coli	Nottingham sub-line	Dr. J. Dubern's lab collection
E. faecalis	NCTC12697	Dr. Tim Sloan, QMC, Nottingham

Table 1: Bacterial strains used in this project

2.6 Biofilm Assay

Biofilm assays are often used to study surface-attached bacteria living in communities [235]. The static biofilm assay techniques used in this project were based on previously published work from Paul William's group, where medical devices of which dimensions are adjusted to appropriate sizes can also be used as a substratum for biofilm production [89, 196, 236-238]. By adapting and modifying, these static biofilm assays allow for analysis of biofilm formation with a variety of readouts, including microscopy of live cells, macroscopic visualization of stained bacteria, and viability counts. Although the methods of culture will vary according to the phenomena investigated, the guiding principle for these assays place importance on cultures being constantly mixed with adequate nutrient supply from media, homogenized and in

equilibrium with the gas phase [239]. Such requirements can be achieved with routine microbiology laboratory incubators and culture media.

To facilitate detection and quantification of biofilms by laser confocal scanning microscope, bacteria used in this project were transformed (procedure carried out by Dr. J. F. Durben) to constitutively express mCherry or gfp reporter proteins. A limitation to this approach is the assumption that fluorescence detected on surfaces will solely be due to viable bacterial cells with no contributions from lysed bacterial cells, notwithstanding the fact that expressed mCherry proteins are stable for up to 6 hours following maturation. However, previous studies from group conducted independently by Hook, Singh and Kurmoo all indicated that live and/or dead staining of very low or high biofilm coverage from *E. coli* and *S. aureus* revealed bacterial cells stayed alive and very little dead cells were present within the biofilm, which is typical of normal biofilms [89].

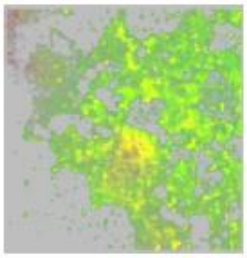

Figure 36. Confocal microscopy images of live/dead stained UPEC biofilms grown for 72 h in RPMI-1640 media on polymer coupons. The bacteria were stained with SYTO 9 green-fluorescent dye for live bacteria and propidium iodide red-fluorescent dye for cell membrane damaged (dead) bacteria. The resulting image is maximum intensity z-projection overlays of the red and green fluorescence. Each image is 160 x 160 μm. Image from Hook *et al.* [89].

These finding however do not negate the possibility of bacterial cell lysis or death occurring as normal physiological process in biofilm growth mode, but show its effects on fluorescence read out values to be minimal and should even out across different polymer surfaces analysed in this project.

2.7 Fluorescence Confocal Microscopy

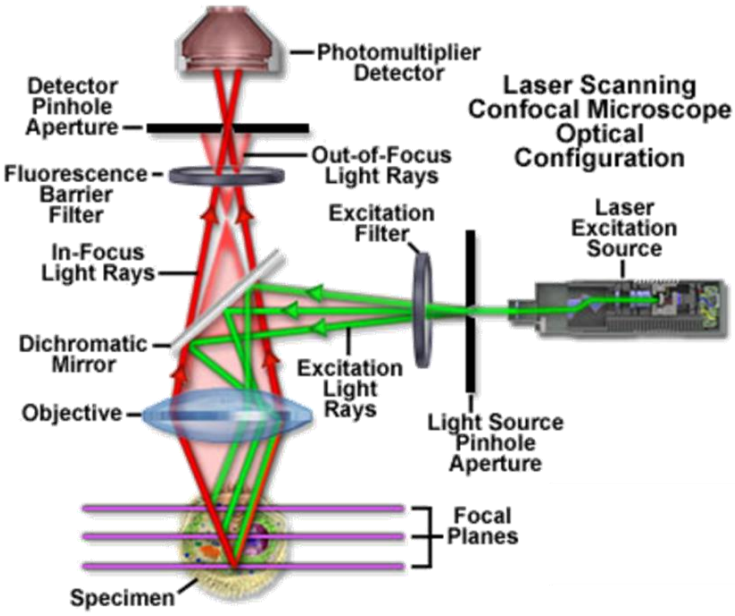

Figure 37. Schematic representation of a confocal microscope. (Image adapted from [240])

The confocal microscope works with the basic principles of a fluorescence microscope. An excitation laser source with high degree of coherence illuminates tightly focused spots on specimen at a set wavelength controlled by excitation filter. The presence of a dichromatic mirror guides excitation laser onto the specimen via a condensing objective lens. Upon hitting the specimen with excitation beam (short wavelength), a beam with longer wavelength is emitted as fluorophore transits from excited state to ground state. This emitted beam then travels through the dichromatic mirror to the detector. The emission filter acts as a barrier to block fluorescence of undesired wavelength. However, there is another possibility of interference from external light sources other than emitted laser from sample that can be detected and produce blurring images. Therefore, confocal microscopes make use of pinholes that allow only focussed light emitted from specimen to pass through to detector, which is the reason for the name confocal, because the pinhole is on same foci (confocal) with the emitting point. The pinhole diameter can be adjusted in order to increase signal to noise ratio, in other words, allowing maximum signal from specimen and little as possible noise for external sources. Ideally, a pinhole diameter should be set to 1 airy unit.

Optical sectioning is another important aspect of confocal microscopy, where the objective lens is able to move along the z axis and image both superficial and deeper planes of sample under study. It is then possible to reconstruct and obtain a summed image of all pixels from different sections.

The light hitting the detector is enhanced thanks to the dynode arrangement in the photomultiplier tube (PMT). Each time the lights hits a node in the PMT, it is multiplied thus enhancing the fluorescence signal. In summary a fluorescence confocal microscope works similarly to a fluorescence microscope but with addition of optical sectioning function and pin hole focussing component.

The work presented in this thesis was carried out using Zeiss LSM 700 confocal microscope (Carl Zeiss, Germany). A 555 nm laser was used as excitation source, with filters set from 578 – 1000 nm to detect mCherry labelled *P. aeruginosa* using 10x objective.

2.8 Ultraviolet visible (UV-Vis) Spectroscopy

UV-Vis can be used in a qualitative manner, to identify functional groups or confirm the identity of a compound by matching the absorbance spectrum. It can also be used in a quantitative manner, as concentration of the analyte is related to the absorbance using Beer's Law [241].

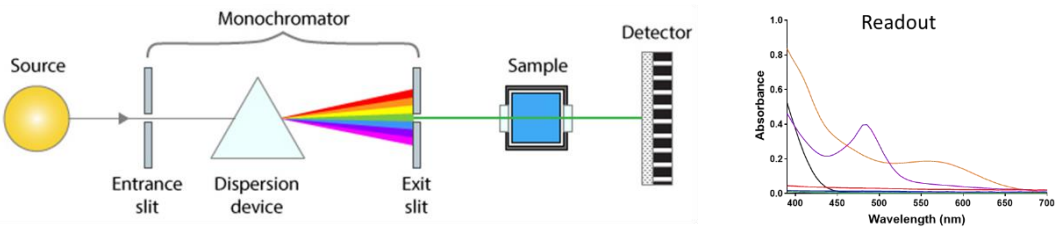

Figure 38. Schematic showing the arrangement of a conventional spectrophotometer.

A typical uv-vis setup consists of a source lamp, monochromator, beam splitter, sample compartment and detectors. In brief, an ignited source lamp creates a variety of light of different

wavelengths (300 – 800 nm). This light passes through the first slit of the monochromator ensuring all the light photons are traveling along parallel pathways, so that when they strike the prism they are diffracted into a rainbow of colours and each wavelength of light moves into a different space. Only one wavelength of light then makes it through the second slit of monochromator. This light splits into two beams of equal intensity upon striking the beam splitter. One beam traverses the reference cell and the other beam traverses the sample cell before reaching the detector.

I_0 is the intensity of the monochromatic light entering the sample and I is the intensity of this light emerging from the same. The transmittance (T) of light by sample is the ratio of intensity of emitted light to the intensity of incident light, $T = I/I_0$. This exponential relationship between concentration and transmittance can be linearized and converted to light absorbance (A) based on Beer-Lambert's mathematical derivations [242].

$$A = \varepsilon \, l \, c$$

Equation 7. Where ε is molar extinction coefficient, l is path length and c is concentration.

It is possible to obtain an absorbance spectrum that shows the absorbance of a compound at different wavelengths. The amount of absorbance at any wavelength is due to the chemical structure of the molecule being tested. The most common transitions that fall in the UV-Vis range are π-π* and n- π*. Pi orbitals arise due to double bonds, and n orbitals are for non-bonding electrons. Pi star are anti-bonding pi orbitals [241].

Chapter 3 - Investigating the Effect of Nutrient Deposition on Polymer Surfaces and Biofilm Formation of *P. aeruginosa*

3.1 Introduction

The initial interaction between bacteria and surfaces has been identified as a key point in determining whether bacteria go on to colonise a surface or not [103]. In protein containing media there is a strong relationship between the adsorbed protein layer formed on materials and both bacterial and mammalian cell attachment. [243-246]. However, in protein-free media such as used by Hook *et al*., this cannot be a contributor to early cell attachment. Consequently, here we carry out detailed surface chemical analysis on the surface of two polymers, one; ethylene glycol dicyclo pentenyl ether acrylate (pEGDPEA), that prevents bacteria biofilms and the other; neopentyl glycol propoxylate diacrylate (pNGPDA) that promotes bacteria biofilms (Figure 39).

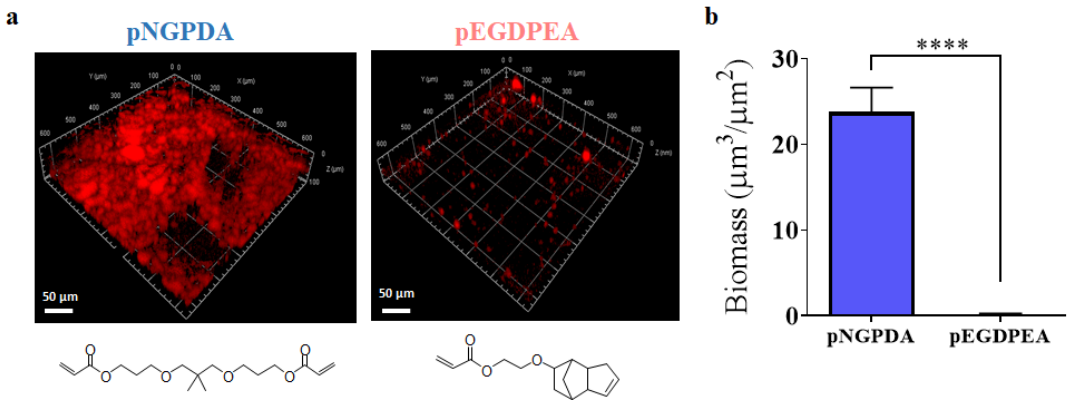

Figure 39. Comparison of *P. aeruginosa* biofilm formation on polymer surfaces. a) Confocal images (10x, 0.3) of *P. aeruginosa* m-cherry tagged after 24 hours on pNGPDA (left) and pEGDPEA (right). Samples were washed twice in PBS and once in H_2O. Scale bar is 20 µm and z step 1 µm. b) Quantification of bacterial biomass for 2 polymer surfaces. Error bars show ± 1 sd (N=3 independent replicates). *** P<0.001. All significances were determined by analysis of variance One-way ANOVA and Tukey's post-test comparison for differences between the indicated samples. (*Data to courtesy of A. Carabelli*)

ToF-SIMS is used to provide molecularly specific surface analysis together with XPS for quantification of the adsorbates identified from exposure to a simple protein-free, amino acid supplemented culture medium. We compare these finding with the surface colonisation by *P. aeruginosa* [7, 68, 72].

3.2 Aims and Objectives

The aim of this chapter was to investigate the conditioning layer formed via the adsorption of nutrients from a simple protein-free media (RPMI) previously used by Hook *et al.* in discovery of bacteria resistant material [89]. We reasoned carrying out experimental investigations with the same conditions employed during discovery may provide new mechanistic insight to anti-attachment polymers. The objectives were as follows:

1. Prepare polymers of pEGDPEA and pNGPDA on methacrylate silanised coverslips.
2. Treat pEGDPEA and pNGPDA surfaces with simple, protein-free RPMI media to produce conditioning layer.
3. Use surface sensitive analytical techniques XPS and ToF-SIMS to quantitatively and qualitatively identify differences in adsorption of nutrients onto surfaces of pEGDPEA and pNGPDA.
4. Model the adsorption phenomena on pEGDPEA and pNGPDA to allow the process to be fully described.

3.3 Experimental

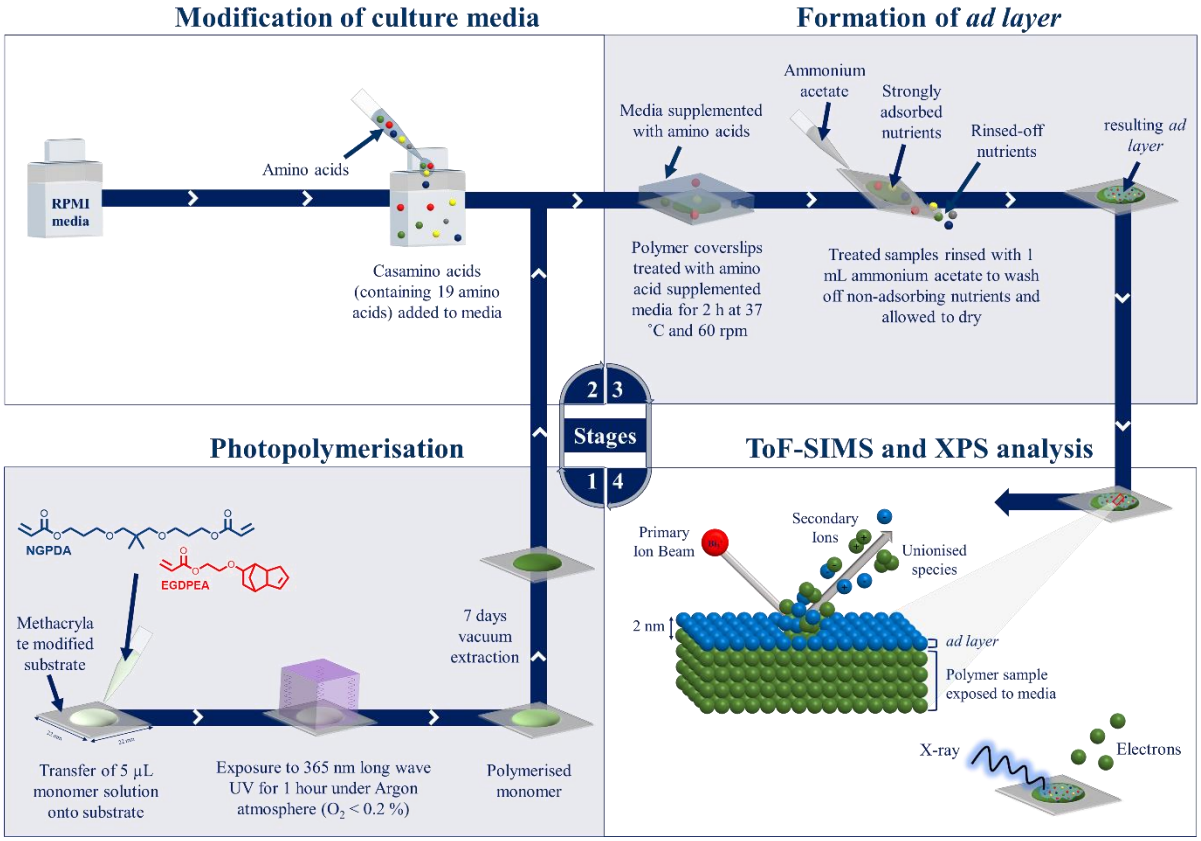

Figure 40. Summary of experimental procedure showing 4 major steps involved. 1) Preparation of polymers. 2) Modification of culture media 3) Formation of *ad layer*. 4) Surface analysis.

3.3.1 Methacrylate Silanisation and UV Polymerisation

Coverslips (22 x 22 mm) were activated by treatment with Oxygen RF plasma with initial pressure set to 0.3 mbar and power at 100W (displaying zero reflected power) for 1 minute intended to clean the surface for reaction. The coverslips were then silanised using 3-(trimethoxysilyl)propyl methacrylate in dried toluene solvent at 50 °C, under Argon for 16 hours. Silanised coverslips were then rinsed and sonicated in acetone to rinse off unbound silane monomer prior to extracting solvent in vacuum oven. 5 µl of 1% (w/v) 2,2-dimethoxy-1,2-diphenylethan-1-one (DMPA) initiator dissolved in NGPDA or EGDPEA was spotted onto methacrylate silanised coverslips under argon atmosphere at O_2 < 2000 ppm and exposed to UV for 1 hour. Coverslips were then left in vacuum oven for at least 7 days before use to remove solvent and any volatile unreacted monomer.

3.3.2 Formation of Adsorption Layer

3.3.2.1 Polymer Treatment with Standard RPMI

Coverslips of pNGPDA and pEGDPEA polymers were incubated with 6 mL of RPMI (Lonza) 1640 media (components listed in Table 2) in a 4 well polystyrene petri dish for 2 hours sufficient for equilibrium to establish at 37 ℃ and 60 rpm. Once completed, media was aspirated and 1 mL of 150 mM ammonium acetate was jetted onto polymer surfaces to get rid of weakly adsorbed nutrients. Rinsed surfaces were dried in vacuum for 1 hour prior to surface analysis. Controls were samples of pNGPDA and pEGDPEA not treated with RPMI media but also incubated at 37 ℃ and 60 rpm for 2 hours.

	Description	*Chemical Formula*	*mg/L*	*mM*
1	Calcium Nitrate	$Ca(NO_3)_2.4H_2O$	100	0.42
2	Dextrose	$C_6H_{12}O_6$	2000	11.10
3	Magnesium Sulfate Heptahydrate	$MgSO_4.7H_2O$	100	0.40
4	Potassium Chloride	KCl	400	5.36
5	Sodium Bicarbonate	$NaHCO_3$	2000	23.80
6	Sodium Chloride	NaCl	6000	102.66
7	Sodium Phosphate Dibasic-7-Hydrate	$Na_2HPO_4.7H_2O$	1512	5.64
8	L-Arginine Free Base	$C_6H_{14}N_4O_2$	200	1.14
9	L-Asparagine	$C_4H_8N_2O_3$	50	0.37
10	L-Aspartic Acid	$HO_2CCH(NH_2)CH_2CO_2H$	20	0.15
11	L-Cystine	$C_6H_{12}N_2O_4S_2$	50	0.20
12	L-Glutamic Acid	$C_5H_9NO_4$	20	0.13
13	Glutathione Reduced	$C_{10}H_{17}N_3O_6S$	1	3.25×10^{-3}
14	Glycine	$HO_2CCH_2NH_2$	10	0.13
15	L-Histidine, Free Base	$(C_3N_2H_3)CH_2CH(NH_2)COOH$	15	0.096
16	L-Hydroxyproline	$C_5H_9NO_3$	20	0.15
17	L-Isoleucine	$HO_2CCH(NH_2)CH(CH_3)CH_2CH_3$	50	0.38
18	L-Leucine	$HO_2CCH(NH_2)CH_2CH(CH_3)_2$	50	0.38
19	L-Lysine Monohydrochloride	$C_6H_{14}N_2O_2.HCl$	40	0.21
20	L-Methionine	$HO_2CCH(NH)CH_2CH_2SCH_3$	15	0.10
21	L-Phenylalanine	$HO_2CCH(NH_2)CH_2C_6H_5$	15	0.090
22	L-Proline	$C_5H_9NO_2$	20	0.17
23	L-Serine	$HO_2CCH(NH_2)CH_2OH$	30	0.28
24	L-Threonine	$HO_2CCH(NH_2)CH(OH)CH_3$	20	0.16
25	L-Tryptophan	$C_{11}H_{12}N_2O_2$	5	0.024
26	L-Valine	$HO_2CCH(NH_2)CH(CH_3)_2$	20	0.17
27	D-Biotin (Vitamin H)	$C_{10}H_{16}N_2O_3S$	0.20	8.18×10^{-4}
28	D-Calcium Pantothenate (Vitamin B5)	$C_{18}H_{32}CaN_2O_{10}$	0.25	5.24×10^{-4}
29	Choline Chloride	$HOCH_2CH_2N(CH_3)_3Cl$	3	0.021
30	Cyanocobalamin (Vitamin B12)	$C_{63}H_{88}CoN_{14}O_{14}P$	0.005	3.68×10^{-6}
31	Folic Acid	$C_{19}H_{19}N_7O_6$	1	2.26×10^{-3}
32	I-Inositol	$C_6H_{12}O_6$	35	0.19
33	Niacinamide (Nicotinamide)	$C_6H_6N_2O$	1	8.18×10^{-3}
34	Pyridoxine Monohydrochloride	$C_8H_{11}NO_3$	1	4.86×10^{-3}
35	Riboflavin (Vitamin B2)	$C_{17}H_{20}N_4O_6$	0.20	5.31×10^{-4}
36	Thiamine Monohydrochloride (Vitamin B1)	$C_{12}H_{18}N_4OSCl_2$	1	2.96×10^{-3}
37	P-Aminobenzoic Acid, PABA	$C_7H_7NO_2$	1	7.29×10^{-3}
38	L-Tyrosine Disodium Salt, Dihydrate	$C_9H_9NO_3Na_2.2H_2O$	28.83	0.11

Table 2: RPMI-1640 components

3.3.2.2 Polymer Treatment with Supplemented RPMI media

To supplement RPMI 1640 media, we used casamino acids (VWR), a mixture of amino acids obtained from acid hydrolysis of casein. It is typically used in microbial growth media. It has all the essential amino acids except tryptophan, which is destroyed upon digestion with sulfuric or hydrochloric acid [247, 248]. In Figure 41 is the percentage abundance (w/w) for individual amino acid components of casamino acid mixture as described by Nolan *et al.* [248].

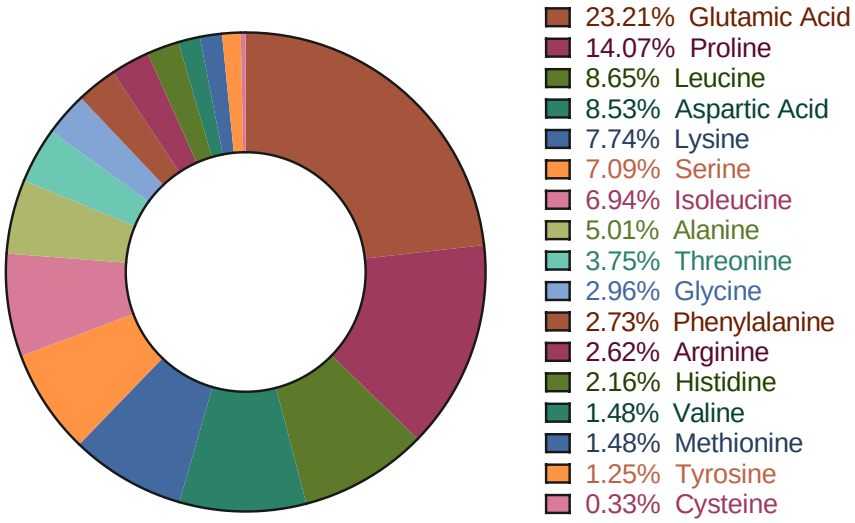

Figure 41. Distribution of amino acid (% w/w) in casamino acids.

Standard RPMI (Lonza) was supplemented with casamino acids (VWR) to obtain 6 different concentrations: 0.05, 0.10, 0.20, 0.30, 0.40 and 0.5 % (w/v). For all solutions measured pH was 8.0 ± 0.3. Coverslips of pNGPDA and pEGDPEA polymers were then treated as described in 3.3.2.1.

3.3.3 Time-of-Flight Secondary Ion Mass Spectrometry

ToF-SIMS measurements were conducted using a ToF-SIMS IV (IONTOF GmbH) instrument operated using a 25 keV Bi_3^+ primary ion source exhibiting a pulsed target current of > 0.3 pA. Samples were scanned at a pixel density of 512 pixels/mm, with 1 shot per pixel over a given area. An ion dose of 2.45×10^{11} ions/cm^2 was applied to each sample area, ensuring static conditions were maintained throughout. Both positive and negative secondary ion spectra were

collected (mass resolution > 5000 at *m*/*z* = 45), over an acquisition period of 15 scans. Owing to the nonconductive nature of the samples, charge compensation was applied in the form of a low-energy (20 eV) electron flood gun. All data analysis was carried out with SurfaceLab 7 software.

3.3.4 Isotherm Models

In general, an adsorption isotherm is a curve describing the phenomenon governing the retention (or release) of a substance from the aqueous media to a solid-phase at a constant temperature and pH [249]. An Adsorption equilibrium is established when the adsorbate containing phase has been contacted with the adsorbent for sufficient time, at which point the adsorbate concentration in the bulk solution is in a dynamic balance with the interface concentration [250]. Typically, the mathematical correlation describing this phenomenon is usually depicted by graphically expressing the solid-phase adsorption against the concentration in media which provides an insight into the adsorption mechanism, surface properties as well as the degree of affinity of the adsorbents. A brief overview of two mathematical models used in this thesis are here presented. Detailed explanations for choice of models are reported in results section 3.4.3.

3.3.4.1 Freundlich Adsorption Isotherm Model

The Freundlich model is given by Equation 8:

$$q_e = K_F C_e^{\frac{1}{n}} \qquad \text{or} \qquad \log q_e = \frac{1}{n}\log C + \log K_F$$

Equation 8

Where q_e (CN^-) is the intensity of adsorbate measured by ToF-SIMS at equilibrium (after 2 hours), C_e is concentration of amino acids in media at equilibrium, K_F is a system specific indicator of adsorption capacity and 1/n is also a system specific measure of intensity of adsorption [250]. Considering Equation 8 in the form y = mx + c, with y-intercept: log K_F and

gradient: 1/n, we can work out the adsorption capacity through K_F values. Also, the gradient (m or 1/n) of the equation indicates the likelihood of adsorption occurring and it is generally greater than 1.

3.3.4.2 Langmuir Adsorption Isotherm Model

The Langmuir equation is generally given by:

$$\frac{c}{x} = \left(\frac{c}{\Gamma_m}\right) + \left(\frac{1}{b\Gamma_m}\right)$$

Equation 9

Where x (CN^-) is the concentration of adsorbate measured by ToF-SIMS, c is concentration of amino acids in RPMI, Γ_m is the monolayer coverage and b is the ratio of rate constants for adsorption and desorption [251]. Considering Equation 9 in the form y = mx + c, with y-intercept: $1/b\Gamma_m$ and gradient: $1/\Gamma_m$, it is possible to firstly work out the b values, that is rate of adsorption and desorption on polymer surface and secondly derive monolayer coverage (Γ_m) values.

3.3.5 X-ray Photoelectron Spectroscopy

Samples were analysed using the Kratos AXIS ULTRA with a monochromated Al Kα X-ray source (1486.6 eV) operated at 10 mA emission current and 12 kV anode potential (60 W). A charge neutralizer filament was used to prevent surface charging. Hybrid-slot mode was used measuring a sample area of approximately 0.5 mm^2. Coverslips with polymer samples were mounted on a standard Kratos sample bar with double-sided tape. The analysis chamber pressure was better than 5×10^{-9} mbar. Three areas per sample were analysed. Wide scans at low resolution (1400–5 eV binding energy range, pass energy 80 eV, step 0.5 eV, sweep time 20 min) were used to estimate the total atomic percentage of the detected elements. High-resolution spectra at pass energy of 20 eV with steps of 0.1 eV and sweep times of 10 min each were also acquired for photoelectron peaks from the detected elements Oxygen, Carbon,

Nitrogen and Sulphur which provided information of the chemical bond nature existing between elements. The high-resolution spectra were charge-corrected at C-C peak to 284.8 eV, CasaXPS (version 2.3.19PR1.0) software was used for data analysis.

3.3.6 Calculating Overlayer Thickness of Adsorbed Amino Acid

The [N] (atomic%) can be converted into amino acid ovelayer thickness using Equation 10 described by Ray and Shard [252].

$$d_{N(1s)} = -L_{N(1s)} \cos\theta \ ln\left(1 - \frac{[N] - [N]_0}{[N]_\infty - [N]_0}\right)$$

Equation 10. Equation to convert [N] (at%) to overlayer thickness.

Where $d_{N(1s)}$ is amino acid overlayer thickness, L is electron attenuation length (3.02 nm), $\cos(\theta=0^\circ) = 1$, $[N]_\infty$ is measured nitrogen in amino acid powder and $[N]_0$ is nitrogen fraction on pristine polymer.

3.3.7 Growth of *P. aeruginosa* in Amino Acid Supplemented RPMI Media

Firstly, an overnight primary culture of *P. aeruginosa* strain PAO1, grown in 10 mL LB at 37 °C and 200 rpm, was re-suspended 10 mL of standard RPMI. Separately, standard RPMI (Lonza) was supplemented with casamino acids (VWR) to obtain 6 different concentrations: 0.05, 0.10, 0.20, 0.30, 0.40 and 0.5 % (w/v). Each supplemented solution was then standardized at an OD_{600} 0.01 with PAO1 and a volume of 200 µl transferred into pEGDPEA or pNGPDA coated (similar procedure as described in section 3.3.1) wells of a 96-well plate in triplicates. Optical density at 600 nm in each well was measured every 30 minutes over 24 h at 37 °C in Tecan Genios Fluo instrument under static conditions.

3.3.8 Biofilm Experiment with *P. aeruginosa*

P. aeruginosa strain PAO1 transformed to express *mCherry* fluorescent protein obtained from lab stocks was streaked out with 1 µL loop on freshly prepared agar plate and left to grow at 37

ºC for 10 hours. A single colony was then added to 10 mL of Lysogeny Broth (LB) media and left to grow overnight with 200 rpm shaking. Bacteria were then re-suspended in RPMI media and brought to a final OD_{600} of 0.01. UV sterilised coverslips of pNGPDA and pEGDPEA polymers were then incubated with *P. aeruginosa* in 6 mL RPMI for 24 hours. Coverslips were then rinsed twice in PBS and once in water to wash off non-adhering bacteria and salts prior to being imaged with a Carl Zeiss LSM 700 laser scanning confocal microscope with excitation laser set to 555 nm and a 10x/NA 0.3 objective. Images were acquired using ZEN 2009 imaging software (Carl Zeiss). Bacterial surface coverage was quantified using Image J 1.44 software (National Institutes of Health, USA) and Comstat B.

3.3.9 Surface Zeta Potential

Polymer films of pEGDPEA and pNGPDA were initially produced by UV radical polymerisation under an Argon atmosphere at O_2 < 2000 ppm. Electrophoretic mobility and electroosmotic measurements were then carried out using a Zetasizer Nano ZS with the surface zeta potential accessory (Malvern, UK). Measurement solutions were prepared in concentration range 1 – 10 mM PBS following guidelines from American Society for Testing and Materials (ASTM) [253]. Monodispersed melamine particles were used as tracer particles at concentrations of 10^{-4} % (w/v). The Zetasizer was set to forward scatter with the attenuator in position ten. The count rate was adjusted to the optimal 250–500 kcps range. The instrument was set to take four distance positions, in 125 µm steps, consisting of three measurements (each measurement consisted of 15 sub-runs with a 60 s interval) at each position. Furthermore, five measurements, consisting of 100 sub-runs with a 60 s interval in between measurements, were used to measure the electrophoretic mobility of the tracer particles. All measurements were carried out at 25 °C.

3.4 Results

3.4.1 ToF-SIMS Analysis of pEGDPEA and pNGPDA Treated with Standard RPMI

To obtain surfaces conditioned with the compounds that bacterial cells would encounter on a polymer surface whilst immersed in media during culture, we employed a previously used mild rinsing procedure intended to remove all liquid and loosely bound compounds whilst leaving more strongly bound material on the surface for analysis [254]. ToF-SIMS spectra were acquired from pNGPDA and pEGDPEA before and after a two hour incubation with commercially available RPMI media (Lonza) following mild rinsing. The results are presented in Figure 42 and Figure 43 where ToF-SIMS spectra for treated and untreated samples are displayed.

Both negative and positive secondary ion spectra were acquired (Figure 42b-c); for pEGDPEA the spectra were dominated by secondary ion peaks (marked in green) characteristic of EGDPEA ($C_2H_3O^-$, C_2H^-, CHO_2^-, C_3H_5, C_4H^-, C_6H^-, $C_5H_7^+$, $C_6H_7^+$, $C_7H_7^+$). The spectra from pNGPDA (Figure 43b-c) were likewise dominated by characteristic fragments of the NGPDA monomer including ethylene glycol moieties ($C_2H_3O^-$, $C_2H_3O_2^-$).

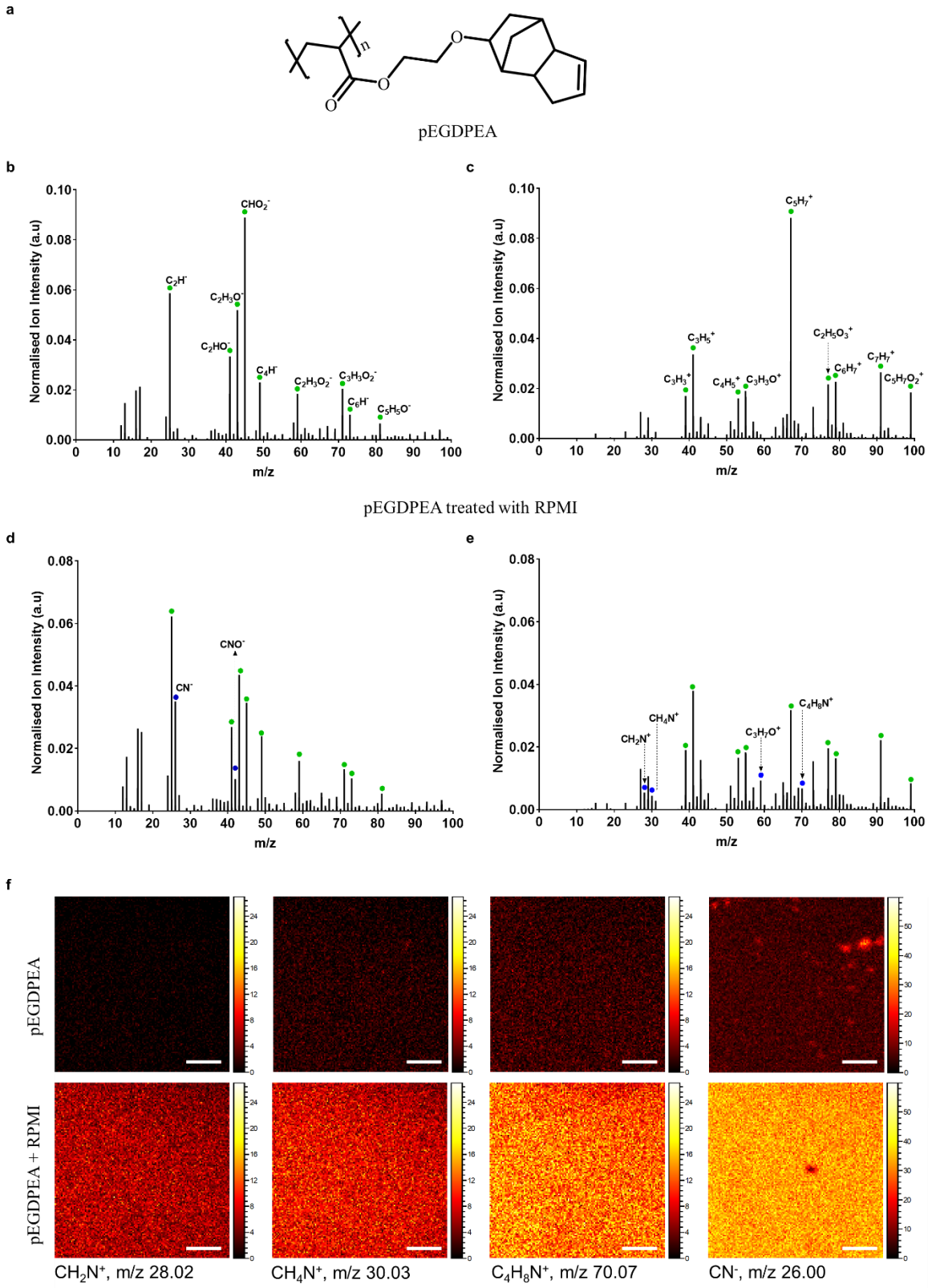

Figure 42. **(a)** Chemical structure for pEGDPEA **(b)-(c)** respectively the negative and positive spectra for untreated pEGDPEA. **(d)-(e)** respectively the negative and positive spectra for pEGDPEA sample treated with standard RPMI. **(f)** ToF-SIMS ion images for pEGDPEA sample treated with and without RPMI. Amino acid generic marker ions are CH_2N^+ (m/z 28.02), CH_4N^+ (m/z 30.03), $C_4H_8N^+$ (70.07) and CN^- (m/z 26.00) adsorbed on surface. Scale bar is 100 µm.

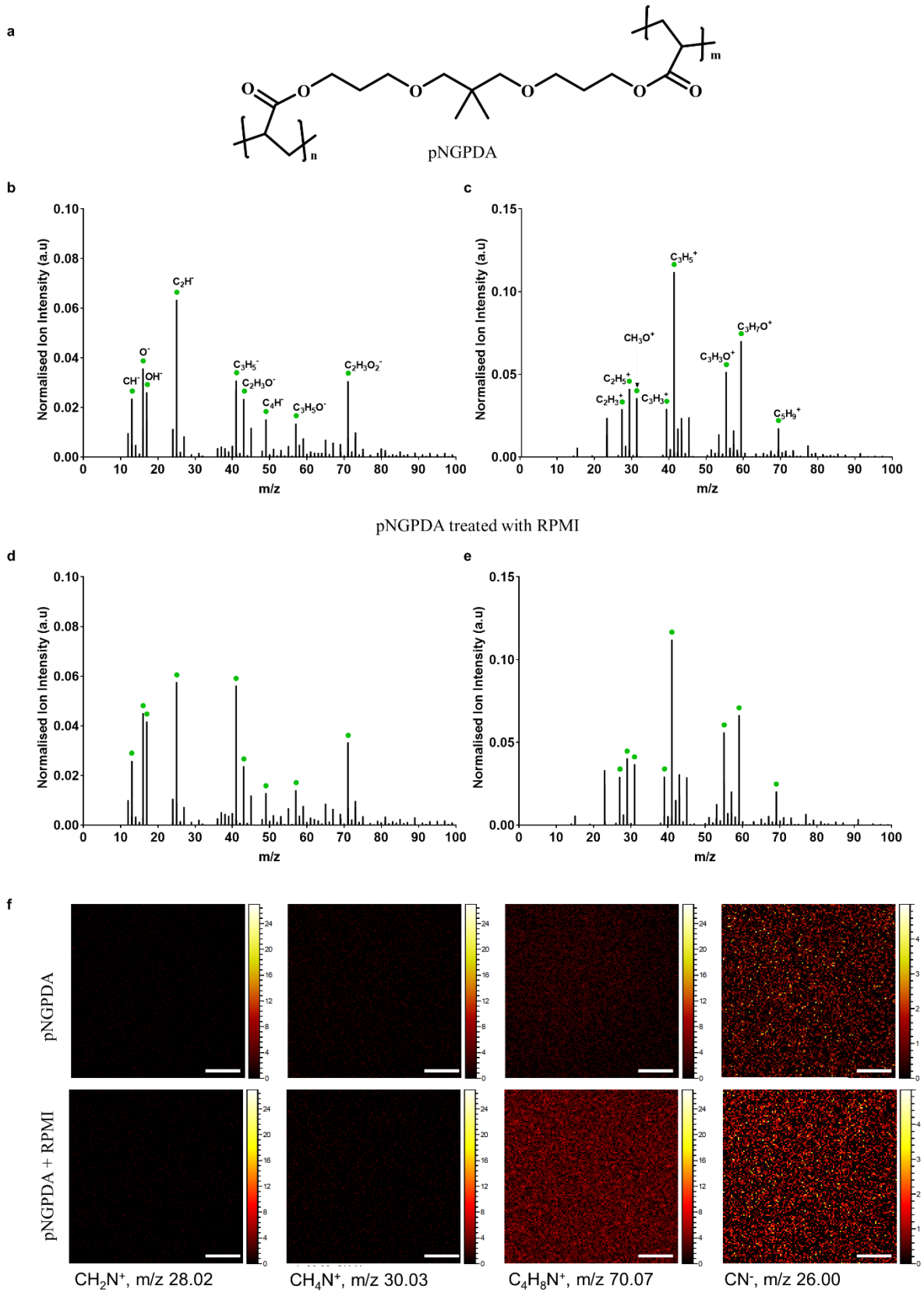

Figure 43. **(a)** Chemical structure for pNGPDA **(b)-(c)** respectively the negative and positive spectra for untreated pNGPDA. **(d)-(e)** respectively the negative and positive spectra for pNGPDA sample treated with standard RPMI. **(f)** ToF-SIMS ion images for pNGPDA sample treated with and without RPMI. Amino acid generic marker ions are CH_2N^+ (m/z 28.02), CH_4N^+ (m/z 30.03), $C_4H_8N^+$ (70.07) and CN^- (m/z 26.00) adsorbed on surface. Scale bar is 100 µm.

No nitrogen containing secondary ions were detected from these polymers prior to media exposure. After media exposure a number of new even-mass nitrogen containing peaks were notable in the positive ion spectrum, whilst the polymer peaks decreased in relative contribution. These were assigned by comparing to literature spectra for all naturally occurring amino acids. We assessed that of the 260 secondary ion fragments reported, 37 negative fragments and 48 positive fragments uniquely represent specific amino acids with the remaining 176 not specific to one amino acid [255].These allowed a total of three amino acids to be uniquely identified by at least one peak in this particular ToF-SIMS experiment.

The secondary ion fragments identified on the surface of treated pEGDPEA in all three replicates shown in Figure 42d-e were generic amino acid peaks; including CN^- (m/z 26.00), CH_2N^+ (m/z 28.02), CH_4N^+ (m/z 30.03) and $C_4H_8N^+$ (m/z 70.07). In comparison, analysis of pNGPDA after RPMI incubation revealed no significant change in secondary ion peaks for amino acid for all three independent replicates and the ions representative of pNGPDA peaks were unaltered (Figure 43d-e) suggesting very little strong adsorption of amino acids onto its surface if any at all.

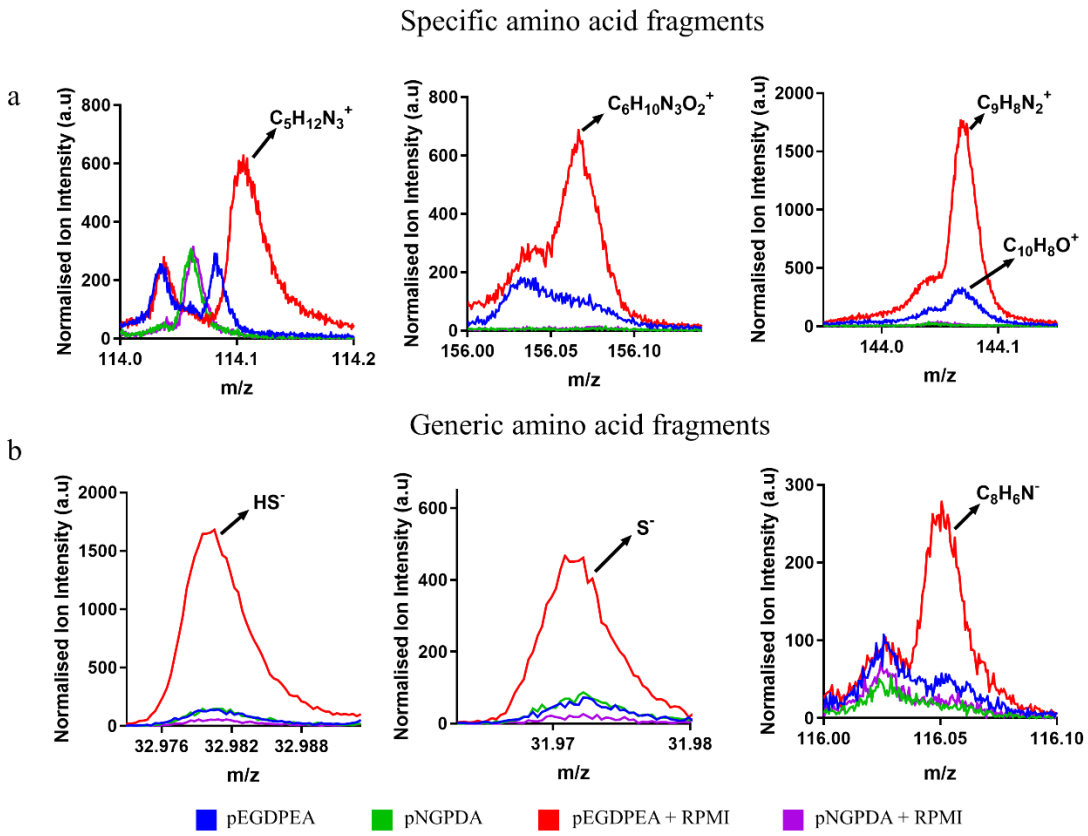

Figure 44. **(a)** Spectra of specific amino acid fragments adsorbed onto surface of pEGDPEA and pNGPDA treated with RPMI (red and purple) and not treated (blue and green). **(b)** Same as (a) for indicative amino acid fragments. All assignment are within a deviation of 50 ppm.

Three unique ions indicative of three different amino acids detected on pEGDPEA from RPMI are shown in Figure 44a; $C_5H_{12}N_3^+$ (m/z 114.10) is an ion fragment solely identifying of Arginine, $C_5H_{10}N_3O_2^+$ is the molecular ion (M + H) of Histidine and $C_9H_8N_2^+$ (m/z 144.07) is an ion fragment from Tryptophan. A targeted approach to identify B vitamins (B1, B2, B5 and B12), folic acid and other constituents of RPMI (see Table 2) through molecular and fragment ion was made. However, no adsorbates from these sources were detected to be retained on the surface, most likely due to their low concentrations (µM) compared to amino acids which were present in mM concentrations.

Two secondary ion fragments S^- (m/z 31.98) and HS^- (m/z 32.98) indicative of cysteine/methionine amino acids were found to have greater intensity on surface of treated pEGDPEA (see Figure 44b). Likewise, $C_8H_6N^-$ (m/z 116.05) secondary ion fragment

detected only on surface of treated pEGDPEA was found to have originated from aromatic ring fragment attributed to either tryptophan or phenylalanine.

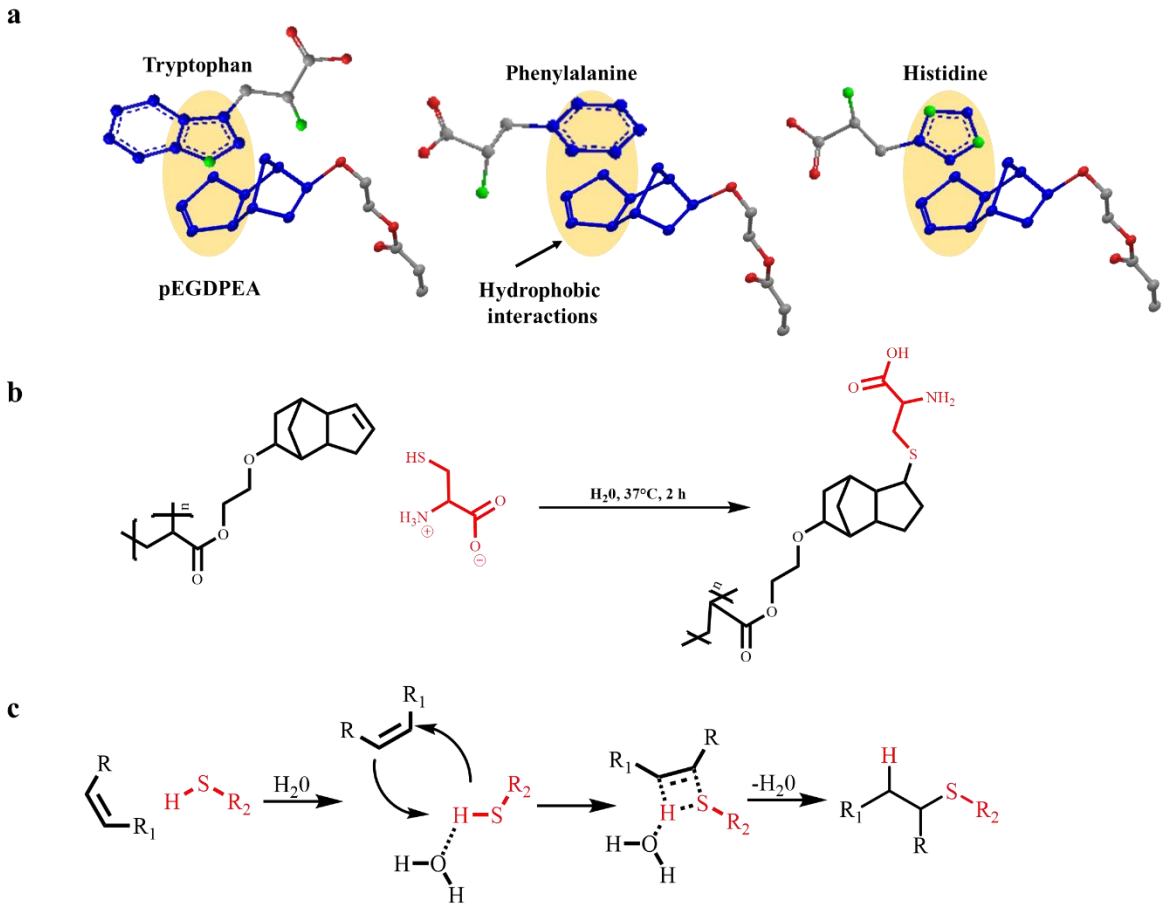

Figure 45. **(a)** Interaction between hydrophobic aromatic groups of tryptophan, phenylalanine and histidine (blue) with hydrophobic tricyclic ring of pEGDPEA (blue). **(b)** Scheme for reaction between cysteine (red) and alkene functionality in pEGDPEA ring. **(c)** Proposed mechanism for water assisted hydrothiolation of alkene.

The largest contributors to hydrophobic interaction within all 20 naturally occurring amino acids are tryptophan and phenylalanine [256, 257]. Respectively, they possess the indole and phenyl non-polar groups capable of forming hydrophobic-hydrophobic interactions with the non-polar tricyclic ring of pEGDPEA (Figure 45a). Here we consider such interaction to be a possible explanation for the relative abundance of aromatic amino acids adsorbed onto the surface of pEGDPEA compared to pNGPDA.

The enrichment of thiol containing amino acid cysteine on surface of pEGDPEA may not only be due to adsorption, but may perhaps occur by an addition reaction between the thiol (cysteine) and alkene (pEGDPEA) functionalities (Figure 45b). This is also supported by reports from

Mandal *et al*., where the addition of thiols to alkenes promoted by water was achieved at room temperature, with no added initiator or formation of radical intermediate [258, 259]. In their protocol, water promotes the nucleophilicity of the thiolate ion through hydrogen bonding with the hydrogen of the thiol, and thus nucleophilic thiolate anion adds across the C=C bond of alkene in a concerted manner leading to the product (Figure 45c) [260].

3.4.2 ToF-SIMS Analysis of pEGDPEA and pNGPDA Incubated with Supplemented RPMI

Adsorption to a surface from a solution can be described using the adsorption isotherm approach adapted from gas-adsorption theory, describing in this case the equilibrium amount of amino acids at the surface for a range of solution concentrations at constant temperature [250]. From this, information about the adsorbate-surface interactions such as on/off-rate and coverage can be calculated by comparison with adsorption theory. In order to obtain the isotherm of amino acids adsorbed onto surfaces of pEGDPEA and pNGPDA in relation to solute concentration, we supplemented commercially available RPMI with amino acid content of 0.068% w/v with a mixture of amino acids obtained from acid hydrolysis of casein (casamino acids) up to 0.5% w/v, seven times its concentration in RPMI media. ToF-SIMS spectra were acquired from freshly prepared polymers of pNGPDA and pEGDPEA following a two hour incubation with media supplemented with amino acids to achieve 5 extra concentrations followed by the same rinsing procedure used before.

a pEGDPEA treated with supplemented media

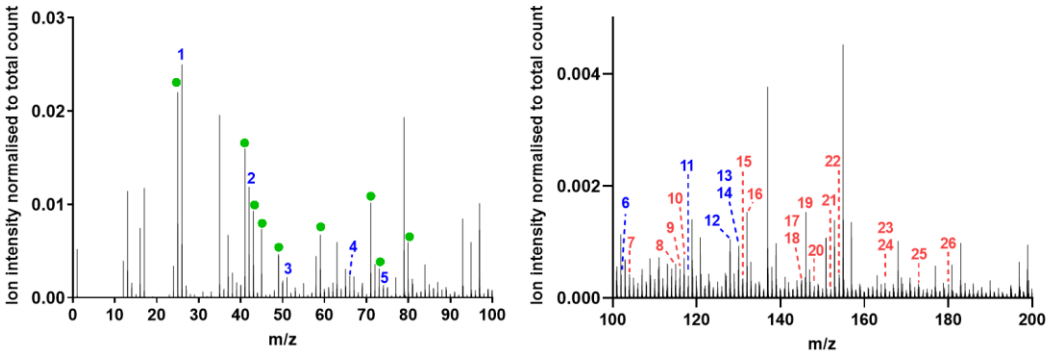

b pNGPDA treated with supplemented media

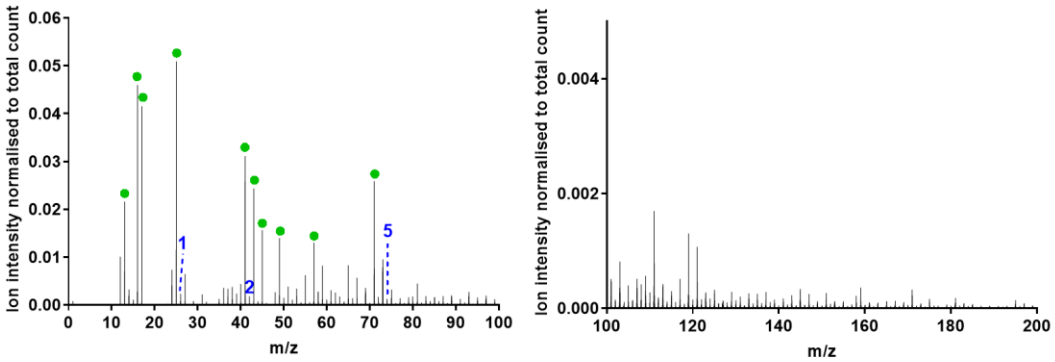

c Table of assignments

s/n	m/z	Ion	Indicative amino acid	s/n	m/z	Ion	Indicative amino acid
1	26.00	CN^-	Generic	14	130.09	$C_6H_{12}NO_2^-$	Iso(leucine) or lysine
2	42.00	CNO^-	Generic	15	131.09	$C_5H_{11}N_2O_2^-$	Arginine
3	49.99	C_3N^-	Generic	16	132.03	$C_4H_6NO_4^-$	Aspartic acid
4	65.99	C_3NO^-	Generic	17	145.06	$C_5H_9N_2O_3^-$	Glutamine
5	74.02	$C_2H_4NO_2^-$	Generic	18	145.11	$C_6H_{13}N_2O_2^-$	Lysine
6	102.04	$C_4H_8NO_2^-$	Generic	19	146.05	$C_5H_8NO_4^-$	Glutamic acid
7	104.03	$C_5H_2N_3^-$	Histidine	20	148.06	$C_5H_{10}NO_2S^-$	Methionine
8	115.00	$C_4H_3O_4^-$	Aspartic acid	21	151.96	$C_3H_6NO_2S_2^-$	Cystine
9	116.06	$C_8H_6N^-$	Multiple	22	154.08	$C_6H_8N_3O_2^-$	Histidine
10	117.02	$C_4H_5O_4^-$	Aspartic acid	23	164.06	$C_5H_{10}NO_3S^-$	Methionine
11	118.05	$C_4H_8NO_3^-$	Multiple	24	164.13	$C_9H_{10}NO_2^-$	Phenylanine
12	128.03	$C_6H_{12}NO_2^-$	Multiple	25	173.15	$C_6H_{13}N_4O_2^-$	Arginine
13	130.04	$C_6H_{12}NO_2^-$	Multiple	26	180.09	$C_9H_{10}NO_3^-$	Tyrosine

Figure 46. ToF-SIMS of freshly prepared pEGDPEA and pNGPDA samples treated with RPMI media sequentially supplemented with amino acids. Each sample is an independent measurement. **(a)** Negative spectra m/z 0 – 200 for pEGDPEA sample treated with 1 mg/ml amino acid media. Marked in green are prominent pEGDPEA peaks, in blue are peaks indicative of amino acids in general and in red are peaks identifying specific amino acids. **(b)** Same convention as (a) but for pNGPDA **(c)** Table of secondary ions identified on polymer surface and assigned amino acids. Standard deviation of assignments < 100 ppm.

In Figure 46 is a summary of ToF-SIMS data obtained from samples of pEGDPEA and pNGPDA treated with different concentrations of supplemented RPMI media. The SIMS spectra for untreated and treated samples (at 1mg/ml) of pEGDPEA and pNGPDA reported here are representative of other spectra obtained at different concentrations reported in Appendix B.

Consistent with the RPMI experiment, spectra of pEGDPEA treated samples were dominated by polymer fragments (in green) and non-specific amino acid ion fragments (in blue) in the mass range 0 to 100 including CN^-, CNO^-, C_3N^-, C_3NO^-, $C_2H_4NO_2^-$ and $C_4H_8NO_2^-$ (Figure 46a-b and Appendix B). At higher mass, more fragments and specific molecular ions for amino acids (in red) were identified. Across the six different media concentrations of amino acid used for incubations, 10 secondary ions from the literature that are unique to a particular amino acid were observed. These were Lysine ($C_6H_{13}N_2O_2^-$), Glutamine ($C_5H_9N_2O_3^-$), Arginine ($C_5H_{11}N_2O_2^-$, $C_6H_{13}N_4O_2^-$), Histidine ($C_5H_2N_3^-$, $C_6H_8N_3O_2^-$) Phenylalanine ($C_9H_{10}NO_2^-$), Tyrosine ($C_9H_{10}NO_3^-$), Aspartic acid ($C_4H_6NO_4^-$), Glutamic acid ($C_5H_8NO_4^-$), Cystine ($C_3H_6NO_2S_2^-$) and Methionine ($C_5H_{10}NO_3S^-$).

The most intense molecular fragment peaks indicative of unique amino acids identified across all spectra for treated pEGDPEA samples were those of Glutamic acid and Aspartic acid (respectively peaks 19 and 16 in Figure 46a). Taking into account amino acids already present in standard RPMI, Glutamic acid makes up 18% (w/w) of amino acid mixture used in the experiment, Isoleucine or Leucine make a combined 15% and Aspartic acid 6% amongst all others (Appendix A). The distribution of these amino acids in modified media was only weakly mirrored in ToF-SIMS spectra acquired for pEGDPEA sample treated with 2 mg/ml, with R^2 = 0.57 (Figure 47). The other five experimental conditions with R^2 less than 0.5 did not reflect media distribution of amino acids (Appendix C), suggesting the adsorption of amino acids onto surface of pEGDPEA is not random and more likely to be specific as shown 3.4.1.

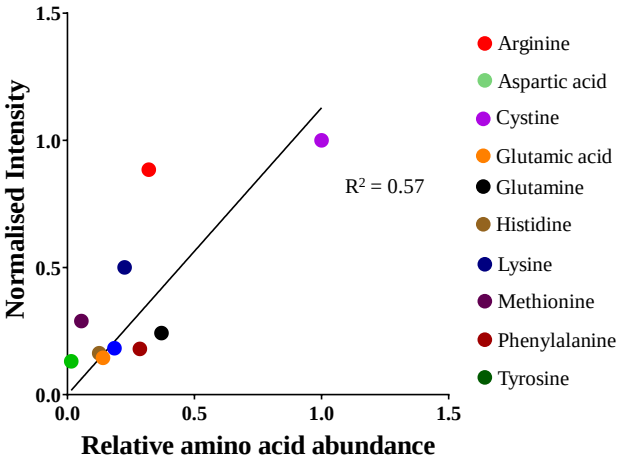

Figure 47. The ToF SIMS intensity of amino acids on polymer surface normalised to glutamic acid plotted versus the theoretically calculated relative abundance of amino acid (w/w) in supplemented RPMI media normalised to glutamic acid. The graph here was obtained from incubating polymer surface with 2mg/ml supplemented RPMI. Line of best fit from which R^2 was calculated is shown in black.

The adsorption of individual amino acids onto surface of both polymer, was mapped by plotting the variation in intensity of the 10 molecular fragments unique to individual amino acids versus media concentration in Figure 48a-b. We observed a similar trend for all 10 amino acids adsorbed onto surface of pEGDPEA with an unvaried intensity for pNGPDA

The ToF-SIMS images of selected secondary ions reveal the distribution of amino acids on polymer surfaces. In Figure 48c, the adsorption of amino acids onto surface of pEGDPEA at 0.5 mg/ml monitored through marker ion CN^- (m/z 26.00) occurred over the entire surface with relatively low intensity when compared to areas of localized and intense adsorption that can be seen as islands/patches. With increasing concentrations, the coverage increases until reaching saturation at 4 mg/ml. In comparison, the secondary ion signals from amino acids onto pNGPDA is very low and not visible on the same scale used for pEGDPEA.

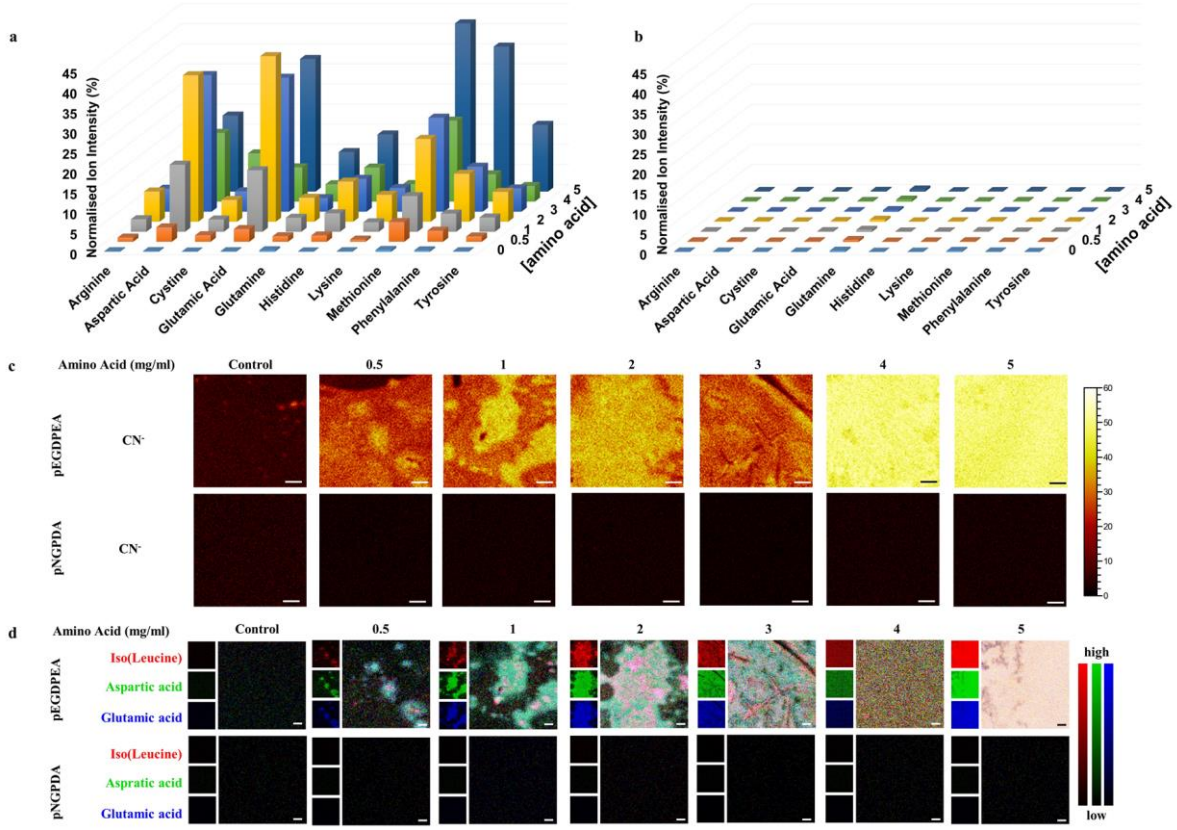

Figure 48. **(a)** 3D bar chart showing ion intensity change (z-axis) of 10 molecular fragments indicative of 10 different amino acids (x-axis) with varying concentration of amino acids in media (y-axis) on pEGDPEA. **(b)** Same as (a) for pNGPDA. **(c)** ToF-SIMS ion images for CN^- (m/z 26.00) generic marker of amino acid on adsorbed on pEGDPEA and pNGPDA treated with different concentrations of amino acids in RPMI. Scale bar is 50 µm. **(d)** Overlay of ToF-SIMS ion images for pEGDPEA and pNGPDA, showing Lysine/Iso(Leucine) ($C_6H_{12}NO_2^-$, m/z 130.09) in red, Aspartic acid ($C_4H_6NO_4^-$, m/z 132.03) in green and Glutamic acid ($C_5H_8NO_4^-$, m/z 146.05) in blue. Scale bar is 50 µm.

In Figure 48d, the distribution of two molecular ions and one fragment ion with high relative peak intensities and indicative respectively of Glutamic acid, Aspartic acid and Iso(leucine) which matched the distribution and intense localisation of CN^- ion observed in Figure 48c, these three amino acids are also seen to account for most nutrient surface adsorption with the exception of 4 mg/ml media condition, where Arginine and Cysteine were the dominant adsorbates on surface (Figure 49). Consistently, adsorption onto pNGPDA surface was minimal and far less than the pEGDPEA.

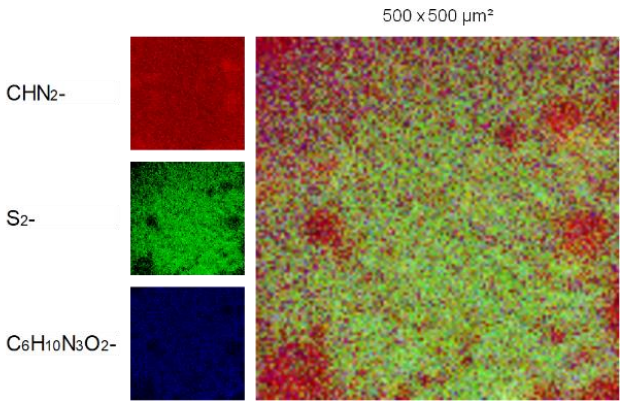

Figure 49. Overlay of ToF-SIMS ion images for pEGDPEA incubated with 4 mg/mL amino acid in RPMI. Arginine (CHN_2^-) in red, Cysteine (S_2^-) in green and Arginine ($C_6H_{10}N_3O_2^-$) in blue.

3.4.3 Adsorption Isotherms

Over the years, a wide variety of equilibrium isotherm models including Langmuir, Freundlich, and Brunauer–Emmett–Teller (BET) amongst many others have been formulated to quantitatively describe gas and solute adsorption to surfaces and these three are the most commonly used models [250].

The Langmuir adsorption isotherm model is largely applied for adsorption from aqueous solutions where a valid assumption is that adsorption does not occur beyond a monolayer coating, that the surface is uniform and that the ability of a molecule to adsorb at a given site is independent of the occupation of neighbouring sites, that is, interaction between adsorbed molecules is considered insignificant [250, 261]. On the other hand, the BET model was developed to derive multilayer adsorption systems and indeed provides a solution to the multilayer adsorption patterns. Similarly, the Freundlich isotherm is empirical and earliest known relationship describing the non-ideal and reversible adsorption, not restricted to the formation of monolayer, a reasonably more appropriate model that allows easy application to multilayer adsorption with non-uniform distribution of adsorbates.

From definitions, the Freundlich isotherm will seem more appropriate to model adsorption phenomena onto pEGDPEA based on non-uniform coverage observed beyond

monolayer in Figure 48d, where islands and areas of localized concentrations of amino acids are obvious. However, linearization was also attempted with Langmuir model regardless of its assumptions and compared to Freundlich's for best fitting.

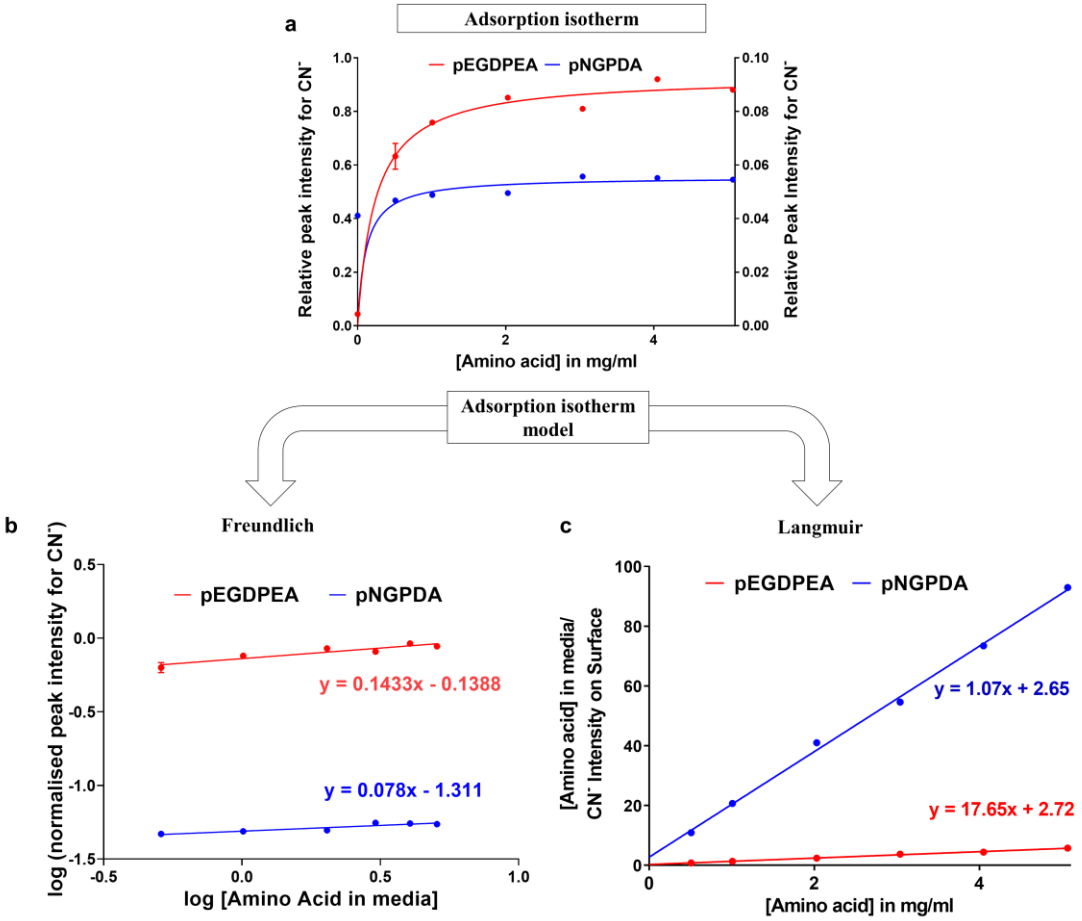

Figure 50. **(a)** Adsorption isotherm of amino acids adsorbed onto surfaces pEGDPEA and pNGPDA. On y-axis (left is pEGDPEA, right is pNGPDA) is ToF-SIMS intensity of CN^- normalised to reference peak of adsorbent polymer: CHO_2^- (m/z 45.00) for pEGDPEA and C_2H^- (m/z 25.00) for pNGPDA. Each data point is the mean intensity from three regions of interest ± 1 SD. **(b)** Freundlich fitting to isotherms for adsorption of amino acids at 37 ˚C on pEGDPEA (in red): R^2 0.83, Y = 0.14*X + 0.14 and pNGPDA (in blue): R^2 = 0.84, Y = 0.078*X – 1.31. **(c)** Langmuir isotherm plots for adsorption of amino acids at 37 ˚C on pEGDPEA (in red): R^2 0.99, Y = 1.072*X + 2.65 and pNGPDA (in blue): R^2 = 0.99, Y = 17.65*X + 2.716.

The isotherms derived from plotting the amino acid concentration (w/v) in the media against the normalised intensity of CN^- (m/z, 26.00) peak unique to amino acid adsorbate are presented in Figure 50a. From which we detect from the y-intercepts, the differences in saturation coverages achieved on pEGDPEA (0.88 au) and pNGPDA (0.05 au). Saturation coverages occurred at amino acid concentrations of 4 mg/ml and 3 mg/ml respectively.

The Freundlich fitting in Figure 50b was obtained by plotting the log of each. Following details reported in section 3.3.4.1, we worked out the adsorption capacity (K_F) values for pEGDPEA (0.73) to be 14 times that of pNGPDA (0.05) and it was deducible from gradients that the process of adsorption is almost twice as likely (1.8 X) to occur on pEGDPEA surface than pNGPDA.

A stronger fit was obtained with a Langmuir model in Figure 50c ($R^2 = 0.99$) with calculated equilibrium monolayer coverages (Γ_m) on pEGDPEA and pNGPDA occurring at amino acid concentrations of 4 mg/ml and 3 mg/ml respectively, which corresponded with values from Freundlich model. The on/off rate of amino acids from the Langmuir model (also referred to as likelihood in Freundlich model) on pNGPDA was calculated to be 6.50 mg/ml and 4.04 mg/ml on pEGDPEA. Leading to conclude that, under the same condition, amino acids were more likely to remain adsorbed onto surface of pEGDPEA than pNGPDA.

3.4.4 XPS Analysis to Determine Amino Acid Adsorption on Polymers

We carried out X-ray photoelectron spectroscopy (XPS) analysis to obtain detailed information about atomic and functional group specificity of adsorbed amino acids, and calculate the thickness of overlayer from adsorbed amino acids. Fresh samples of pEGDPEA and pNGPDA exposed to amino acid supplemented media were XPS analysed following the same rinsing procedure for ToF SIMS.

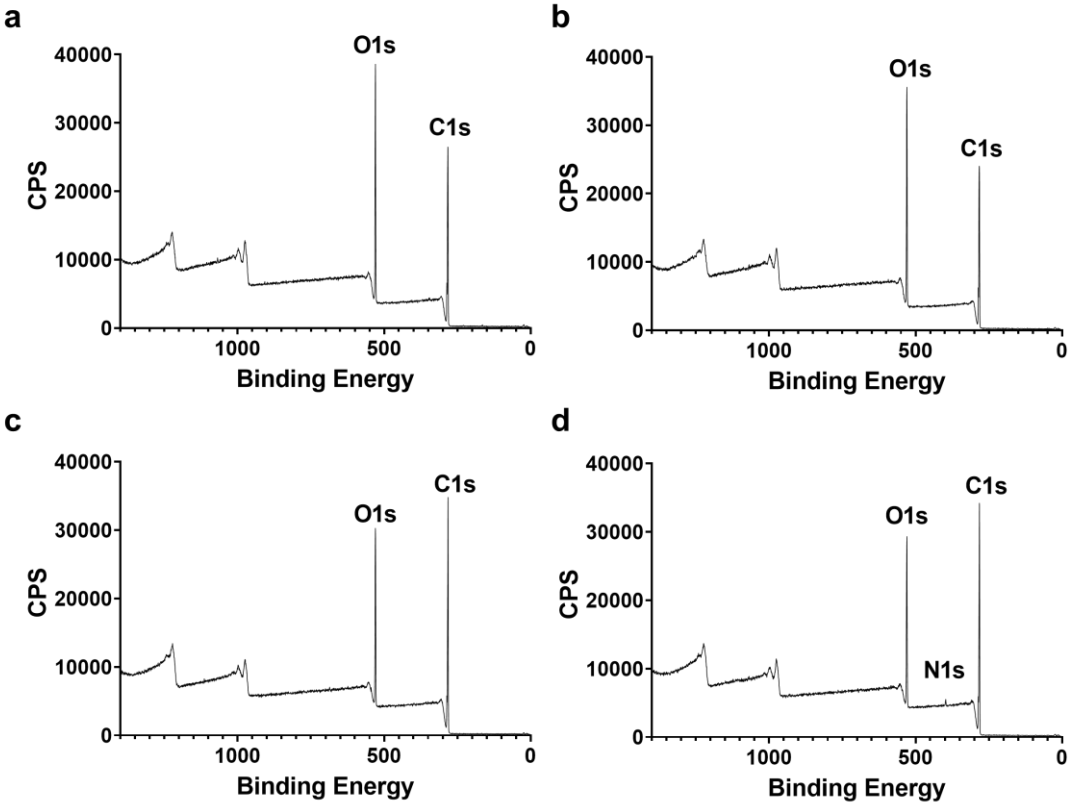

e

			Atomic (%) on media treated pNGPDA					
Core level	Peak (eV)	FWHM (eV)	0.5 mg/ml	1 mg/ml	2 mg/ml	3 mg/ml	4 mg/ml	5 mg/ml
O 1s	531.94	2.21 ± 0.02	22 ± 0.1	23 ± 0.1	23 ± 0.26	23 ± 0.16	23 ± 0.48	23 ± 0.08
C 1s	284.69	2.71 ± 0.02	78 ± 0.1	77 ± 0.1	77 ± 0.31	77 ± 0.09	78 ± 0.43	77 ± 0.01
N 1s	400.32	1.47 ± 2.72	0.03 ± 0.1	0.10 ± 0.1	0.05 ± 0.1	0.05 ± 0.1	0.04 ± 0.1	0.05 ± 0.1
			Atomic (%) on media treated pEGDPEA					
Core level	Peak (eV)	FWHM (eV)	0.5 mg/ml	1 mg/ml	2 mg/ml	3 mg/ml	4 mg/ml	5 mg/ml
O 1s	531.94	2.45 ± 0.1	18 ± 0.1	18 ± 0.1	16 ± 0.4	17 ± 0.4	17 ± 0.4	17 ± 0.5
C 1s	284.44	2.12 ± 0.1	82 ± 0.1	81 ± 0.1	83 ± 0.5	82 ± 0.4	82 ± 0.3	82 ± 0.8
N 1s	399.25	2.02 ± 0.2	0.4 ± 0.1	0.4 ± 0.1	0.3 ± 0.1	0.3 ± 0.0	0.4 ± 0.1	0.6 ± 0.3

Figure 51. XPS analysis from samples pEGDPEA and pNGPDA treated with amino acid supplemented RPMI media. Survey spectrum of: **(a)** pNGPDA without treatment **(b)** pNGPDA treated with 2mg/ml supplemented RPMI media **(c)-(d)** Same convention as (a) and (b) but for pEGDPEA **(e)** Table of elemental composition and atomic percentages showing C 1s, N 1s and O 1s from spectra of pNGPDA and pEGDPEA treated with RPMI supplemented media. Values reported are the average of three regions ± 1 sd.

In Figure 51 is a summary of XPS data obtained from samples of pEGDPEA and pNGPDA treated with different concentrations of supplemented RPMI media. The survey spectra for untreated and treated samples (at 2mg/ml) of pEGDPEA and pNGPDA reported here are representative of other survey spectra obtained at different concentrations shown Appendix D). The table of elemental composition and atomic percentages summarises information obtained from all six treatment conditions.

Consistent with the ToF-SIMS analysis, the survey spectra of 2 mg/ml media treated pNGPDA presented with a similar profile to untreated control sample (Figure 51a-b). In contrast, treated pEGDPEA showed an increase in nitrogen concentration when compared to untreated sample (Figure 51c-d). The N 1s concentration on pEGDPEA increased with increasing amino acid content in media (Figure 52).

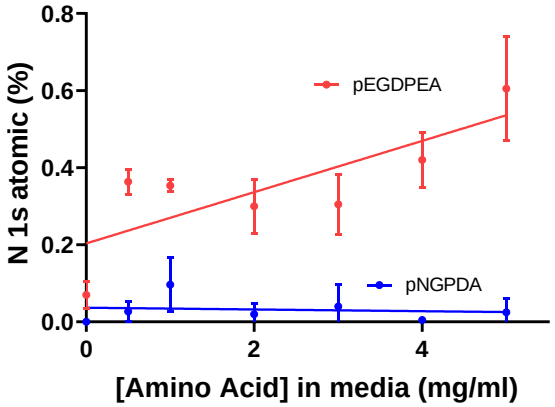

Figure 52. Plot showing variation in N 1s concentration of pEGDPEA (R^2 = 0.53) and pNGPDA (R^2 = 0) with increasing amino acid concentration. Each data point is mean ± 1 s.d (n = 3).

The Nitrogen concentration determined from the N 1s core level can be converted into amino acid overlayer thickness following methods previously reported in literature and detailed in section 3.3.6 [252]. The averaged overlayer thickness of amino acid adsorbed onto surface of pEGDPEA at 5 mg/ml was calculated to be 0.43 ± 0.06 nm.

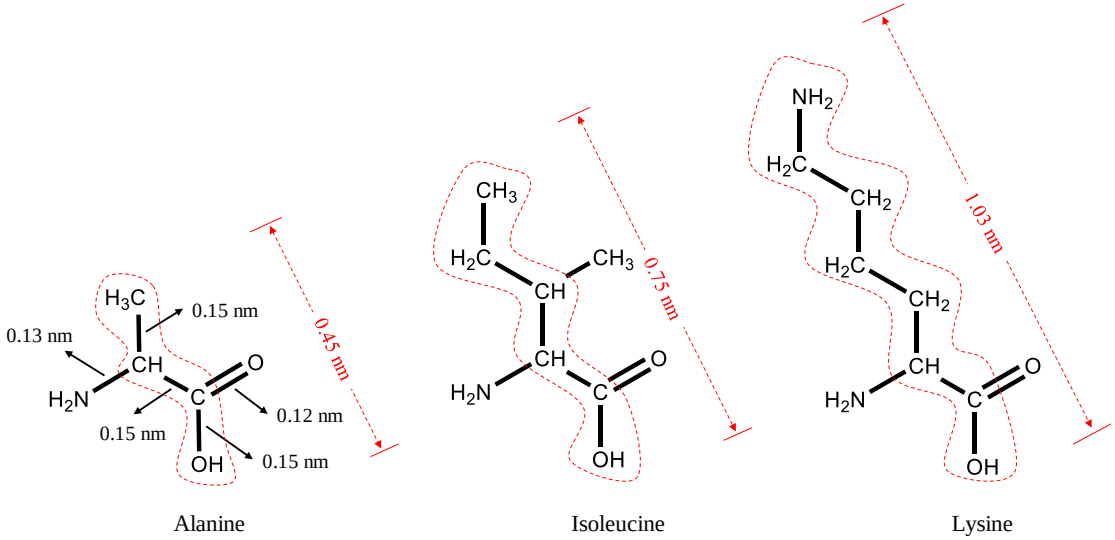

Figure 53. Bond lengths and molecule dimension for alanine, isoleucine and lysine. Outlined with dotted red lines are longest chains for each amino acid molecule.

A typical amino acid molecule is generally accepted to be between 0.35 - 1 nm in its longest dimension (see Figure 53) and it is reasonable to assume using measurements from overlayer thickness that monolayer adsorption of amino acids occurred on surface of pEGDPEA at 5 mg/ml if oriented in this manner [262, 263].

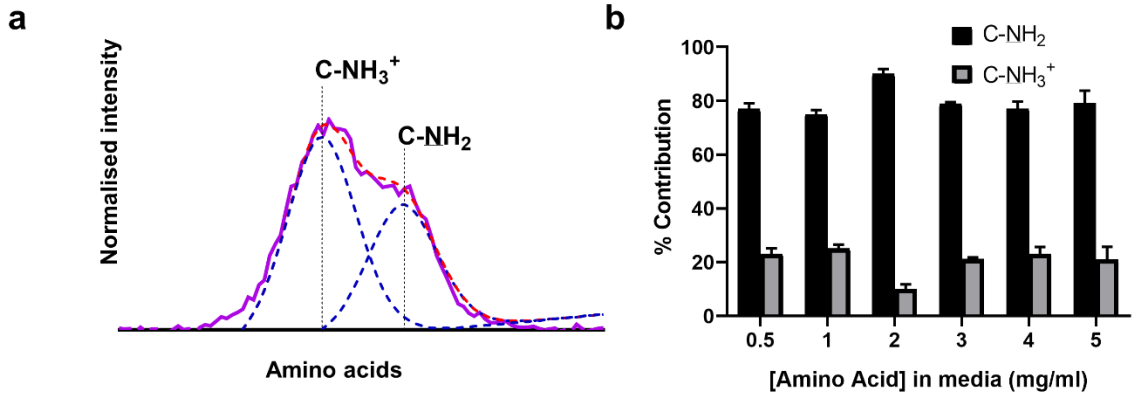

c

			Atomic (%) on media treated pEGDPEA					
Core level	Peak (eV)	FWHM (eV)	0.5 mg/ml	1 mg/ml	2 mg/ml	3 mg/ml	4 mg/ml	5 mg/ml
C-$\underline{N}H_2$	399.60	1.74 ± 0.1	77 ± 2	75 ± 2	88 ± 5	78 ± 2	77 ± 3	78 ± 4
C-$\underline{N}H_3^+$	401.11	1.74 ± 0.1	23 ± 2	25 ± 2	12 ± 5	22 ± 2	23 ± 3	21 ± 4

Figure 54. **(a)** High-resolution core level N 1s spectra of amino acid mixture. The fitted envelopes are presented in red, while the individual contributions of different functional groups present are represented with blue lines. **(b)** Plot showing the ratio of pronated Nitrogen (C-NH_3^+) to non-protonated Nitrogen (C-NH_2). **(c)** Table of contributions from protonated and non-protonated Nitrogen obtained from spectra of pEGDPEA treated with RPMI supplemented media. Values reported are the average of three regions ± 1 s.d.

In Figure 54a, the N 1s spectrum of pure amino acids in powdered form showed two contributions at approximately 399.5 and 401.5 eV, arising from the amine group in neutral

(35%) and protonated (65%) states respectively [264]. When adsorbed on the pEGDPEA the amine groups are observed to be less protonated (20%) than in the solid amino acid (35%) (Figure 54b). We interpret this protonation of the amine group as arising from the acceptance of carboxylic acid protons from other proximal molecules in the solid, such as glutamic and aspartic acid. Adsorbed to pEGDPEA in the vacuum environment of the XPS instrument there are few proximal amino acid molecules, thus causing this degree of amine protonation.

3.4.5 Surface Zeta Potential and Water Contact Angle of pEGDPEA and pNGPDA

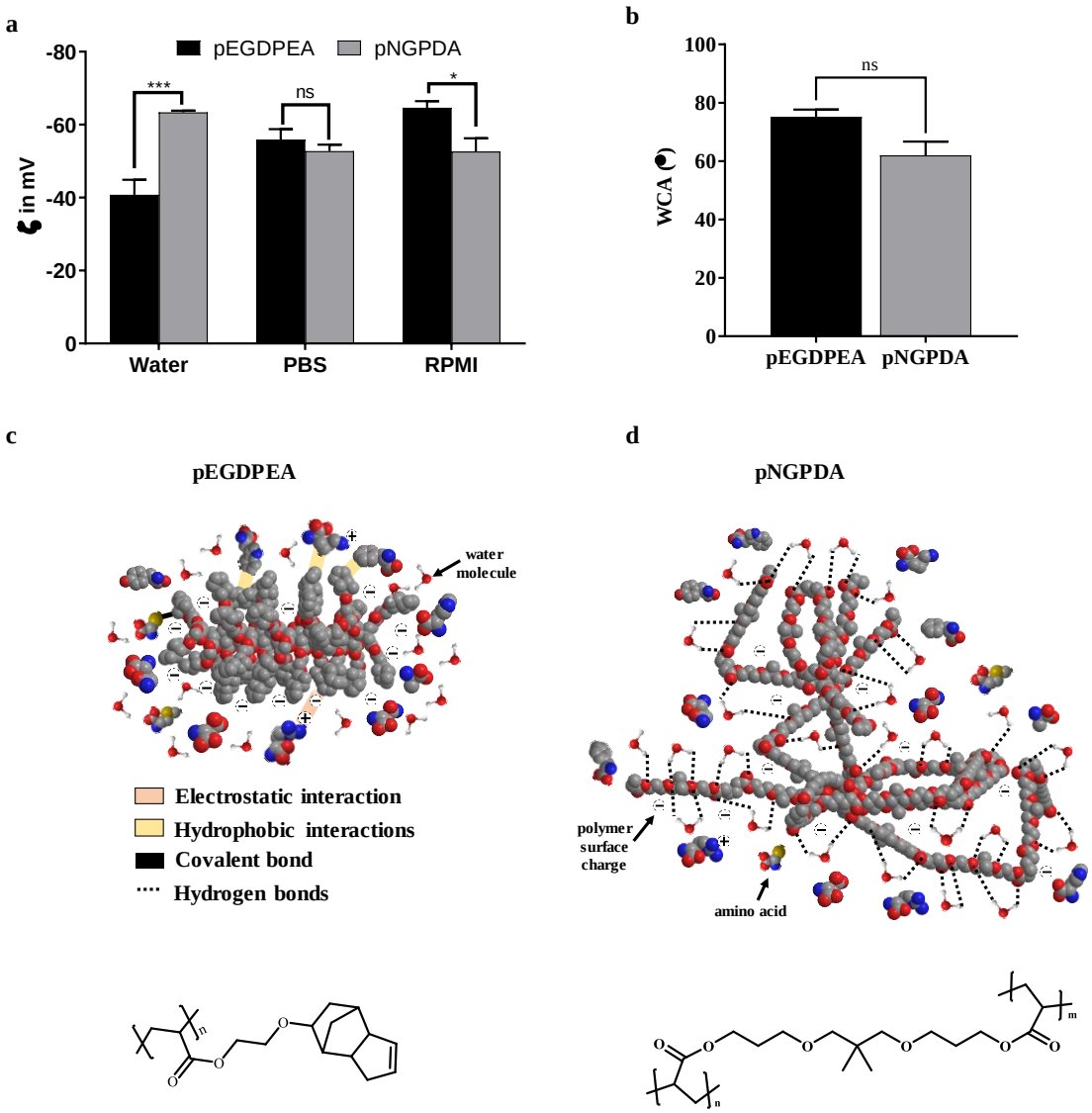

Figure 55. **(a)** Surface Zeta Potential measured on films of pNGPDA and pEGDPEA in three different solutions. p values < 0.05. Data point are mean ± 1 s.d (n=2). **(b)** Water contact angle values for pEGDPEA and pNGPDA. Data point are mean ± 1 s.d (n=3). All significances were determined by paired t-test comparison for differences between the indicated samples. **(c)** 3D space filling model for structure of negatively charged pEGDPEA in aqueous environment interacting with hydrophobic and charged amino acids. **(d)** 3D space filling model for structure of negatively charged pNGPDA interacting with water via h-bonds and surrounded by amino acids.

Surface charge and wettability are two of the most frequently mentioned factors that are responsible for a range of biological effects [91, 265]. Examining surface charge phenomena can be used in an attempt to rationalise interactions that occur during the events of amino acid adsorption [226]. In Figure 55 is reported the surface zeta potential and water contact angle values measured on pEGDPEA and pNGPDA following detailed methods in section 2.3.5 and 2.3.2.

The surface charge for pEGDPEA (-64.6 ± 1.25 mV) and pNGPDA (-52.6 ± 2.55 mV) was estimated by measuring their surface zeta potential value in RPMI. In terms of wettability, pNGPDA (62°) wets better than pEGDPEA (75°). Building on these parameters, a mechanistic model to explain differences in adsorption phenomena for both surfaces was evaluated using 3D ChemDraw structures for pEGDPEA and pNGPDA (Figure 55c-d). Firstly, the polymer architecture for pEGDPEA presents with more bulky tricyclic hydrophobic groups on external surface that do mask hydrogen bond acceptor oxygen atoms (in red), which makes it more difficult for water atoms to interact with pEGDPEA. On pNGPDA, the oxygen-rich linear chains are more accessible to water molecules and stronger interactions via hydrogen bonds can be formed, which accounts for differences in wettability between the two surfaces.

Assuming no disparity in the charge contribution to adsorption process on surfaces of pEGDPEA and pNGPDA, positively polarised hydrogen atoms from water molecules and positively charged amino acids at pH 8 (i.e. lysine and arginine) will potentially interact equally with negative charge on polymer surfaces. The observed adsorption differences may then be explained in terms of energetics, e.g. for adsorption to occur on pNGPDA, organized water molecules around its surface must be displaced, which comes at an enthalpic cost due to breaking of multiple hydrogen bond interactions (Figure 55d). This process will only be favourable if entropic gain for disorganized water molecules compensates for this enthalpic penalty. The relatively reduced interaction between pEGDPEA and water molecules makes it

energetically more favourable for hydrophobic amino acids, such as leucine, isoleucine and tryptophan to interact with exposed and more accessible hydrophobic tricyclic ring of pEGDPEA (Figure 55c).

3.4.6 Correlation of Surface Adsorbed Nutrients with Attachment of PAO1 on Polymer Surface and Twitching

Prior to studying the attachment of PAO1 onto surfaces of pEGDPEA and pNGPDA in supplemented media, we ensured there was no disparity in growth of PAO1 in media when exposed to both polymers. The growth of PAO1 in media supplemented with amino acids was monitored over a 24 h period in well-plates coated with pEGDPEA and pNGPDA.

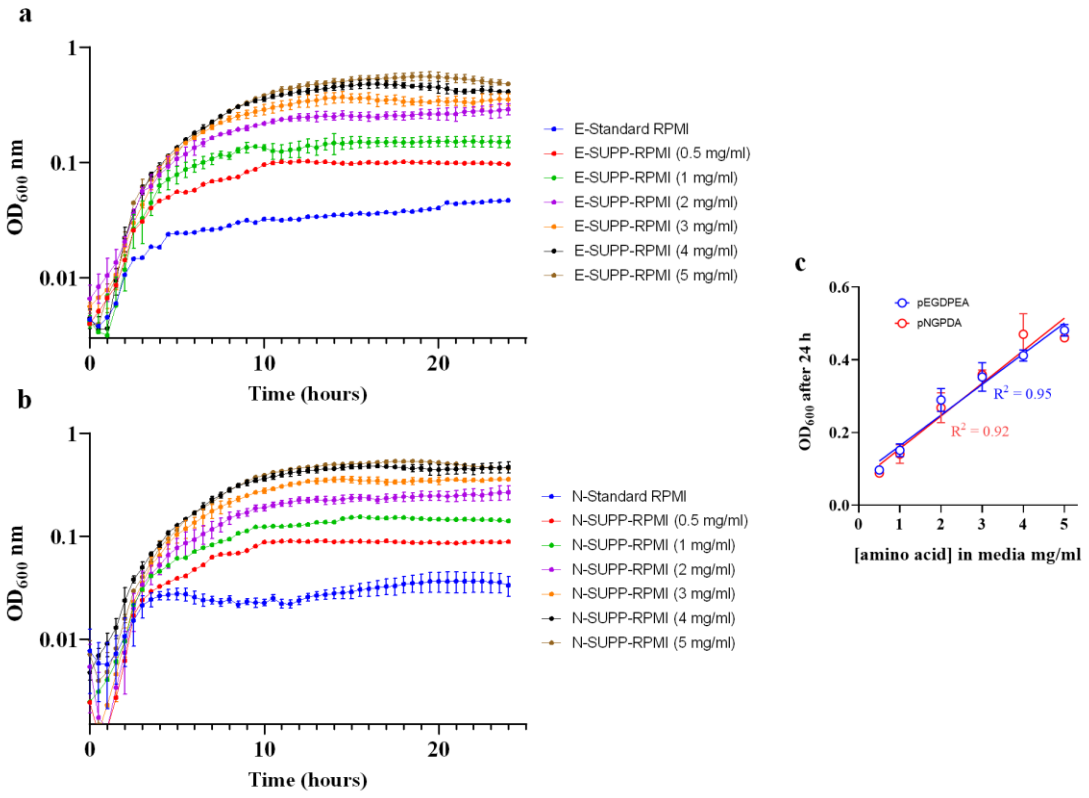

Figure 56. **(a)** Growth curves for *P. aeruginosa* in presence of pEGDPEA incubated at 37 °C for 24 h with media of varying amino acid concentrations. **(b)** Same convention as (a) but for pNGPDA. **(c)** Linear relation between amino acid content in supplemented RPMI media and growth (OD_{600}) of PAO1 after 24 h in presence of pEGDPEA (in blue) and pNGPDA (in red). Error bars are 1 sd, n = 3 biological replicates.

As seen from growth curves in Figure 56a, the growth of PAO1 in media is largely dependent on the abundance of nutrients and this irrespective of pEGDPEA or pNGPDA. This is due to the fact that bacteria are more likely to grow as planktonic cells than form biofilms in a nutrient

rich media [266]. A strong linear relationship (R^2 = 0.92 and 0.95) between amino acid content in supplemented RPMI and growth of PAO1 after 24 hour was observed for both pEGDPEA and pNGPDA (Figure 56c), which suggests the growth in media of PAO1 is the same either in presence of pEGDPEA or pNGPDA, and differences in surface attachment of PAO1 can solely be attributed to surface properties or conditions of polymer surface.

We believe that the abundance of nutrients on a surface in a much similar way to rich media will promote bacterial growth and not drive towards biofilm formation. To verify this, we separately conducted a 24 h biofilm assay with PAO1 and quantified thickness of biofilm formed with confocal fluorescence microscope.

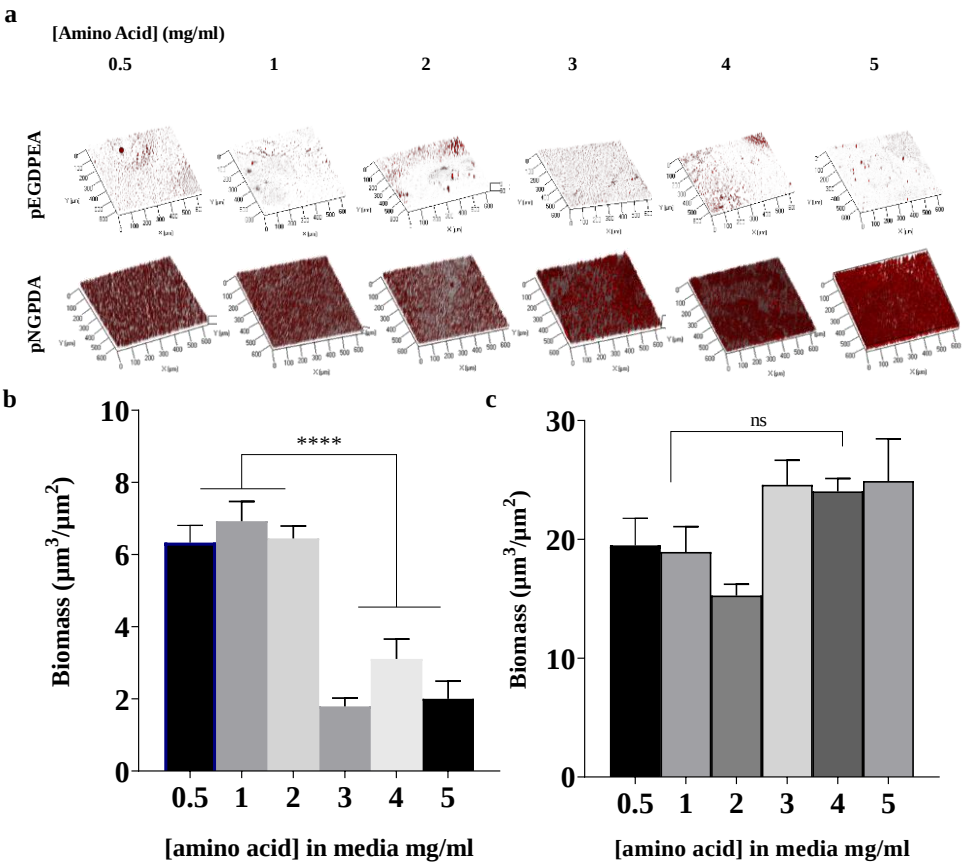

Figure 57. **(a)** Images from confocal microscopy for mCherry tagged *P. aeruginosa* growing on each polymer surface in media with varying amino acid concentrations. Scale bar is 100 µm. **(b)** Biomass of quantified biofilms after 24 h incubation with *P. aeruginosa*. Error bars equal ± 1 sd unit, n = 6 measurements from two biological replicates. Statistics conducted based on analysis of variance p < 01.

The average PAO1 biomass on nutrient rich pEGDPEA surface was calculated to be 4.4 ± 2.3 $\mu m^3/\mu m^2$ and 21.2 ± 4.1 $\mu m^3/\mu m^2$ on nutrient poor pNGPDA surface. For pEGDPEA surfaces,

there is a significant decrease in biomass of PAO1 when nutrient concentration in media is above 2 mg/ml. Whiles for pNGPDA there is no significant change in biomass of PAO1 across the six different media conditions used. We interpret this to be in line with nutrient adsorption results obtained from surface analysis of treated pEGDPEA and pNGPDA. That is, in a much similar way to growth in media reported in Figure 56, the increased concentration of amino acids adsorbed onto the surface of pEGDPEA promotes growth of bacteria as planktonic cells rather than a biofilm community. Conversely, the significantly reduced adsorption of nutrients onto surface of pNGPDA triggers the biofilm mode of growth for PAO1.

It is true that besides sessile aggregation, surface-associated PAO1 can carry out a form of movement termed twitching, mediated via the type IV pili surface appendage and often described as early process that precedes biofilm formation [98, 99]. This twitching movement can be altered based on distinctive nutrient conditions, for example, *P. aeruginosa* showed enhanced twitching motility when incubated with iron-diminished media on agar, which led to a disrupted pattern of biofilm development [267, 268]. It is also true that when presented with chemoattractants (phosphatidylethanolamine, amino acids or nucleotides), *P. aeruginosa* undergoes chemotaxis via twitching motility as an effective way to approach the source [269-271]. Results from these studies were performed on well-known microbiology surfaces, i.e., agar and glass. The twitching behaviour of PAO1 on polymer surfaces of pEGDPEA and pNGPDA studied by A. Carabelli, demonstrated that the average speed of twitching cells on pNGPDA was significantly slower than on pEGDPEA [272].

At this point, we carried out an experiment to assess the effect on twitching motility of increased surface adsorbed nutrients on pEGDPEA compared to pNGPDA. Differently from previous experiment conducted by A. Carabelli in standard RPMI, here twitching motility for *P. aeruginosa* tracked over a period of 4 hours was conducted is in PBS, on surfaces of pEGDPEA and pNGPDA pre-treated with supplemented RPMI (4 mg/ml) for 2 hours. PBS did not only

serve as a nutrient-deficient media for true assessment of the effect of surface adsorbed amino acids on polymers, but also served as an isotonic solution to prevent lysis of bacteria cells that would otherwise occur in water.

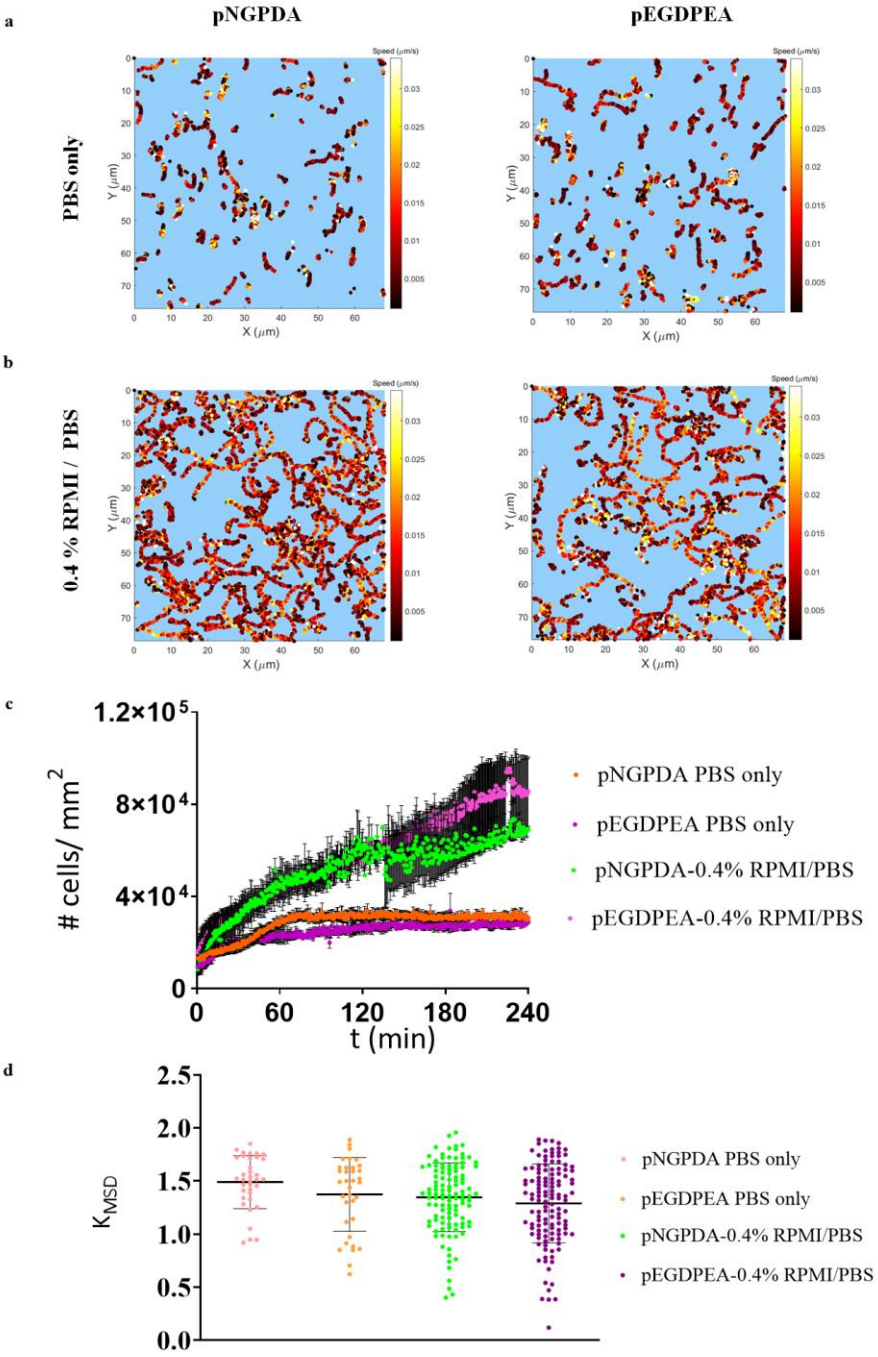

Figure 58. **(a)** Representative colour maps of tracks of *P. aeruginosa* on pNGPDA and pEGDPEA measured *in situ* over 1 h of exposure of surfaces in PBS. **(b)** Representative colour maps of tracks of *P. aeruginosa* on pNGPDA and pEGDPEA measured *in situ* over 1 h of exposure to surfaces pre-incubated with supplemented RPMI (4 mg/ml) prior to PBS. **(c)** Number of bacteria per frame vs. time for pEGDPEA and pNGPDA treated with 4 mg/ml supplemented RPMI and PBS. Dots represent mean ± 1 standard deviation (N=3). **(d)** Categorical scatter plot showing mean square displacement for PAO1 on surfaces of pEGDPEA and pNGPDA treated with 4 mg/ml supplemented RPMI and PBS.

Experimental procedures and data processing to courtesy of A. Carabelli. O. Sanni prepared all polymer samples, carried out adsorption experiments and cultured P. aeruginosa used in experiments. A. Carabelli carried out single cell tracking on microscope and processed data with Matlab software.

Figure 58a-b respectively show maps of bacterial tracks of PAO1 on pristine and treated surfaces of pEGDPEA and pNGPDA in PBS. After four hours, the number of cells on pristine pNGPDA and pEGDPEA incubated in PBS were comparable, with an average count of 3.0 x $10^4 \pm 2.5 \times 10^3$ cells/mm^2 (see Figure 58c). For pEGDPEA surfaces pre-incubated with 4 mg/ml supplemented RPMI, cell count after four hours was $8.4 \times 10^4 \pm 1.5 \times 10^4$ cells/mm^2, whiles cell count for pNGPDA was lower, but not significantly different at $6.8 \times 10^4 \pm 2.6 \times 10^4$ cells/mm^2. No difference in speed and directionality (K_{MSD}) was observed between pNGPDA and pEGDPEA after nutrient incubation, Figure 58d.

Cells were classified as stationary or motile depending on twitching speed with cut-off at 10 nms^{-1}. There was no difference in twitching speed of PAO1 on pre-treated polymer surfaces. A significant difference was only observed between bacterial cells exposed to polymers and PBS media, Figure 59a. A comparison of the fraction of twitching cells on both surfaces over a 4 hour period, showed meaningful differences. At time zero, the fraction of twitching cells on both polymer surfaces was dependent on concentration of nutrients in media, that is, 0.27 in PBS and 0.63 in supplemented RPMI. On pNGPDA surface pre-treated with 4 mg/ml RPMI (blue line in Figure 59b), there was a rapid decline in fraction of twitching cells compared to pEGDPEA (blue line in Figure 59c). After 4 hours (240 mins), the fraction of twitching cells on surface of pEGDPEA (0.27) is about twice the fraction of twitching cells on surface of pNGPDA (0.15).

We hypothesize that the greater abundance of nutrients on surface of pEGDPEA is reason for higher twitching fraction of cells on its surface compared to pNGPDA. Here our hypothesis is based on at least two assumptions. Firstly, we have assumed based on huge differences observed from ToF-SIMS and XPS analysis with three independent replicates (see 3.4.1) and six different media conditions (see 3.4.2), that amino acid adsorption occurs to a greater degree on pEGDPEA surface over pNGPDA when treated with supplemented RPMI (4mg/ml). Secondly,

we have conducted no surface analysis for pEGDPEA and pNGPDA post-exposure to bacteria because exudates from bacteria such as nucleotides, phospholipids and proteins (see 1.4.1) can lead to false positive results.

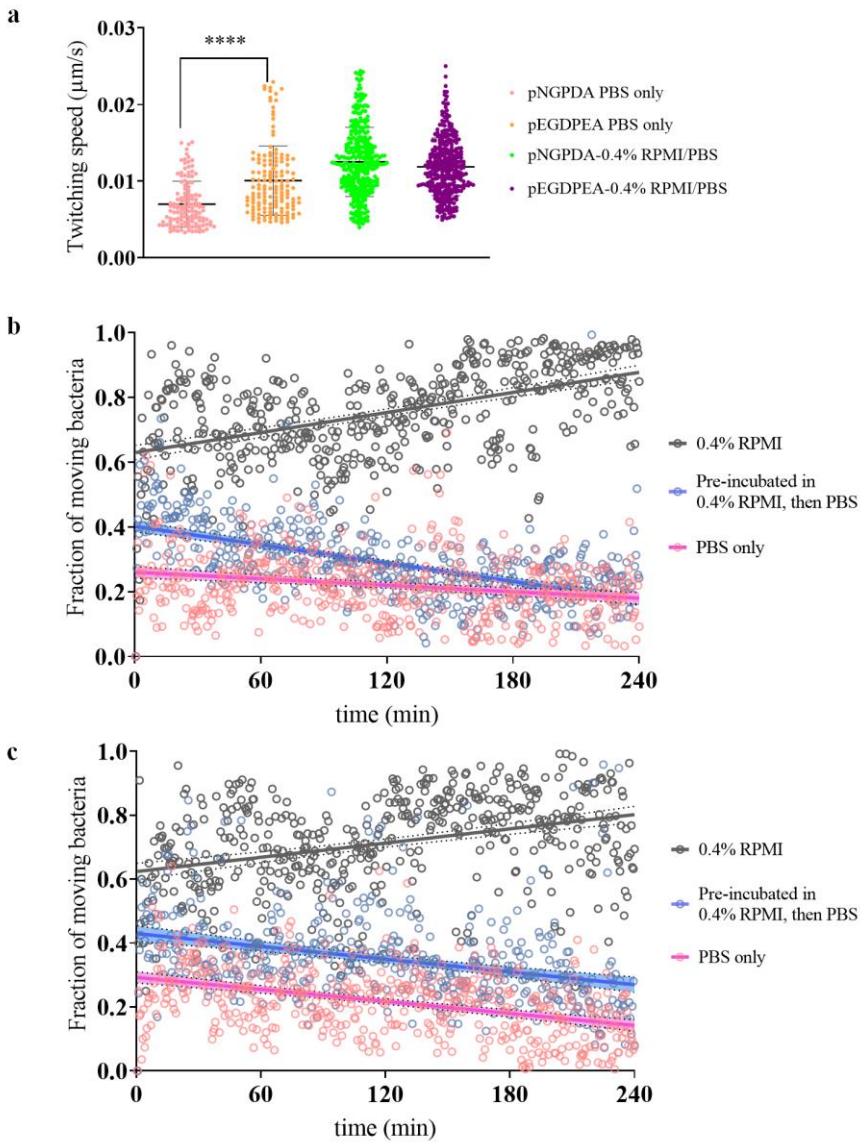

Figure 59. **(a)** Categorical scatter plot showing twitching speed for PAO1 over four hours on surfaces of pEGDPEA and pNGPDA treated with 4 mg/ml supplemented RPMI and PBS. All significances were determined by analysis of variance One-way ANOVA, $p < 01$. **(b)** Scatter plot showing the fraction of moving bacteria cells per frame over a period of 4 hours on pNGPDA in PBS (pink), 4 mg/ml supplemented RPMI (black) and 4 mg/ml RPMI/PBS (Blue). **(c)** Same convention as (b), but for pEGDPEA.

Experimental procedures and data processing to courtesy of A. Carabelli. O. Sanni prepared all polymer samples, carried out adsorption experiments and cultured P. aeruginosa used in experiments. A. Carabelli carried out single cell tracking on microscope and processed data with Matlab software.

3.5 Conclusions

- More amino acids adsorb onto surface of anti-biofilm pEGDPEA compared to pNGPDA.
- With ToF-SIMS analysis, all 10 of the amino acids which have a unique secondary ion were identified on surface of pEGDPEA
- There is an increase in adsorption of amino acids onto the surface of pEGDPEA with increasing amino acid concentration in media.
- The Freundlich and Langmuir adsorption isotherm revealed a pEGDPEA has a greater adsorbent capacity compared to pNGPDA and the on/off rate is quicker on pNGPDA compared to pEGDPEA.
- XPS revealed the overlayer coverage of amino acids on surface of pEGDPEA is 0.43 ± 0.06 nm on average.
- The non-protonated state of amino acids were the more dominant form on surface of pEGDPEA.
- Both pEGDPEA and pNGPDA have similar magnitude of surface zeta potential.
- Growth of PAO1 was shown to be dependent on the nutrient concentration in media.
- The greater fraction of twitching cells after 24 hours on surface of pre-treated pEGDPEA is most likely due to greater amounts of adsorbed nutrients.

It is our inference that nutrient adsorbed onto surface of anti-biofilm pEGDPEA plays a significant role in preventing biofilm formation onto its surface by *P. aeruginosa.* We theorize that in the presence of nutrients, bacteria are not nutrient deprived and therefore do not exhibit a stress response to form biofilm, whilst in the absence of nutrients, they are more likely to exhibit the biofilm formation stress response to protect themselves.

Chapter 4 - High Throughput Quantification with Ninhydrin and Chemometric Analysis of Amino Acid Adsorption onto Polymer Microarray Library

4.1 Introduction

In the previous chapter we established the adsorption of amino acids from bacteria culture media (RPMI) was different for two materials (pEGDPEA and pNGPDA) that exhibited drastically different biofilm prevention capabilities from *P. aeruginosa*. The adsorption phenomena was fitted with both Freundlich and Langmuir models, from which we were able to determine key descriptive parameters such as adsorption capacity and on/off (adsorption/desorption) rate of amino acids on two polymer surfaces.

Here we move from the conventional surface science approach which focused on small sample numbers with detailed analysis in Chapter 3 to a high throughput material analysis approach to explore structure-function relationships [273]. With this approach, a wealth of information can be obtained to facilitate the identification of structure-function relationships across a broad range of material chemistries, more specifically the influence of surface chemistry on adsorption of amino acids.

Historically, HTS has strongly relied on the microarray platform that allowed the successful screening of microspots of DNA, protein or small organic compounds that can be probed with possible binding ligands. Together with advances in fluorescence-based techniques for detecting the incidence of interactions, we are equipped with the possibility of simultaneous analysis of thousands of variables in a single experiment [206].

In this chapter we adapt a cheap staining technique to fluorescently quantify amount of adsorbed amino acids from standard RPMI onto polymer microarray in high throughput manner. ToF-

SIMS was then employed to obtain ions fragments from polymer microarray for multivariate analysis.

4.2 Aims and Objectives

This chapter aimed to identify a structure-function relationship between polymer surface chemistry and adsorbed amino acids. The objectives were:

1. Develop a cheap staining technique to quantify amino acids adsorbed onto polymer surface in high throughput manner.
2. Quantify amount of adsorbed amino acids onto surfaces of 284 polymers on microarray.
3. Carry out partial least squares regression multivariate analysis using secondary ion fragments obtained from ToF-SIMS and adsorption data.
4. Understand correlation between attachment of *P. aeruginosa* and amino acid adsorption.

4.3 Experimental

4.3.1 Polymer Microarray Production

Glass slides 25 x 75 mm were epoxy silanised and then dip-coated in 4% (w/v) pHEMA solution dissolved in 96% (v/v) ethanol in water following methods detailed in 2.2.1. Microarray printing was then carried out under an argon atmosphere at O_2 < 2000 ppm, 27 °C and 30% relative humidity as detailed in 2.2.2. The freshly printed arrays with 284 materials (Appendix G) were vacuum extracted at < 50 mTorr for 1 week to remove un-polymerised monomer and solvent. Each printed microarray slide contained three replicates per polymer spot separated by 20 mm.

4.3.2 Time-of-Flight Secondary Ion Mass Spectrometry

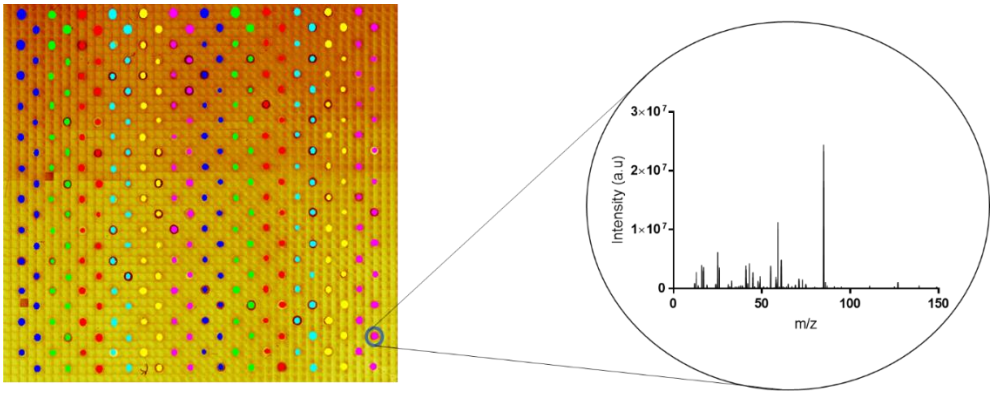

Figure 60. The process to extract surface chemistry of each polymer spot from ToF-SIMS chemical image. Region of interest is drawn around polymer of interest to acquire fragments specific to polymer.

ToF-SIMS analysis of the native array was performed using an IONTOF (GmbH) ToF-SIMS IV instrument utilizing a 25 keV Bi_3^+ primary ion source. An area of 18.5 mm × 18.5 mm was analysed using the macroraster (large area) scanning facility encompassing the entire 284 polymer spot microarray in the "high-current bunched" mode. Data were acquired with a single scan of the analysis area at a resolution of 100 pixels per mm and 1 shot per pixel. Owing to the insulating nature of the sample, charge compensation was applied in the form of a low energy (~20 eV) electron flood gun. Both positive and negative secondary ion data was collected and data analysis was carried out with SurfaceLab 7 software. The resulting chemical

images were then used to select regions of interest (ROIs), shown as various coloured dots for each polymer spot to acquire ToF-SIMS spectra as shown in Figure 60. The individual ToF-SIMS spectrum can be used to link surface chemistry of each material to their biological performance such as amino acid adsorption or bacterial attachment.

4.3.3 Incubation of Polymer Microarray with Standard RPMI and Staining with Ninhydrin

Microarray slide with 284 unique polymers (Appendix G) was incubated with 10 mL of Roswell Park Memorial Institute (RPMI) medium without glutamate and phenol red in a 4-well polystyrene dish for 2 hours at 37 ℃ and 60 rpm. 1 mL of 2% (w/v) ninhydrin dissolved in methanol was pipetted onto RPMI incubated array slide until fully submerged and left for 1 minute. Ninhydrin treated slide was then allowed to develop for 30 minutes in pre-heated oven set at 60 ˚C and treated again for 1 minute with 1 mL of 112 mM zinc chloride dissolved in methanol and then allowed to develop for another 30 minutes in oven at 60 ˚C. Control microarray slide not treated with RPMI was likewise stained with both ninhyrdin and zinc chloride as described above.

Slides were then scanned using a GenePix 4000B Scanner (Molecular Devices, US), with settings at 532 nm excitation laser and standard green emission filter (540 – 700 nm). Power was set to 100%, pixel size 10 μm, line to average 1 au and focus point of 20 μm. The total fluorescence intensity from polymer spots was acquired using GenePix Pro 6 software (Molecular Devices, US).

To find the fluorescence due to adsorbed amino acid from RPMI ($F_{amino\ acid}$), the auto-fluorescence from control slide sequentially stained with ninhydrin and zinc (F_{NZ}) was subtracted from fluorescence recorded on the slide incubated with RPMI and sequentially

stained with ninhydrin and zinc chloride (F_{RNZ}). In order to increase reliability of measured $F_{amino\ acid}$ and filter out background noise, its value was accepted if larger than three standard deviations of F_{NZ}, else its values were classified as below the limit of detection (LOD). In this study, 3 polymers were considered to be below LOD, thus reducing number of polymers to 281.

$$F_{amino\ acid} = F_{\mathrm{RNZ}} - F_{\mathrm{NZ}}$$

$$LOD_{Famino\ acid} < 3\ x\ SD_{\mathrm{FNZ}},\ (n{=}3)$$

4.3.4 Incubation of Polymer Microarray with *P. aeruginosa*

Briefly, a single colony *P. aeruginosa* O1 Washington strain transformed to express *mCherry* fluorescent protein was grown overnight in 10 mL of LB media. Bacteria was then re-suspended in RPMI media and brought to a final OD_{600} of 0.01. UV sterilised polymer microarray slide was incubated with *P. aeruginosa* in 10 mL RPMI for 24 hours. Slide was then rinsed to wash off non-adhering bacteria and salts prior to being imaged with GenePix Autoloader 4000B fluorescent scanner (Molecular Devices, US) with settings at 635 nm excitation laser and standard red emission filter (650 – 700 nm). Control slide was incubated with media alone and to find the fluorescence due to bacterial attachment ($F_{pseudomonas}$), the fluorescence on the media control (F_{rpmi}) was subtracted from fluorescence recorded on the slide incubated with bacteria ($F_{rpmi\ +\ pseudomonas}$). In order to increase reliability of measured $F_{pseudomonas}$ and filter out background noise, the value was accepted if larger than three standard deviation of F_{rpmi}, else the value was classified as below the limit of detection (LOD).

4.3.5 Partial Least Squares Regression Analysis

Correlations between ToF-SIMS spectra and amino acid adsorption were analysed using PLS regression. In total 384 positive and 388 negative ions were selected to form the peak list m/z range 0 - 300, selected based on molecular weight of amino acids. Both positive and negative ion peak intensities in a ToF-SIMS spectrum were dead time corrected and then normalized to

the respective total secondary ion counts to remove the influence of primary ion beam fluctuation. The positive and negative ion intensity data were arranged into one concatenated data matrix, which was mean-centred and unit variance scaled prior to analysis. PLS analysis was carried out using PLS Toolbox 5.2 software (Eigenvector). For cross-validation, the dataset was randomly split into a training group, containing 80% of the samples, and a test set, containing the remaining 20% of samples. The test set were selected by ranking the samples by adsorption intensity and randomly selecting 20% of samples from the lowest 20%, middle 60% and highest 20% of samples. The training set was formed from the remaining samples. This method was done to ensure both the test and training set contained polymers representing an even spread of low, middle and high amino acid adsorption. A "leave one out" cross validation method was used in the PLS regression analysis of the training set. PLS models were constructed using 5 latent variables and PLS model were validated by applying to the test set. The final PLS model was constructed using the latent variable whereby the R^2 value for the test set was at maximum and close to the R^2 value of the training set.

4.4 Results

4.4.1 Polymer Microarray

A polymer microarray was printed using 284 monomers (Appendix G) to produce unique polymers spots printed in triplicate on a single slide after photo polymerisation.

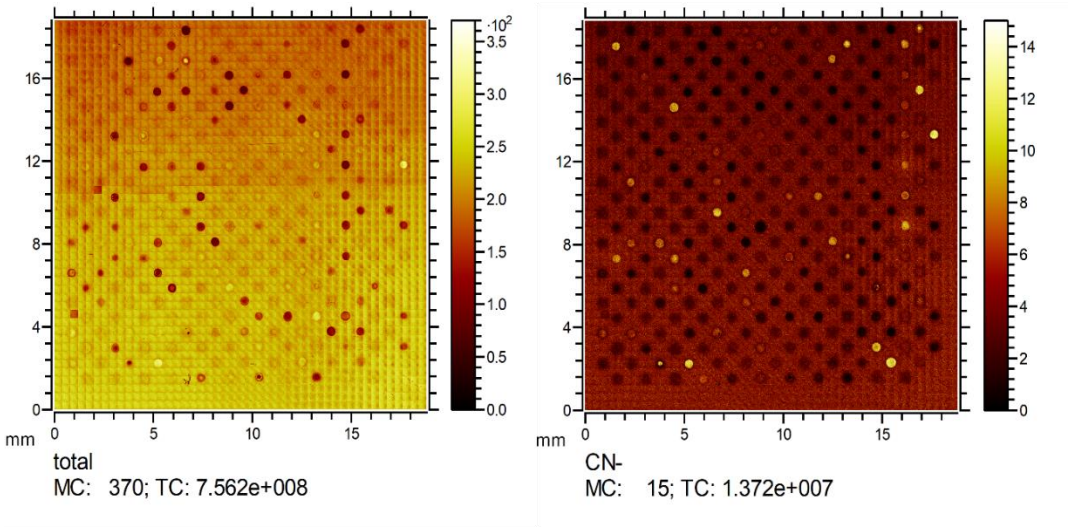

Figure 61. ToF-SIMS image of total ion count for polymer microarray with 284 different chemistries and ToF-SIMS image for CN^- (m/z 26.00).

Time-of-flight secondary ion mass spectrometry (ToF-SIMS) was employed to monitor spot printing fidelity, exclude nitrogen containing polymers and also obtain ion fragments for multivariate analysis.

4.4.2 Application of Ninhydrin Stain to Polymer Array for Detection and Quantification of Adsorbed Amino Acids

Ninhydrin (Ny) has been used for detection of amino acids and amines since the early 19th century and has found numerous applications in analysis of peptides, agricultural products, biomedical and forensic sciences, mainly due to the opportunity of easy colorimetric quantification and analysis it provides [131, 274, 275]. There are however simple modifications that can be made post-Ny treatment to convert to a fluorescent metal complex that exhibits strong fluorescent properties [276]. Reported in Figure 62 is the summary of key results

obtained from fundamental analysis of the Ny stain on polymer surfaces printed onto microarray to detect amino acids.

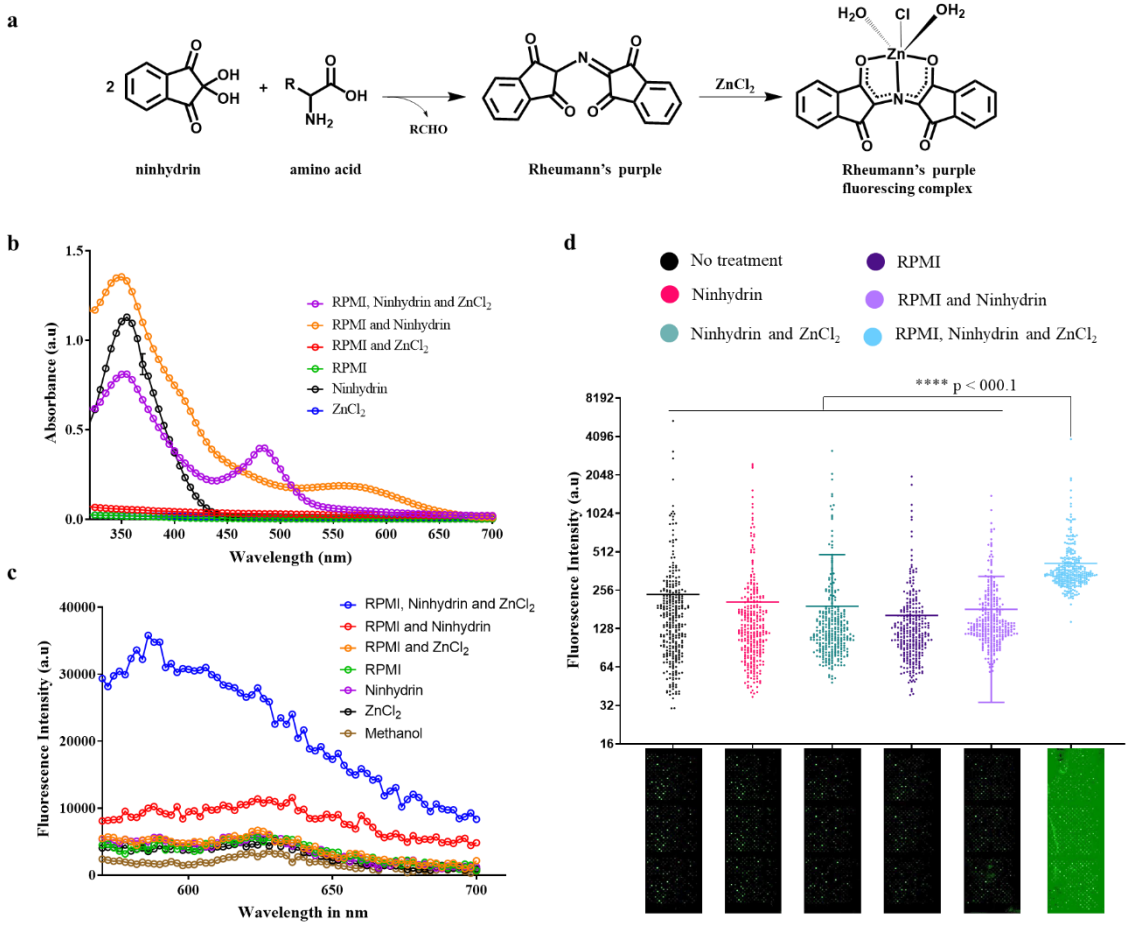

Figure 62. Summary of optimisation experiments for ninhydrin stain applied to polymer microarray. **(a)** Chemical equation for reaction of ninhydrin with amino acid to form Ruhemann's purple that fluoresces upon complexation with zinc chloride. **(b)** Absorbance spectrum (320 – 700 nm) for various chemical components involved in staining polymer microarray. **(c)** Same as (b) but emission spectra (exictation at 532 nm). **(d)** Effect of different treatments on fluorescence intensity from polymer microarray. All significances were carried out using one-way ANOVA test, ****$p < 0.001$.

The guiding principle of the chemical reaction is based on condensation of Ny with amine group resulting in a corresponding coloured compound referred to as the Ruhemann's purple (RP). This compound can be complexed with metals such as nickel, cadmium, zinc etc. to produce a complex that fluoresces upon excitation with 532 nm laser (Figure 62a). For this particular application, zinc chloride was used.

In Figure 62b all three solutions with Ny had absorbance maximum (λ_{max}) at 350 nm due to presence of aromatic ring in its structure. The solution of RPMI + Ny (in orange) had a second

λ_{max} at 570 nm due to formation and presence of RP, whiles a solution of RP complexed with zinc had λ_{max} occurring at 490 nm. These findings are in line with reported λ_{max} values for RP only and its complexation with zinc [274]. RPMI and Zinc chloride had a similar absorbance profile to baseline (methanol solvent).

The emission spectra in Figure 62c were obtained with excitation at 532 nm to mimic standard settings of fluorescence scanner. The fluorescence emission profile for RP complexed with zinc (in blue) is significantly higher than solution with RP only (in red). Solutions of RPMI, Zn, Ny, RPMI + Zn and methanol solvent do not fluoresce when excited at 532 nm, which is important to obtaining high signal to noise ratio.

The results from application of Ny staining method to polymer microarray (Figure 62d) mirrored results obtained from fundamental studies. Polymer microarray treated with RPMI then sequentially stained with Ny and Zinc had a significantly higher fluorescence intensity (also from pHEMA background) when compared to untreated arrays stained with Ny and Zinc only. This is easily interpreted as formation of RP on polymer surface due to adsorbed amino acids.

The ability of pHEMA to interact with water molecules and retain a high water content leads to a reduced concentration of network chains in the swollen state which in turn facilitates interpenetration by compounds [199]. This property of pHEMA is positively exploited in polymer microarray production to physically entrap interpenetrating polymer spots [209, 277]. However, it is also reasonable to consider the possible consequences of amino acids penetrating through the pHEMA substrate and reacting with epoxide ring of underlying silane at ambient conditions (Figure 63) [278]. The anticipated formation of morpholinones derivatives via one-step cyclization has yet to be realised directly in aqueous environment such as the RPMI. Results from Dyker *et al*. showed that the realisation of such products occurred with a catalyst

promoted synthesis under basic conditions with DMF solvent [279]. A different product that can occur as a result of direct ring opening of epoxide ring with amino acid is the beta-amino alcohol [280]. However, this reaction is not very efficient due to the low nucleophilicity of amino acids comparable to that of aromatic amines and thus to require an activator [281].

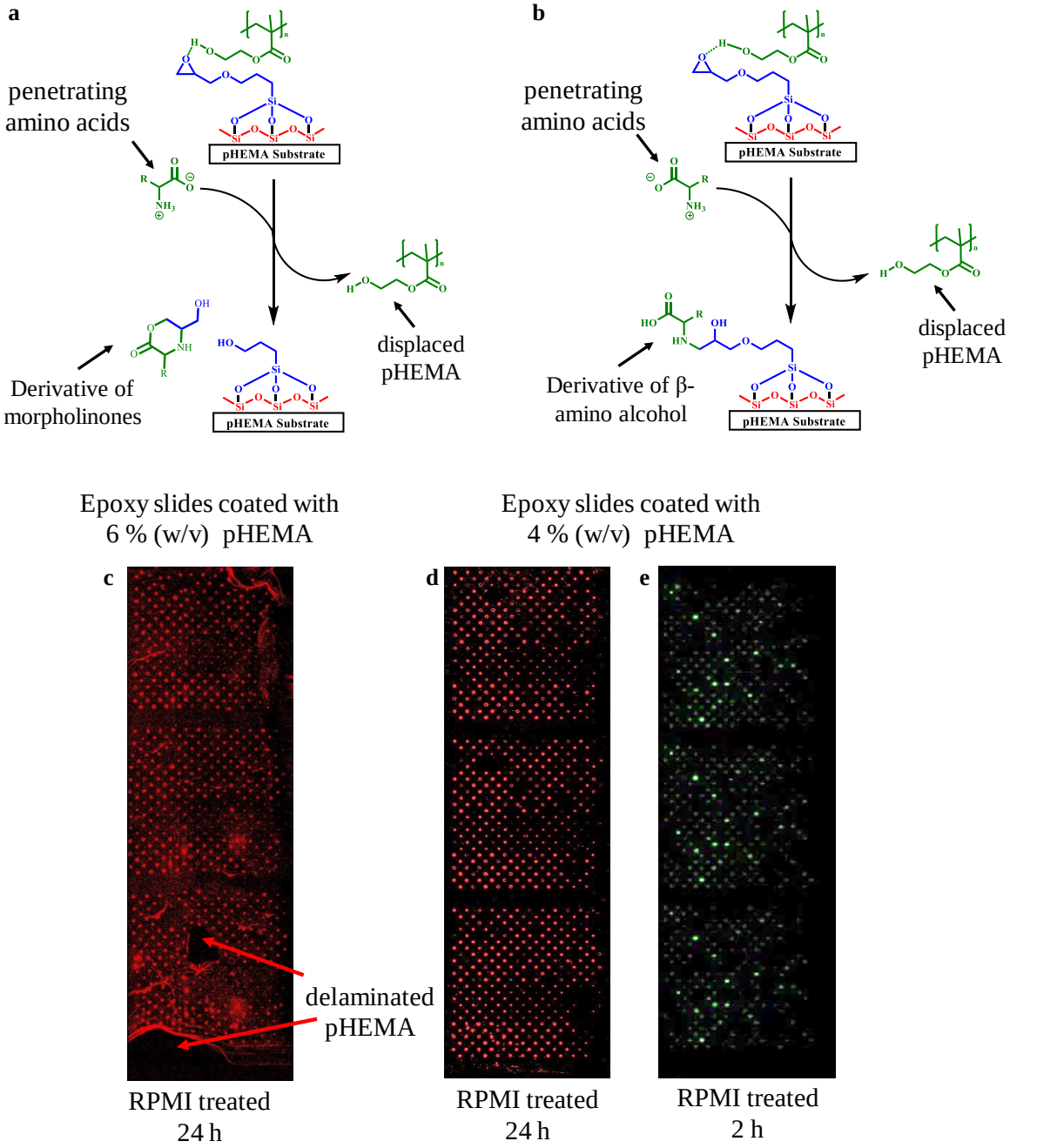

Figure 63. **(a)** Scheme showing possibility of displacement of pHEMA and annulation of epoxide caused by interpenetrating amino acid molecule, leading to formation of morpholinones. **(b)** Scheme showing possibility for displacement of pHEMA and ring opening of epoxide caused by interpenetrating amino acid molecule leading to formation of β-amino alcohol. **(c)** Scanned image at 635 nm of polymer microarray printed on epoxy slide coated with 6% (w/v) pHEMA and incubated with standard RPMI for 24 hours. Red arrows indicate areas of pHEMA delamination. **(d)** Scanned image at 635 nm of polymer microarray printed on epoxy slide coated with an optimised solution of 4% (w/v) pHEMA and incubated with standard RPMI for 24 hours. **(e)** Same as (d), scanned with 532 nm laser and incubated for 2 hours similar to nutrient adsorption experiments.

It is however true that efficient ring opening of epoxides with aliphatic amines (no amino acid tested) in water and at ambient conditions have been reported [282, 283]. For amino acids, the extraction of a hydrogen from NH_3^+ in zwitterions state will result in the formation of a nucleophilic primary amine that can readily participate in the ring-opening reaction with epoxide. However, Wong *et al.* reported low reactivity and suggested the electrostatic interaction between zwitterions played a role [284]. We reason that in a scenario where amino acids interpenetrate pHEMA, only histidine whose side chain has a pKa of 6.04 will possess a deprotonated nucleophilic amine at experimental pH of 7.4. Histidine's nucleophile is however part of an aromatic system and aromatic amines are proven to be more reactive with epoxides in fluoro-alcohols as solvents and not water [281].

In addition, an interference with the hydrogen bond interaction formed between pHEMA and epoxide group could potentially lead to delamination as seen in Figure 45c, where epoxy slides coated with pre-optimised 6% (w/v) pHEMA solution delaminate after 24 hour incubation in standard RPMI. No such events were observed for epoxy slides coated with 4% (w/v) pHEMA solution after 24 h or 2 h, respectively Figure 63d-e. We therefore assume that, for the experimental conditions used in this project, amine functionalities on amino acids are accessible and available to react with ninhydrin.

To the best of our knowledge, this is the first instance where a simple modification of Ny stain on surfaces was successfully applied to polymer array and proven to be compatible with high throughput assessment of adsorption, allowing polymers to be assessed.

4.4.3 High Throughput Quantification of Amino Acid Adsorption on Polymer Microarray

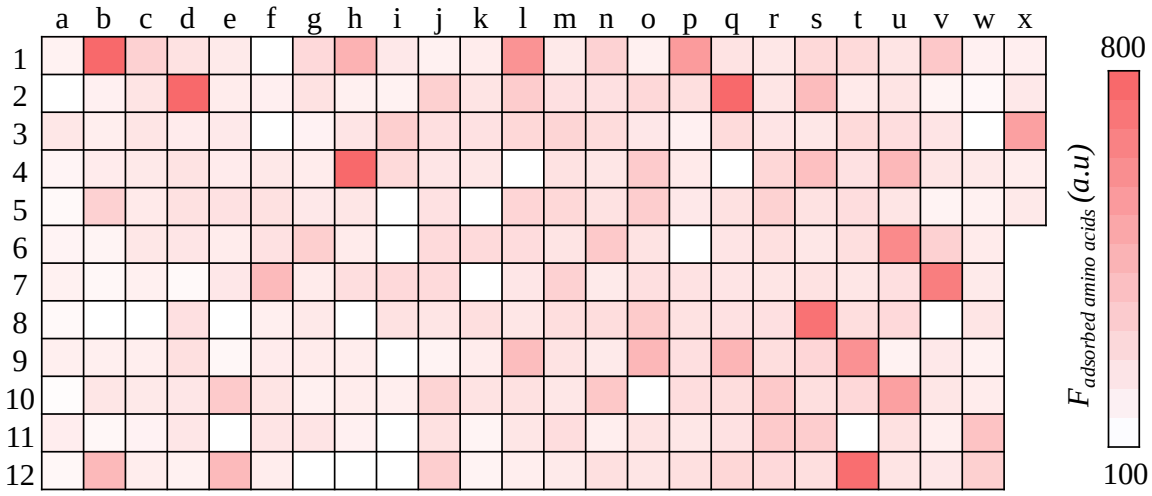

Figure 64. Intensity map showing fluorescence of adsorbed amino acids from standard RPMI media onto 281 unique polymer spots (Appendix H) after 2 hours incubation at 37 ˚C and 60 rpm. Each square represents the mean fluorescence value (N = 3) due to adsorbed amino acids stained with Ninhydrin and Zinc chloride. Labels on y and x axes provide unique identification for each material.

In Figure 64 is a colour map for intensity of adsorbed amino acid onto polymer surfaces from standard RPMI as determined by Ny staining technique. A white colour code is indicative of low amino acid adsorption and a red colour is indicative of high adsorption of amino acids. As expected, varying levels of amino acid adsorption onto the different polymer surfaces was observed. The polymer of EGDPEA, located in cell H1 presented with high fluorescence value and served as good positive control to confirm successful Ny staining of amino acids on polymer surface.

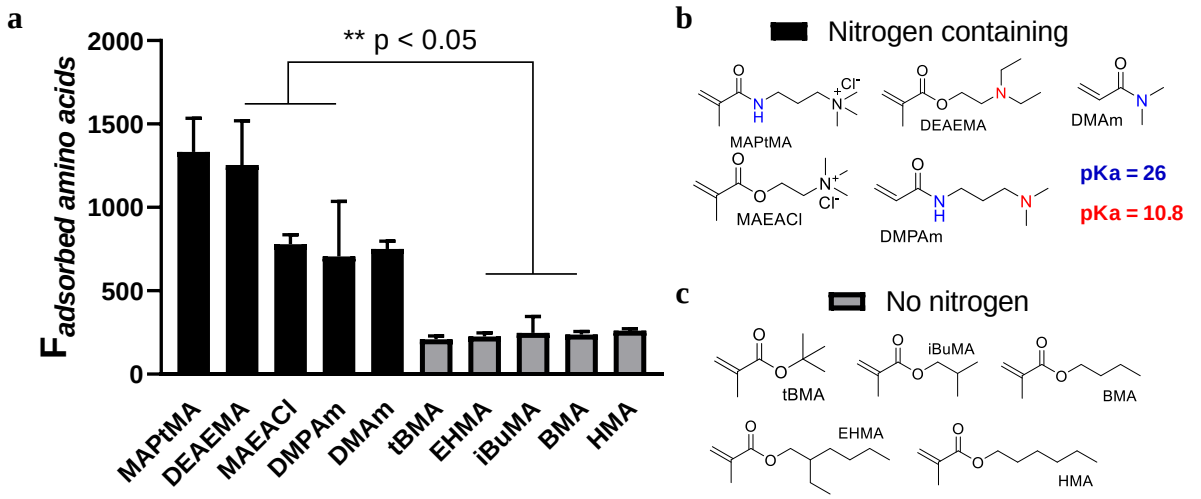

Figure 65. **(a)** Plot showing adsorption of amino acids from RPMI 1640 media onto 5 nitrogen containing polymers and 5 polymers with linear pendant group containing no nitrogen. All significances were carried out using one-way ANOVA test, **p < 0.05. **(b)** Chemical structure for nitrogen containing polymers with associated pKa values. Colour coded in blue are nitrogen atoms within amide functionality (pKa 26) and in red are tertiary nitrogen atoms (pKa 10.8) **(c)** Chemical structures for polymers with linear pendant groups containing no nitrogen atoms.

To avoid quantifying adsorption of amino acids mediated via electrostatic interactions with charged nitrogen atoms present in polymers, excluded from further analysis were polymers with acrylamide/meth(acrylamide) functionalities and polymers whose pendant group possessed either secondary, tertiary or quaternary nitrogen groups, see Figure 65b. Based on reported pKa values [285], this set of polymers have a net positive charge on their nitrogen at pH 7.4 in aqueous conditions, hence are capable of interacting with amino acids via their negatively charged carboxyl terminus under experimental conditions used here. This is confirmed with high fluorescence values obtained for MAEACl, DEAEMA, DMAm, MAPtMA and DMPAm materials when compared to materials containing no nitrogen but with comparable linear pendant groups, that is, having between three to eight carbon atoms in pendant group Figure 65a-c. Consequently, a total of 192 polymers were considered for further analysis.

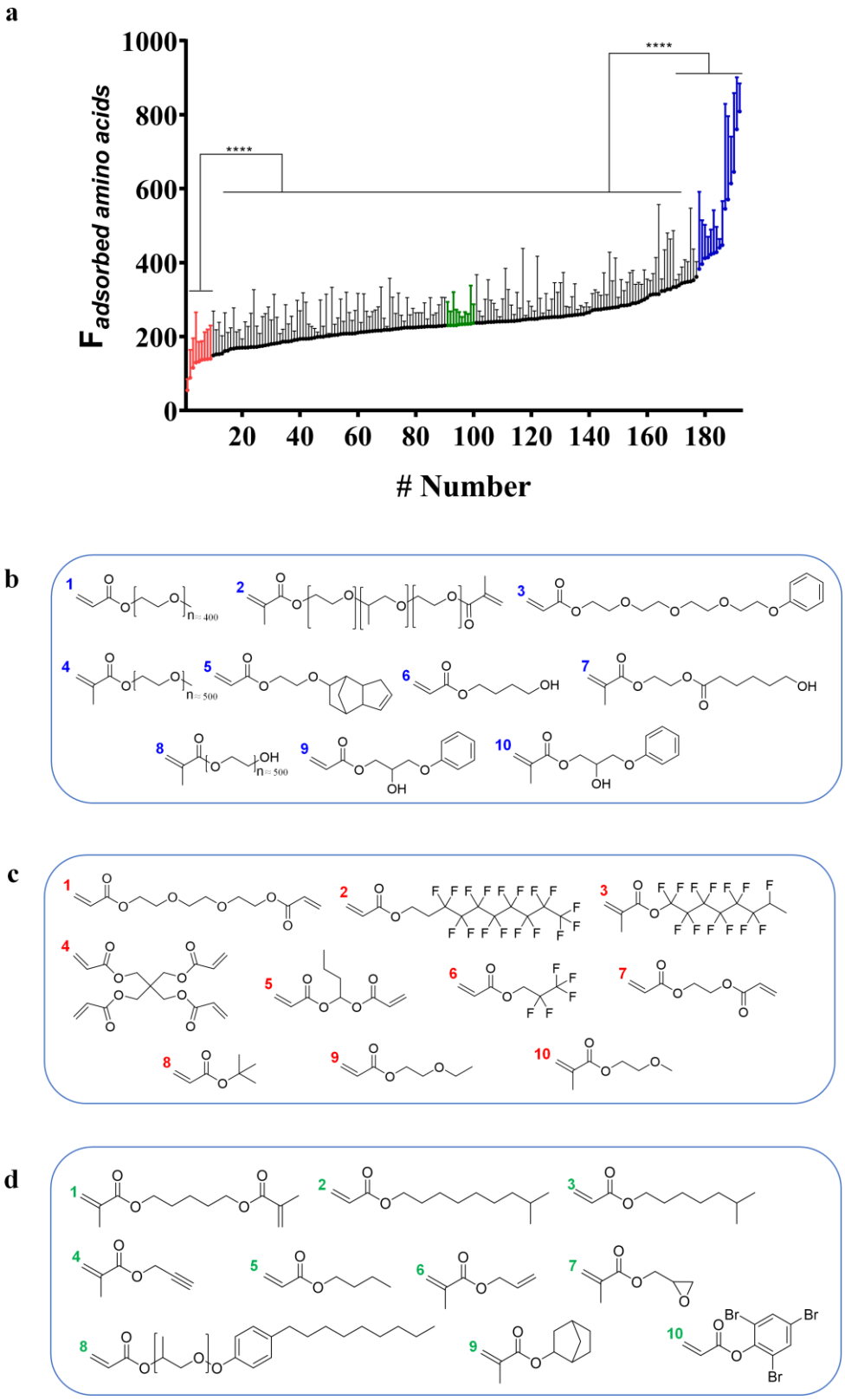

Figure 66. **(a)** Rank order plot showing adsorption of amino acids from RPMI 1640 media on 192 unique polymer spots after 2 hours incubation at 37 ˚C and 60 rpm. Each data point represents the mean fluorescence value (N = 3) due to adsorbed amino acids after staining with Ninhydrin and Zinc chloride. 96 spots have been excluded for reasons either due to LOD or chemistries contained Nitrogen. In blue are polymers with chemical structure in **(b)** with highest amount of adsorbed amino acid whose difference is statistically significant ("****", t-test, $p<0.05$) from population average. Labelled in red are polymers with chemical structure in **(c)** with lowest amount of adsorbed amino acid whose difference is statistically significant ("****", t-test, $p<0.05$) from population average determined. Labelled in green are polymers, chemical structure in **(d)** with average adsorption of amino acids on surface.

To identify chemical structures with low or high adsorption of amino acids, fluorescence from stained polymers were plotted in rank order as seen in Figure 66a. A simple categorical analysis was then conducted to identify polymers with significantly different amino acid adsorption when compared to average value from all 192 samples.

In Figure 66b is selection of ten monomers with significantly higher adsorption of amino acids compared to population average. Firstly, monomer 5 (Figure 66b) is the chemical structure identifying of EGDPEA, its appearance in list of top ten structures with high adsorption of amino acids is corroborative of earlier findings from using ToF-SIMS and XPS reported in Chapter 3. The selection is also dominated by repeating units ($n > 3$) of ethylene or glycol moieties and where absent, a ring or cyclic functionality is present as seen in chemical structures 6 – 10 in Figure 66b. The two monomers 9 and 10 only differ for presence of methyl group on acrylate functionality, a finding that would suggest a more important role is played by pendant group over acrylate or methacrylate functionality.

On the other hand, structures in Figure 66c represent polymers with significantly smaller adsorption of amino acids. We observed that fluorinated pendant groups are present in three of the selected chemical structures (monomers 2, 3 and 6), whilst monomers 8, 9 and 10 have short linear pendant groups not longer than four carbon atoms. Interestingly, monomers 1, 4, 5 and 7 (Figure 66c) with dimeric or tetrameric structures similar to pNGPDA often referred to as diacrylates or tetracrylate exhibited low amino acid adsorption. Chemical structures in Figure 66d are representative of compounds that displayed an average amino acid adsorption.

From the thermodynamic viewpoint, it is thought that the repeating unit of ethylene glycol in materials with adsorbed amino acids (1, 2, 3, 4 and 8, Figure 66a) endows polymers with a degree of flexibility that allows them to easily adapt and compensate the entropic loss of adsorbed amino acids [81]. This speculation was also consistent for less mobile polymers (4-5

and 7-10 in Figure 66b) with shorter chains, where the observed reduction in amount of adsorbed amino acids was assumed to be due to the inability of these polymers to rearrange and compensate the entropic loss of adsorbing amino acids.

The ability of fluoropolymers with similar chemical structure to materials 2, 3 and 6 in Figure 66b to adsorb very little amino acids, is an expected outcome for this subset of (meth)acrylates materials based on their low surface energy and the inertness of carbon-fluorine bond [286, 287]. Fluoropolymers are known to resist the formation of strong bonds or interactions with other chemical compounds and are thus only capable of weakly interacting with adsorbates, in this case amino acids [288].

An attempt to find a correlation between amount of adsorbed amino acids with wettability or flexibility based on the entire tested library produced no discernible trend (Appendix K). Flexibility of a molecule as fully described in section 5.3.1 was estimated from the number of rotatable bonds present in molecule. It is thought that the absence of a discernible trend is indicative of more contributory factors in addition to wettability or flexibility.

To obtain a more robust analysis and identify key moieties responsible for adsorption of amino acids, the wealth of data obtained from ToF-SIMS analysis of array was used to conduct a partial least squares regression analysis where training model was constructed with 80% of dataset and then tested with remnant 20% (full details in section 4.3.5).

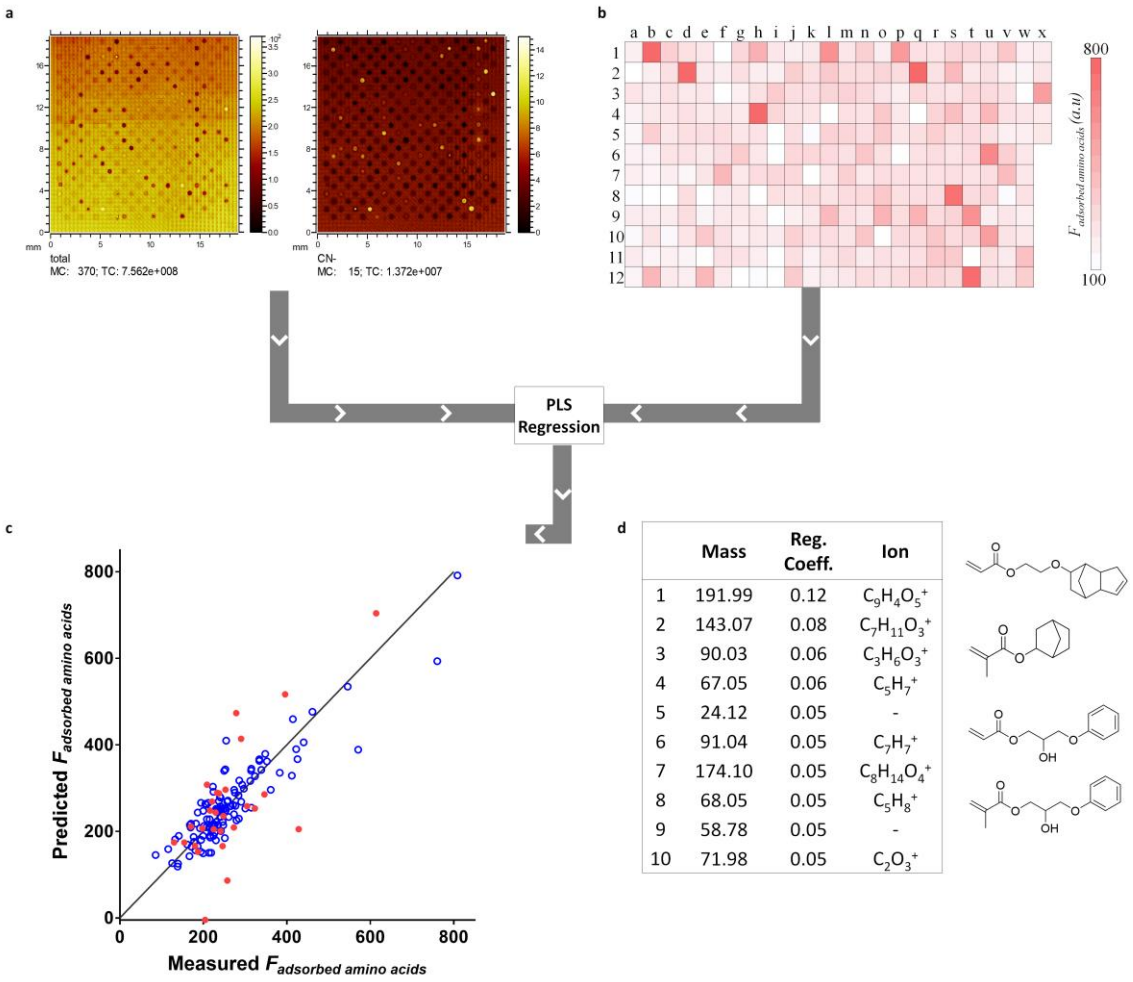

Figure 67. Schematic depiction of the PLS regression model used to predict the amino acid adsorption on materials by correlating fluorescence intensity of adsorbed amino acid with the ToF-SIMS fragments. (a) ToF-SIMS image of total ion count for polymer microarray with 284 different chemistries and ToF-SIMS image for CN^- (m/z 26.00). (b) Intensity map showing fluorescence of adsorbed amino acids from RPMI 1640 media onto 281 unique polymer spots after 2 hours incubation at 37 ˚C and 60 rpm. Each square represents the mean fluorescence value (N = 3) due to adsorbed amino acids stained with Ninhydrin and Zinc chloride. (c) The predicted amino acid adsorption determined from the PLS regression model. Training set (R^2 = 0.79) in blue and test set in red (R^2 = 0.53) The $y = x$ line is drawn as a guide. The key ions identified to be important by PLS regression analysis for the surface adsorption of amino acids.

The initial PLS analysis with all 192 non-nitrogen containing polymers resulted in a poor predictive model (see Appendix L), which we attributed to the presence of non-oxygen heteroatoms in monomer structure. A refined PLS regression model conducted on 141 polymers successfully predicted the fluorescence values of adsorbed amino acids ($F_{adsorbed\ amino\ acid}$) from the ToF-SIMS fragments, as evidenced by the linear relationship between the predicted and experimental $F_{adsorbed\ amino\ acid}$ values in Figure 67c, with an R^2 value of 0.53.

The effective prediction of amino acid adsorption from the ToF-SIMS fragments demonstrates that the adsorption of these compounds is dependent on the polymer surface chemistry. More specifically, the influence of each of the hundreds of ions in the SIMS spectra on amino acid adsorption is quantified by the regression coefficient, where a positive coefficient indicates that the ion in question promotes adsorption. The surface chemical moieties assigned to secondary ion fragments with the highest PLS regression coefficients are shown in Figure 67d. Cyclic hydrocarbon fragments and species with multiple oxygen atoms promoted adsorption of amino acids, $C_9H_4O_5^+$, $C_7H_{11}O_3^+$, $C_3H_6O_3^+$, $C_5H_7^+$, $C_7H_7^+$ and $C_8H_{14}O_4^+$. This aligns with chemical structure of pEGDPEA on which greater adsorption of amino acids is observed. Chemical compounds with aromatic and norbornyl ring also demonstrated increased adsorption of amino acids.

4.4.4 High Throughput Quantification of Attachment of *P. aeruginosa* on Polymer Microarray and Correlation with Adsorbed Amino Acids

To correlate the adsorption of amino acids onto surfaces of polymers with biofilm formation of PAO1. The polymer microarray was screened against PAO1 tagged with fluorescently labelled *mCherry*.

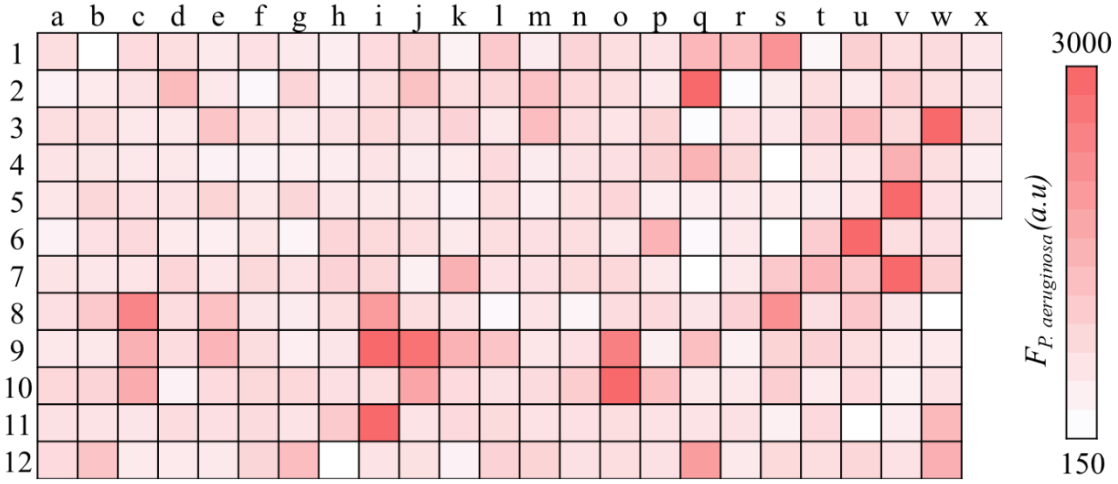

Figure 68. Intensity map showing fluorescence value after background subtraction ($F_{p.aeruginosa}$) for 281 materials (Appendix H) incubated for 24 h with *P. aeruginosa* in RPMI. Each square represents the mean fluorescence value (N = 3). Labels on y and x axes provide unique identification for each material.

The attachment of fluorescently labelled *P. aeruginosa* to each polymer spot on the microarray was measured and presented with an intensity map seen in Figure 68. Each cell is the mean fluorescence read out from three polymer spots. A white colour code indicates polymers with low bacteria attachment and a red colour code, polymers with high bacteria attachment.

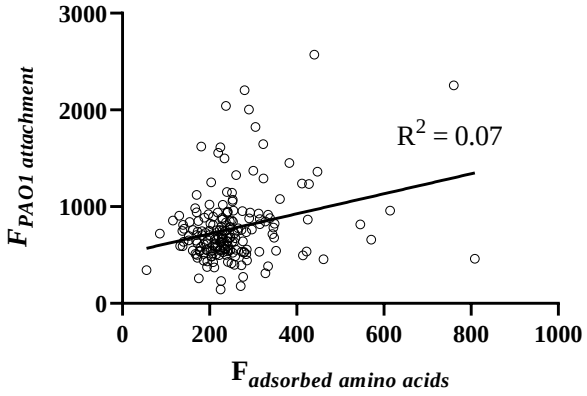

Figure 69. Plot showing relationship between adsorbed amino acid on surface of polymers and attachment of PAO1.

In Figure 69 is a plot of adsorbed amino acid and attachment of PAO1 after 24 h. A poor correlation with $R^2 = 0.07$ is observed, which is likely due to the wide chemical space under study with 192 different polymeric materials, with linear, cyclic, aromatic and halogen containing pendant groups. Indeed, the speculations from categorical analysis in section 4.4.3 revealed multiple mechanisms (based on chemical functionalities) for materials which enhanced or repelled amino acid adsorption. The reality of these different mechanisms makes it harder to generate a simple linear correlation or a model that fits all. The findings from ToF-SIMS corroborated by XPS are however clear and showed a greater amount of amino acids adsorbed onto surface of anti-biofilm pEGDPEA compared to pro-biofilm pNGPDA.

4.5 Conclusion

- Ninhydrin stain was successfully modified to stain amino acids on surfaces of 192 polymer in high throughput manner.

- A simple classification that took into account polymers with significantly higher and lower adsorption of amino acids revealed that, polymers with either long repetitive units of ethylene glycol alone or in combination with hydroxyl and cyclic moieties displayed greater adsorption of amino acids. Whilst structures with acrylate dimers, rich in fluorine atoms and possessing of short linear chains adsorbed less amino acids.
- A PLS regression model was successfully constructed for hydrocarbon monomers with Oxygen. Cyclic hydrocarbon fragments and species with multiple oxygen atoms promoted adsorption of amino acids, $C_9H_4O_5^+$, $C_7H_{11}O_3^+$, $C_3H_6O_3^+$, $C_5H_7^+$, $C_7H_7^+$ and $C_8H_{14}O_4^+$. Which aligned with chemical structure of pEGDPEA on which greater adsorption of amino acids is observed.
- The drastically different observations seen on surfaces of pEGDPEA and pNGPDA was not applicable to the entire library of polymers, due to the presence of a wide chemical space in library.

Chapter 5 - Validating a Predictive Structure-Property Relationship by Discovery of Novel Polymers which Reduce Bacterial Biofilm Formation

5.1 Introduction

The concept of the post-antibiotic era is becoming a reality, with patients presenting with infections from bacterial pathogens that resist multiple last line antibiotics while at the same time, very few novel antimicrobial drugs are coming onto the market. As multi-antibiotic resistance becomes widespread, the prevention of bacterial infections has become an urgent healthcare priority in order to reduce morbidity and mortality [289].

Clearly, it would be ideal if we could fully describe and understand the diverse sensing and signalling mechanisms that bacteria employ to determine when they are near or on a surface and if the surface is suitable for attachment and biofilm formation. Such knowledge would allow the direct, rational design of surfaces that do not support bacterial colonization. Sadly, mechanistic information is still far from complete and as highlighted in section 1.4, pathogens use diverse sophisticated strategies to colonize a surface including multiple surface appendages and macromolecules such as pili, flagellar, proteins and exopolysaccharides [290].

Consequently, we are not yet at the point where sufficient information is available to permit the rational design of low attachment surfaces as an effective and reliable strategy for new materials discovery. High throughput materials discovery screens provide an alternative solution to this challenge and have been utilised to discover polymers that reduce bacterial surface colonization in order to circumvent our poor understanding of bacteria-surface interactions that leaves us ill-equipped to design new materials from first principles [291].

Novel coatings were identified by screening a commercially available (meth)acrylate monomer library for polymers that successfully reduced biofilm formation by *P. aeruginosa*, *S. aureus*

and *E. coli* in laboratory cultures *in vitro* and *in vivo* in a foreign-body mouse infection model [89, 196]. Such screening experiments facilitate the rapid assessment of readily available monomers to identify hit materials for a particular application, such as reducing bacterial fouling of surfaces in industry and healthcare, the expansion of pluripotent stem cells, increasing the maturation of cardiomyocyte derived from stem cells, and providing bio-instructive implant materials [196, 204, 292, 293].

Typical polymer microarray approaches use unbiased screening of as wide a range of materials or *chemical space* as possible to maximize the chances of identifying hit materials that surpass the performance of existing material solutions. To date, this process has been very successful in identifying a class of monomers that surpass conventional silicone catheters for preventing catheter associated urinary tract infections, resulting in the granting of a CE mark for a urinary catheter device [196, 204, 254].

To guide synthesis beyond the commercially available compounds computational modelling has been used to generate structure-function relationships that can predict the biological performance of virtual materials [294-296]. In the case of bacterial biofilm formation a simple composite parameter termed *alpha* (Equation 11) that takes into consideration contributions from the partition coefficient (logP) and the number of rotatable bonds (nRotB) for hydrocarbon acrylate pendant groups pointed a route to a more targeted approach for materials discovery, although until now this has not been experimentally validated [122].

$$\alpha = 0.44nRotB - clogP$$

Equation 11 – *Equation for alpha parameter*

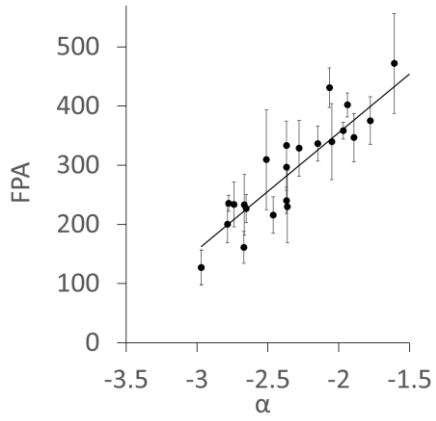

Figure 70. Summary of *alpha* model. a) Correlation between bacterial attachment with molecular flexibility and polarity of material. The fluorescence due to the attachment of *P. aeruginosa* (F^{PA}) is plotted against the composite parameter α (R^2 = 0.83) for each polymer. Error bars equal ±1 s.d. unit, n = 6.

In this chapter, we focus on validating a modification of that QSAR by extrapolating from the correlation identified between the bacterial biofilm formation and monomer material *alpha* value (see Figure 70), to predict, synthesize and screen novel biofilm resistant monomers which were not included in the initial library.

5.1.1 Aims and Objectives

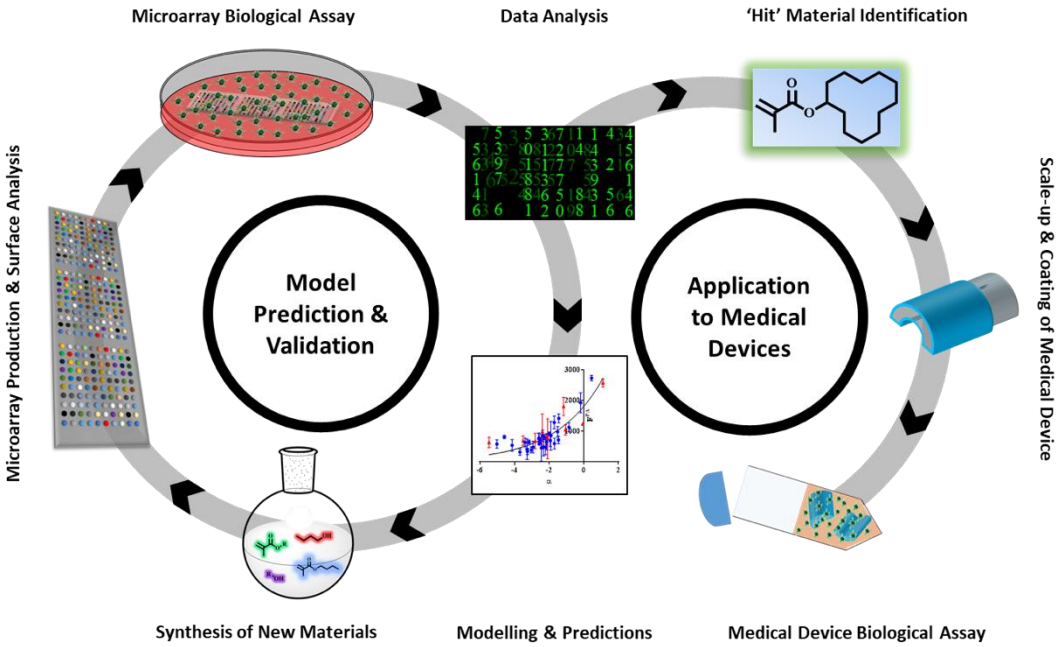

Figure 71. Schematic for developing and validating a predictive model at the microscale level including testing on a medical device. Hundreds of materials are assessed for their ability to reduce bacterial biofilm formation via high throughput screening. Processed data is used to identify a 'hit' material and scaled up to coat medical devices for confirmatory *in vitro* studies. Analysed data together with material properties are used to generate models that predict new untested materials which are synthesized and reincorporated into the materials library for further screening. This repeated cycle refines the theoretical model and makes it a more powerful predictor of 'hit' materials.

The aim of this chapter was to validate the *alpha* QSAR, see schematic in Figure 71. The objectives were as follows:

1. Predict and synthesize new materials from *alpha* model.
2. Produce polymer microarray with newly synthesized materials.
3. Assess materials' ability to reduce bacterial biofilm formation via high throughput screening with *P. aeruginosa and Pr. mirabilis.*
4. Use screening data to validate *alpha* model.
5. Scale up predicted 'hit' material and confirm *in vitro* performance with *P. aeruginosa, Pr. Mirabilis, E. faecalis, K. pneumonia, UPEC and S. aureus.*

5.2 Experimental

5.2.1 Materials

Synthesized materials *trans*-3, 7-dimethyl-2, 6-octadienyl methacrylate (GeMA), 5-methyl-2-(1-methylethyl) cyclohexyl methacrylate (LMMA) and dodecyl methacrylate (DdMA) were obtained from laboratory stocks of Dr. A. Dundas (see section 5.2.3.2). Cyclododecyl methacrylate was synthesized and purified in the course of this work. Triethylamine, methacryloyl chloride, azobisisobutyronitrile (AIBN), PhCoBF, dodecanol, cyclododecanol, MEDI-161 silane, monomers (EGDPEA, DEGMA, BMA, tBCHA, BnMA and NpMA) were used as received from Sigma Aldrich and VWR. All solvents were used as received from Thermoscientific. Silicone catheter (Bard Medical, U.K.) and silver hydrogel catheter Bardex® I.C. Aquafil with a hydrogel and silver alloy were commercially sourced.

5.2.2 Prediction from *alpha* Model

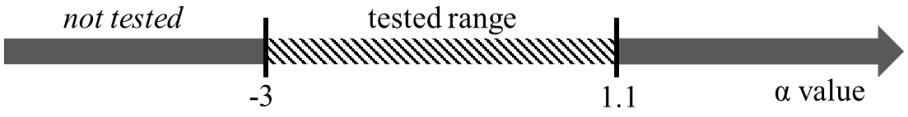

Figure 72. Alpha value number line showing previously tested range and untested range.

To predict monomers capable of preventing bacteria biofilm formation, the *alpha* parameter equation (Equation 11) was used. Acrylate and meth(acrylate) monomers whose *alpha* value was less than -3 were identified. The search was not limited to readymade monomers from chemical suppliers but extended to alcohols from which meth(acrylate) monomers were derivable. Control materials whose alpha value was in the range of -3 to 1.1 were also selected.

5.2.3 Synthesis

5.2.3.1 Esterification

In a standard reaction, triethylamine (3.40g = 3.18 mL, 32.55 mmol) was added to a vessel with cyclododecanol (5g, 27.13 mmol) dissolved in DCM and allowed to cool to 0 ˚C over ice.

Methacryloyl chloride (3.29g = 4.54 mL, 32.55 mmol) was then added dropwise and reaction was left to stir for 2 hours at ambient conditions. Reaction was monitored by TLC using a 3:1 hexane-ethylacetate solvent system. Upon completion, product was extracted with copious amount of hexane solvent and then filtered. Crude extract was further purified by running through a silica plug with hexane solvent.

5.2.3.2 Transesterification

In a typical reaction butyl methacrylate (Sigma-Aldrich) (14 g, 98.5 mmol) was introduced into a 50 ml vessel along with the required quantity of individual target alcohols cyclododecanol (VWR) (13 g, 70.5 mmol), trans-3,7-dimethyl-2,6-octadien-1-ol (10.8 g, 70.3 mmol**)** 5-methyl-2-(1-methylethyl) cyclohexanol (11.2 g, 71.6 mmol) or 1-dodecanol (sigma-aldrich) (13.1 g, 70.3 mmol)] to form a 7:5 molar ratio. Then titanium butoxide (Sigma-Aldrich) catalyst at a concentration of 1% by molar ratio (relative to butyl methacrylate) and 1000 ppm of 4-methoxyphenol (Sigma-Aldrich) inhibitor were added. The reaction was heated to 160 ˚C and stirred for 45 minutes at which point a nitrogen gas sparge was introduced to increase the rate of removal of butanol by-product. The reaction was monitored every 15 minutes by NMR, samples were quenched at lower temperatures in a freezer prior to NMR analysis. Butyl methacrylate was chosen as the methacrylate precursor for these reactions to allow these elevated temperature to be multisided to drive the reaction kinetics and equilibrium toward full completion in a short timescale.

This part of the work involving monomer synthesis via transesterification was entirely carried out by Dr. A. Dundas.

5.2.4 Bacteria Toxicity Assay

We determined that leaching alcohol residuals from in-house synthesized monomers had no toxic effects on the growth of *P. aeruginosa*. Under an argon atmosphere, 20 μL solutions of 1% (w/v) DMPA photoinitiator dissolved in monomers (CyDMA, DdMA, GeMA, LMMA or tBCHA) were transferred into separate wells of a 96-well plate in triplicates. The plate was then

irradiated with a long wave UV for 1 hour under argon and vacuum dried for 7 days. An overnight primary culture of *P. aeruginosa* grown in 10 mL LB at 37 °C and 200 rpm was standardized to an OD_{600} of 0.01 in LB stock prior to transferring 200 μL into test wells. Growth (optical density at 600 nm) was measured every 30 min over 24 h at 37 °C in Tecan Genios Fluo instrument under static conditions.

Further toxicity tests were performed to examine the effect of other residual alcohols and unpolymerised monomers on growth of bacteria. BMA, butanol, dodecanol and lauryl methacrylate were introduced into test plates of a 96-well plate at concentrations from 0.01 μL/ml to 1 μL/ml in fivefold increments. A total volume of 200 μL per well was reached through addition of LB inoculated with PAO1 at OD_{600} 0.01. Growth (optical density at 600 nm) was measured every 30 min over 24 h at 37 °C in Tecan Genios Fluo instrument under static conditions.

5.2.5 Polymer Microarray Printing

Glass slides 25 x 75 mm were epoxy silanised and then dip-coated in 4% (w/v) pHEMA solution dissolved in 96% (v/v) ethanol in water following methods detailed in 2.2.1. Microarray printing was then carried out under an argon atmosphere at O_2 < 2000 ppm, 27 °C and 30% relative humidity as detailed in 2.2.2. The freshly printed arrays with 61 materials were vacuum extracted at < 50mTorr for 1 week to remove unpolymerised monomer and solvent. Each printed microarray slide contained three replicates per polymer spot separated by 20 mm.

5.2.6 ToF-SIMS Characterisation

ToF-SIMS analysis of the native array was performed using an IONTOF (GmbH) IV instrument utilizing a 25 keV Bi_3^+ primary ion source. An area of 13 mm × 10 mm was analysed using the macroraster (large area) scanning facility encompassing the entire 61 polymer spot microarray in the sawtooth mode. Data was acquired with a single scan of

the analysis area at a resolution of 1600 pixels per mm and 1 shot per pixel. Owing to the insulating nature of the sample, charge compensation was applied in the form of a low energy (~20 eV) electron flood gun. Both positive and negative secondary ion data was collected and data analysis was carried out with SurfaceLab 7 software.

5.2.7 Water Contact Angle

Water contact angle measurements were carried out as detailed in section 2.3.2. In brief, measurements were performed using ultrapure water on a Krüss DSA 100 apparatus fitted with a piezodoser head. The piezodoser allowed small ultrapure water droplets (110 pL) to be deposited onto the polymer spots. Sample positions and data acquisition were automated, with droplet side profiles being recorded (a dual camera system was used, one to record a spot's side profile and the other to record a bird's eye view to ensure that the water droplet was deposited at the centre of each spot) for data analysis. WCA calculations were performed using a circle segment function as required for small water droplets. Data acquisition was obtained from a total of three microarrays printed onto the same glass slide.

5.2.8 Partial Least Squares Regression Analysis

Correlations between ToF-SIMS spectra and water contact angle were analysed using PLS regression. In total 373 positive and 390 negative ions were selected to form the peak list m/z range 0 - 400. Both positive and negative ion peak intensities in a ToF-SIMS spectrum were dead time corrected and then normalized to the respective total secondary ion counts to remove the influence of primary ion beam fluctuation. The positive and negative ion intensity data were arranged into one concatenated data matrix, which was mean-centred and square-root mean scaled prior to analysis. PLS analysis was carried out using PLS Toolbox 5.2 software (Eigenvector). For cross-validation, the dataset was randomly split into a training group, containing 75% of the samples, and a test set, containing the remaining 25% of samples. The test set were selected by ranking the samples by WCA values and randomly selecting 25% of

samples from the lowest 25%, middle 50% and highest 25% of samples. The training set was formed from the remaining samples. This method was done to ensure both the test and training set contained polymers representing an even spread of low, middle and high water contact angle. A “leave one out” cross validation method was used in the PLS regression analysis of the training set. PLS models were constructed using 8 latent variables and PLS model were validated by applying to the test set. The final PLS model was constructed using the latent variable whereby the R^2 value for the test set was a maximum and close to the R^2 value of the training set.

5.2.9 Bacteria Biofilm Assay on Microarray

Microarray slides were UV sterilized for 10 mins and inoculated (OD_{600} = 0.01) with either *mcherry* tagged *P. aeruginosa* or *dsRed* tagged *Pr. mirabilis* in 20 mL of standard RPMI medium in a petri dish and incubated for 24 h at 37 ˚C at 60 rpm shaking. Control slides were also incubated under the same conditions without bacteria. After incubation, slides were twice rinsed with phosphate-buffered saline at room temperature for 5 min and then with distilled water for 5 min. Fluorescence images were then taken for both control and treated slides using a GenePix Autoloader 4200AL (Molecular Devices, US) scanner.

5.2.10 Thermal Polymerisation

5.2.10.1 CyDMA

In a reaction vessel, purified monomer of CyDMA (3.2 g, 12.69 mmol) was dissolved in 20 mL of toluene. Chain transfer agent PhCoBF (2.95 mg, 0.02 mmol) and thermal initiator AIBN (21 mg, 0.13 mmol) were then added and the mixture degassed for 60 mins under argon. Reaction mixture was then stirred and allowed to polymerise at 75 ˚C overnight for 18 hours in oil bath. The crude reaction mixture was precipitated in excess of hexane and dried prior to application testing.

5.2.10.2 EGDPEA-co-DEGMA

Co-polymerisation of EDGPEA and DEGMA was carried out using similar procedures reported in section 5.2.10.1. Quantities of reactants used were: EGDPEA (7.5 mL, 32.77 mmol), DEGMA (2.5 mL, 13.24 mmol), toluene (40 mL), PhCoBF (3.5 mg, 0.02 mmol) and thermal initiator AIBN (35 mg, 0.23 mmol)

5.2.11 Coating Catheter Sections with Polymers

PDMS catheters (1 cm) in length were sliced through longitudinally into equal parts and sonicated in acetone for 10 minutes. Using a needle inserted into catheter walls, sliced sections were dipped eight times in a 10 mL solution of Nusil MED1-161 primer and air dried for 5 minutes at room temperature. Nusil MED1-161 is a 20% (v/v) mixture of tetrabutyl titanate, tetrapropylsilicate, and tetra (2-methoxyethoxy)silane in naphtha solvent [211]. It condenses upon exposure to water from air to form polysiloxane oligomers. These form hydrogen bonds with the silicone surfaces followed by formation of covalent bonds through hydrolysis. The exposed R group is a linker of specific chain length that helps adhere to polymer, Figure 73.

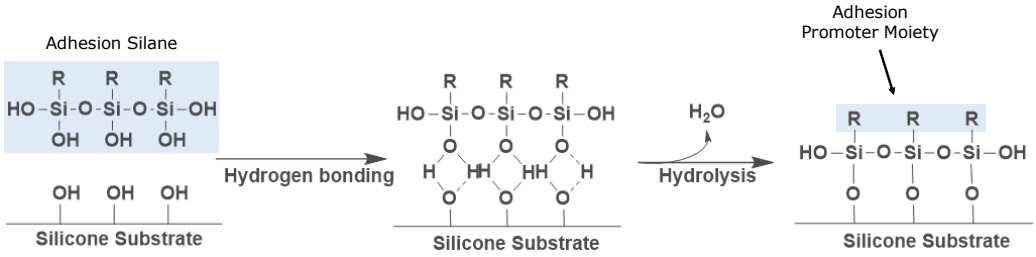

Figure 73. Reaction mechanism for adhesion promoter on poly(dimethoxy silane) substrate. Initial exposure of silane primer to atmospheric water leads to hydrolysis and formation of silanol, which interacts via hydrogen bonds with PDMS catheters and finally bonds through loss of water.

Silane primed catheter sections then underwent three dipping cycles in 30% (w/v) polymer in DCM. For each cycle, catheter sections were dipped 8 times into polymer solution and left to dry for 5 minutes before the process was repeated.

A Jeol 6060LV variable pressure scanning electron microscope (Jeol UK Ltd.) was used to scan the surface of the polymer coated catheter sections to visualise coating thickness. The samples were gold coated for four minutes prior to analysis using a Leica EM SCD005 sputter coater to achieve appropriate conductivity for the SEM to function.

5.2.12 Bacterial Strains, Growth Conditions and Biofilm Assay

Pr. mirabilis strain Hauser 1885, *P. aeruginosa strain* PAO1 (Washington sub-line, Nottingham collection), *S. aureus* SH1000, *E. faecalis* NCTC12697, *Klebsiella pneumoniae* NCIMP10104 and Uropathogenic *E. coli* (UPEC) were routinely grown at 37˚C in LB with shaking at 200 rpm or on LB agar (2% w/v). Where required, plasmids for constitutively expressing fluorescent proteins GFP (pBK-miniTn7-egfp) and mCherry (pMMR) were introduced into the relevant host strain by conjugation or electroporation. Bacterial biofilm formation assays were conducted as previously described. Briefly, UV-sterilized polymer coupons or polymer-coated catheters segments were incubated with bacteria at 37˚C with 60 rpm shaking for 72 h in Artificial Urine (AU) [297]. The composition of AU was: peptone L37 (1 g/L), yeast extract (0.005 g/L); lactic acid (0.1 g/L); citric acid (0.4 g/L); sodium bicarbonate (2.1 g/L); urea (10 g/L); uric acid (0.07 g/L); creatinine (0.8 g/L); calcium chloride dihydrate (0.37 g/L); sodium chloride (5.2 g/L); iron(II) sulphate heptahydrate (0.0012 g/L); magnesium sulphate heptahydrate (0.49 g/L); sodium sulphate decahydrate (3.2 g/L); potassium dihydrogen phosphate (0.95 g/L); di-potassium hydrogen phosphate (1.2g/L); ammonium chloride (1.3 g/L).

Air-dried samples were examined using a Carl Zeiss LSM 700 laser scanning confocal microscope fitted with 405 nm, 488 nm and 555 nm excitation lasers and a 10x/NA 0.3 objective. Images were acquired using ZEN 2009 imaging software (Carl Zeiss). Bacterial surface coverage was quantified using Image J 1.44 software (National Institutes of Health, USA) and Comstat B.

For single-species biofilm formation, polymer coated catheters sections were incubated with AU (20 ml) containing 1 µM (syto64) and/or 2µM calcein (Sigma) and inoculated with *Pr. mirabilis, P. aeruginosa, S. aureus, E. faecalis, K. pneumonia* or *UPEC* cells at an OD_{600} of 0.01. Biomass was quantified using confocal fluorescence microscopy. For mixed-species biofilms, polymer coated coverslips were incubated with AU (20ml) and inoculated with *P. aeruginosa* and *S. aureus* mixed in a 1:10 ratio.

This part of the work involving biofilm assay for six different bacteria species was entirely carried out by Dr. J. F. Durben. O. Sanni provided catheter sections coated with polymers.

5.3 Results

5.3.1 Predicted Monomers

a

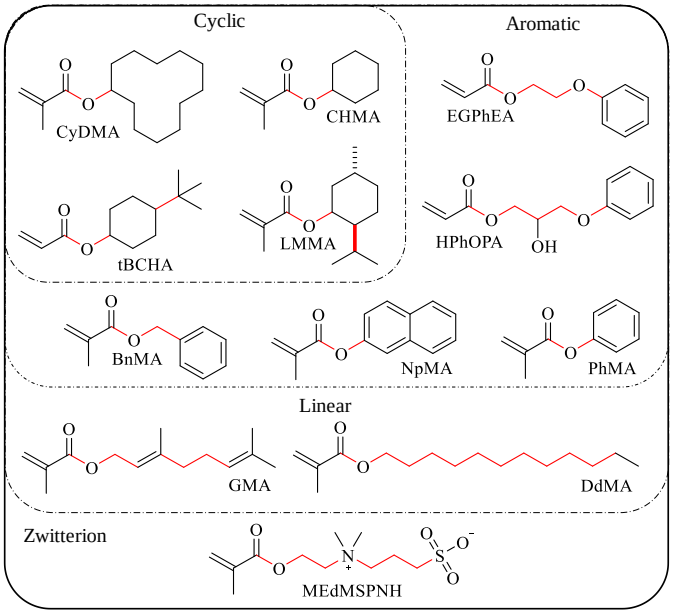

b

Materials	nRB	clogP	alpha value
CyDMA*	2	6.35 ±0.25	-5.47
GMA*	6	4.77 ±0.46	-2.13
LMMA*	3	4.83 ±0.26	-3.51
DdMA*	12	6.75 ±0.25	-1.47
EGPhEA	5	2.27 ±0.26	-0.07
BnMA	3	2.38±0.35	-1.06
CHMA	2	2.97 ±0.25	-2.09
PhMA	2	2.05 ±0.43	-1.17
HPhOPA	6	1.54 ±0.29	1.1
NpMA	2	3.28 ±0.43	-2.4
MEdMSPNH	8	-5.66 ±0.76	n/a
tBCHA	3	4.13 ±0.24	-2.81

Figure 74. **(a)** Materials library made up of 12 monomers used to validate *alpha* model. Rotatable bonds in each molecule are colour coded in red. **(b)** The table shows number of rotatable bonds (nRB), calculated logP values (clogP) and resulting alpha value for each monomer. Materials with asterisk (*) were synthesized.

In Figure 74a, the number of rotatable bonds (in red) were defined as any single bond, not in a ring, bound to a nonterminal heavy (i.e., non-hydrogen) atom [298]. The molecular structures of four monomers (CyDMA, GMA, LMMA and DdMA) with low *alpha* parameter values were identified for synthesis as shown in Figure 74b to expand the chemical space in order to identify improved materials and also test the validity of correlation between bacterial biofilm formation and the *alpha* parameter beyond the initial library limited to commercially available compounds**.** An *alpha* value of -5.47 was calculated for CyDMA and -3.51 for LMMA, which is lower than any material previously tested (*alpha* = -3 to 1). In addition to the four synthesized monomers, eight commercially available monomers that had been previously tested were also included for comparison.

Due to having drastically different structure from materials used for the *alpha* model, *alpha* value for MedMSPNH a zwitterionic material could not be reliably calculated nor predicted using the model but was included on the array for comparison purposes.

5.3.2 One-step Esterification Synthetic Route

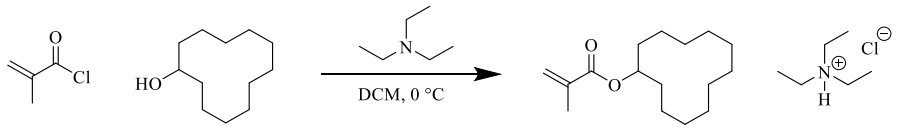

Figure 75. Chemical equation for one-step esterification procedure to synthesize new methacrylate monomers.

To maximize the productivity of materials discovery screening campaigns, bespoke synthesis of predicted monomers should ideally be cheap, easy to process and readily accessible, i.e. not time consuming. Acrylate/(meth)acrylate monomers that are commercially available with wide chemical diversity (hundreds of different compounds) are suitable for this as they are readily printable and amenable to *in situ* polymerization [209, 243]. We employed a single step esterification synthetic route, that utilises commercially available alcohols (thousands are readily available) to create bespoke monomer building blocks that significantly expand the chemical space relative to the commercial (meth)acrylates used to date. A 74% yield of CyDMA monomer was obtained after purification. Spectra obtained from ^{1}H and ^{13}C NMR analysis can be found in Appendix N.

Non-purified, synthesized materials (GMA, LMMA and DdMA) obtained from laboratory stocks of *A. Dundas* were used as received, but were however tested for toxic effect on bacteria. To determine whether unreacted reagents (monomers and their associated alcohols) could inhibit bacterial growth and hence reduce bacterial attachment and biofilm formation, *P. aeruginosa* was cultured over 24 h in RPMI media dosed with monomers and the associated alcohols at concentrations of 0.01 to 0.1% (v/v).

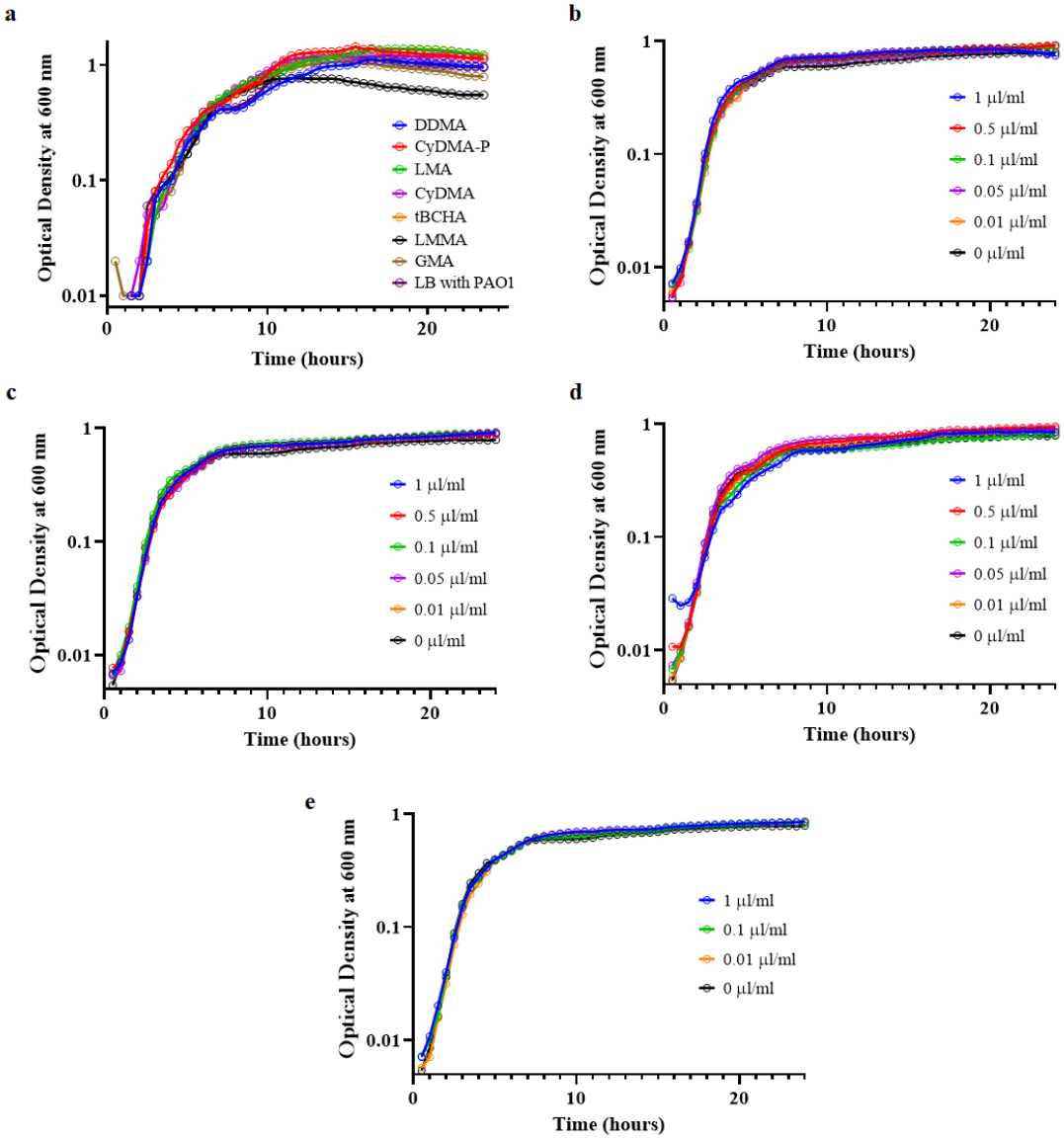

Figure 76. Toxicity assay performed using **(a)** Monomers **(b)** BMA **(c)** Butanol **(d)** Dodecanol **(e)** Lauryl methacrylate. Optical density (OD_{600}) of bacteria was measured every 30 minutes over 24 hours. LB medium inoculated with PAO1 only was used as positive controls. Measurements were made from n = 3 biological replicates.

Synthesised polymers (CyDMA, DdMA and GeMA) all promoted PAO1 growth comparable to that of LB control with bacteria only. This suggested that the residual alcohol within the polymers was not altering bacteria growth in culture experiments. However, LMMA was excluded from any scale-up experimentation as it showed a slight decrease in the bacterial growth when compared to the control (Figure 75a), possibly due to excess alcohol resulting from lower conversion (69%). Secondly, purified CyDMA allowed for the same bacterial growth as both the control and the impure CyDMA (Figure 75a), suggesting that polymers with

have a high conversion (> 84 %) and consequently low residual alcohol do not alter bacterial growth.

Concentrations selected were based upon a possible worst-case scenario assuming all of starting material stayed unreacted or unpolymerized for all the spots on a polymer microarray (200 spots with each spot approximately 1 nL in volume) is incubated using 20 mL of RPMI media resulting in concentration of 0.1 μL/ml. It was observed that there was no effect on the bacteria with increasing concentration of starting reagents (Figure 75b-c) or unpolymerized lauryl methacrylate (Figure 75e). There is a slight deviation with high concentrations of dodecanol during the log phase of bacterial growth (Figure 75d), however this was shown to not be statistically different from the growth of bacteria in medium alone.

5.3.3 Polymer Microarray Surface Characterisation

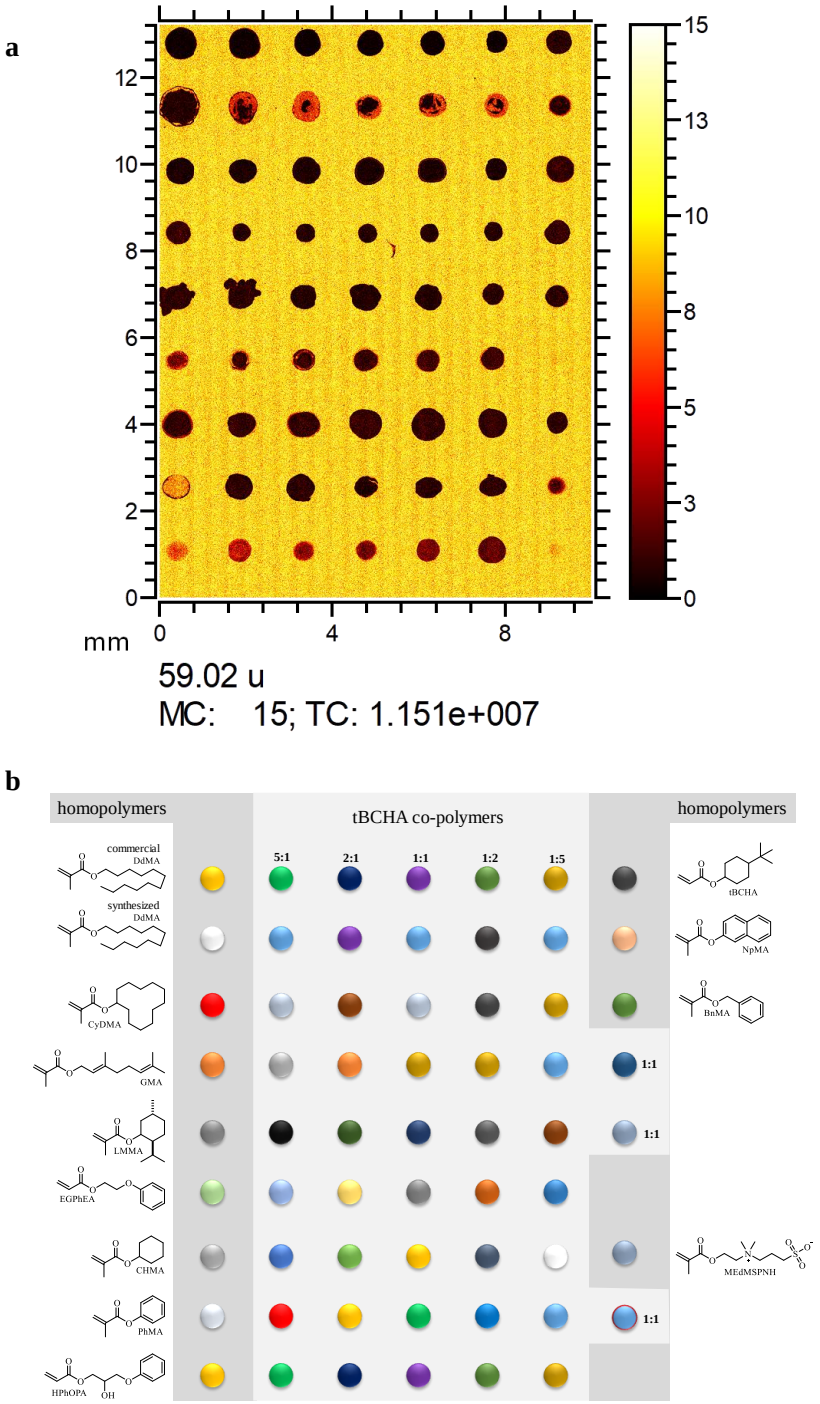

Figure 77. **(a)** ToF-SIMS ion image for pHEMA background marker $C_2H_3O_2^-$ (m/z 59.02) normalized to total ion counts. **(b)** Schematic diagram showing microarray print layout of 11 monomers mixed pairwise with tBCHA monomer in different proportions. Shaded in dark grey are regions with homopolymers and shaded in light grey are regions with copolymers of tBCHA.

A polymer microarray was printed using the 12 monomers with an *alpha* value range of -5.47 to 1.1 mixed pairwise with *tert*-butyl cyclohexyl acrylate (tBCHA) to produce unique polymers spots printed in triplicate on a single slide after photo polymerisation (Figure 77).

5.3.3.1 ToF-SIMS

ToF-SIMS was employed to monitor spot printing fidelity and provide surface analysis to detect any surface segregation due to de-mixing of monomers as previously reported by Hook *et al.* [299].

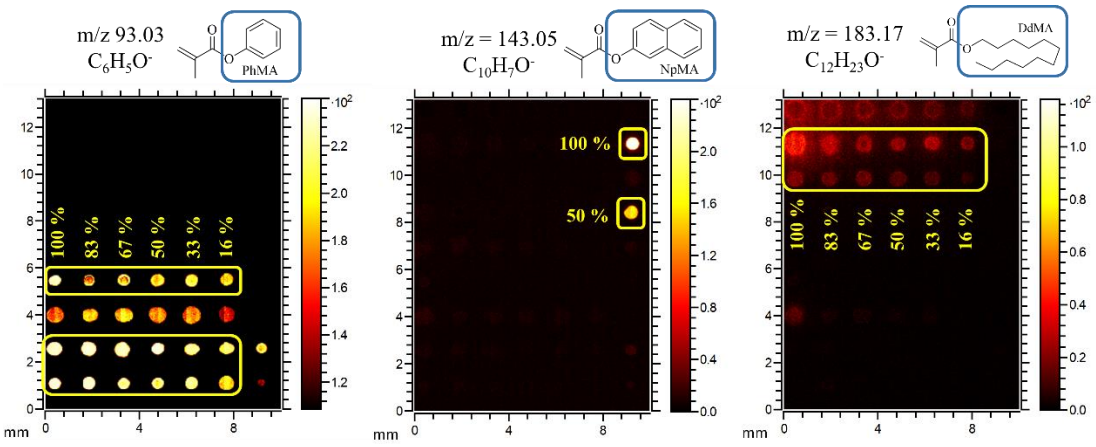

Figure 78. ToF-SIMS chemical images of the microarray built using an ion marker identifying of aromatic rings and long hydrocarbon moieties. Polymers with expected aromatic rings or long hydrocarbon chains are encased in yellow rectangle.

With the exception of structurally related LMMA, tBCHA and CHMA, unique ions were identified for most monomers and used to monitor the relationship between monomer feed ratio and the surface composition of the polymer product. From images in Figure 78, it can be seen that ion intensity of phenoxy ring decreases with decreasing concentrations of monomers possessing this moiety. The more specific naphthyl aromatic ring uniquely identifying of NpMA and can also be seen to decrease on 50% copolymer spot with tBCHA, DdMA and CyDMA both possess a 12 carbon pendant group and follow the same decreasing trend with decreasing monomer concentrations. Interestingly, it appears that linear monomer DdMA ionises to a greater degree compared to its structural isomer CyDMA. Hence the appearance of brighter more intense spots on same scale.

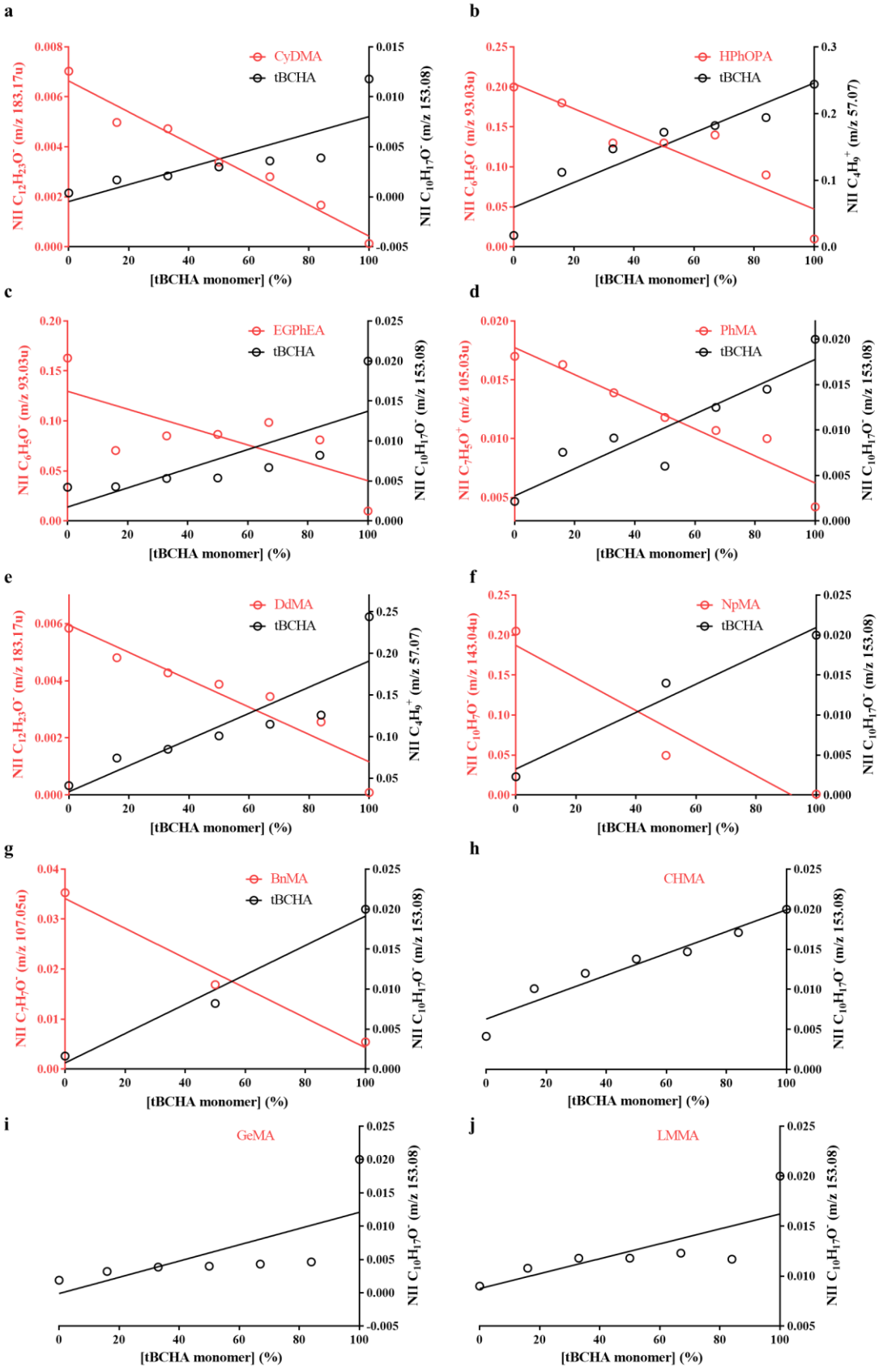

Figure 79. Series of diagrams showing mixing of copolymer series where ions identifying of tBCHA ($C_4H_9^+$ or $C_{10}H_{17}O^-$) are plotted in black on right y-axis, and plotted in red are ions associated to to **(a)** CyDMA **(b)** HPhOPA **(c)** EGPhEA **(d)** PhMA **(e)** DdMA **(f)** NpMA **(g)** BnMA **(h)** CHMA **(i)** GeMA or **(j)** LMMA. Copolymer series which had poor mixing were not compared with *alpha* in copolymer data.

The ion intensities indicate linear trends for the SIMS ion intensity versus composition when mixing the two monomers, for example, in Figure 79a, CyDMA and tBCHA with correlation coefficients of R^2 = 0.97 and R^2 = 0.68 respectively. In both cases the pure monomers exhibit slightly higher intensity than predicted by a straight line fit to all the data, suggesting possible matrix effect non linearity. All the copolymer series were found to approximate to the bulk ratios apart from GeMA and EGPhEA where surface segregation when mixed with tBCHA was detected. This is likely due to differences in the miscibility of the monomers causing to phase separation before polymerisation is complete, copolymers which exhibited this were not studied further herein [300].

5.3.3.2 Water Contact Angle

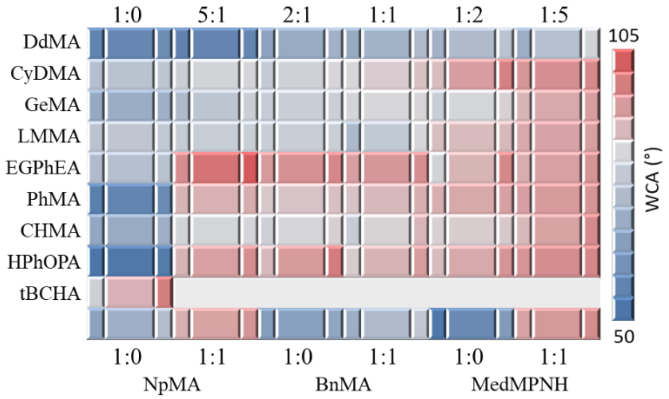

Figure 80. Results from polymer microarray water contact angle measurements. Monomer identity is organised into rows and mixing ratio with *tert*-Butyl cyclohexyl acrylate (tBCHA) into columns. The center square is mean value of WCA, whilst the narrow columns to the left or right indicate ± 1 sd unit respectively (N = 3).

The wettability of each polymer spot on the microarray was measured by water contact angle. The results are presented in heat map shown in Figure 80, where a visible trend of decreasing wettability with increasing content of tBCHA monomer is observed. Previous investigations exist that correlated polymer surface chemistry, as inferred by ToF-SIMS data, with wettability across a library of samples [301]. To achieve a correlation between polymer surface functionality and wettability, WCA measurements made on all 61 polymers within the library were related to ToF-SIMS data via the use of partial least-squares (PLS) regression technique.

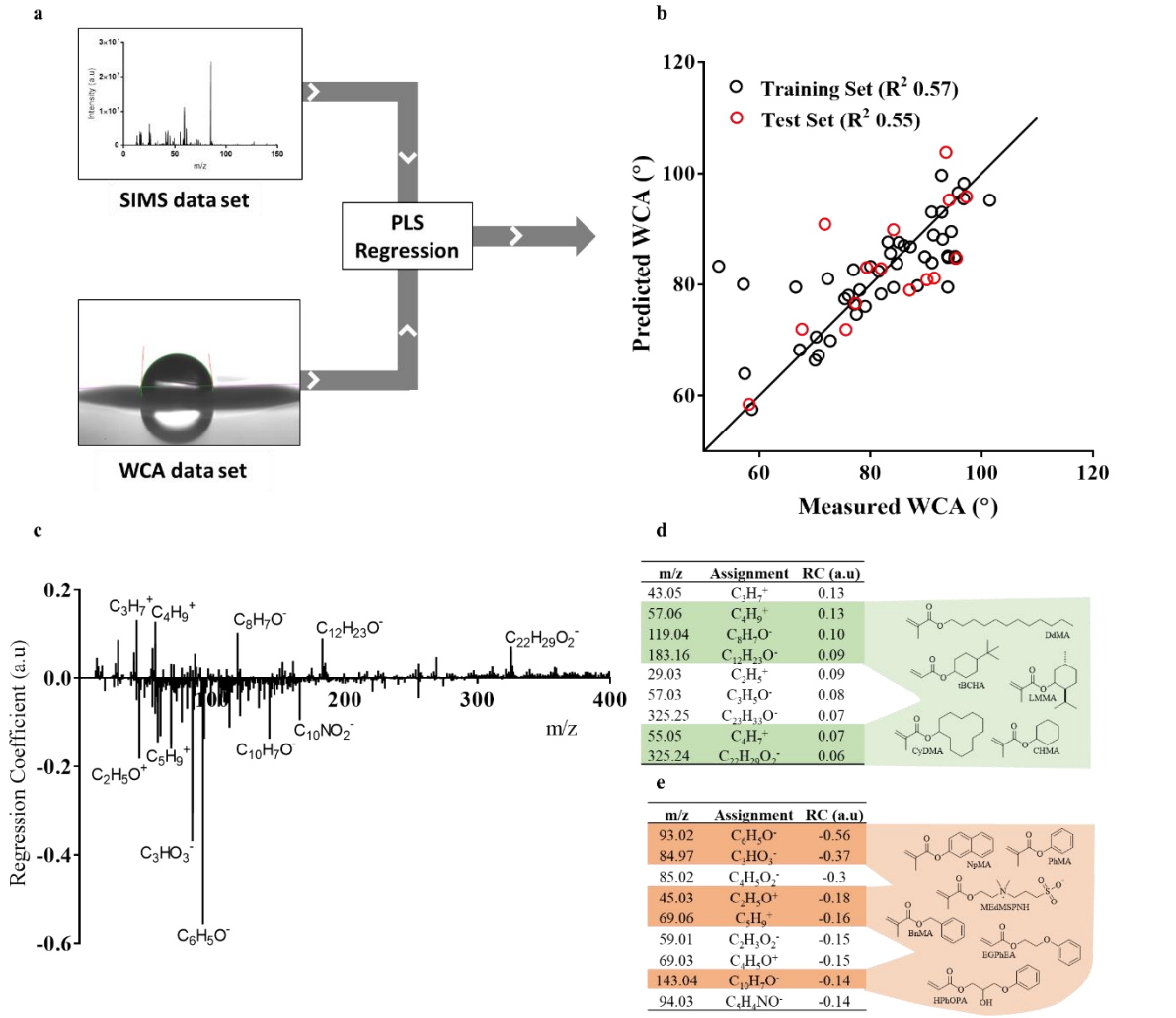

m/z	Assignment	RC (a.u)
43.05	$C_3H_7^+$	0.13
57.06	$C_4H_9^+$	0.13
119.04	$C_8H_7O^-$	0.10
183.16	$C_{12}H_{23}O^-$	0.09
29.03	$C_2H_5^+$	0.09
57.03	$C_3H_5O^-$	0.08
325.25	$C_{22}H_{33}O^-$	0.07
55.05	$C_4H_7^+$	0.07
325.24	$C_{22}H_{29}O_2^-$	0.06

m/z	Assignment	RC (a.u)
93.02	$C_6H_5O^-$	-0.56
84.97	$C_3HO_3^-$	-0.37
85.02	$C_4H_5O_2^-$	-0.3
45.03	$C_2H_5O^+$	-0.18
69.06	$C_5H_9^+$	-0.16
59.01	$C_2H_3O_2^-$	-0.15
69.03	$C_4H_5O^+$	-0.15
143.04	$C_{10}H_7O^-$	-0.14
94.03	$C_4H_4NO^-$	-0.14

Figure 81. Summary of the PLS regression model used to predict the wettability of polymers by correlating water contact angle measuremets with the ToF-SIMS data. **(a)** Schematic representation of modeling process with multivariate tof-sims data and univariate WCA data. **(b)** The predicted WCA values determined from the PLS regression model. Training set (R^2 = 0.57) in black and test set in red (R^2 = 0.55) The y = x line is drawn as a guide. **(c)** The regression vector for the PLS model showing the regression coefficients for both positive and negative ions. (d and e) Table of secondary ions with the **(d)** highest and **(e)** lowest regession coefficient. The key ions and respective monomers are shown.

The PLS model produced by this analysis successfully predicted the wettability of tested polymers as evidenced by the linear relationship (R^2 = 0.55) between predicted and measured WCA values shown in Figure 81b. The influence of each of the 763 ions from sims spectra used to construct PLS model is quantified by the regression co-efficient plotted in Figure 81c. A positive score for an ion is indicative of high WCA values or poor wettability whiles a negative score is indicative of low WCA values or good wettability. The terms low and high used here are relative to range of WCA values obtained from polymers, that is, from 50° – 90° as seen in Figure 80.

Interestingly, the surface chemical moieties assigned to secondary ion fragments with highest PLS regression coefficients shown in Figure 81d is dominated by four monomers with cyclic aliphatic pendant groups and 1 monomer with linear aliphatic group. On the contrary, monomers with aromatic rings are predominant contributors to fragments with lowest PLS regression coefficients. Aided by the initial monomers selection, an unintentional comparison between aromatic and aliphatic compounds was clear, the findings suggested chemical moieties with aromatic rings possess greater wettability compared to cyclic aliphatic compounds. The finding can be attributed to greater affinity of aromatic hydrocarbons for water due to presence of π-interaction with increased electron density compared to cyclic aliphatic compounds. [302, 303]. The successful prediction of wettability of these polymers demonstrates the dependence of this phenomena on polymer surface chemistry.

5.3.4 Attachment of *P. aeruginosa and Pr. mirabilis* to Polymer Microarray

The human pathogenic bacteria *P. aeruginosa,* and *Pr. mirabilis* were chosen for initial biofilm formation experiments with polymer microarrays, shown in Figure 82, as they are frequently involved with healthcare-associated infections including CAUTI [304].

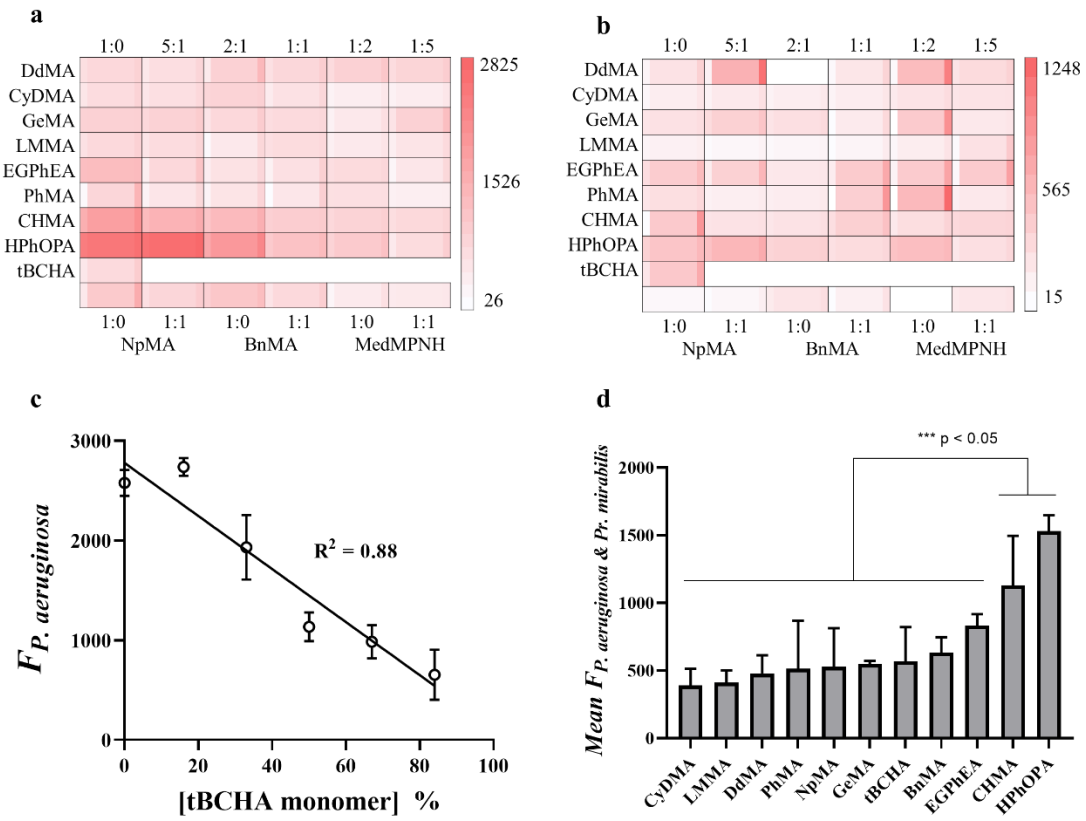

Figure 82. **(a)** Results from polymer microarray biological assay with *mCherry* tagged *P. aeruginosa* strain. Monomer identity is organised into rows and mixing ratio columns with *tert*-Butyl cyclohexyl acrylate (tBCHA). The centre square is the fluorescence value for attachment of *P. aeruginosa*, whilst the narrow columns to the left or right indicate ± 1 sd unit respectively (N = 3). **(b)** Results from the same experiment as (a) but with dsRed tagged *Pr. mirabilis* (N = 3). **(c)** Plot showing attachment of *P. aeruginosa* on HPhOPA and tBCHA copolymers. **(d)** Rank order plot showing averaged attachment of *P. aeruginosa* and *P. mirabilis* on homopolymers.

The attachment of fluorescently labelled *P. aeruginosa* and *Pr. mirabilis* to each polymer spot on the microarray was measured and presented with an intensity map seen in Figure 82. Each cell is the mean fluorescence read out from three polymer spots. A white colour code indicates polymers with low bacteria attachment and a red colour code polymers with high bacteria attachment.

From Figure 82a, it was clear that polymers spots with high concentration of HPhOPA monomer exhibited high attachment for both *P. aeruginosa* and *Pr. mirabilis*. This observation is consistent with previous findings from Hook *et al*, where they established that hydroxyl containing methacrylate monomers promoted bacteria attachment [196]. This capability of HPhOPA is reversed with increasing content of tBCHA in copolymers series (see Figure 82c) to reduced attachment of *P. aeruginosa*. This was independently verified on a large scale in a

different study by Durben *et al* (unpublished data). In Figure 82d, across the two bacteria species, CyDMA and LMMA homopolymers presented with the lowest attachment of bacteria.

5.3.5 Validation of the *Alpha* Parameter

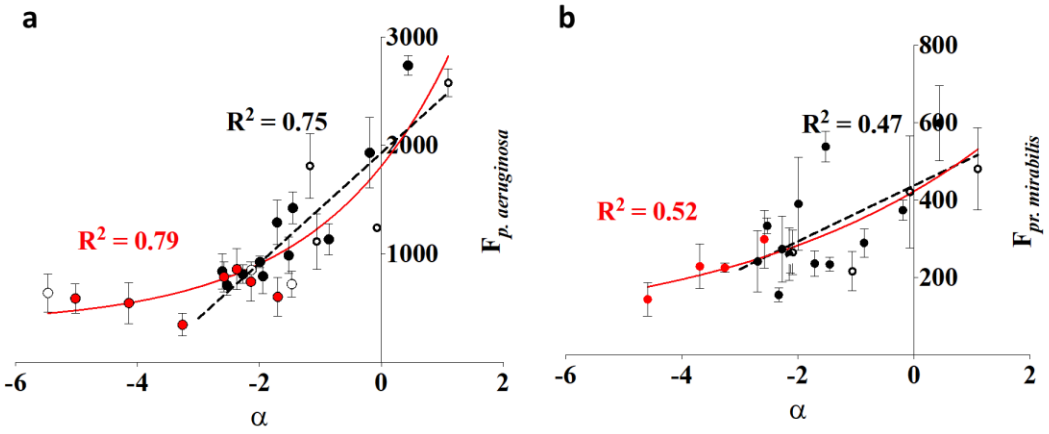

Figure 83. **(a)** Fluorescence intensity measured from *P. aeruginosa* attachment to the polymer microarray. The unfilled/solid black symbols represent materials used to build the alpha model (homopolymers/copolymers respectively), the dashed black line is the linear relationship from -3 to 1.1, R^2 = 0.75. The red unfilled/solid symbols are materials used to extend alpha range (homopolymers/copolymers respectively) and red solid line is exponential relationship with values from -5.47 to 1.1, R^2 = 0.79, error bars shown are ± 1 sd (n = 3). **(b)** Fluorescence from *Pr. mirabilis* attachment to the polymer library using the same display conventions as for (a).

A linear correlation (R^2 = 0.75) was observed between the bacterial load measured as fluorescence intensity of *P. aeruginosa* versus alpha between -3 and 1.1 (Figure 83a) [122]. However, when materials in the extended range of alpha of -5.47 to 1.1 were considered, a poorer linear correlation (R^2 = 0.61) was observed. As alpha decreased, bacterial fluorescence approached a lower limit under these microarray assay conditions. An exponential fit better described the relationship between alpha and *P. aeruginosa* attachment for the full polymer library dataset (R^2 = 0.79) (Figure 83a). While weaker correlation was observed for *Pr. mirabilis* (R^2 = 0.52) (Figure 83b), these correlations do suggest that both species respond to the physiochemical properties described by the alpha value (hydrophilicity and molecular rigidity).

As the lowest alpha parameter materials were statistically similar for both bacterial species (see Figure 82d), the CyDMA homopolymer was taken forward for further investigation as a coating

on silicone catheter segments in order to carry out initial comparison with the biofouling performance of existing devices.

5.3.6 Multispecies Bacterial Attachment Assay on Polymer Coated Silicone Catheters

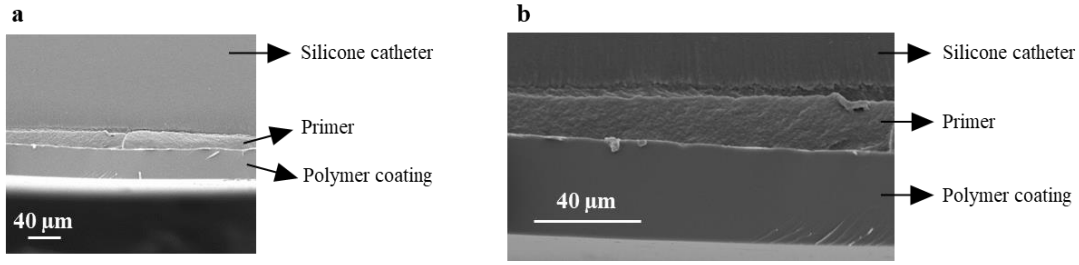

Figure 84. SEM images **(a)** 160X magnification **(b)** 900X magnification of the cross-section of a silicone catheter firstly coated with silane primer to promote adhesion, then coated with pCyDMA (thickness, 30–38 µm).

Polymerisation of CyDMA was undertaken using thermal polymerisation procedures described in section 5.2.10 to produce a polymer solution with which to dip-coat silicone catheter segments. The thickness of polymer coating on catheter was on average 35 ± 3 µm (Figure 84). For comparison, highly performing acrylate copolymer material previously reported in the literature to prevent bacterial biofilm formation, poly(ethylene glycol dicyclopentenyl ether acrylate-co-diethyleneglycol methacrylate p(EGDPEA-co-DEGMA), was similarly polymerised and coated onto silicone catheter segments [89]. GPC data for polymers can be found in Appendix F

Uncoated silicone catheter sections and a commercially available silver hydrogel coated catheter (BARDEX® I.C.™) were also tested as controls. To mimic more realistic environmental conditions associated to CAUTI, bacteria were cultured in AU and used to test the ability of pCyDMA coated catheter segments to prevent single or mixed species bacterial biofilm formation with clinically relevant bacterial species: *P. aeruginosa, Pr. mirabilis, E. faecalis, K. pneumoniae, E. coli and S. aureus* (Figure 85).

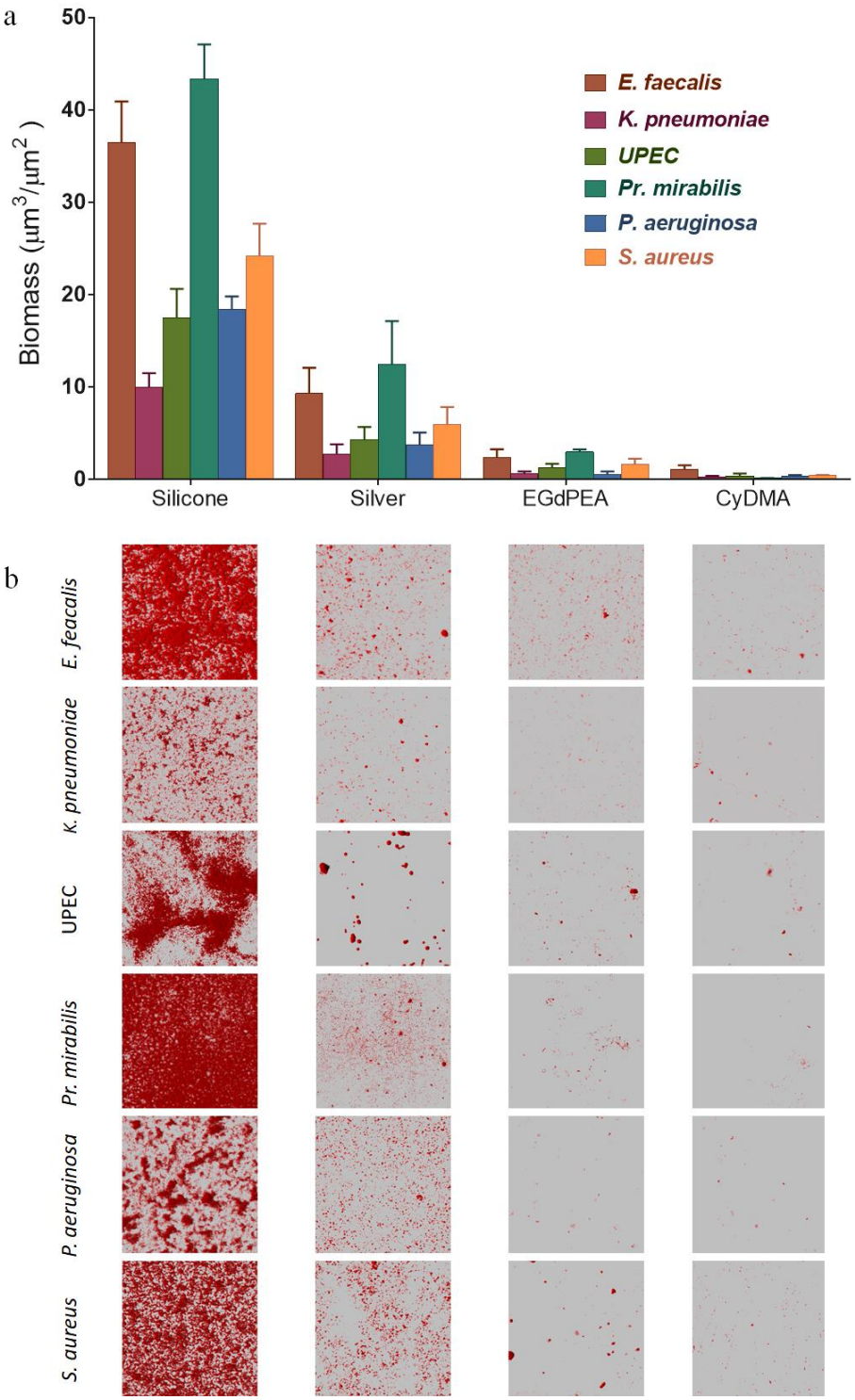

Figure 85. **(a)** Surface coverage of *E. faecalis*, *K. pneumonia*, UPEC, *Pr. mirabilis*, *P. aeruginosa* and *S. aureus* biofilm measured after 72 h incubation on silicone, silver hydrogel, pCyDMA and p(EGDPEA-co-DEGMA) coated silicone catheter segments in AU. Error bars equal ± one standard deviation unit, n = 3. (**b**) The corresponding confocal microscopy images for of Syto64 stained *E. faecalis*, *K. pneumonia*, uropathogenic *E. coli* (UPEC), *Pr. mirabilis*, *P. aeruginosa* and *S. aureus* growing on each surface. Each image is 160 x 160 µm.

Experimental procedures and data processing to courtesy of Dr. J. Durben. O. Sanni synthesised and prepared all polymer coated samples used in this experiments. Dr. J. Durben carried out biofilm assay and processed images.

On silicone catheter segments an average bacterial biomass of 25 ± 2.9 $\mu m^3/\mu m^2$ was observed compared with the reduced load of 6.4 ± 2.2 $\mu m^3/\mu m^2$ on a commercial silver hydrogel coated catheter (Figure 85). In contrast, the pCyDMA coated catheter segment successfully prevented biofilm formation by all six individual bacterial species used in experiment with an average biomass of only 0.5 ± 0.2 $\mu m^3/\mu m^2$ as shown in Figure 85. The p(EGDPEA-co-DEGMA) coating also performed well, with average biomass of 1.6 ± 0.4 $\mu m^3/\mu m^2$, although this was surpassed in performance by the pCyDMA discovered in this QSAR process.

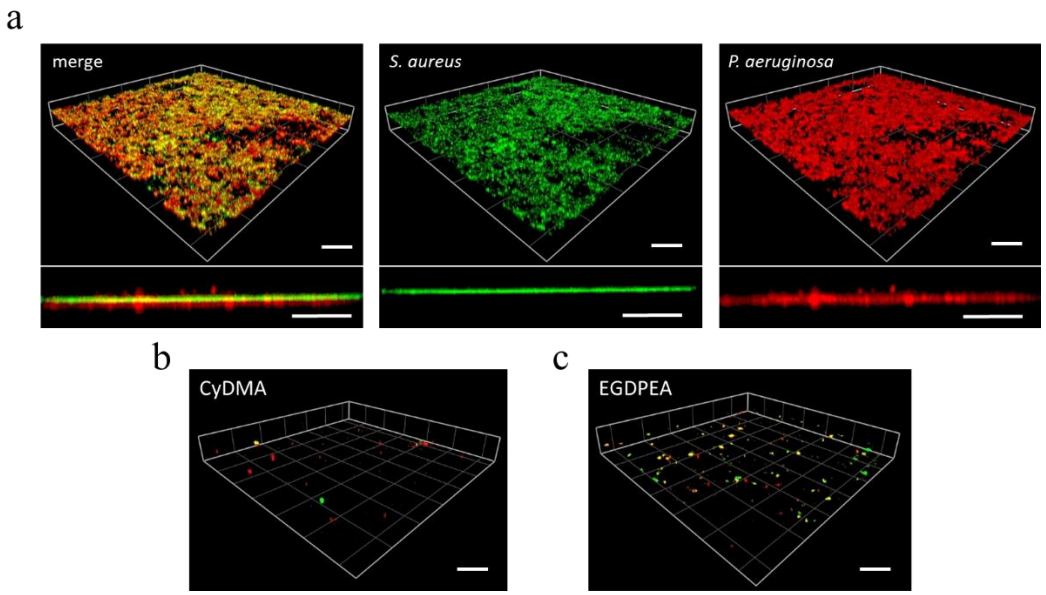

Figure 86. **(a)** 3D representation and transverse view of a dual-species biofilm formed on silicone: GFP-tagged *S. aureus SH1000* (green) and *mCherry* labelled *P. aeruginosa* (red) in a 10:1 ratio. **(b)-(c)** 3D representation and transverse view showing the lack of mature biofilm on pCyDMA and p(EGDPEA-co-DEGMA). Scale bars represent 50µm.

Experimental procedures and data processing to courtesy of Dr. J. Durben. O. Sanni synthesised and prepared all polymer coated samples used in this experiments. Dr. J. Durben carried out biofilm assay and processed images.

Most CAUTI infections are polymicrobial [305]. To test the biofilm resistance of a dual species biofilm, we used gfp-labelled S. *aureus* SH1000 (green) and mCherry labelled *PAO1* (red) inoculated onto the catheter segments in a 10:1 ratio. Figure 86a-c shows that for silicone, pCyDMA and p(EGDPEA-co-DEGMA) after 72 h incubation, the dual species biofilm completely covered the silicone surface, whereas very little biofilm coverage was observed on p(EGDPEA-co-DEGMA) and was almost completely absent on pCyDMA.

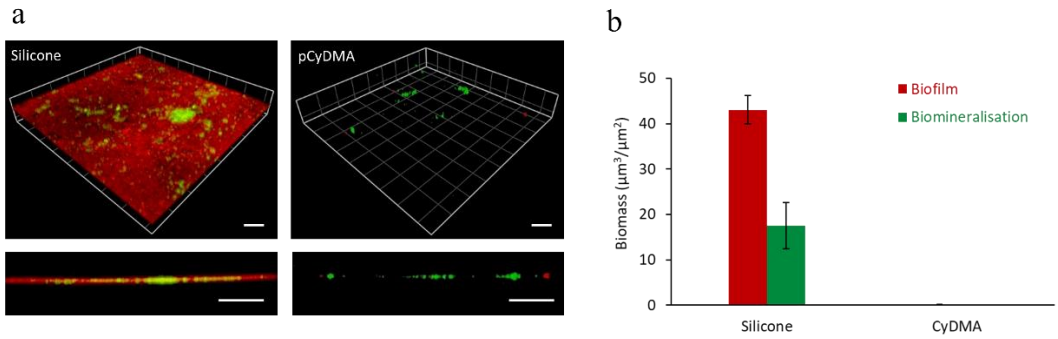

Figure 87. (a) Three dimensional representation and transverse view showing biofilm (red) and biomineralisation (green) by *Pr. mirabilis*. Scale bars represent 50µm. (b) Quantification of biomass and biomineralization by *Pr. mirabilis* on silicone or on pCyDMA coated silicone catheter sections. Values given are the means of four images, error bars are ± one standard deviation unit.

Experimental procedures and data processing to courtesy of Dr. J. Durben. O. Sanni synthesised and prepared all polymer coated samples used in this experiments. Dr. J. Durben carried out biofilm assay and processed images.

It is known that *Pr. mirabilis* can promote biofilm formation via ureolytic biomineralization, where urea is hydrolyzed resulting in salt crystalline deposit on surface. A natural progression for this work was to test the ability of model elected CyDMA to resist biomineralization. Consequently, we incubated pCyDMA with gfp-labelled *Pr. mirabilis* in AU and stained with calcein for calcium and magnesium minerals. The results shown in Figure 87 highlight, in contrast to silicone, very little biofilm formed on pCyDMA and absence of large mineral crystal deposits. The biomass of mineral deposits and biofilms formed on silicone is at least 250 times more than calculated values on pCyDMA.

5.4 Discussion

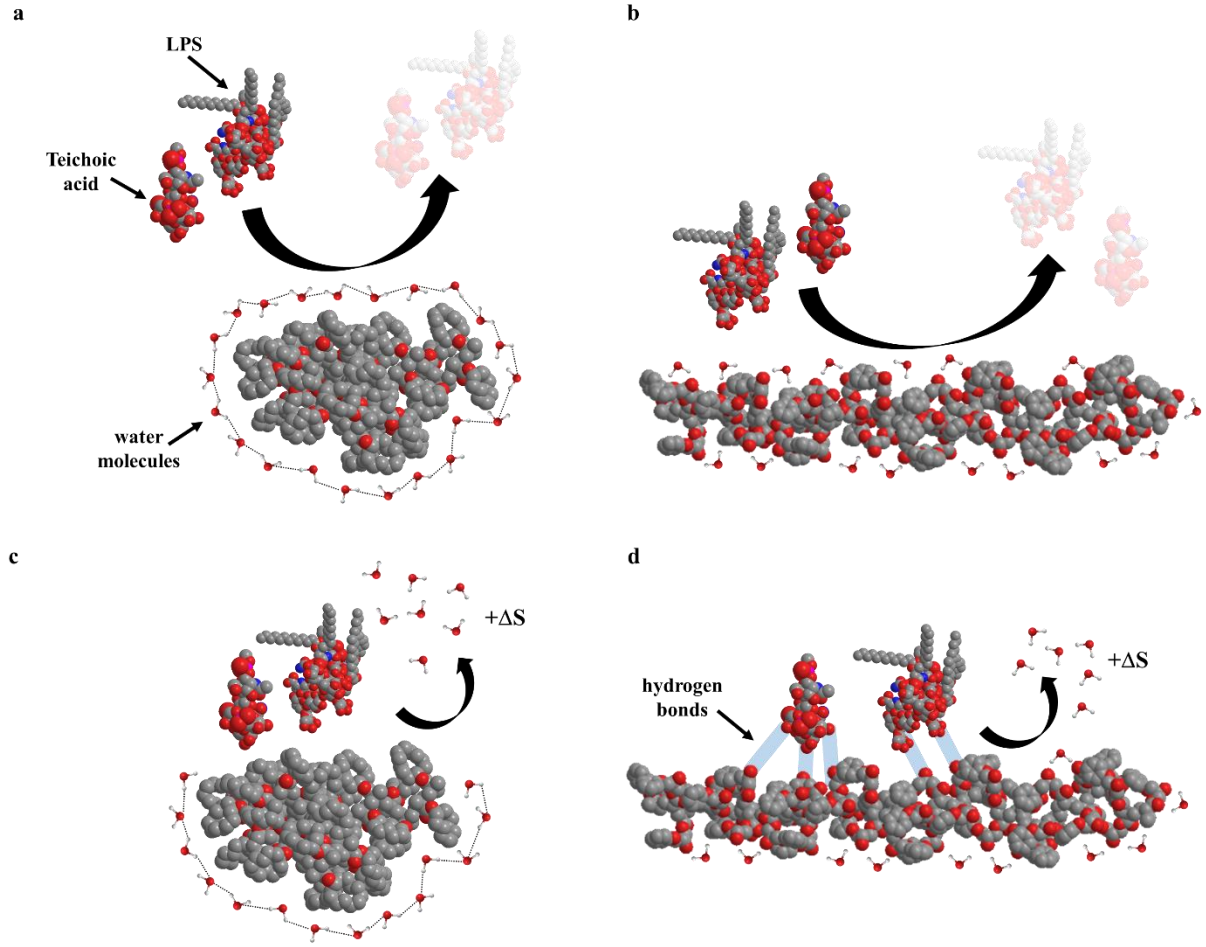

Figure 88. **(a)** 3D space filling model for structure of pCyDMA surrounded by ordered water molecules repelling cell wall surface structures for Gram-positive (teichoic acid) and Gram-negative (lipopolysaccharide). **(b)** 3D space filling model for structure of pHPhOPA interacting with water molecules via hydrogen bonds, repelling teichoic acid and LPS. **(c)** Approaching LPS and teichoic acid displace ordered water molecules surrounding pCyDMA resulting in entropic gain. **(d)** Approaching LPS and teichoic acid displace ordered water molecules surrounding pHPhOPA resulting in interaction via hydrogen bonds with LPS and teichoic acid.

In an attempt to understand the mechanistic mode of action of rigid pCyDMA, we compared the two materials with the highest alpha value (pHPhOPA) and lowest (pCyDMA). Compared to each other, pHPhOPA with alpha value 1.1 is considered more flexible and less hydrophobic than pCyDMA with alpha value (-5.47). Using 3D ChemDraw structures we modelled the polymer architecture of pCyDMA and pHPhOPA, see Figure 88a-b. It was observed that pCyDMA presented with bulky hydrophobic cyclododecyl rings on external surface which in turn masked hydrogen bond acceptor oxygen atoms (in red). In aqueous solutions such as that encountered in biological environment, water molecules unable to interact with pCyDMA may preferentially interact with each other in an ordered manner to surround pCyDMA. It is possible

that the presence of this organised layer (similar to ice cage structure) of water molecules, makes it difficult for surface structures on Gram-positive (teichoic acid) and Gram-negative (lipopolysaccharide) bacteria to interact with polymer surface. From the view point of energetics, the displacement of ordered water molecules around the surface of pCyDMA will result in an entropic gain, however, teichoic acid and LPS rich in hydrogen bond donor and acceptor atoms will interact poorly if at all with pCyDMA surface deficient in these atoms, which results in an enthalpic penalty and prevention of bacteria attachment Figure 88c.

In the case of pHPhOPA however, its inability to prevent attachment of bacteria requires further investigation. It is true that materials with long flexible chains such as quaternary ammonium compounds prevent surface colonisation thanks to their ability to interpenetrate, disrupt and cause damage to bacterial cell wall. It is also true that for antifouling PEG materials with long chains, compression of long chains by fouling agent leads to entropically unfavourable conformational changes that hinders the fouling process. The ability to tightly bind water molecules is also known to be the antifouling mechanism for materials such as PEG and pHEMA. For pHPhOPA, the oxygen-rich linear chains are more accessible to water molecules and stronger interactions via hydrogen bonds can be formed (Figure 88c). However, the inability of pHPhOPA to prevent attachment of bacteria would suggest that the enthalpic gain from interactions (e.g. hydrogen bonding) of bacteria surface structures (LPS and Teichoic acid) with polymer surfaces compensates the energy penalty for displacing water molecules (Figure 88d), which as a result allows bacteria to bind to surface.

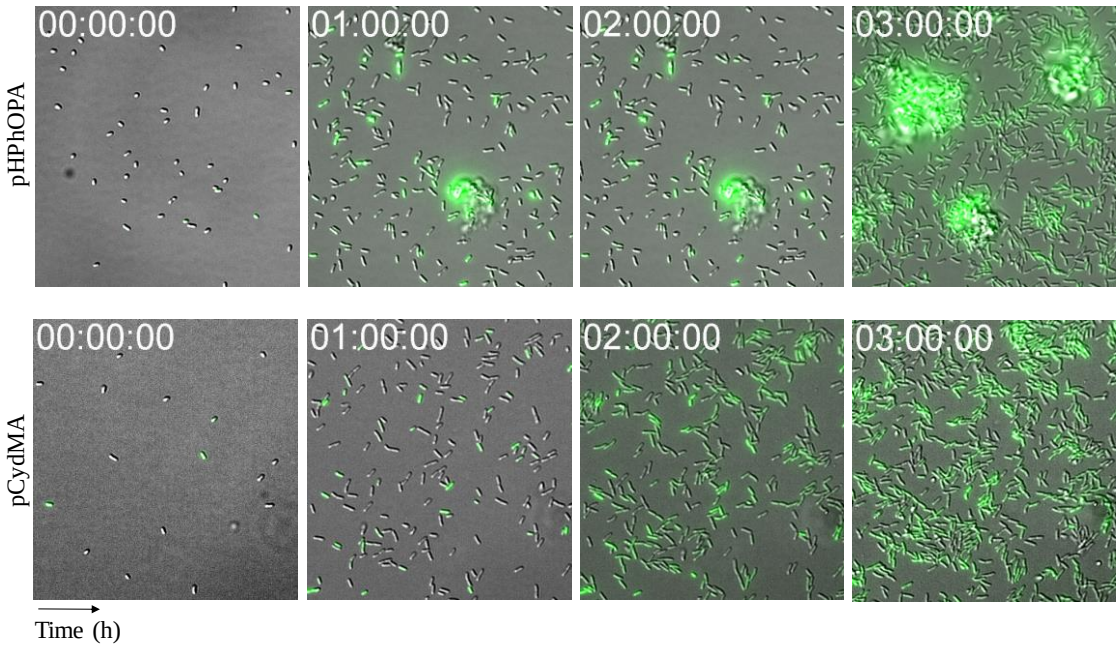

Figure 89. Representative epifluorescence microscopy (40x,1.3) time series images of PAO1-wt cdrA::gfp over the first 3 h of incubation. Image size is 150 x 150 µm. Image from work of Dr. A. Carabelli.

Experimental procedures and data processing to courtesy of Dr. A. Carabelli and Dr. J. Durben, O. Sanni synthesised and prepared polymer samples used in this experiments.

The consequence of bacteria binding to the surface is not limited to biofilm formation alone, other outcomes such as swarming and signal transduction have been investigated. For e.g. a secondary messenger cyclic-di-GMP (c-di-GMP) is known to mediate the switch from reversible to irreversible attachment. High intracellular concentrations of c-di-GMP has been ascribed to regulation of EPS production, enhancement of biofilm formation and inhibition of bacterial motility, although the elicited mechanism is not completely understood [306-309].

By using a cdrA::gfp fusion as a fluorescence biosensor, *A. Carabelli* showed the inability of *P. aeruginosa* cells interacting with pCyDMA to up-regulate c-di-GMP was contrasted markedly with the induction of high levels of fluorescence indicating cyclic diguanylate production of cells on pHPhOPA, see Figure 89. These data suggest that on pCyDMA, *P. aeruginosa* is unable to switch from the reversible to irreversible attachment stage.

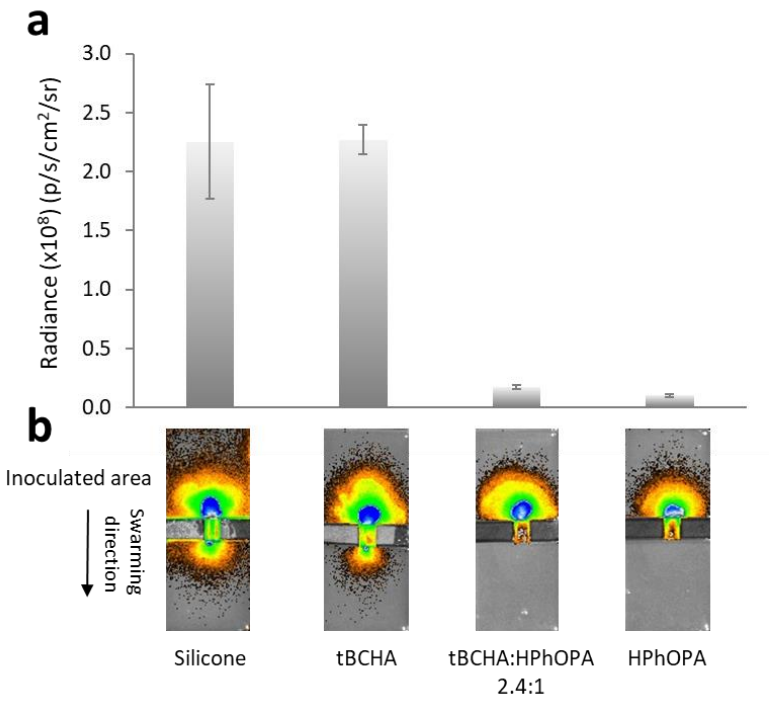

Figure 90. **(a)** Swarming motility of *Pr. mirabilis* 1885 across artificial urine (AU) conditioned silicone catheter bridges coated with tBCHA, HPhOPA or the tBCHA:HPhOPA 2.4:1 copolymer respectively showing a the fluorescence quantified on the surface of the lower agar block. Values are the mean of three parallel experiments, error bars equal ± one standard deviation. **(b)** Fluorescence images of the agar bridge assembly after 16 h migration across AU-conditioned catheter bridges. Bacteria were inoculated onto the upper agar block and the lower block imaged after 16h.

(Image from *Durben et al.*)

In addition to studying the influence of molecular flexibility and hydrophilicity on bacterial biofilm, the consequence of these on swarming motility of bacteria have recently been investigated in an independent work conducted by Durben *et al*., the results of which are summarised and discussed here. To explore the monomer structure function relationship in the context of swarming, a partial least squares regression was performed using molecular descriptors calculated for the eleven monomers used in their experiments. A total of 223 molecular descriptors, including molecular properties, functional group counts, charge, topological and geometrical descriptors, were calculated. The molecular descriptors identified related to hydrophilicity and molecular rigidity, suggesting that both of these molecular properties influence the ability of a given polymer to inhibit swarming. More specifically in their findings was the ability of pHPhOPA (*alpha* value 1.1) to prevent the swarming of *Pr. mirabilis*, as seen in Figure 90, contrasted with the inability of tBCHA (*alpha* value -2.19) to prevent swarming (*Dubern et al. unpublished data*). One may reason that firmly attached

bacteria on surface of pHPhOPA would preferably not swarm, whiles loosely attached (if at all) bacteria on surface of anti-biofilm tBCHA can engage in swarming motility. However, the copolymer of HPhOPA and tBCHA mixed in ratio 2.4:1 (Figure 90) does provide both anti-biofilm and anti-swarming properties, which indicates the prevention of swarming motility by pHPhOPA is not a consequence of immobilised bacterial biofilm on its surface, rather a function of its chemical structure. These findings from Durben *et al*., even if lacking specific data on pCyDMA, can be used as a speculative model to predict that pCyDMA with lowest *alpha* value (-5.49) may lack the ability to prevent bacteria from swarming on its surface.

5.5 Conclusions

- The alpha QSAR model successfully predicted the bacterial biofilm formation on a new polymer (pCyDMA).
- Microarray screening revealed pCyDMA as the best performing homopolymer in preventing attachment from *P*. a*eruginosa* and *Pr. mirabilis.*
- Surface characterisation of polymers firstly indicated surface chemistry to be a good predictor of wettability. Secondly, that aromatic rings have a greater affinity for water compared to aliphatic rings.
- Coating of catheter segments with pCyDMA reduced biofilm formation by 6 commonly associated urinary tract pathogens by an average 32-fold reduction compared to an uncoated silicone catheter and was a 9-fold improvement compared to a commercial silver hydrogel coated catheter.
- pCyDMA coated catheters outperformed our previously identified best polymer (pEGDPEA) determined by experimental screening using a high throughput discovery approach with an average 4-fold improvement.

- Furthermore pCyDMA prevented the formation of dual-species biofilm in artificial urine, exemplifying the uses of the material in a more realistic medical device associated infection scenario.
- Bio-mineralisation on pCyDMA was negligible compared to silicone.

This illustrates how validated QSAR models with simple physical molecular descriptions can be used to predict novel materials that improve on previously established materials that have great potential to reduce medical device associated infections.

Chapter 6 - Investigating Possible Degradation of Pendant Group from Polymer Surface on Biofilm Formation

6.1 Introduction

Recently discovered materials by Hook *et al.* are known to prevent initial adherence of bacteria, but unlike other anti-biofilm approaches, there was no real understanding of mechanistic mode of action. It was however demonstrated through live/dead staining technique that these novel polyacrylates were not bactericidal, thus eliminating the possibility of toxicity from polymer material [89].

It is known that the actual performance of many biomaterials depends largely on their degradation behaviour since the degradation process may affect a range of events, such as cell growth, tissue regeneration, drug release, host response and specific to this application, material's anti-biofilm function. Even though desired in fields of tissue engineering and drug delivery for polymer scaffolds/carriers to degrade into non-toxic physiological components, degradation of polymer materials such as resins for application in dentistry and coatings on surfaces of medical devices remains an unwanted outcome [310, 311].

To guard against mechanical degradation due to wear and tear for polymers with anti-biofilm properties, Adlington *et al.* copolymerised novel antibiolfilm material (EGDPEA) with plasticiser. The flexibility of resultant copolymer was tuned such that it passed the flexing fatigue test when coated upon catheters, a test the homopolymer failed [312].

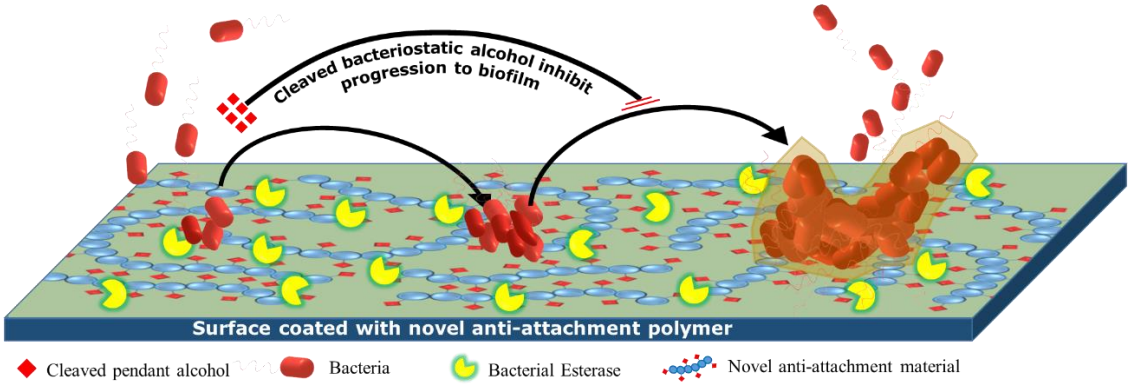

Figure 91. Schematic of hypothetical enzymatic degradation of pendant group from novel polyacrylate materials with anti-biofilm properties.

While degradation caused from mechanical stress is currently controlled and avoidable, biodegradation of novel anti-biofilm poly(acrylate) materials facilitated by esterase enzymes has long been a moot point [311]. Apart from unwanted potential loss of functional material from biodegraded surfaces of medical device, a new hypothesis for mechanistic mode of action of these novel poly(acrylate) materials can be generated. That is, esterase enzymes able to de-esterify chemical bonds of poly(acrylate) materials coated onto biomedical surfaces may release toxic compounds and toxic residues for bacteria (Figure 91).

In this chapter, we investigated the effect of quick acting porcine liver esterase (PLE) on a suitable anti-biofilm methacrylate polymer selected from expanded library of compounds.

6.1.1 Aims & Objectives

The aim of this chapter was to test the action of porcine liver esterase on novel materials that prevent biofilm formation. The objectives were as follows:

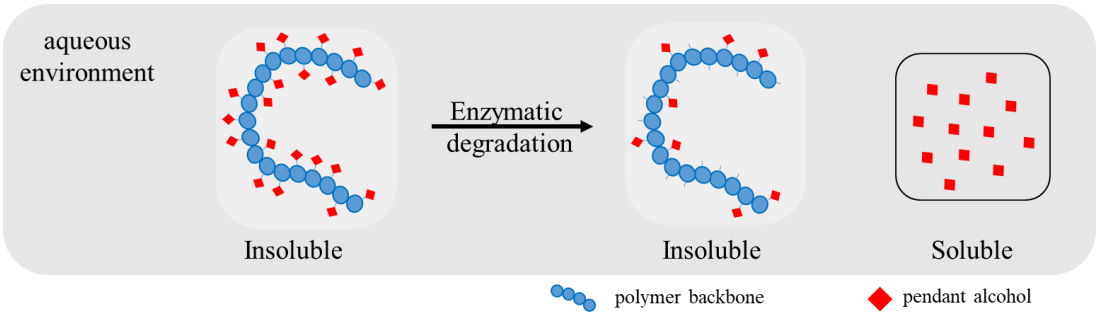

Figure 92. Schematic representation for enzymatic degradation of polymer in aqueous environment. A water soluble pendant alcohol can be quantified by UV.

1. Identify candidate material to be tested with porcine liver esterase whose pendant component is water soluble and detectable by UV-visible spectroscopy (Figure 92).
2. Build calibration curves with different concentrations of pendant alcohol.
3. Test toxicity of pendant group to growth of *P. aeruginosa.*
4. Carry out enzymatic assay on selected monomer and polymer.

6.2 Experimental

6.2.1 Materials

Chemicals were used as supplied by Sigma-Aldrich unless otherwise stated. Benzyl methacrylate (BnMA), benzyl alcohol (BnOH), methacrylic acid (MAA), porcine liver esterase (PLE), lysogen broth (LB), RPMI 1640 without phenol red, phosphate buffered saline (PBS) tablets.

Gel permeation chromatography (GPC) was carried out using the GPC Systems model PL GPC50 as manufactured by Polymers Labs (now Agilent), fitted with differential refractive index and variable wavelength UV detectors and PL AS-RT autosampler. Molecular weight and weight distribution of sample was calculated by comparing to polystyrene as standard.

Nuclear magnetic resonance (NMR) spectroscopy was carried out on the Bruker DPX400 UltraShield^{TM}, model 1mm TX1. Chemical shifts are reported in part per million (ppm) δ units downfield from internal tetramethylsilane (TMS) or from –OD signal of deuterated solvent.

6.2.2 Identification of Candidate Material

6.2.2.1 Printing Polymer Microarray

Microarray printing was carried out under an argon atmosphere at O_2 < 2000 ppm, 27 °C and 30% relative humidity. Contact printed polymer microarrays were formed using a XYZ3200 pin printing workstation (Biodot). Slotted metal pins (946MP6B, Arrayit), each with a tip diameter of 220 mm were used to transfer approximately 2.4 nL of polymerization solution onto pHEMA coated substrates before slides were irradiated with a long wave UV (365 nm) source for 1 minute, resulting in an average polymer spot size of 435 μm. Each printed microarray slide had three replicates separated by 20 mm. Spots within array were printed adopting an isometric pattern that increased spot density per square area, each spot was

separated by 1.5 mm in both X and Y directions. The freshly printed arrays with 283 materials (Appendix G) were vacuum extracted at < 50mTorr for 1 week to remove un-polymerised monomer and solvent.

6.2.2.2 Incubation with *P. aeruginosa*

Microarray slides were UV sterilized for 10 mins and inoculated (OD_{600} = 0.01) with *mcherry* tagged *P. aeruginosa* O1 in 10 mL of standard RPMI medium in a 4-well polystyrene dish and incubated for 24 h at 37 ˚C at 60 rpm shaking. Control slides were also incubated under the same conditions without bacteria. After incubation, slides were twice rinsed with phosphate-buffered saline at room temperature for 5 min and then with distilled water for 5 min. Fluorescence images were then acquired for both control and treated slides using a GenePix Autoloader 4200AL (Molecular Devices, US) scanner. The limit of detection (LOD) formula reported in section 4.3.3 was applied prior to data analysis and 59 samples of the 283 tested were eliminated (Appendix G).

6.2.3 Thermal Polymerization of Benzyl Methacrylate

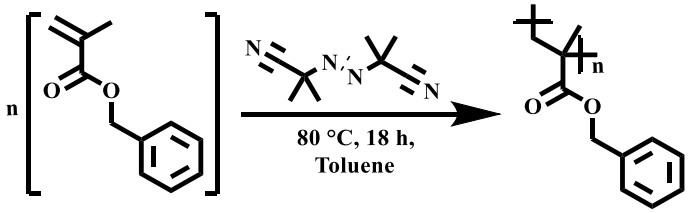

Figure 93. Thermal polymerisation of benzyl methacrylate monomer with AIBN.

In brief, 40 mg (0.73 mmol) of azobisisobutyronitrile (AIBN) together with 16 mg PhCoBF was added to 31.2 g of Benzyl methacrylate (177.06 mmol) dissolved in 60 mL of Toluene in a 500 mL test tube. The mixture was degassed for 30 minutes and left in oil bath at 80 ºC for 18 hours. Polymerisation was stopped by exposing to air and cooling on ice. The polymer was then precipitated dropwise in 4 x 120 mL hexane and left to dry in a vacuum oven at 70 ºC.

6.2.4 Toxicity Assay of Benzyl Alcohol on *P. aeruginosa*

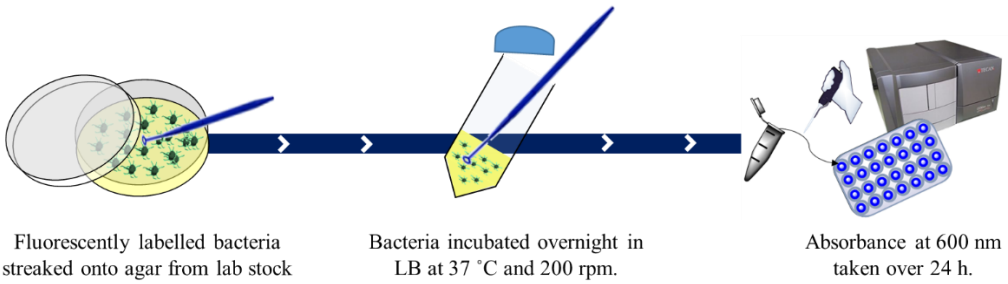

Figure 94. Schematic of experimental procedure for toxicity assay of Benzyl alcohol.

An overnight primary culture of *P. aeruginosa* strain PAO1, grown in 10 mL LB at 37 °C and 60 rpm, was standardized to an OD_{600} of 0.01 in 8 mL LB. In autoclaved Eppendorf vials, seven 1 mL solutions of benzyl alcohol dissolved in PBS with concentrations starting at 9.25 mM with stepwise increase of 0.5 mM until reaching 36.99 mM were prepared. Solutions were then diluted a hundred times in LB standardized at an OD_{600} 0.01 and a volume of 200 µl transferred into test wells of a 96-well plate in triplicates. Optical density at 600 nm was measured every 30 minutes over 24 h at 37 °C in Tecan Genios Fluo instrument under static conditions.

6.2.5 UV Calibration Curves

Ten tablets of phosphate buffered saline from sigma Aldrich were dissolved in 2 L of de-ionised water to yield 0.01 M phosphate buffer, 0.0027 M potassium chloride and 0.137 M sodium chloride, pH 7.4 at 25 °C.

Two 50 mL stock solutions of lyophilised porcine liver esterase (PLE) E3019-3.5KU were prepared by dissolving 27.8 mg of PLE in 50 mL PBS, equivalent to 10 units/mL. One unit of PLE will hydrolyse 1.0 µmole of ethyl butyric acid and ethanol per minute at pH 8.0 at 25 °C. PLE solution was filtered with 0.22 µm syringe filter to remove particulates and stored at -20 °C before use.

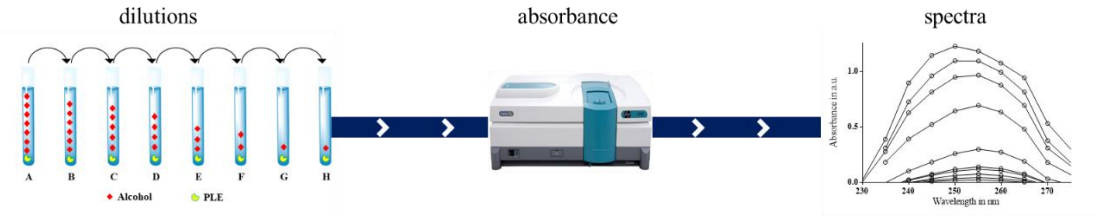

Figure 95. Schematic of procedure followed to obtain calibration curves. The absorbance for multiple solutions with different concentrations of UV active substance was determined and absorbance spectra constructed.

Calibration curve for benzyl alcohol. Five stock solutions of benzyl alcohol (BnOH) dissolved in 10units/mL PLE in PBS were prepared: A (9.25 mM), B (7.40 mM), C (5.55 mM), D (3.70 mM) and E (1.85 mM). These were further diluted in factors of ten till 18 solutions with concentrations ranging from 92.5 nM to 9.25 mM were obtained. The UV absorbance spectrum for 300 µL of each solution of BnOH in 10units/mL PLE dissolved in PBS was obtained by taking measurements in ascending order in a 370 µL glass cuvette with Varian Cary 50 Bio UV-VIS spectrophotometer in the wavelength range of 200 – 800 nm. Blank sample was 10 units/mL PLE in PBS.

Calibration curve for benzyl alcohol and methacrylic acid. Five stock solutions of methacrylic acid (MAA) and BnOH dissolved in 10units/mL PLE in PBS were prepared: A (11.62 / 9.25 mM MA/BA), B (9.29 / 7.40 mM MA/BA), C (6.97 / 5.55 mM MA/BA), D (4.65 / 3.70 mM MA/BA) and E (2.32 / 1.85 mM MA/BA). These were further diluted in factors of ten till 18 solutions with concentrations ranging from 92.5 nM to 11.62 mM were obtained. The UV absorbance spectrum for 300 µL of each solution of BnOH and MA in 10units/mL PLE in PBS was acquired by taking measurements in ascending order in a 370 µL glass cuvette with Varian Cary 50 Bio UV-VIS spectrophotometer in the wavelength range of 200 – 800 nm: blank sample was 10 units/mL PLE in PBS.

The limit of detection for both systems was calculated using Equation 12 below:

$$LOD = \frac{3.3(\sigma)}{m}$$

Equation 12. Equation for calculating limit of detection. Where σ is standard deviation of y-intercept from calibration curve and m is gradient of calibration curve.

6.2.6 Incubation of pBnMA with Porcine Liver Esterase

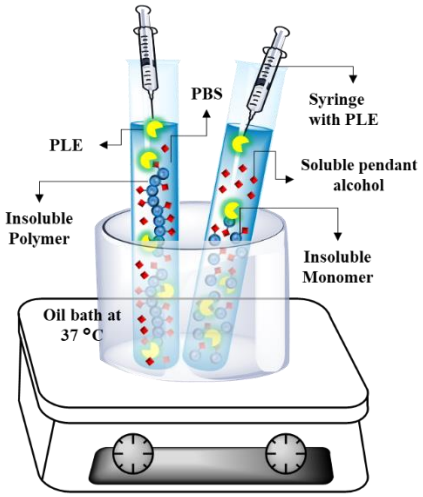

Figure 96. Experimental setup used to incubate polymer with porcine liver esterase.

Three separate test tubes, one with solid pBnMA (10 mg) insoluble in PBS, a second with BnMA (80 mg, 78.43 µL) also insoluble in PBS and a third with no substrate were brought to 37 °C in an oil bath and each infused with 8 mL of 10 units/mL porcine liver esterase dissolved in PBS. Two other test tubes with pBnMA (80 mg) and BnMA (80 mg, 78.43 µL) respectively were infused with PBS only and also brought to 37 °C in an oil bath.

Using a timer and 1 mL syringe, 400 µL aliquots were drawn out every 2 mins for first 16 mins, which increased to 15 mins interval thereafter until reaching 120 mins. Aliquots were filtered with 0.22 µm syringe filter into 0.5 mL Eppendorf vials and kept at – 4 °C until UV absorbance at 255 nm was measured in glass cuvettes with Varian Cary 50 Bio UV-VIS spectrophotometer. Maximum time elapsed between obtaining UV measurements for aliquots and drawing out samples was 20 min. The absorbance value at 255 nm for each time point was used to interpolate concentration in µg/mL from BnOH calibration curve and MAA/BnOH calibration curve

accordingly. Values were then expressed as percentage of starting mass or percentage degradation and plotted versus time.

6.3 Results

6.3.1 Identification of UV Active Material Capable of Preventing Attachment of *P. aeruginosa*

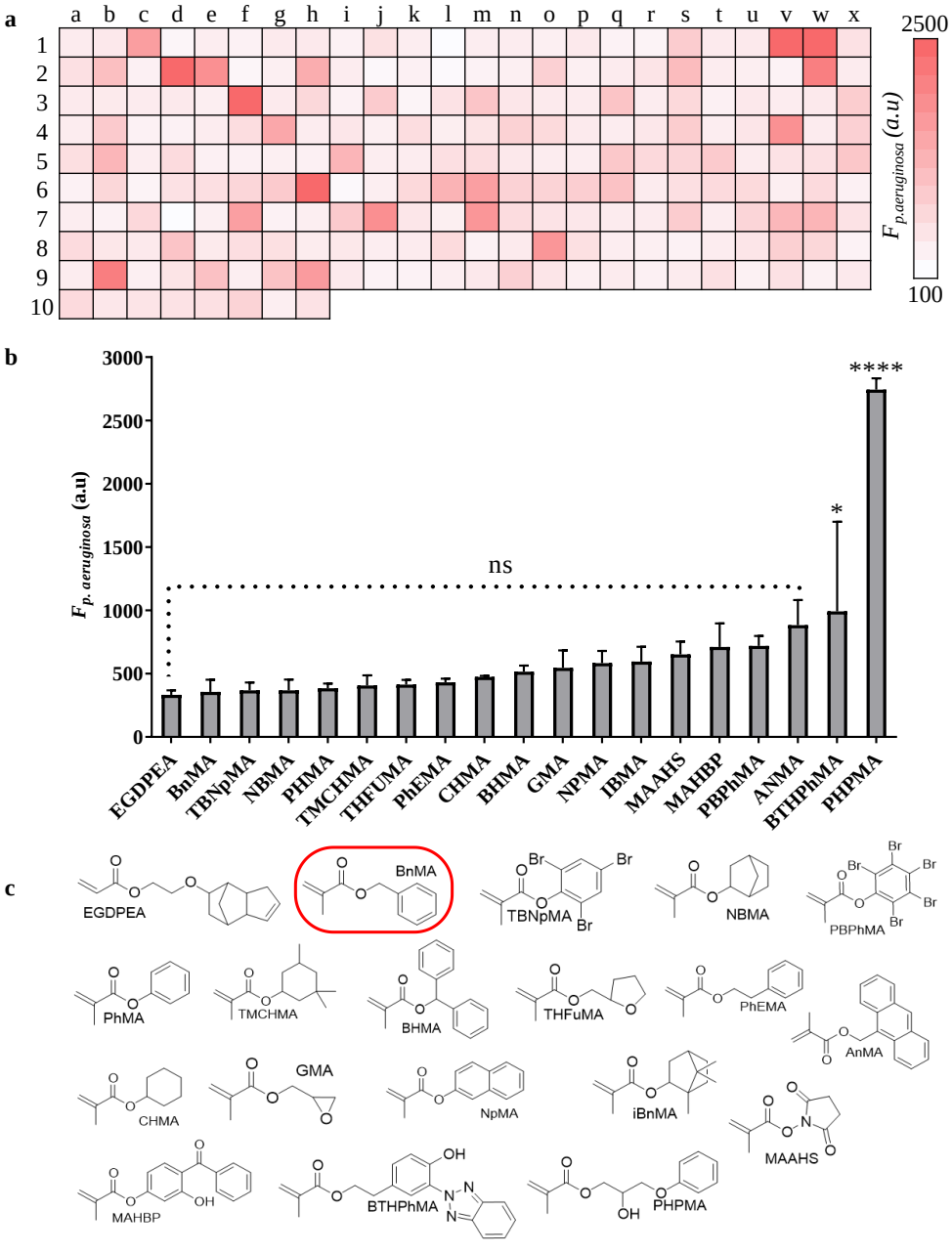

Figure 97. Summary of results from screening polymer microarray with *P. aeruginosa*. **(a)** Intensity map showing fluorescence value after background subtraction ($F_{p.aeruginosa}$) for 224 materials (Appendix J) incubated for 24 h with *P. aeruginosa* in RPMI. Each square represents the mean fluorescence value (N = 3). Labels on y and x axes provide unique identification for each material. **(b)** Rank order plot showing attachment of *P. aeruginosa* on meth(acrylates) materials with cyclic pendant groups. Acrylate EGDPEA included as control. All significances were carried out using one-way ANOVA test, *p < 0.05, ****p < 01 **(c)** Chemical structure for materials in (b).

To find an anti-biofilm material with a UV active and water soluble pendant group, an expanded library of 283 materials inclusive of all 126 materials previously tested by Hook *et al.* was screened against *P. aeruginosa.* The results are displayed in Figure 97a with an intensity plot where materials that exhibited high bacterial attachment are colour coded red and materials that exhibited a low bacteria attachment are colour coded white.

The selection window was narrowed down to 18 materials based on previous findings that methacrylate materials with cyclic pendant groups were generally better at resisting bacterial attachment [122]. In Figure 97b is displayed the performance of 18 methacrylate materials with cyclic pendant group together with a negative control, pEGDPEA and a positive control, pHPhOPMA both reported in literature to respectively resist and promote bacteria biofilms [89]. These controls performed as predicted with very low bacterial attachment value for pEGDPEA and very high for pHPhOPMA.

Polymer of benzyl methacrylate (pBnMA) showed reduced bacteria attachment comparable to that of pEGDPEA and had previously been reported to exhibit broad spectrum anti-attachment resistance to pathogens including *E. coli, S. aureus* and *P. aeruginosa* [196].

For a suitable polymer to be tested, a good biological performance alone was not sufficient, it was essential for its pendant group to be both soluble in water and UV active. The polymer of BnMA is insoluble in water and its pendant benzyl alcohol (BnOH) is both soluble in water and UV active with contribution from aromatic ring [313]. These biological and physicochemical properties of pBnMA made it a suitable candidate to be tested with porcine liver esterase.

6.3.2 Breakdown Compounds of pBnMA

To test the hypothesis of enzymatic degradation, the toxicity on bacteria for BnOH and poly(methacrylic acid) (that is pMAA) which are both potential degradation products for pBnMA must be assessed.

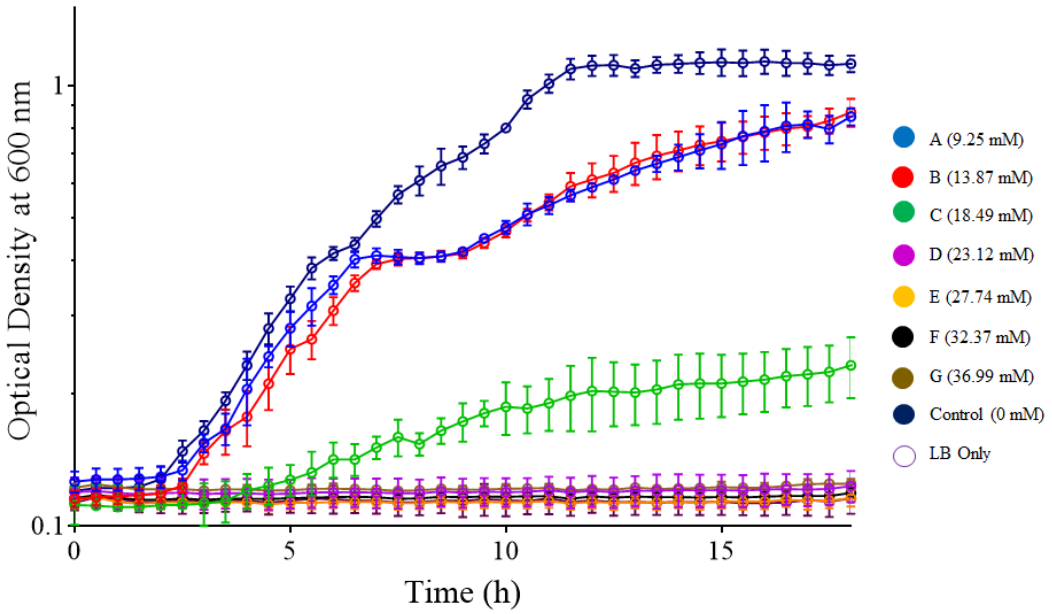

Figure 98. Growth curve of *P. aeruginosa* PAO1 incubated at 37 °C for 24 h. Error bars 1 SD, n = 3 biological replicates. ●Control, ●-A (9.25 mM), ●-B (13.87 mM), ●-C (18.49 mM), ●-D (23.13 mM), ●-E (27.74 mM), ●-F (32.37 mM), ●-G (36.99 mM) and ○- LB Only.

The toxicity of potentially cleaved benzyl alcohol was conducted as reported in section 6.2.4. In Figure 98 is the growth of PAO1 over 18 hours systematically dosed with different concentrations of BnOH. PAO1 grown in LB with no BnOH showed healthy growth over 18 h with 2.5 h in lag phase, 8 h in log and reaching stationary phase after 12 h.

PAO1 dosed with 9.25 mM and 13.37 mM of BnOH showed no differences to control in the lag and log phase, a 2 hour delayed growth was however observed at time point 7.5 h, which indicated slower growth compared to control at these concentrations of BnOH.

The bacteriostatic effect of BnOH was evident at 18.49 mM concentrations with very little growth observed after 18 h. There was a total inhibition of PAO1 growth at concentrations beyond 18.49 mM.

Results from this experiment showed that an enzymatic cleavage of polymer pendant alcohol could potentially prevent or disrupt bacteria biofilms, inhibit bacteria growth and leave them in vulnerable planktonic state where host immune cells can act in greater numbers.

It is also known from literature that BnOH is a well-established antiseptic commonly used as an antibacterial agent in a variety of formulations, including bacteriostatic sodium chloride and bacteriostatic water that are intended for intravenous administration [314]. It is used as an antiseptic at 1% w/v in parenteral formulations and reported to be bacteriostatic at 0.2% w/v [315].

Furthermore, the ability of aromatic alcohols to promote growth inhibition, lethal effect and cytological damage in Gram-negative bacteria was reported by *Lucchini et al*. where they suggested the lipophilic properties of these compound played a role in their toxicity and more specifically were able to inhibit protein synthesis [316]. These results were recently corroborated by *Simm et al*. with findings that BnOH induced a reversible fragmentation of the Golgi apparatus and acts as a membrane fluidising agent [317].

Cleavage of BnOH off pBnMA also results in formation p(MAA-co-BnMA) in ratios dependent on activity of esterase enzyme. In 2014, *Gratzl et al*. published a work that revealed the antimicrobial activity of poly(acrylic acid) (that is pAA) block copolymers on *S. aureus, E. Coli* and *P. aeruginosa* pathogens. Copolymers with pAA contents less than 22% exhibited no observable antimicrobial activity whilst those with pAA content over 40% were highly bactericidal and killed all bacteria within 3 h [318]. They concluded antimicrobial activity

depended solely on acrylic acid content, independent of the block copolymer partner polystyrene or poly(methyl methacrylate) used in their studies.

It is reasonable to conclude that in a scenario where pBnMA is cleaved by esterase enzymes, the release of bacteriostatic BnOH and bactericidal pMAA would partly explain the mechanistic mode of action for novel poly(acrylates).

6.3.3 Calibration Curves

Two different calibration curves were constructed, one to quantify the water soluble degradation product of pBnMA that is BnOH and the second to quantify water soluble degradation products of BnMA monomer, which are BnOH and methacrylic acid (MAA) (Figure 99a).

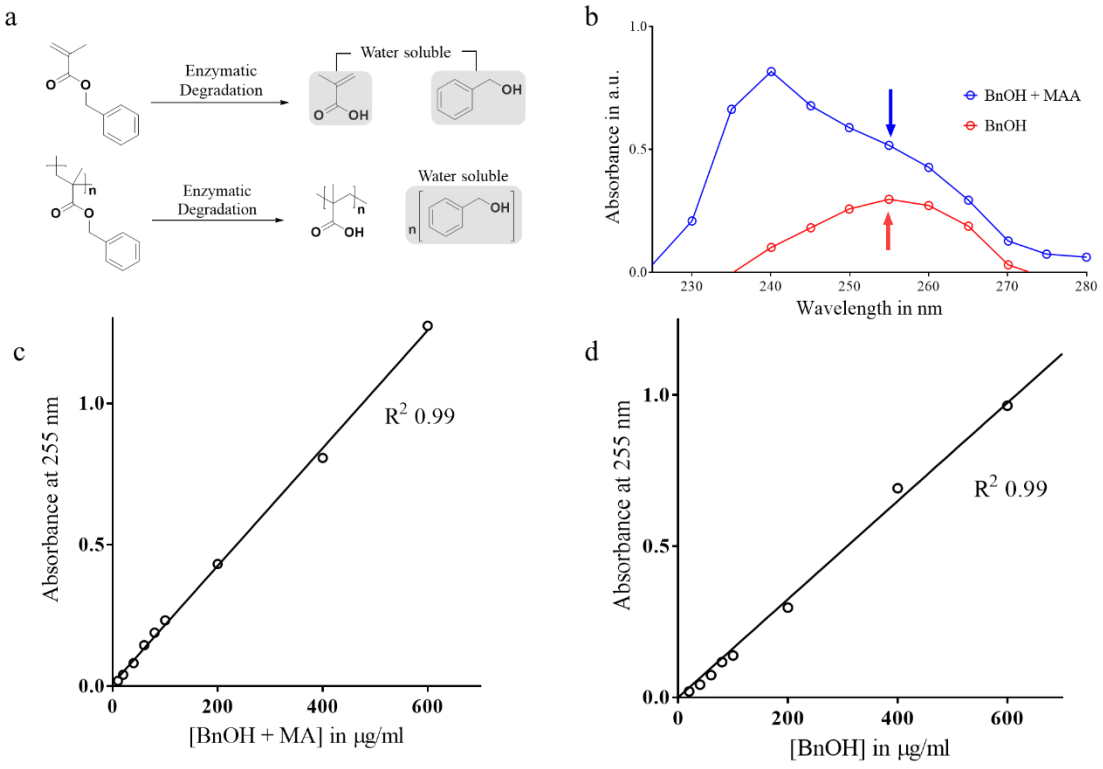

Figure 99. **(a)** Scheme of enzymatic degradation products for pBnMA and BnMA. Water soluble products are shaded in grey. **(b)** UV absorbance spectrum (225 – 280 nm) for BnOH (1.85 mM) in red and co-solutions of 2.32 mM MAA + 1.85 mM BnOH in blue. Arrows at 255 nm indicate wavelength used for calibration curves. **(c)** Absorbance at 255 nm for different concentrations of BnOH + MAA. Each data point is mean ±1 s.d. N=3. **(d)** Same convention as (c) for BnOH.

Coloured with red in Figure 99b is the absorbance spectrum for BnOH with an absorption maximum (λ_{max}) at 255 nm due to aromatic ring. The co-solutions of BnOH and MAA coloured in blue showed maximum absorption at 240 nm.

Calibration curves in Figure 99d were constructed by measuring absorbance at 255 nm for each sample at various concentrations. Concentrations below 10 µg/mL gave inconsistent readings over experimental repeats and limit of detection (lod) for these experiments was set at 40 µg/mL (400 ppm) following Equation 12 reported in experimental section 6.2.5. Concentrations greater than 10 µg/mL followed a linear trend for the two sets of calibration curves, both with R^2 values of 0.99.

The λ_{max} of BnOH at 255 nm (Figure 99b) agreed with values reported in literature and for co-solutions of BnOH and MAA, λ_{max} was at 240 nm. The absorbance spectrum for MAA only has a reported λ_{max} at 220 nm in literature [313]. It is thought that the presence of MAA broadens the absorbance spectrum of BnOH which in turn causes a red shift for λ_{max} of MAA, from 220 nm to 240 nm.

6.3.4 Thermal Polymerisation of BnMA

BnMA was thermally polymerised following methods reported in section 6.2.3 and its molecular weight and polydispersity are reported in Appendix F. The thermal polymerisation approach was preferred in this experiment firstly to avoid absorbance at 255 nm from DMPA photo-initiator used during UV radical polymerisation, secondly to obtain pure and monomer free pBnMA achieved through multiple rounds of precipitation. The NMR spectra for purified samples of pBnMA used in this experiments are reported in Appendix M.

6.3.5 Summary of Optimisation with Porcine Liver Esterase

To select an appropriate esterase enzyme for use in this work, we considered possible sources of esterases in urinary tract. The renal tissue is the main source of most enzymes in the urine, such as alkaline phosphatases, peptidases, beta-galactosidase and lactate dehydrogenases. Other potential sources of esterase enzymes include: blood plasma with cholinesterases, carboxylesterases and arylesterases. Blood cells such as leukocytes are also responsible for increased levels of leukocyte esterase in urine during inflammation. However, the presence of these enzymes in urine only occur in pathological states of increased glomerular filtration due to diseases of the kidney [319-322].

Infection of the urinary tract by bacteria such as *P. aeruginosa* can be another source of esterase enzymes. Several lipolytic enzymes are secreted by *P. aeruginosa*, including the esterase EstA, which is an autotransporter protein located in the outer membrane involved in rhamnolipid production (see 1.4.2). It plays a role in the biofilm structure by maintaining fluid channels and the detachment of cells from mature biofilm communities [323, 324]. Studies from protein sequence analysis have revealed that the active site of EstA enzyme has a catalytic triad composed of serine, histidine and aspartate [325, 326].

The cost for purifying EstA to conduct *in vitro* enzymatic assays can be considerably reduced by using cheaper, commercially available enzymes with same mechanism of action to EstA. Hence, the use of porcine liver esterase in this work. PLE is a quick acting enzyme with a catalytic triad of serine, histidine and aspartate. Histidine together with other aromatic amino acids absorb UV light at wavelength between 270 – 280 nm and could interfere with absorbance of BnOH at 255 nm [327].

A possible solution was to precipitate PLE with trichloroacetic acid (TCA) from samples prior to UV measurements, which typically involves two steps. Firstly, precipitation with TCA and

secondly extraction of TCA traces with solvents capable of solubilizing samples. Such approach would lead to sample loss and also unreliable absorbance measurements [328]. An alternative solution was to use ultrafiltration methods to filter PLE (168 kDa). This approach is however expensive, lengthy and often labour-demanding technique to separate PLE from very small aliquots. Consequently a solution of PLE dissolved in PBS was used as blank sample for UV readings. The stability of PLE, pBnMA and BnMA dissolved in PBS and incubated at 37 °C was studied for 6 days.

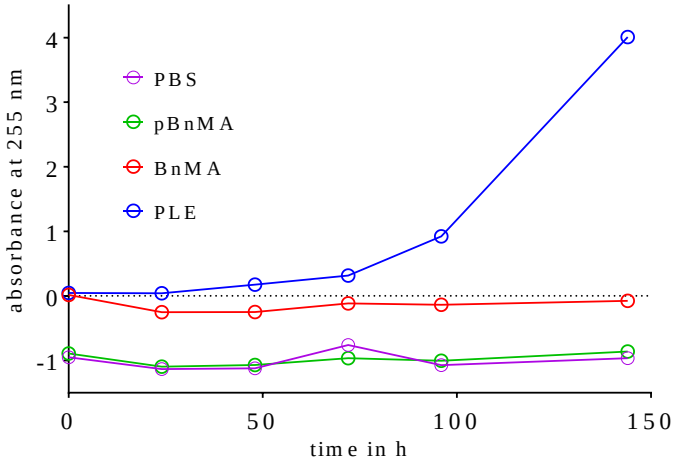

Figure 100. Changes in absorbance (255 nm) for solutions of pBnMA, BnMA and PLE dissolved in PBS over 144 hours at 37 °C. Blank sample is a solution of PLE dissolved in PBS. Dotted line y = 0 is kept as guide. Each point is mean ± 1sd, n = 3.

In Figure 100, a solution of PBS alone gave readings below the zero baseline (PLE dissolved in PBS) over a period of six days, which indicated PLE enzyme absorbed at 255 nm as expected due to aromatic amino acids. Negative readings were also recorded for pBnMA in PBS which in turn showed the insolubility of pBnMA in PBS.

The monomer of BnMA also displayed constant readings below the baseline for six days. Its less negative absorbance value compared to PBS suggested trace amounts of solubilized BnMA below LOD of 400 ppm. This is in line with reported poor solubility for BnMA, estimated at 390 ppm in water at 75 °C [329].

UV absorbance for PLE enzyme is seen to be stable at baseline for first 24 hours after which an increased absorbance at 255 nm is measured. After 96 hours, the PLE enzyme had aggregated/denatured and solution turned cloudy/white. Since pH of solution remained unaltered at 7.4, we clarified that prolonged exposure to 37 °C caused conformational changes in PLE enzyme.

These stability studies revealed PLE could be used in experimental procedures for up 24 hours and remain stable.

6.3.6 Effect of Porcine Liver Esterase on BnMA and pBnMA

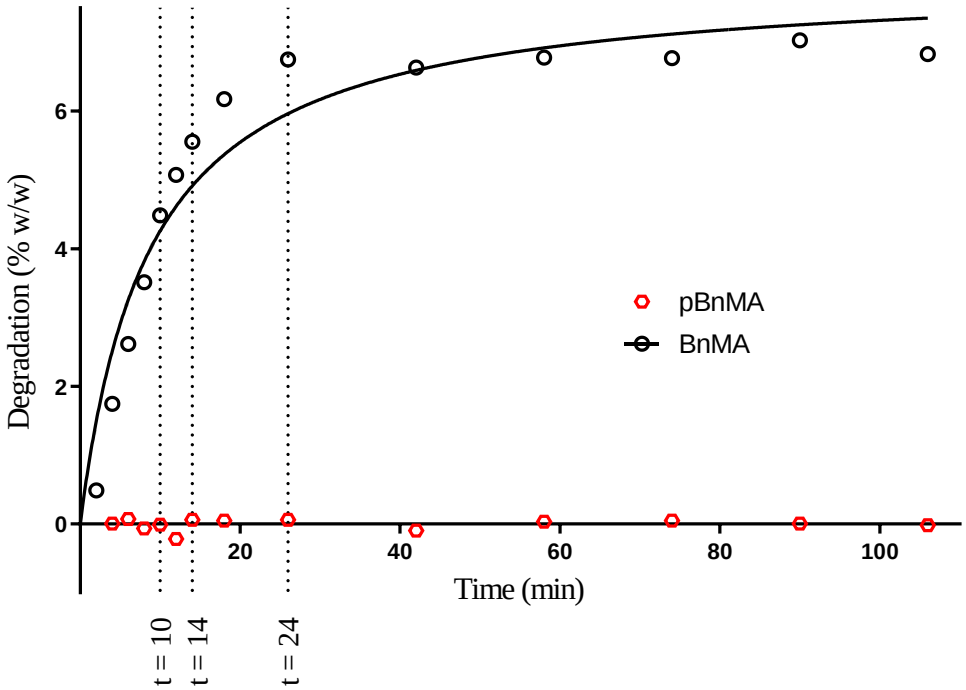

Figure 101. Degradation of BnMA (in black) and pBnMA (in red) by PLE over 120 minutes at 37 °C. Degradation reported as percentage of starting materials. Each data point is mean ± 1 s.d, n = 3. Non-linear fit (black solid line) for degradation of BnMA, $R^2 = 0.92$.

The effect of PLE on BnMA monomer compared to pBnMA is strikingly different (Figure 101). The degradation profile for BnMA indicated over 6% (w/w) was degraded within 25 minutes at different rates. In first 10 minutes the degradation rate by PLE was 44.85 µg/min and reduced to 26.75 µg/min in subsequent 4 minutes. The lowest rate of 10 µg/min was observed between 14 – 24 minutes. Degradation of BnMA plateaued after 25 minutes with a corresponding change

in colour of solution from clear to cloudy due to enzyme aggregation/denaturation. Since the stability of PLE at 37 °C for at least 24 hour was previously demonstrated in section 6.3.4, it was reasoned that the presence of MAA (0.06% w/v) in solution as degraded product of BnMA is causative of PLE denaturation. A finding that was confirmed with a measured change in pH from 7.4 (at t = 0 mins) to 4.3 (at t = 25 mins).

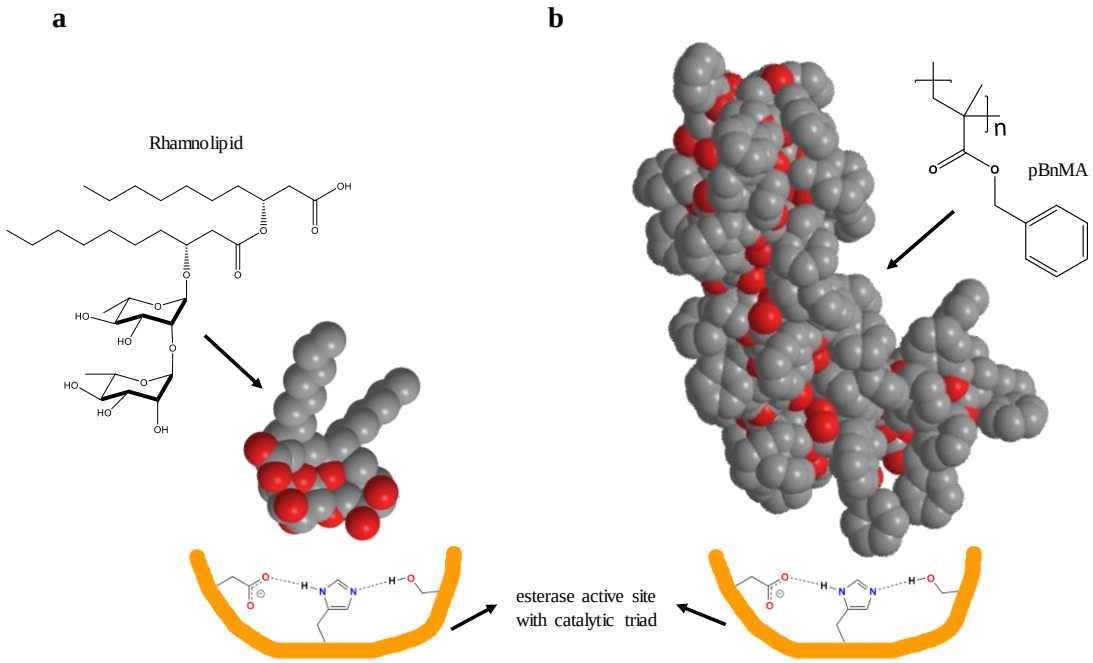

Figure 102. Schematic representative of active site for PAO1 EstA enzyme with catalytic triad aspartate, histidine and serine. **(a)** Rhamnolipid substrate (3D model from ChemDraw) approaching esterase. **(b)** pBnMA substrate (3D model from ChemDraw) approaching enzyme.

In contrast, the amount of BnOH degraded from pBnMA was either below the limit of detection (400 ppm) or no benzyl alcohol was cleaved off from pBnMA over 2 hours and this despite the quick onset of action of PLE. The absorbance measured at 255 nm constantly aligned with baseline. It is thought that, in contrast to accessible ester groups on rhamnolipids (see Figure 102a), the increased steric hindrance from benzyl groups on the exterior surface of pBnMA makes the ester functionality inaccessible to active site of enzyme and prevents cleavage (Figure 102b)

6.4 Conclusions

- High throughput screening of expanded library of materials confirmed anti-biofilm performance of pBnMA comparable to that of pEGDPEA.
- The potential breakdown alcohol product of pBnMA was shown to be toxic to *P. aeruginosa* at concentrations greater 18 mM.
- PLE cleaved over 6% BnMA monomer in less than 30 minutes. Despite quick onset of action from PLE, the amount of BnOH degraded from pBnMA was either below the lod of 400 ppm or no benzyl alcohol was cleaved off from pBnMA.
- It is strongly believed that the mechanistic mode of action of these novel materials is very reliant on intrinsic surface chemistry with no evidence to suggest the involvement of degradation products from action of esterase enzymes.

Chapter 7 - Conclusions and Future Work

7.1 Summary

The aim of this project was to identify the mechanism of action for novel antibiofilm polymers discovered by Hook *et al.* currently undergoing clinical trials [330]. This was considered fundamental knowledge necessary to guide the rational design of novel materials capable of instructing biological response beyond the chemical space investigated to date.

In chapter 3, we set out to investigate the very early stages of biofilm formation and determine composition of the adsorbed layer formed on two polymers (pEGDPEA and pNGPDA) that exhibited different biofilm formation using ToF-SIMS and XPS. Our results showed that anti-biofilm pEGDPEA presented with greater adsorption of amino acid nutrients on its surface when exposed to the simple protein free biological media (RPMI), whilst pNGPDA showed a significantly reduced adsorption. Adsorption isotherm models fitted to better understand phenomenon on both surfaces revealed anti-biofilm pEGDPEA intrinsically possessed greater adsorbent capacity compared to pNGPDA, and surface adsorbed nutrients on pEGDPEA were less likely to desorb. We identified that the greater fraction of twitching PAO1 cells on pEGDPEA compared to pNGPDA was dependent on abundance of surface adsorbed nutrients. Furthermore, results from biofilm assays with PAO1 carried out at different nutrient conditions confirmed nutrient-deficient pNGPDA surface promoted biofilm formation whilst nutrient-rich pEGDPEA surface prevented biofilm formation.

In chapter 4, we adopted a modification of the ninhydrin-stain for amino acids on surfaces which allowed us to simultaneously quantify in high throughput manner the adsorption of amino acids onto surfaces of 281 polymers in a microarray. The results from the microarray firstly corroborated previous findings of greater amount of nutrients being adsorbed onto surface of pEGDPEA compared to pNGPDA. A simple rank order analysis revealed monomers

with repeating units of ethylene glycol, hydroxyl or cyclic groups in monomer chemical structure presented with greater amount of adsorbed nutrients. Whilst monomers with diacrylates functionality, fluorine atom or short hydrocarbon chains exhibited low nutrient adsorption. PLS regression models constructed using secondary ions generated by SIMS for 141 polymer materials confirmed monomers with bulky cyclic ring moieties such as found in EGDPEA were major contributors to increased adsorption of amino acids on surfaces. The moieties identified here were similar to those previously reported in literature to reduce bacteria attachment.

In chapter 5, we illustrated how validated QSAR models with simple physical molecular descriptions can be used to predict novel materials that improve on previously established materials that have great potential to reduce medical device associated infections. The alpha QSAR model successfully predicted the bacterial biofilm formation on a new polymer (pCyDMA). Microarray screening revealed pCyDMA as the best performing homopolymer in preventing attachment from *P. aeruginosa* and *Pr. mirabilis*. Catheter segments coated with pCyDMA reduced biofilm formation by 6 commonly associated urinary tract pathogens by an average 32-fold reduction compared to an uncoated silicone catheter with a 9-fold improvement compared to a commercially available silver hydrogel coated catheter.

In chapter 6, we investigated the possible degradation of pendant group from polymer surface on biofilm formation. High throughput screening of an expanded library of materials was used to identify anti-biofilm pBnMA as material to be tested with comparable performance to that of pEGDPEA. The alcohol breakdown product of pBnMA was shown to be toxic to *P. aeruginosa* at concentrations greater 18 mM. We demonstrated PLE cleaved over 6% BnMA monomer in less than 30 minutes and despite quick onset of action from PLE, the amount of BnOH degraded from pBnMA was either below the LOD of 400 ppm or no benzyl alcohol was cleaved off from polymerised BnMA.

7.2 Future Work

A natural progression for this work will be to carry out a subcutaneous foreign body infection model *in vivo* to test the performance of pCyDMA predicted from *alpha* model as capable of preventing attachment of PAO1 and proven to inhibit biofilm formation from five clinically relevant bacterial species. The alpha model was initially constructed using data obtained from PAO1 long appreciated by investigators for its biofilm formation and here validated with *Pr. mirabilis* and PAO1. It will be interesting to see a model constructed using data obtained from other species with the aim to validate with PAO1.

Our investigation of nutrient deposition onto two polymer surfaces that exhibit different capabilities in preventing biofilm formation was a first step towards understanding what chemical compounds bacteria encounter upon reaching polymer surfaces in the very early stages of biofilm formation. The approach of studying the adsorption phenomena with the exclusion of bacteria in this project was deemed relevant and proven effective in eliminating complexities brought about from biological processes, for example, exopolysaccharide, DNA and lipid secretion by bacteria or utilization of amino acids adsorbed on the surface. It is however possible to circumvent or reduce the dimension of such complexities by tracking adsorption of exogenously labelled amino acids (^{13}C or ^{2}H) adsorbed onto surfaces of polymers even in the presence of bacteria.

Appendices

Appendix A - Components of Incubating Media

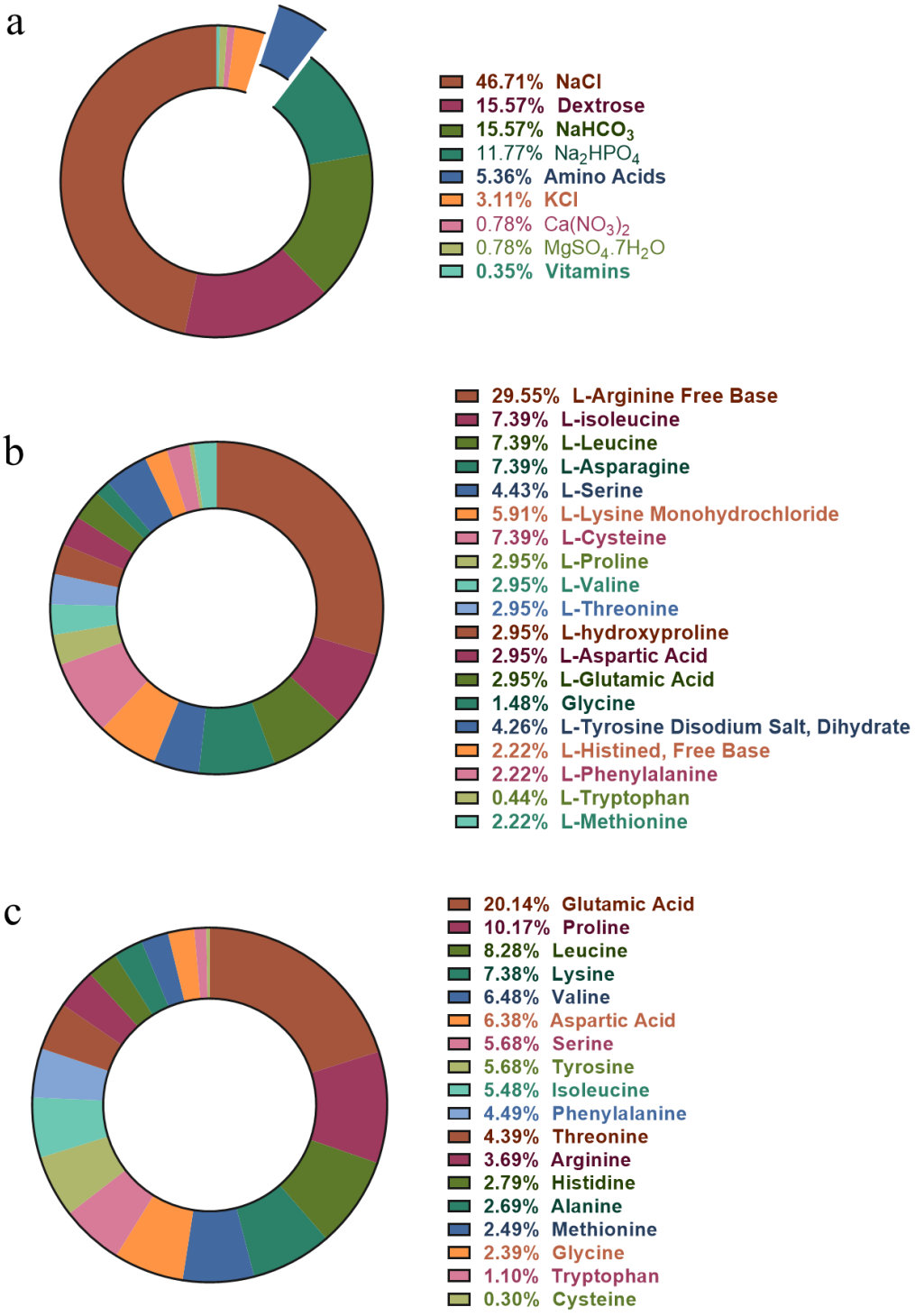

Figure 103. **(a)** Composition (g/l) of commercially available RPMI Lonza. **(b)** Breakdown of amino acid distribution %w/w of total amino acids in commercially available RPMI Lonza. **(c)** Breakdown of amino acid distribution %w/w in RPMI supplemented with casamino acids.

Appendix B - ToF-SIMS Negative Spectra for pEGDPEA and pNGPDA Treated RPMI Supplemented with Casamino Acids

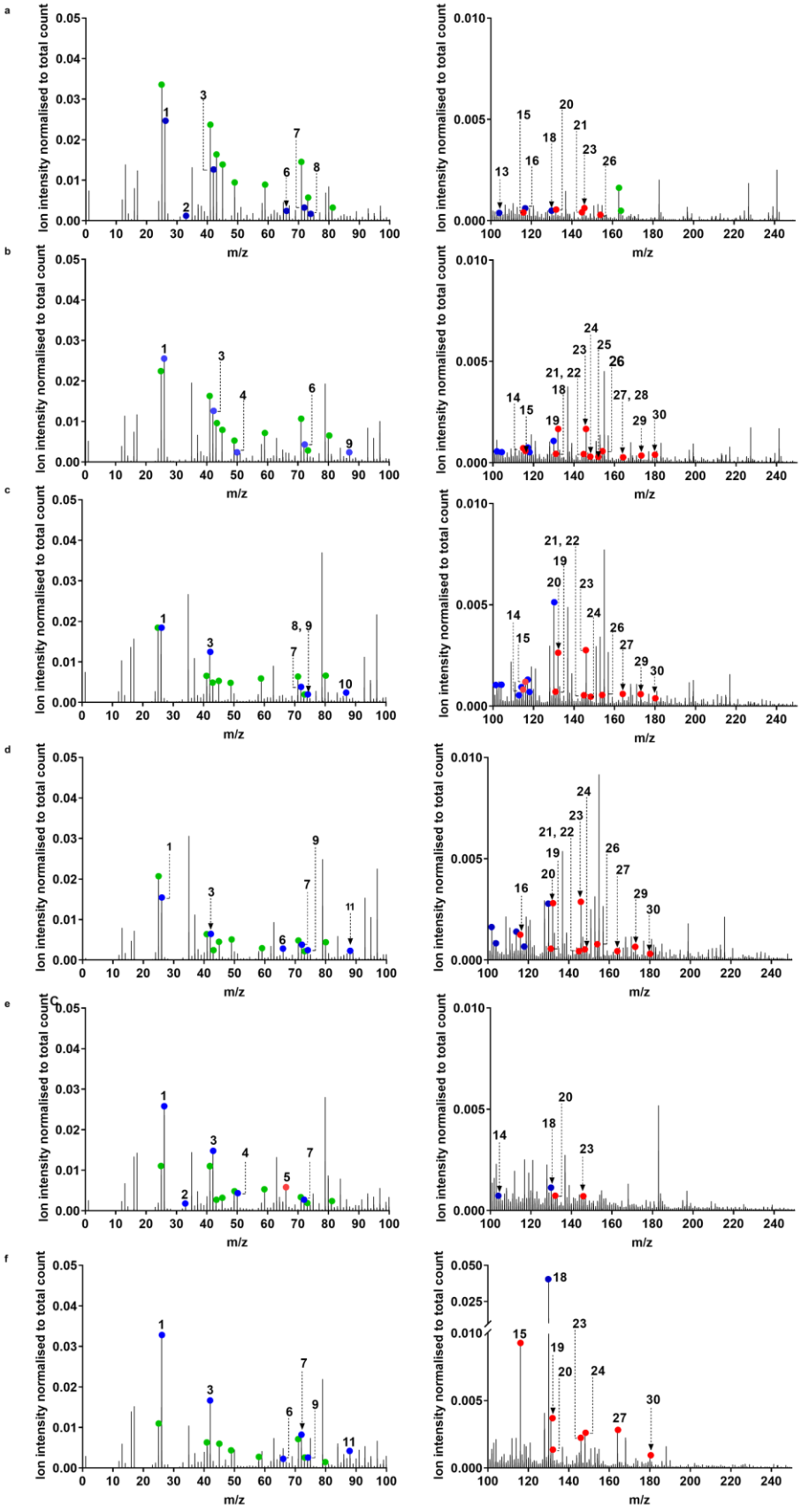

Figure 104. Negative polarity ToF-SIMS spectra (m/z 0 – 250) for pEGDPEA samples exposed to amino acid supplemented media at 37 ˚C and 60 rpm for 2 hours. (a) 0.5 mg/ml, (b) 1 mg/ml, (c) 2 mg/ml, (d) 2 mg/ml, (e) 3 mg/ml, (f) 4 mg/ml and (g) 5 mg/ml.

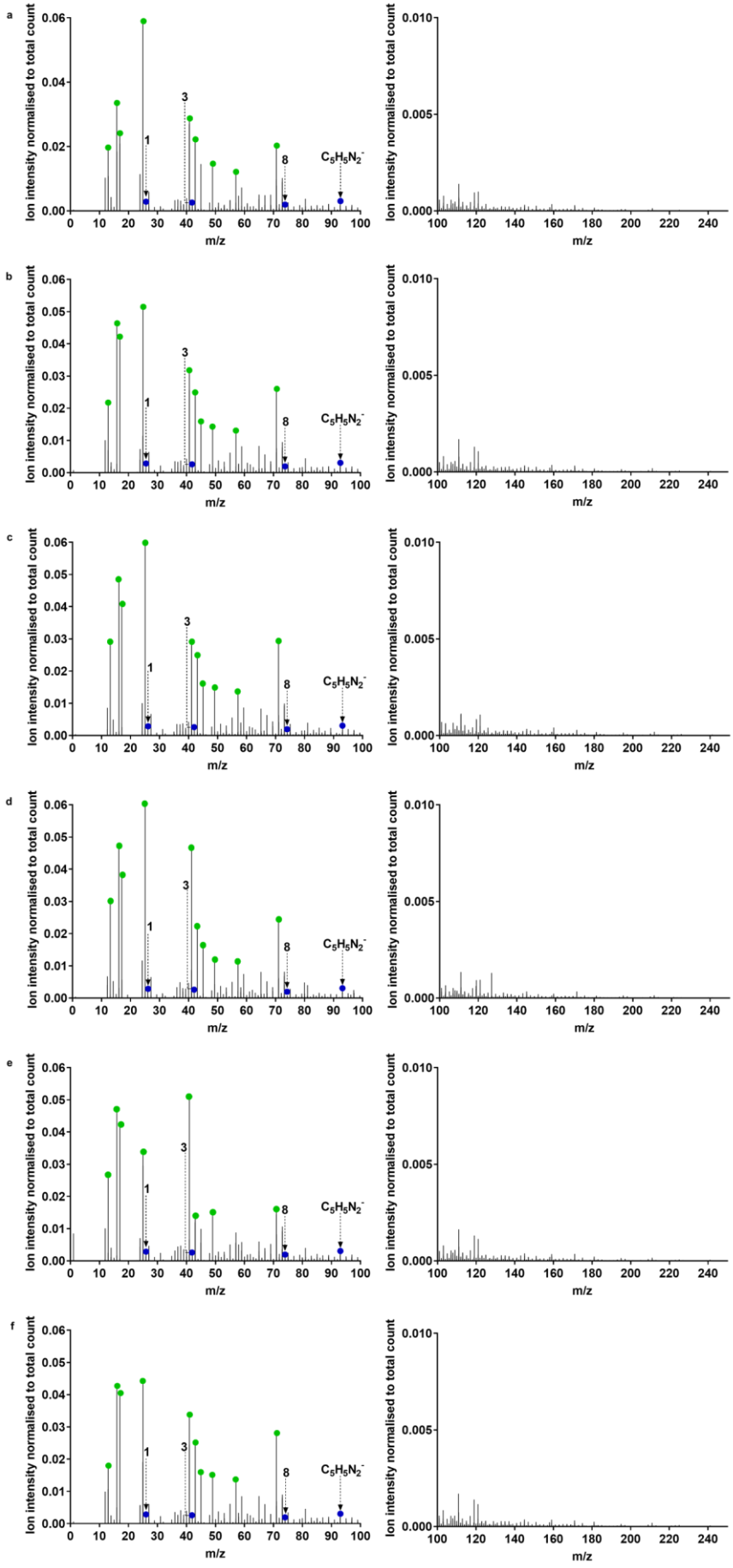

Figure 105. Negative polarity ToF-SIMS spectra (m/z 0 – 250) for pNGPDA samples exposed to amino acid supplemented media at 37 ˚C and 60 rpm for 2 hours. (a) 0.5 mg/ml, (b) 1 mg/ml, (c) 2 mg/ml, (d) 2 mg/ml, (e) 3 mg/ml, (f) 4 mg/ml and (g) 5 mg/ml.

Appendix C – Comparison of Amino Acid distribution in media versus ToF-SIMS intensity on pEGDPEA surface

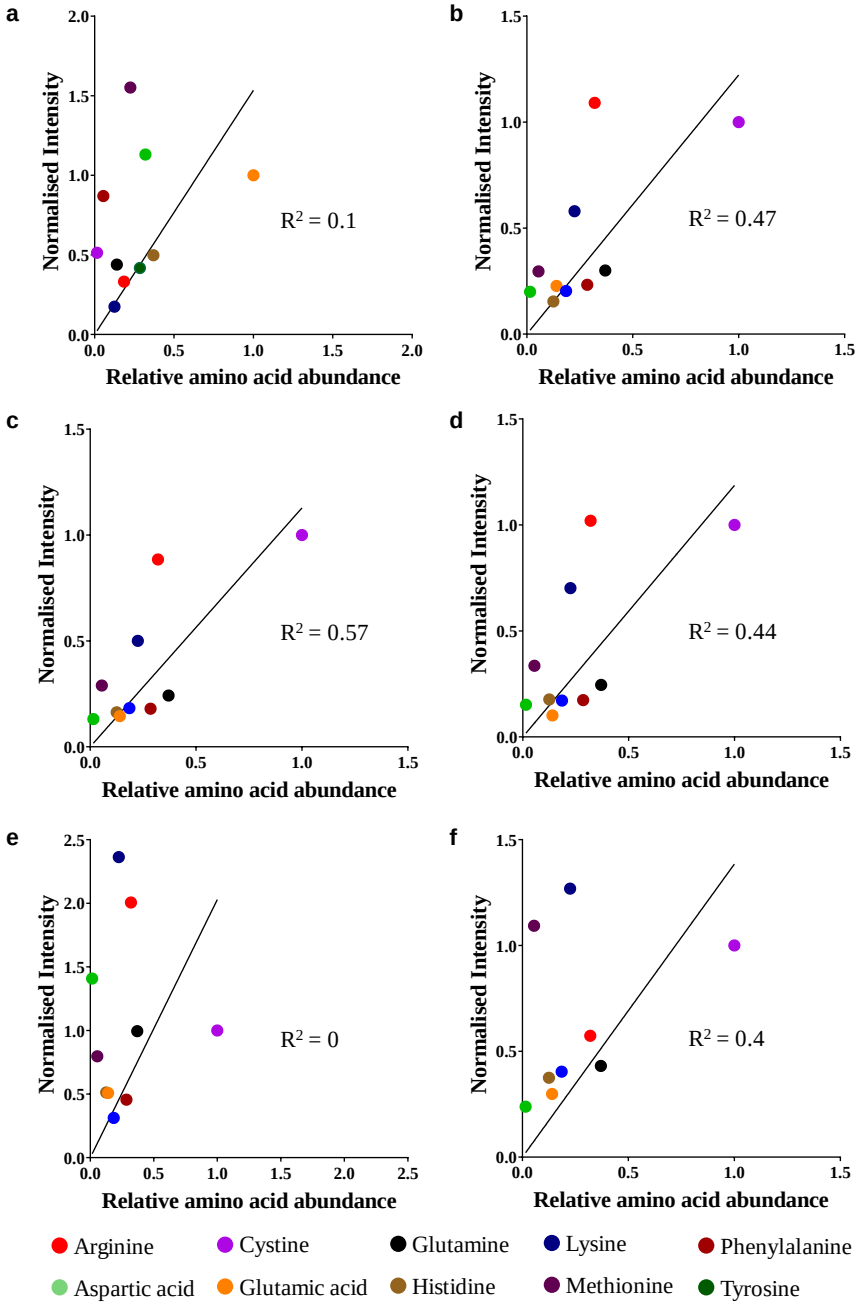

Figure 106. The ToF SIMS intensity of amino acids on polymer surface normalised to glutamic acid plotted versus the theoretically calculated relative abundance of amino acid (w/w) in casamino acid supplemented RPMI media normalised to glutamic acid. Respectively **(a)-(f)** are plots for 0.5 mg/ml, 1 mg/ml, 2 mg/ml, 3 mg/ml, 4 mg/ml and 5 mg/ml experimental conditions. Line of best fit from which R^2 was calculated is shown in black.

Appendix D - XPS Survey Spectra for pEGDPEA and pNGPDA Treated with RPMI Supplemented with Casamino Acids

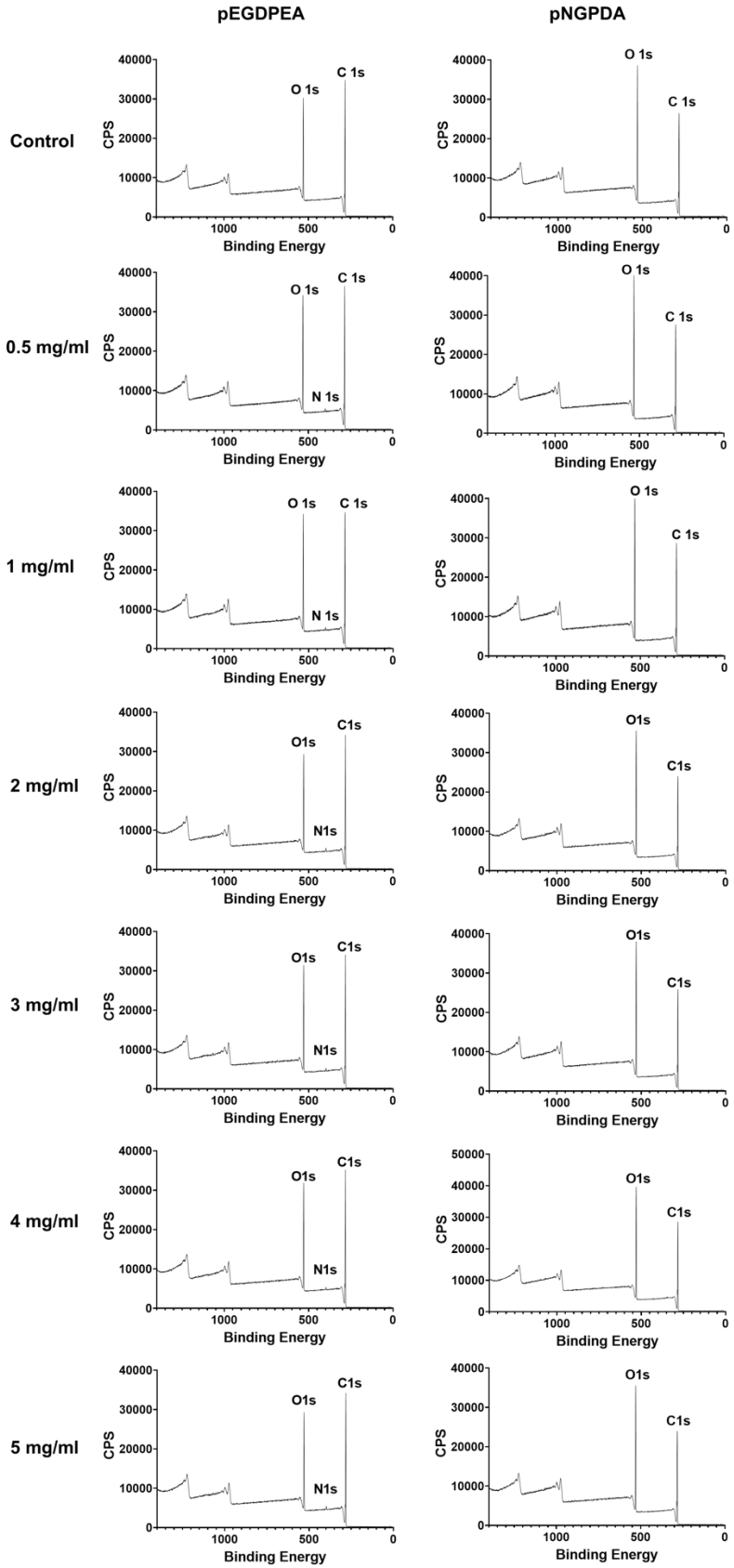

Figure 107. Survey spectrum for pEGDPEA and pNGPDA with treated with RPMI supplemented with casamino acids at different conentrations.

Appendix E - Table of Monomer Materials for Printing Microarrays

	Acronym	Name	CAS number
1	13BDDA	Butanediol-1,3 diacrylate	19485-03-1
2	13BDDMA	1,3-Butanediol dimethacrylate, 98%	1189-08-8
3	14BDDMA	1,4-Butanediol dimethacrylate	2082-81-7
4	2EhMA	2-ethylhexyl methacrylate	
5	AA	Allyl acrylate	999-55-3
6	AAcAm	Diacetone acrylamide	2873-97-4
7	AAm	Acrylamide	79-06-1
8	AcAPAm	N-[2-(Acryloylamino)phenyl]acrylamide	
9	AEAm.C	N-(2-aminoethyl)acrylamide hydrochlide	54641-27-9
10	AEMA.C	2-Aminoethyl methacrylate hydrochloride,	2420-94-2
11	AEMAm.C	N-(2-aminoethyl) methacrylamide hydrochloride	76259-32-0
12	AMA	Allyl methacrylate	96-05-9
13	AnMA	Anthracenylmethylacrylate	31645-34-8
14	AODMBA	(R)-α-Acryloyloxy-β,β-dimethyl-γ-butyrolactone	102096-60-6
15	AOHPMA	Acryloyloxy-2-hydroxypropyl methacrylate	1709-71-3
16	APMAm.C	N-(3-Aminopropyl)methacrylamide hydrochloride	
17	BA	Butyl acrylate	141-32-2
18	BAC	N,N'-Bis(acryloyl)cystamine	60984-57-8
19	BACOEA	Butylamino carbonyl oxy ethyl acrylate	63225-53-6
20	BAGDA	Bisphenol A glycerolate diacrylate	4687-94-9
21	BAPA	1,4-Bis(acryloyl)piperazine	6342-17-2
22	BAPODA	Bisphenol A propoxylate diacrylate	67952-50-5
23	BDDA	Butanediol diacrylate	1070-70-8
24	BFEODA	Bisphenol F ethoxylate diacrylate	120750-67-6
25	BHMA	Benzhydryl methacrylate	25574-72-5
26	BHMOPhP	2,2-Bis[4-(2-hydroxy-3-methacryloxypropoxy)phenyl]propane	1565-94-2
27	BMA	Butyl methacrylate	97-88-1
28	BMAM	N-Benzylmethacrylamide	3219-55-4
29	BMAOEP	Bis[2-(methacryloyloxy)ethyl] phosphate	32435-46-4
30	BMENBC	Bis(2-methacryloxyethyl) N,N’-1,9-nonylene biscarbamate	72869-86-4
31	BnA	Benzyl acrylate	2495-35-4
32	BnMA	Benzyl methacrylate	2495-37-6
33	BnPA	Benzyl 2-n-propyl acrylate	118785-93-6
34	BOEMA	Butoxyethyl methacrylate	13532-94-0
35	BOMAm	N-(Butoxymethyl)acrylamide	1852-16-0
36	BPAPGDA	Bisphenol A propoxylate glycerolate diacrylate	105650-05-3
37	BPDMA	Bisphenol A dimethacrylate	3253-39-2
38	BPEODA	Bisphenol A ethoxylate diacrylate	64401-02-1
39	BTHPhMA	Benzotriazol-2-yl)-4-hydroxyphenyl]ethyl methacrylate	96478-09-0
40	BzHPEA	Benzoyl-3-hydroxy-phenoxy)ethyl acrylate	16432-81-8
41	CEA	Carboxyethyl acrylate	24615-84-7
42	CeMA	cetyl methacrylate	
43	CHA	Cyclohexyl acrylate	3066-71-5
44	CHMA	Cyclohexyl methacrylate	101-43-9
45	CHPMA	Chloro-2-hydroxy-propyl methacrylate	13159-52-9
46	CiMA	cinnamyl methacrylate	
47	ClbMA	2-chlorobenzyl methacrylate	
48	ClEA	2-Chloroethyl acrylate	2206-89-5
49	CMAOE	Caprolactone 2-(methacryloyloxy)ethyl ester	85099-10-1
50	CNEA	Cyanoethyl acrylate	106-71-8
51	COEA	2-Cinnamoyloxyethyl acrylate	52049-17-9
52	CyDMA	cyclododecyl methacrylate	
53	CzEA	Carbazol-9-yl ethyl acrylate	6915-68-0
54	DAAM	N,N-Diallylacrylamide	3085-68-5
55	DDDMA	1,10-Decanediol dimethacrylate	6701-13-9
56	DdMA	dodecyl methacrylate	
57	DEAEA	Diethylamino ethyl acrylate	2426-54-2

58	DEAEMA	Diethylaminoethyl methacrylate	105-16-8
59	DEGDA	Di(ethylene glycol) diacrylate	4074-88-8
60	DEGDMA	Diethylene glycol dimethacrylate	2358-84-1
61	DEGEEA	Di(ethylene glycol) ethyl ether acrylate	7328-17-8
62	DEGEHA	Di(ethylene glycol) 2-ethylhexyl ether acrylate	117646-83-0
63	DEGMA	Di(ethylene glycol) methyl ether methacrylate	45103-58-0
64	DFFMOA	Dodecafluoro-7-(trifluoromethyl)-octyl acrylate	50836-65-2
65	DFHA	Dodecafluoroheptyl acrylate	2993-85-3
66	DFHNMA	Dodecafluoro-2-hydroxy-8-(trifluoromethyl)nonyl methacrylate	16083-81-1
67	DHEBAM	N,N'-(1,2-Dihydroxyethylene)bisacrylamide	868-63-3
68	DHPA	2,3-dihydroxypropyl acrylate	
69	DiPEMA	2-Diisopropylaminoethyl methacrylate	16715-83-6
70	DMA	Decyl methacrylate	3179-47-3
71	DMAEA	Dimethylamino-ethyl acrylate	2439-35-2
72	DMAEMA	Dimethylamino-ethyl methacrylate	2867-47-2
73	DMAm	N,N'-Dimethylacrylamide	07/03/2680
74	DMAPA	Dimethylamino-propyl acrylate	18526-07-3
75	DMCSPMA	Dimethylchlorosilylpropyl methacrylate	24636-31-5
76	DMEMAm	N-[2-(N,N-Dimethylamino)ethyl]methacrylamide	13081-44-2
77	DMMAm	N,N-Dimethylmethacrylamide	6976-91-6
78	DMPAm	N-[3-(Dimethylamino)propyl]acrylamide	3845-76-9
79	DMPMAm	N-[3-(Dimethylamino)propyl]methacrylamide	5205-93-6
80	DOAm	Disperse Orange 3 acrylamide	150375-01-2
81	DPEPHA	Dipentaerythritol penta/hexa-acrylate	60506-81-2
82	DRA	Disperse red 1 acrylate	13695-46-0
83	DVAd	Divinyl Adipate	4074-90-2
84	DVSeb	Divinyl sebacate	10355-50-7
85	DYA	Disperse yellow 7 acrylate	80839-78-7
86	E3GDA	Triethylene glycol diacrylate	1680-21-3
87	EA	Ethyl acrylate	140-88-5
88	EaNIA	Ethyl trans-a-cyano-3-indole-acrylate	62309-96-0
89	EBAM	N,N'-Ethylenebisacrylamide	2956-58-3
90	EbCNA	Ethyl-cis-B-cyano-acrylate	40594-97-6
91	ECNTA	Ethyl-2-cyano-3-(2-thienyl)acrylate	31330-51-5
92	EEA	Ethyl 2-ethylacrylate	3070-65-3
93	EEMA	Ethoxyethyl methacrylate	2370-63-0
94	EG3DMA	Tri(ethylene glycol) dimethacrylate	109-16-0
95	EG4DMA	Tetraethylene glycol dimethacrylate	109-17-1
96	EGDA	Ethylene glycol diacrylate	05/11/2274
97	EGDCMA	Ethylene glycol dicyclopentenyl ether methacrylate	68586-19-6
98	EGDMA	Ethylene glycol dimethacrylate	97-90-5
99	EGDPEA	Ethylene glycol dicyclopentenyl ether acrylate	65983-31-5
100	EGMEA	Ethylene glycol methyl ether acrylate	3121-61-7
101	EGMMA	Ethylene glycol methyl ether methacrylate	6976-93-8
102	EGPEA	Ethylene glycol phenyl ether acrylate	48145-04-6
103	EGPhMA	Ethylene glycol phenyl ether methacrylate	10595-06-9
104	EHA	Ethylhexyl acrylate	103-11-7
105	EHMA	Ethylhexyl methacrylate	688-84-6
106	EMA	Ethyl methacrylate	97-63-2
107	EOEA	Ethoxyethyl acrylate	106-74-1
108	EPA	Ethyl 2-propylacrylate	09/06/3550
109	ETMSA	Ethyl 2-(trimethylsilylmethyl)acrylate	74976-84-4
110	ExA	Epoxidized acrylate	91722-14-4
111	F6BA	Hexafluorobutyl acrylate	54052-90-3
112	F6BMA	Hexafluorobutyl methacrylate	36405-47-7
113	F7BA	Heptafluorobutyl acrylate	424-64-6
114	F7BMA	Heptafluorobutyl methacrylate	13695-31-3
115	FDA	Fluorescein O,O'-diacrylate	7262-39-7
116	FMHPNMA	Trifluoro-2′-(trifluoromethyl)-2′-hydroxy)propyl]-3-norbornyl methacrylate	824411-04-3
117	FOA	Fluorescein O-acrylate	193419-86-2

118	FuMA	Furfuryl methacrylate	3454-28-2
119	GA	Glycidyl acrylate	106-90-1
120	GDGDA	Glycerol 1,3-diglycerolate diacrylate	60453-84-1
121	GDMA	Glycerol dimethacrylate	1830-78-0
122	GMA	Glycidyl methacrylate	106-91-2
123	GMA-AD	geranyl methacrylate	
124	GMMA	Glycerol monomethacrylate	5919-74-4
125	GPOTA	Glycerol propoxylate triacrylate	52408-84-1
126	HA	Hexyl acrylate	2499-95-8
127	HBA	Hydroxybutyl acrylate	06/10/2478
128	HBMA	Hydroxybutyl methacrylate	29008-35-3
129	HBOPBA	Hexanediylbis[oxy(2-hydroxy-3,1-propanediyl)] bisacrylate	83045-03-8
130	HDDMA	1,6-Hexanediol dimethacrylate,	6606-59-3
131	HDFDA	Heptadecafluorodecyl acrylate	27905-45-9
132	HDFDMA	Heptadecafluorodecyl methacrylate	1996-88-9
133	HDFHUA	Heptadecafluoro-2-hydroxyundecyl acrylate	76962-34-0
134	HDMA	1-Hexadecyl methacrylate	2495-27-4
135	HDMPDA	Hydroxy-2,2-dimethylpropyl 3-hydroxy-2,2-dimethylpropionate diacrylate	30145-51-8
136	HEA	Hydroxyethyl acrylate	818-61-1
137	HEAm	N-Hydroxyethyl acrylamide	7646-67-5
138	HEMA	Hydroxyethyl methacrylate	868-77-9
139	HEODA	Hexanediol ethoxylate diacrylate	
140	HfCEA	Hafnium carboxyethyl acrylate	
141	HFDA	Heneicosafluorododecyl acrylate	17741-60-5
142	HFHUMA	Hexadecafluoro-2-hydroxy-10-(trifluoromethyl)undecyl methacrylate	88752-37-8
143	HFiPA	Hexafluoroisopropyl acrylate	2160-89-6
144	HFiPMA	Hexafluoroisopropyl methacrylate	3063-94-3
145	HFPDA	Hexafluoropent-1,5-diyl diacrylate	918-36-5
146	HMA	Hexyl methacrylate	142-09-6
147	HMAm	N-(Hydroxymethyl)acrylamide	924-42-5
148	HMBAM	N,N’-Hexamethylenebisacrylamide	7150-41-6
149	HMBMAm	N,N'-Hexamethylenebis(methacrylamide)	16069-15-1
150	HMDA	Hexamethylene diacrylate	13048-33-4
151	HPA	Hydroxypropyl acrylate	25584-83-2
152	HPhMA	N-(4-Hydroxyphenyl)methacrylamide	19243-95-9
153	HPhOPA	Hydroxy-3-phenoxypropyl acrylate	16969-10-1
154	HPHPBAH	Hydroxypivalyl hydroxypivalate bis[6-(acryloyloxy)hexanoate]	91381-58-7
155	HPMA	Hydroxypropyl methacrylate	27813-02-1
156	HPMAm	N-(2-Hydroxypropyl)methacrylamide	21442-01-3
157	HPMAP	Hydroxypropyl 2-(methacryloyloxy)ethyl phthalate	68406-95-1
158	HTFDA	Hexadecafluoro-9-(trifluoromethyl)decyl acrylate	15577-26-1
159	iBA	Isobutyl acrylate	106-63-8
160	IBESMA	1,7,7-trimethylbicyclo[2.2.1]heptan-2-yl 6-(methacryloyloxy)-4-oxohexanoate	
161	iBMA	Isobornyl methacrylate	7534-94-3
162	iBOA	Isobornyl acrylate	5888-33-5
163	iBOMAm	N-(Isobutoxymethyl)acrylamide	16669-59-3
164	iBuMA	Isobutyl methacrylate	97-86-9
165	iCEMA	Isocyanatoethyl methacrylate	30674-80-7
166	iDA	Isodecyl acrylate	1330-61-6
167	iDMA	Isodecyl methacrylate	29964-84-9
168	iOA	Isooctyl acrylate	29590-42-9
169	iPAm	N-Isopropylacrylamide	2210-25-5
170	IPBMA	p-isopropylbenzyl methacrylate	
171	LaA	Lauryl acrylate	2156-97-0
172	LMA	Lauryl methacrylate	142-90-5
173	LMMA	L-menthyl methacrylate	
174	MA	Methyl acrylate	96-33-3
175	MAA	Methyl 2-acetamidoacrylate	35356-70-8

176	MAAH	Methacrylic anhydride	760-93-0
177	MAAHS	Methacrylic acid N-hydroxysuccinimide ester	38862-25-8
178	MAEA	Methacryloyloxy)ethyl acetoacetate	21282-97-3
179	MAEACl	[2-(Methacryloyloxy)ethyl]trimethylammonium chloride solution	5039-78-1
180	MAEP	Monoacryloxyethyl phosphate	32120-16-4
181	MAEPC	2-Methacryloyloxyethyl phosphorylcholine	67881-98-5
182	MAETA	4-Methacryloxyethyl trimellitic anhydride	70293-55-9
183	MAHBP	4-Methacryloxy-2-hydroxybenzophenone	2035-72-5
184	MAL	Methacryloyl-L-Lysine	45158-94-9
185	Mam	Methacrylamide	79-39-0
186	MAPtMA	Methacrylamidopropyltrimethylammonium chloride,	51410-72-1
187	MAPU	2-methacryloxyethyl phenyl urethane	51727-47-0
188	MBAm	N,N'-Methylenebisacrylamide	110-26-9
189	MbMA	4-methylbenzyl methacrylate	
190	MBMAm	N,N'-Methylenebismethacrylamide	2359-15-1
191	MClMA	Methyl 2-(chloromethyl)acrylate	922-15-6
192	MEDMSAH	[2-(Methacryloyloxy)ethyl]dimethyl-(3-sulfopropyl) ammonium hydroxide	3637-26-1
193	MHMB	Methyl 3-hydroxy-2-methylenebutyrate	18020-65-0
194	MMA	Methyl methacrylate	80-62-6
195	MMAm	N-Methylmethacrylamide	03/02/3887
196	mMAOEM	mono-2-(Methacryloyloxy)ethyl maleate	51978-15-5
197	mMAOES	mono-2-(Methacryloyloxy)ethyl succinate	20882-04-6
198	MOPAm	N-(3-Methoxypropyl)acrylamide	107374-86-7
199	MPDSAH	Methacryloylamino)propyl]dimethyl(3-sulfopropyl)ammonium hydroxide inner salt	5205-95-8
200	MpMA	4-methylpentan-2-yl methacrylate	
201	MSPMA	Methyldiethoxysilyl-propyl methacrylate	65100-04-1
202	MTEMA	Methylthioethyl methacrylate	14216-23-0
203	NAM	N-Acryloylmorpholine	5117-12-4
204	NaPhA	Sodium 3-phenyl-acrylate	
205	NAS	N-Acryloxysuccinimide	38862-24-7
206	NBMA	Norbornyl methacrylate	29753-02-4
207	NBMAm	N-(Butoxymethyl)acrylamide	1852-16-0
208	NBnMA	o-Nitrobenzyl methacrylate, . 95%	
209	NDDMA	1,9-Nonanediol dimethacrylate	65833-30-9
210	NDMAm	N-Dodecylmethacrylamide	1191-39-5
211	NGDA	Neopentyl glycol diacrylate	2223-82-7
212	NGPDA	Neopentyl glycol propoxylate diacrylate	84170-74-1
213	NibMA	4-nitrobenzyl methacrylate	
214	NMEMA	2-N-Morpholinoethyl methacrylate, 95%	2997-88-8
215	nOcMA	n-Octyl methacrylate,	
216	NpA	Naphthyl acrylate	52684-34-1
217	NPhPMA	Nitrophenyl-2-pyrrolidonemethyl acrylate	152100-45-3
218	NpMA	Naphthyl methacrylate	10475-46-4
219	ODA	Octadecyl acrylate	4813-57-4
220	OFHMA	Octafluoro-2-hydroxy-6-(trifluoromethyl)heptyl methacrylate	16083-79-7
221	OFPA	Octafluoropentyl acrylate	376-84-1
222	OFPMA	Octafluoropentyl methacrylate	355-93-1
223	PA	Propargyl acrylate	10477-47-1
224	PAHEMA	Phosphoric acid 2-hydroxyethyl methacrylate ester	52628-03-2
225	PBBA	Pentabromobenzyl acrylate	59447-55-1
226	PBPhA	Pentabromophenyl acrylate	52660-82-9
227	PBPhMA	Pentabromophenyl methacrylate	18967-31-2
228	PDA	1,4-Phenylene diacrylate	6729-79-9
229	PDDMA	1,5-Pentanediol dimethacrylate	13675-34-8
230	PEDAM	Pentaerythritol diacrylate monostearate	92092-01-8
231	pEGDA	Polyethylene glycol diacrylate	26570-48-9
232	pEGDMA	Poly(ethylene glycol) (600) dimethacrylate	25852-47-5
233	pEGMA	Poly(ethylene glycol) methacrylate	25736-86-1
234	pEGMEA	Poly(ethylene glycol) methyl ether acrylate	32171-39-4

235	pEGMEMA	Poly(ethylene glycol) methyl ether methacrylate	26915-72-0
236	pEGPhEA	Poly(ethylene glycol) phenyl ether acrylate	56641-05-5
237	PETA	Pentaerythritol tetraacrylate	4986-89-4
238	PETrA	Pentaerythritol triacrylate	3524-68-3
239	pFDA	Perfluorodecyl acrylate	27905-45-9
240	PFPA	Pentafluoropropyl acrylate	356-86-5
241	PFPhA	Pentafluorophenyl acrylate	71195-85-2
242	PFPhMA	Pentafluorophenyl methacrylate, 95%	13642-97-2
243	PFPMA	Pentafluoropropyl methacrylate	45115-53-5
244	PhA	Phenyl acrylate, 95%	937-41-7
245	PhEA	2-Phenylethyl acrylate	3530-36-7
246	PhEMA	2-Phenylethyl methacrylate	
247	PhMA	Phenyl methacrylate	2177-70-0
248	PhMAm	N-Phenylmethacrylamide	1611-83-2
249	PHPMA	3-Phenoxy 2 hydroxy propyl methacrylate	16926-87-7
250	PiMA	pivaloyl methacrylate	
251	PMA	Propargyl methacrylate	13861-22-8
252	PMAm	N-(Phthalimidomethyl)acrylamide	80500-44-3
253	PMMA	1-Pyrenylmethyl methacrylate	86112-79-0
254	PPDDA	3-phenoxypropane-1,2-diyl diacrylate	
255	pPGA	Poly(propylene glycol) acrylate	50858-51-0
256	pPGDA	Poly(propylene glycol) diacrylate	52496-08-9
257	pPGDMA	Poly(propylene glycol) (400) dimethacrylate	25852-49-7
258	pPGMEA	Poly(propylene glycol) methyl ether acrylate	
259	pPGNEA	Poly(propylene glycol) 4-nonylphenyl ether acrylate	71926-19-7
260	PPPDMA	PEO(5800)-b-PPO(3000)-b-PEO(5800) dimethacrylate	
261	SEMA	2-Sulfoethyl methacrylate	
262	SMA	Stearyl methacrylate	32360-05-7
263	SolA	Solketal acrylate	
264	SPAK	Sulfopropyl acrylate potassium salt	31098-20-1
265	SPMAK	3-Sulfopropyl methacrylate potassium salt	31098-21-2
266	TAHTA	1,3,5-Triacryloylhexahydro-1,3,5-triazine	959-52-4
267	TAIC	Tris[2-(acryloyloxy)ethyl] isocyanurate	40220-08-4
268	tBA	Tert-butyl acrylate	1663-39-4
269	tBAEMA	Tert-butylamino-ethyl methacrylate	3775-90-4
270	tBAm	N-tert-Butylacrylamide	107-58-4
271	tBCHA	Tert-butylcyclohexylacrylate	84100-23-2
272	tBCHMA	Tertbutylcyclohexyl methacrylate	46729-07-1
273	tBEMAm	N-(3,3-dimethylbutyl)methacrylamide	
274	tBMA	Tert-butyl methacrylate	585-07-9
275	tBMAm	N-tert-Butylmethacrylamide	6554-73-0
276	TBNpMA	Tribromoneopentyl methacrylate	
277	tBOCAPAm	N-(t-BOC-aminopropyl)methacrylamide	219739-79-4
278	TBPhA	2,4,6-Tribromophenyl acrylate	3741-77-3
279	TBPMA	Tribromophenyl methacrylate	37721-71-4
280	TCDMDA	Tricyclodecane-dimethanol diacrylate	42594-17-2
281	TCSPMA	Trichlorosilyl propyl methacrylate	7351-61-3
282	TDFOcA	Tridecafluorooctyl acrylate	17527-29-6
283	TDFOMA	Tridecafluorooctyl methacrylate	2144-53-8
284	TEGDA	Tetra(ethylene glycol) diacrylate	17831-71-9
285	TEGMA	Tri(ethylene glycol) methyl ether methacrylate	24493-59-2
286	TFCAm	7-[4-(Trifluoromethyl)coumarin]acrylamide	480438-94-6
287	TFPMA	Tetrafluoropropyl methacrylate	45102-52-1
288	THFuA	Tetrahydrofurfuryl acrylate	2399-48-6
289	THFuMA	Tetrahydrofurfuryl methacrylate	2455-24-5
290	THMMAm	N-[Tris(hydroxymethyl)methyl]acrylamide	13880-05-2
291	TMBAm	N-(1,1,3,3-Tetramethylbutyl)acrylamide	
292	TMCHMA	Trimethylcyclohexyl methacrylate	7779-31-9
293	TMHA	Trimethylhexyl acrylate	45125-03-9
294	TMOBDA	Trimethylolpropane benzoate diacrylate	79720-88-0
295	TMOPTMA	1,1,1-Trimethylolpropane trimethacrylate	3290-92-4

296	TMOSPA	Trimethoxysilyl propyl acrylate	4369-14-6
297	TMOSPMA	Trimethoxysilyl propyl methacrylate	2530-85-0
298	TMPDAE	Trimethyl propane diallyl ether	682-09-7
299	TMPETA	Trimethylolpropane ethoxylate triacrylate	28961-43-5
300	TMPOTA	Trimethylolpropane propoxylate triacrylate	53879-54-2
301	TMPTA	Trimethylolpropane triacrylate	15625-89-5
302	TMSA	Trimethylsilylacrylate	13688-55-6
303	TMSMA	Trimethylsilyl methacrylate	13688-56-7
304	TMSOEMA	Trimethylsilyloxy)ethyl methacrylate	17407-09-9
305	TMSOSMA	Tris(trimethylsilyloxy)-silyl propyl methacrylate	17096-07-0
306	tOcAm	N-tert-Octylacrylamide	
307	TPEMDA	Trimethylolpropane ethoxylate methyl ether diacrylate	302911-84-8
308	TPGDA	Tri(propylene glycol) diacrylate	42978-66-5
309	TPhMAm	N-(Triphenylmethyl)methacrylamide	275371-79-4
310	VMA	Vinyl methacrylate	4245-37-8
311	ZnA	Zinc acrylate	14643-87-9
312	ZrA	Zirconium acrylate	60653-57-8
313	ZrBNCTA	Zirconium bromonorbornanelactone carboxylate triacrylate	
314	ZrCEA	Zirconium carboxyethyl acrylate	123633-53-4

Appendix F - Polymers and Molecular Weights

Material	Molecular weight	Mn	Polydispersity
pCyDMA	1.230×10^5	5.515×10^4	2.230
pEGDPEA-co-DEGMA	5.474×10^4	2.380×10^4	2.300
pBnMA	5.629×10^5	1.459×10^5	3.881
pHPhOPA	7.077×10^5	3.880×10^5	1.824
pNGPDA	9.217×10^5	3.185×10^5	2.894

Appendix G – Table of 284 Monomers Printed

	a	b	c	d	e	f	g	h	i	j	k	l	m	n	o	p	q	r	s	t	u	v	w	x
1	F6BA		DEGEEA		EPA		HPMA		ExA		AAm		THMMAm		PBPhA		GMA		CHPMA		pPGNEA		BAPA	
2		NMEMA		OFPA		PAHEMA		EGDPEA		BzHPEA		DMAm		BnA		pEGMEMA		CNEA		TCDMDA		MOPAm		HBMA
3	DMAEA		TBPhA		DDDMA		OFHMA		NaPhA		BAPODA		BMAM		HFiPA		DEAEMA		pEGMA		NBMA		TDFOMA	
4		AODMBA		MAPtMA		DFHA		ODA		NpMA		HPHPBAH		DVAd		TMPETA		BnMA		pPGDA		HMBMAm		EGPhMA
5	EGDMA		nOcMA		iBMA/tBAEMA		pPGDMA		TBNpMA		BPAPGDA		DVSeb		VMA		HPA		SMA		MEDMSAH		NBnMA	
6		HA		PFPMA		DEAEA		DPEPHA		tBMAm		NGPDA		MAHBP		DEGDA		TMCHMA		pPGMEA		MMAm		
7	PFPA		EA		EEA		MAA		FMHPNMA		AOHPMA		TPhMAm		PBPhMA		pPGA		MAEA		ZrBNCTA		AAcAm	
8		MA		PDDMA		OFPMA		PHPMA		PMAm		DYA		CHA		PA		THFuMA		TMOBDA		HEAm		NAM
9	tBA		MMA		IBESMA		tBEMAm		AEMAm.C		SEMA		PhEMA		BHMA		CHMA		HFPDA		BnPA		TFPMA	
10		THFuA		NDMAm		DEGDMA		PETrA		PEDAM		HPMAP		HMBAM		tBMA		MTEMA		HDMPDA		DMPMAm		SolA
11	DMMAm		DAAM		AcAPAm		HFHUMA		DOAm		BPDMA		AMA		iOA		EHMA		mMAOEM		MAEACl		TAHTA	
12		pFDA		14BDDMA		GA		BAGDA		TPGDA		PBBA		MAPU		DMAPA		iDMA		DEGEHA		PhMAm		
13	TMHA		HFiPMA		F7BMA		HTFDA		iBOMAm		APMAm.C		MAEPC		PFPhMA		MHMB		DMA		GDMA		ZrCEA	
14		BDDA		E3GDA		PPPDMA		HDMA		TMPTA		HDFHUA		BHMOPhP		BA		BOEMA		HEODA		DMPAm		EG3DMA
15	EGDA		DRA		DMAEMA		LaA		PDA		TMPOTA		F7BA		PhA		iCEMA		HPhOPA		MPDSAH		PFPhA	
16		DMEMAm		pEGDMA		BMENBC		AnMA		SPMAK		MAAHS		HPMAm		BMA		tBAEMA		tBCHA		HPhMA		DHPA
17	13BDDMA		HBOPBA		BTHPhMA		HDDMA		PMMA		CzEA		PMA		pEGPhEA		FuMA/tBAEMA		TEGDA		EBAM		iPAM	
18		13BDDA		iBuMA		EbCNA		GPOTA		ZnA		TEGMA		NAS		EEMA		iBMA		pEGMEA		iBOA		
19	EGMEA		MAAH		F6BMA		HDFDMA		MBMAm		BAC		HfCEA		AEMA.C		HMA		EGDCMA		CMAOE		TMBAm	
20		EGPEA		MAL		AA		TBPMA		NpA		HFDA		COEA		HEODA/EEMA		DEGMA		BPEODA		HMAm		EG4DMA
21	DiPEMA		TAIC		MAEP		DFHNMA		NPhPMA		BFEODA		TMPDAE		iDA		EHA		TMOPTMA		tBCHMA		PhEA	
22		HDFDA		PETA		TDFOcA		GDGDA		tBAm		MBAm		MAETA		CEA		PhMA		BACOEA		Mam		PPDDA
23	EOEA		EMA		pEGDA		ECNTA		BMAOEP		DHEBAM		tBOCAPAm		iBA		FuMA		mMAOES		BOMAm		HEA	
24		HBA		GMMA		DFFMOA		EaNIA		ZrA		TFCAm		NDDMA		EGMMA		NGDA		SPAK		LMA		

Appendix H - Table of 281 Monomers Analysed for Amino Acid Adsorption & Bacteria Biofilm

	a	b	c	d	e	f	g	h	i	j	k	l	m	n	o	p	q	r	s	t	u	v	w	x
1	F6BA	NMEMA	DEGEEA	OFPA	EPA	PAHEMA	HPMA	EGDPEA	ExA	BzHPEA	AAm	DMAm	THMMAm	BnA	PBPhA	pEGMEMA	GMA	CNEA	CHPMA	TCDMDA	pPGNEA	MOPAm	BAPA	HBMA
2	DMAEA	AODMBA	TBPhA	MAPtMA	DDDMA	DFHA	OFHMA	ODA	NaPhA	NpMA	BAPODA	HPHPBAH	BMAM	DVAd	HFiPA	TMPETA	DEAEMA	BnMA	pEGMA	pPGDA	NBMA	HMBMAm	TDFOMA	EGPhMA
3	EGDMA	HA	nOcMA	PFPMA	iBMA/tBAEMA	DEAEA	pPGDMA	DPEPHA	TBNpMA	tBMAm	BPAPGDA	NGPDA	DVSeb	MAHBP	VMA	DEGDA	HPA	TMCHMA	SMA	pPGMEA	MEDMSAH	MMAm	NBnMA	NAM
4	PFPA	MA	EA	PDDMA	EEA	OFPMA	MAA	PHPMA	FMHPNMA	PMAm	AOHPMA	DYA	TPhMAm	CHA	PBPhMA	PA	pPGA	THFuMA	MAEA	TMOBDA	ZrBNCTA	HEAm	AAcAm	EG3DMA
5	tBA	THFuA	MMA	NDMAm	IBESMA	DEGDMA	tBEMAm	PETrA	AEMAm.C	PEDAM	SEMA	HPMAP	PhEMA	HMBAM	BHMA	tBMA	CHMA	MTEMA	HFPDA	HDMPDA	BnPA	DMPMAm	TFPMA	EG4DMA
6	DMMAm	pFDA	DAAM	14BDDMA	AcAPAm	GA	HFHUMA	BAGDA	DOAm	TPGDA	BPDMA	PBBA	AMA	MAPU	iOA	DMAPA	EHMA	iDMA	mMAOEM	DEGEHA	MAEACl	PhMAm	TAHTA	
7	TMHA	BDDA	HFiPMA	E3GDA	F7BMA	PPPDMA	HTFDA	HDMA	iBOMAm	TMPTA	APMAm.C	HDFHUA	MAEPC	BHMOPhP	PFPhMA	BA	MHMB	BOEMA	DMA	HEODA	GDMA	DMPAm	ZrCEA	
8	EGDA	DMEMAm	DRA	pEGDMA	DMAEMA	BMENBC	LaA	AnMA	PDA	SPMAK	TMPOTA	MAAHS	F7BA	HPMAm	PhA	BMA	iCEMA	tBAEMA	HPhOPA	tBCHA	MPDSAH	HPhMA	PFPhA	
9	13BDDMA	13BDDA	HBOPBA	iBuMA	BTHPhMA	EbCNA	HDDMA	GPOTA	PMMA	ZnA	CzEA	TEGMA	PMA	NAS	pEGPhEA	EEMA	FuMA/tBAEMA	iBMA	TEGDA	pEGMEA	EBAM	iBOA	iPAM	
10	EGMEA	EGPEA	MAAH	MAL	F6BMA	AA	HDFDMA	TBPMA	MBMAm	NpA	BAC	HFDA	HfCEA	COEA	AEMA.C	HEODA/EEMA	HMA	DEGMA	EGDCMA	BPEODA	CMAOE	HMAm	TMBAm	
11	DiPEMA	HDFDA	TAIC	PETA	MAEP	TDFOcA	DFHNMA	GDGDA	NPhPMA	tBAm	BFEODA	MBAm	TMPDAE	MAETA	iDA	CEA	EHA	PhMA	TMOPTMA	BACOEA	tBCHMA	Mam	PhEA	
12	EOEA	HBA	EMA	GMMA	pEGDA	DFFMOA	ECNTA	EaNIA	BMAOEP	ZrA	DHEBAM	TFCAm	tBOCAPAm	NDDMA	iBA	EGMMA	FuMA	NGDA	mMAOES	SPAK	BOMAm	LMA	HEA	

Figure 108. Table of monomers tested for amino acid adsorption.

Appendix I - Table of 283 Monomers Printed in Array

	a	b	c	d	e	f	g	h	i	j	k	l	m	n	o	p	q	r	s	t	u	v	w	x
12	iBOA	iPAM	ZrCEA	EG3DMA	PFPhA		LMA	HEA	TMBAm	EG4DMA	PhEA		BAPA	HBMA	TDEOMA	EGPhMA	NBuMA		AAcAm	NAM	TFPMA		TAHTA	
11	pEGMEA	EBAM	GDMA	DMPAm	MPDSAH	HPhMA	SPAK	BOMAm	CMAOE	HMAm	tBCHMA	Mam	pPGNEA	MOPAm	NBMA	HMBMAm	MEDMSAH	MMAm	ZrBNCTA	HEAm	BnPA	DMPMAm	MAEACl	PhMAm
10	iBMA	TEGDA	DMA	HEODA	HPhOPA	tBCHA	NGDA	mMAOES	EGDCMA	BPEODA	TMOPTMA	BACOEA	CHPMA	TCDMDA	pEGMA	pBGDA	SMA	pPGMEA	MAEA	TMOBDA	HFPDA	HDMPDA	mMAOEM	DEGEHA
9	EEMA	FuMA/tBAEMA	MHMB	BOEMA	iCEMA	tBAEMA	EGMMA	FuMA	HMA	DEGMA	EHA	PhMA	GMA	CNEA	DEAEMA	BnMA	HPA	TMCHMA	pPGA	THFuMA	CHMA	MTEMA	EHMA	iDMA
8	NAS	pEGPhEA	PFPhMA	BA	PhA	BMA	NDDMA	iBA	AEMA.C	HEODA/EEMA	iDA	CEA	PBPhA	pEGMEMA	HFiPA	TMPETA	VMA	DEGDA	PBPhMA	PA	BHMA	tBMA	iOA	DMAPA
7	TEGMA	PMA	MAEPC	BHMOPhP	F7BA	HPMAm	TFCAm	tBOCAPAm	HfCEA	COEA	TMPDAE	MAETA	THMMAm	BnA	BMAM	DVAd	DVSeb	MAHBP	TPhMAm	CHA	PhEMA	HMBAM	AMA	MAPU
6	Anm	DMAm	BAPODA	HDJHUA	BPAPGDA	MAAHS	AOHPMA	FDA	SEMA	HEDA	BPDMA	MBAm	APMAm.C	DYA	TMPOTA	HPHPBAH	CzEA	NGPDA	BAC	FOA	BFEODA	HPMAP	DHEBAM	PBBA
5	ExA	BzHPEA	NaPhA	NpMA	TBNpMA	tBMAm	FMHPNMA	PMAm	AEMAm.C	PEDAM	DOAm	TPGDA	iBOMAm	TMPTA	PDA	SPMAK	PMMA	ZnA	MBMAm	NpA	NPhPMA	tBAm	BMAOEP	ZrA
4	HPMA	EGDPEA	OFHMA	OPA	pPGDMA	DPEPHA	MAA	PHPMA	tBEMAm	PETrA	HFHUMA	BAGDA	HTFDA	HDMA	LaA	AnMA	HDDMA	GPOTA	HDFDMA	TBPMA	DFHNMA	GDGDA	ECNTA	EaNIA
3	EPA	PAHEMA	DDDMA	DFHA	iBMA/tBAEMA	DEAEA	EEA	OFPMA	IBESMA	DEGDMA	AcAPAm	GA	F7BMA	PPPDMA	DMAEMA	BMENBC	BTHPhMA	EbCNA	F6BMA	AA	MAEP	TDFOcA	pEGDA	DFFMOA
2	DEGEEA	OFPA	TBPhA	MAPtMA	nOcMA	PFPMA	EA	PDDMA	MMA	NDMAm	DAAM	14BDDMA	HFiPMA	E3GDA	DRA	pEGDMA	HBOPBA	iBuMA	MAAH	MAL	TAIC	PETA	EMA	GMMA
1	F6BA	NMEMA	DMAEA	AODMBA	EGDMA	HA	PFPA	MA	IBA	THFuA	DMMAm	pEDA	TMHA	BDDA	EGDA	DMEMAm	13BDDMA	13BDDA	EGMEA	EGPEA	DiPEMA	HDPDA	EOEA	HBA

Figure 109. Table of monomers printed in 9.0 array. Cells with diagonal line indicate materials eliminated from analysis after screening with *P. aeruginosa* due to poor signal to noise ratio.

Appendix J - Table of 224 Monomers Analysed from Array

	a	b	c	d	e	f	g	h	i	j	k	l	m	n	o	p	q	r	s	t	u	v	w	x
1	iBOA	iPAM	ZrCEA	EG3DMA	LMA	TMBAm	EG4DMA	PhEA	BAPA	HBMA	EGPhMA	NAM	TFPMA	TCDMDA	NBMA	HMBMAm	HPA	MMAm	MAEA	TMOBDA	BnPA	DMPMAm	MAEACl	PhMAm
2	iBMA	EBAM	GDMA	DMPAm	HPhOPA	tBCHA	NGDA	BOMAm	CMAOE	HMAm	tBCHMA	Mam	pPGNEA	CNEA	pEGMA	BnMA	VMA	pPGMEA	pPGA	THFuMA	HFPDA	HDMPDA	mMAOEM	iDMA
3	EEMA	TEGDA	DMA	HEODA	iCEMA	tBAEMA	NDDMA	tBOCAPAm	EGDCMA	BPEODA	TMOPTMA	BACOEA	CHPMA	BnA	HFiPA	TMPETA	CzEA	TMCHMA	PBPhMA	PA	CHMA	MTEMA	EHMA	DMAPA
4	TEGMA	FuMA/tBAEMA	MHMB	BOEMA	PhA	MAAHS	TFCAm	FDA	HMA	DEGMA	EHA	PhMA	GMA	DYA	BMAM	DVAd	HDDMA	DEGDA	TPhMAm	CHA	BHMA	HMBAM	iOA	MAPU
5	ExA	pEGPhEA	PFPhMA	BHMOPhP	F7BA	tBMAm	AOHPMA	PMAm	HfCEA	HEODA/EEMA	iDA	MAETA	PBPhA	TMPTA	TMPOTA	HPHPBAH	BTHPhMA	MAHBP	BAC	FOA	PhEMA	HPMAP	AMA	PBBA
6	HPMA	BzHPEA	MAEPC	NpMA	BPAPGDA	DPEPHA	FMHPNMA	PHPMA	SEMA	COEA	TMPDAE	MBAm	APMAm.C	HDMA	PDA	AnMA	HBOPBA	NGPDA	MBMAm	TBPMA	BFEODA	tBAm	BMAOEP	EaNIA
7	EPA	EGDPEA	BAPODA	DFHA	TBNpMA	DEAEA	EEA	OFPMA	tBEMAm	PETrA	BPDMA	TPGDA	iBOMAm	PPPDMA	LaA	BMENBC	13BDDMA	ZnA	HDFDMA	AA	DFHNMA	GDGDA	ECNTA	DFFMOA
8	DEGEEA	OFPA	NaPhA	MAPtMA	pPGDMA	PFPMA	PFPA	PDDMA	IBESMA	DEGDMA	DOAm	BAGDA	HTFDA	E3GDA	DMAEMA	pEGDMA	GPOTA	F6BMA	MAL	DiPEMA	TDFOcA	pEGDA	HBA	DMMAm
9	F6BA	NMEMA	OFHMA	AODMBA	iBMA/tBAEMA	HA	MMA	NDMAm	HFHUMA	14BDDMA	F7BMA	BDDA	EGDA	DMEMAm	EbCNA	MAAH	EGPEA	PETA	EOEA	TBPhA	EGDMA	DAAM	TMHA	13BDDA
10	DDDMA	nOcMA	THFuA	AcAPAm	HFiPMA	iBuMA	EGMEA	DMAEA																

Figure 110. Table of monomers analysed from 9.0 array.

Appendix K – Influence of Wettability or Flexibility on Adsorption of Amino Acids onto Polymer Surfaces.

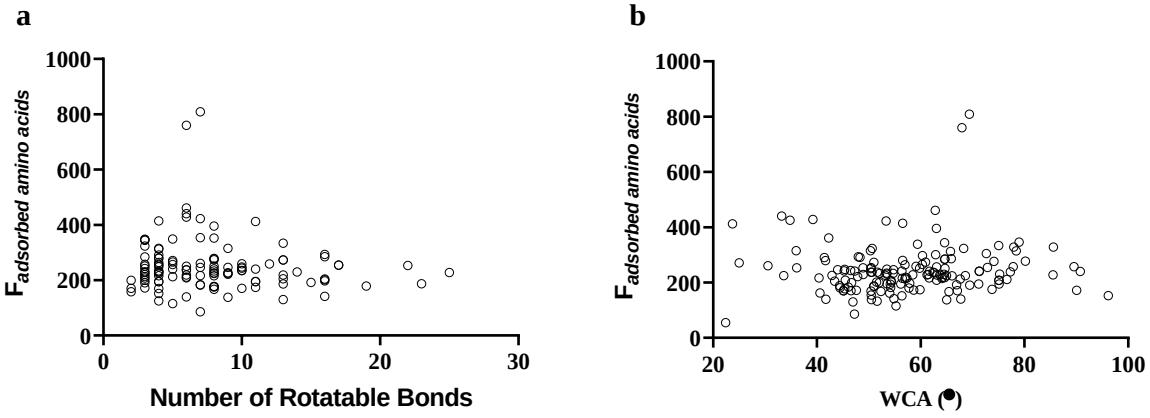

Figure 111. **(a)** Relationship between number of rotatable bonds (flexibility) in a molecule and measured fluorescence intensity of adsorbed amino acids. **(b)** Same as (a) but for wettability.

Appendix L - PLS Analysis for Nutrient Adsorption on 192 Polymer Spots

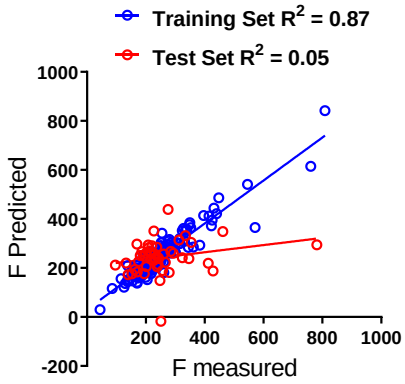

Figure 112. The predicted amino acid adsorption determined from the PLS regression model. Training set (R^2 = 0.87) in blue and test set in red (R^2 = 0.05).

Appendix M - NMR Spectra for BnMA and Purified pBnMA

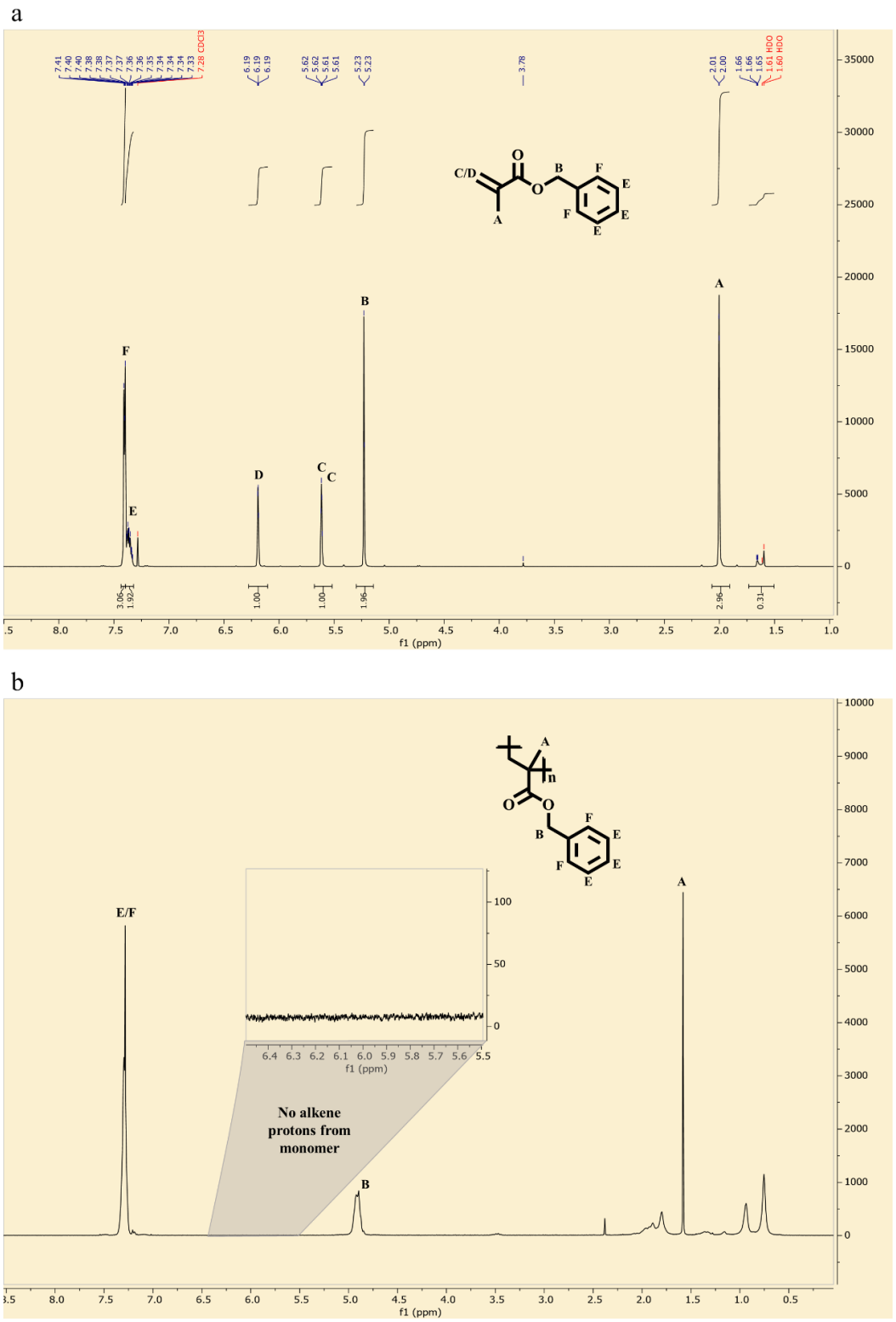

Figure 113. **(a)** [1]HNMR spectrum for BnMA monomer with integrals and assigned peaks labelled from A to F. **(b)** Same convention as (a) but for pBnMA with no integrals.

[1]HNMR (400 MHz, $CDCl_3$): δ (ppm) = 2.01 (s, 3H, CH_3), 5.24 (s, 2H, $1CH_2$), 5.61 (s, 1H, =CH), 6.19 (s, 1H, =CH), 7.32 – 7.39 (m, 2H, 2CH), 7.40 – 7.43 (d, 3H, 3CH).

Appendix N - NMR Analysis for Synthesized CyDMA

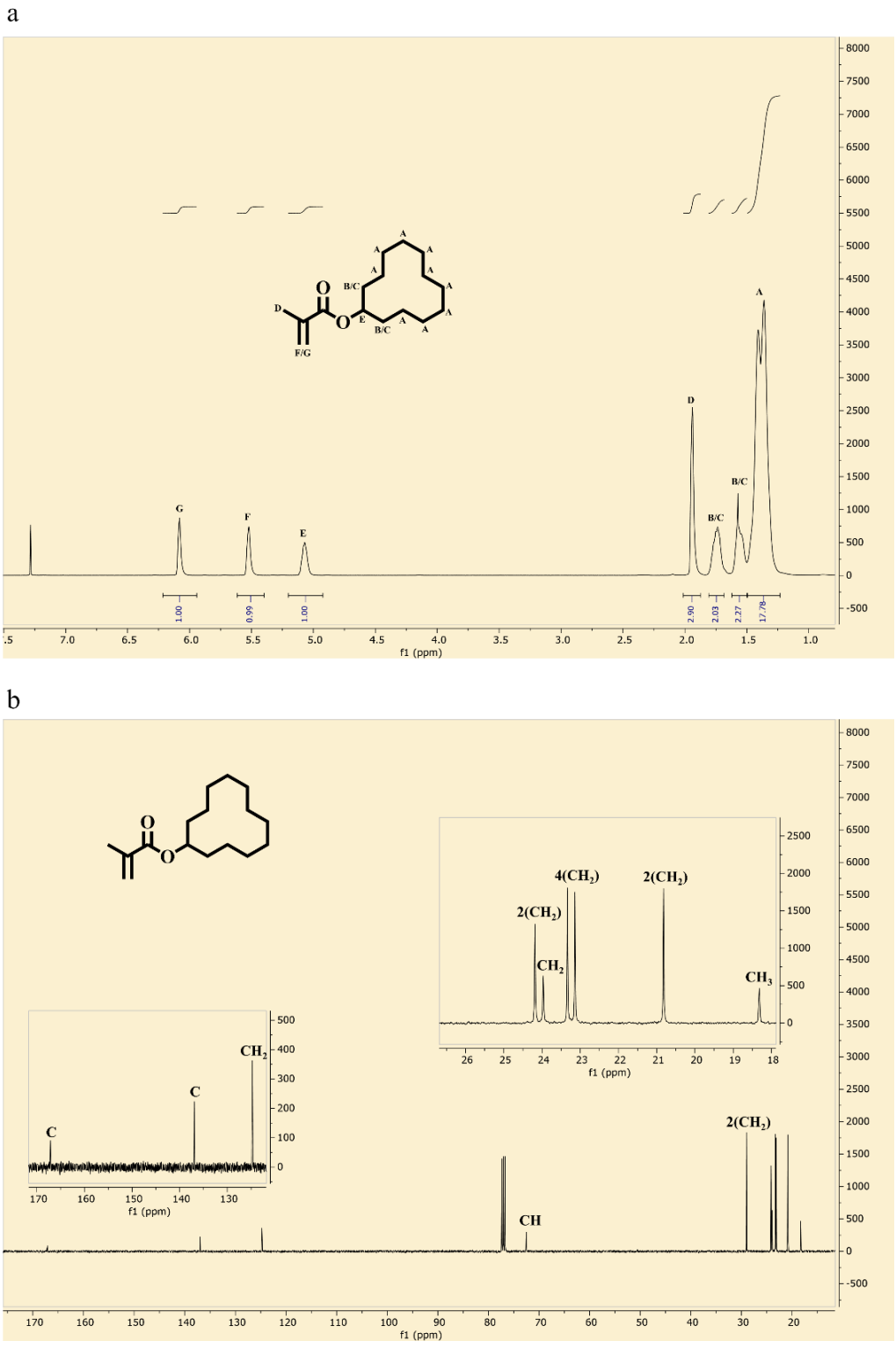

Figure 114. **(a)** [1]HNMR spectrum for CyDMA monomer with integrals and assigned peaks labelled from A to G. **(b)** [13]C NMR for CyDMA monomer.

[1]HNMR (400 MHz, $CDCl_3$): δ (ppm) = 1.38 (s, 18H, $9CH_2$), 1.57 (s, 2H, $1CH_2$), 1.74 (s, 2H, $1CH_2$), 1.94 (s, 3H, $1CH_3$), 5.07 (s, 1H, CH), 5.53 (s, 1H, =CH), 6.09 (s, 1H, =CH).

[13]C NMR (100 MHz, $CDCl_3$): δ 18.31 (CH_3), 20.81 ($2CH_2$), 23.13 ($2CH_2$), 23.34 ($2CH_2$), 23.97 (CH_2), 24.17 ($2CH_2$), 29.00 ($2CH_2$), 72.41 (CH), 124.77 (CH_2), 177.14 (C), 220.19 (C).

Appendix O - NMR spectrum for pCyDMA

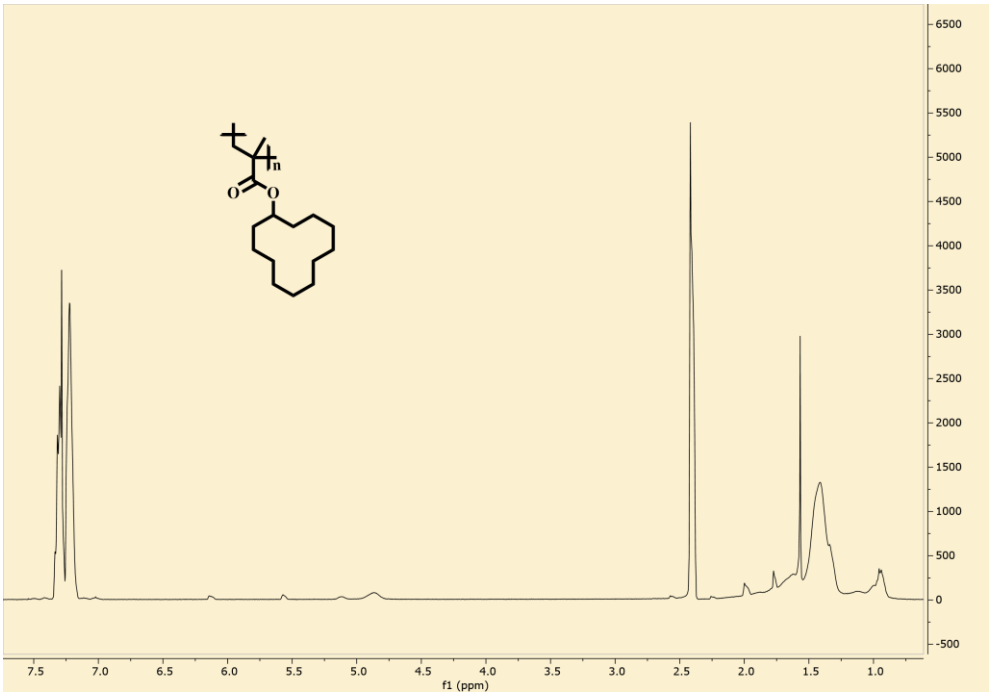

Figure 115. **(a)** ^{1}HNMR spectrum for pCyDMA.

References

1. Dieltjens, L., et al., *Inhibiting bacterial cooperation is an evolutionarily robust anti-biofilm strategy.* Nature Communications, 2020. **11**(1): p. 107.

2. O'NEILL, J. *TACKLING DRUG-RESISTANT INFECTIONS GLOBALLY*. [Review] 2016 [cited 2019 11/02/2019]; Available from: https://amr-review.org/.

3. Stancil, U.D.a.B., *The World Order in 2050*. April 2010, Carnegie Endowment for International Peace Policy Outlook: Carnegie Endowment for International Peace Policy Outlook.

4. Tan, S.Y. and Y. Tatsumura, *Alexander Fleming (1881-1955): Discoverer of penicillin.* Singapore Med J, 2015. **56**(7): p. 366-7.

5. Tuson, H.H. and D.B. Weibel, *Bacteria-surface interactions.* Soft Matter, 2013. **9**(18): p. 4368-4380.

6. Bos, R., H.C. van der Mei, and H.J. Busscher, *Physico-chemistry of initial microbial adhesive interactions--its mechanisms and methods for study.* FEMS Microbiol Rev, 1999. **23**(2): p. 179-230.

7. Costerton, J.W., et al., *Microbial biofilms.* Annu Rev Microbiol, 1995. **49**: p. 711-45.

8. Di Pippo, F., et al., *Biofilm growth and control in cooling water industrial systems.* FEMS Microbiol Ecol, 2018. **94**(5).

9. Nix, I.D., A. Frontzek, and D.P. Bockmuhl, *Characterization of Microbial Communities in Household Washing Machines.* Tenside Surfactants Detergents, 2015. **52**(6): p. 432-440.

10. Debnath, T., et al., *Presence of Multidrug-Resistant Bacteria on Mobile Phones of Healthcare Workers Accelerates the Spread of Nosocomial Infection and Regarded as a Threat to Public Health in Bangladesh.* J Microsc Ultrastruct, 2018. **6**(3): p. 165-169.

11. Meadows, P.S., *The attachment of bacteria to solid surfaces.* Arch Mikrobiol, 1971. **75**(4): p. 374-81.

12. Zhang, W., et al., *Marine biofilms constitute a bank of hidden microbial diversity and functional potential.* Nat Commun, 2019. **10**(1): p. 517.

13. Busscher, H.J. and H.C. van der Mei, *How do bacteria know they are on a surface and regulate their response to an adhering state?* PLoS Pathog, 2012. **8**(1): p. e1002440.

14. Aykin, E., B. Omuzbuken, and A. Kacar, *Microfouling bacteria and the use of enzymes in eco-friendly antifouling technology.* Journal of Coatings Technology and Research, 2019. **16**(3): p. 847-856.

15. Song, S., *An investigation into the effect of biofouling on the ship hydrodynamic characteristics using CFD.* Ocean Engineering, 2019. **175**: p. 122-137.

16. Nurioglu, A.G., A.C.C. Esteves, and G. de With, *Non-toxic, non-biocide-release antifouling coatings based on molecular structure design for marine applications.* Journal of Materials Chemistry B, 2015. **3**(32): p. 6547-6570.

17. Rogelj, J., et al., *Paris Agreement climate proposals need a boost to keep warming well below 2 degrees C.* Nature, 2016. **534**(7609): p. 631-9.

18. Römling, U., et al., *Microbial biofilm formation: a need to act.* Journal of internal medicine, 2014. **276**(2): p. 98-110.

19. Raghupathi, P.K., et al., *Microbiomes in Dishwashers: Analysis of the microbial diversity and putative opportunistic pathogens in dishwasher biofilm communities.* Appl Environ Microbiol, 2018.

20. Liu, D.P., et al., *Characteristics of biofilm community structure in a reclaimed water cast iron pipeline.* Environmental Science-Water Research & Technology, 2018. **4**(10): p. 1489-1500.

21. Medicine, I.o., *Public Policy Options for Better Dental Health: Report of a Study*. 1980, Washington, DC: The National Academies Press. 167.

22. Yu, O.Y., et al., *Dental Biofilm and Laboratory Microbial Culture Models for Cariology Research.* Dentistry journal, 2017. **5**(2): p. 21.

23. Jamal, M., et al., *Bacterial biofilm and associated infections.* J Chin Med Assoc, 2018. **81**(1): p. 7-11.

24. Garrett, T.R., M. Bhakoo, and Z. Zhang, *Bacterial adhesion and biofilms on surfaces.* Progress in Natural Science, 2008. **18**(9): p. 1049-1056.

25. Khan, H.A., F.K. Baig, and R. Mehboob, *Nosocomial infections: Epidemiology, prevention, control and surveillance.* Asian Pacific Journal of Tropical Biomedicine, 2017. **7**(5): p. 478-482.

26. Cloutier, M., D. Mantovani, and F. Rosei, *Antibacterial Coatings: Challenges, Perspectives, and Opportunities.* Trends Biotechnol, 2015. **33**(11): p. 637-52.

27. Follmer, C., *Ureases as a target for the treatment of gastric and urinary infections.* Journal of Clinical Pathology, 2010. **63**(5): p. 424.

28. Pezzaniti, J.L., et al., *Preliminary investigation of near-infrared spectroscopic measurements of urea, creatinine, glucose, protein, and ketone in urine.* Clinical Biochemistry, 2001. **34**(3): p. 239-246.

29. McCoy, C.P., et al., *An Infection-Responsive Approach To Reduce Bacterial Adhesion in Urinary Biomaterials.* Molecular Pharmaceutics, 2016. **13**(8): p. 2817-2822.

30. Espinosa-Ortiz, E.J. and R. Gerlach, *Struvite Stone Formation by Ureolytic Biofilms*, in *The Role of Bacteria in Urology*, D. Lange and K.B. Scotland, Editors. 2019, Springer International Publishing: Cham. p. 61-70.

31. Marcus, R.J., et al., *Biofilms in nephrology.* Expert Opinion on Biological Therapy, 2008. **8**(8): p. 1159-1166.

32. Choong, S., et al., *Catheter associated urinary tract infection and encrustation.* International Journal of Antimicrobial Agents, 2001. **17**(4): p. 305-310.

33. Rice, L.B., *Federal funding for the study of antimicrobial resistance in nosocomial pathogens: no ESKAPE.* J Infect Dis, 2008. **197**(8): p. 1079-81.

34. De Angelis, G., et al., *Incidence and antimicrobial resistance trends in bloodstream infections caused by ESKAPE and Escherichia coli at a large teaching hospital in Rome, a 9-year analysis (2007-2015).* European Journal of Clinical Microbiology & Infectious Diseases, 2018. **37**(9): p. 1627-1636.

35. Silhavy, T.J., D. Kahne, and S. Walker, *The Bacterial Cell Envelope.* Cold Spring Harbor Perspectives in Biology, 2010. **2**(5): p. a000414.

36. Cabeen, M.T. and C. Jacobs-Wagner, *Bacterial cell shape.* Nature Reviews Microbiology, 2005. **3**(8): p. 601-610.

37. Kaplan, M.L. and L. Kaplan, *The Gram Stain and Differential Staining.* Journal of bacteriology, 1933. **25**(3): p. 309-321.

38. Beveridge, T.J. and L.L. Graham, *Surface layers of bacteria.* Microbiological Reviews, 1991. **55**(4): p. 684.

39. Meroueh, S.O., et al., *Three-dimensional structure of the bacterial cell wall peptidoglycan.* Proceedings of the National Academy of Sciences of the United States of America, 2006. **103**(12): p. 4404-4409.

40. Navarre, W.W. and O. Schneewind, *Surface Proteins of Gram-Positive Bacteria and Mechanisms of Their Targeting to the Cell Wall Envelope.* Microbiology and Molecular Biology Reviews, 1999. **63**(1): p. 174.

41. Fischetti, V.A., *Surface Proteins on Gram-Positive Bacteria.* Microbiology spectrum, 2019. **7**(4): p. 10.1128/microbiolspec.GPP3-0012-2018.

42. Tankeshwar, A. *Teichoic Acid/Lipoteichoic acid: Characteristics and Medical Importance*. 2013 [cited 2020 21/02/2020]; Available from: https://microbeonline.com/teichoic-acid-of-gram-positive-bacteria-characteristics-and-medical-importance/.

43. Swoboda, J.G., et al., *Wall Teichoic Acid Function, Biosynthesis, and Inhibition.* ChemBioChem, 2010. **11**(1): p. 35-45.

44. Brown, S., J.P.S.M. Jr., and S. Walker, *Wall Teichoic Acids of Gram-Positive Bacteria.* Annual Review of Microbiology, 2013. **67**(1): p. 313-336.

45. Neuhaus, F.C. and J. Baddiley, *A Continuum of Anionic Charge: Structures and Functions of d-Alanyl-Teichoic Acids in Gram-Positive Bacteria.* Microbiology and Molecular Biology Reviews, 2003. **67**(4): p. 686.

46. Naseem, S. and J.B. Konopka, *N-acetylglucosamine Regulates Virulence Properties in Microbial Pathogens.* PLoS pathogens, 2015. **11**(7): p. e1004947-e1004947.

47. Peschel, A., et al., *Inactivation of the dlt operon in Staphylococcus aureus confers sensitivity to defensins, protegrins, and other antimicrobial peptides.* J Biol Chem, 1999. **274**(13): p. 8405-10.

48. Jucker, B.A., H. Harms, and A.J. Zehnder, *Adhesion of the positively charged bacterium Stenotrophomonas (Xanthomonas) maltophilia 70401 to glass and Teflon.* Journal of Bacteriology, 1996. **178**(18): p. 5472.

49. Anderson, E.M., et al., *Peptidoglycomics reveals compositional changes in peptidoglycan between biofilm- and planktonic-derived Pseudomonas aeruginosa.* Journal of Biological Chemistry, 2019.

50. Chang, J.D., et al., *Peptidoglycan Compositional Analysis of Enterococcus faecalis Biofilm by Stable Isotope Labeling by Amino Acids in a Bacterial Culture.* Biochemistry, 2018. **57**(7): p. 1274-1283.

51. van Loosdrecht, M.C., et al., *Electrophoretic mobility and hydrophobicity as a measured to predict the initial steps of bacterial adhesion.* Applied and Environmental Microbiology, 1987. **53**(8): p. 1898.

52. Beveridge, T.J., *Structures of Gram-Negative Cell Walls and Their Derived Membrane Vesicles.* Journal of Bacteriology, 1999. **181**(16): p. 4725.

53. Osborn, M.J., et al., *Lipopolysaccharide of the Gram-Negative Cell Wall.* Science, 1964. **145**(3634): p. 783.

54. Zamyatina, A., *Aminosugar-based immunomodulator lipid A: synthetic approaches.* Beilstein journal of organic chemistry, 2018. **14**: p. 25-53.

55. King, J.D., et al., *Review: Lipopolysaccharide biosynthesis in Pseudomonas aeruginosa.* Innate Immunity, 2009. **15**(5): p. 261-312.

56. Gunn, J.S. and R.K. Ernst, *The structure and function of Francisella lipopolysaccharide.* Annals of the New York Academy of Sciences, 2007. **1105**: p. 202-218.

57. Makin, S.A. and T.J. Beveridge, *The influence of A-band and B-band lipopolysaccharide on the surface characteristics and adhesion of Pseudomonas aeruginosa to surfaces.* Microbiology, 1996. **142**(2): p. 299-307.

58. Walker, S.L., J.A. Redman, and M. Elimelech, *Role of Cell Surface Lipopolysaccharides in Escherichia coli K12 Adhesion and Transport.* Langmuir, 2004. **20**(18): p. 7736-7746.

59. Ciornei, C.D., et al., *Biofilm-forming Pseudomonas aeruginosa bacteria undergo lipopolysaccharide structural modifications and induce enhanced inflammatory cytokine response in human monocytes.* Innate Immunity, 2009. **16**(5): p. 288-301.

60. Chalabaev, S., et al., *Biofilms Formed by Gram-Negative Bacteria Undergo Increased Lipid A Palmitoylation, Enhancing In Vivo Survival.* mBio, 2014. **5**(4): p. e01116-14.

61. Zabłotni, A., et al., *Changes in the lipopolysaccharide of Proteus mirabilis 9B-m (O11a) clinical strain in response to planktonic or biofilm type of growth.* Medical microbiology and immunology, 2018. **207**(2): p. 129-139.

62. Katsikogianni, M. and Y.F. Missirlis, *Concise review of mechanisms of bacterial adhesion to biomaterials and of techniques used in estimating bacteria-material interactions.* Eur Cell Mater, 2004. **8**: p. 37-57.

63. Dang, H. and C.R. Lovell, *Microbial Surface Colonization and Biofilm Development in Marine Environments.* Microbiol Mol Biol Rev, 2016. **80**(1): p. 91-138.

64. Characklis, W.G. and K.E. Cooksey, *Biofilms and Microbial Fouling.* Advances in Applied Microbiology, 1983. **29**: p. 93-138.

65. Van Houte, J. and D.B. Green, *Relationship between the concentration of bacteria in saliva and the colonization of teeth in humans.* Infect Immun, 1974. **9**(4): p. 624-30.

66. Duddridge, J.E., C.A. Kent, and J.F. Laws, *Effect of Surface Shear-Stress on the Attachment of Pseudomonas-Fluorescens to Stainless-Steel under Defined Flow Conditions.* Biotechnology and Bioengineering, 1982. **24**(1): p. 153-164.

67. Lorite, G.S., et al., *The role of conditioning film formation and surface chemical changes on Xylella fastidiosa adhesion and biofilm evolution.* Journal of Colloid and Interface Science, 2011. **359**(1): p. 289-295.

68. Gristina, A.G., P. Naylor, and Q. Myrvik, *Infections from biomaterials and implants: a race for the surface.* Med Prog Technol, 1988. **14**(3-4): p. 205-24.

69. Schmidt, D.R., H. Waldeck, and W.J. Kao, *Protein Adsorption to Biomaterials*, in *Biological Interactions on Materials Surfaces: Understanding and Controlling Protein, Cell, and Tissue Responses*, D.A. Puleo and R. Bizios, Editors. 2009, Springer US: New York, NY. p. 1-18.

70. Rabe, M., D. Verdes, and S. Seeger, *Understanding protein adsorption phenomena at solid surfaces.* Advances in Colloid and Interface Science, 2011. **162**(1): p. 87-106.

71. Recek, N., et al., *Protein Adsorption on Various Plasma-Treated Polyethylene Terephthalate Substrates.* Molecules, 2013. **18**(10).

72. Zobell, C.E., *The Effect of Solid Surfaces upon Bacterial Activity.* J Bacteriol, 1943. **46**(1): p. 39-56.

73. González-García, C., et al., *The strength of the protein-material interaction determines cell fate.* Acta Biomaterialia, 2018. **77**: p. 74-84.

74. Arima, Y. and H. Iwata, *Preferential adsorption of cell adhesive proteins from complex media on self-assembled monolayers and its effect on subsequent cell adhesion.* Acta Biomaterialia, 2015. **26**: p. 72-81.

75. Xu, L.-C. and C.A. Siedlecki, *Effects of surface wettability and contact time on protein adhesion to biomaterial surfaces.* Biomaterials, 2007. **28**(22): p. 3273-3283.

76. Vogler, E.A., *Water and the acute biological response to surfaces.* Journal of Biomaterials Science, Polymer Edition, 1999. **10**(10): p. 1015-1045.

77. Prime, K.L. and G.M. Whitesides, *Adsorption of proteins onto surfaces containing end-attached oligo(ethylene oxide): a model system using self-assembled monolayers.* Journal of the American Chemical Society, 1993. **115**(23): p. 10714-10721.

78. Sethuraman, A., et al., *Effect of Surface Wettability on the Adhesion of Proteins.* Langmuir, 2004. **20**(18): p. 7779-7788.

79. Chapman, R.G., et al., *Surveying for Surfaces that Resist the Adsorption of Proteins.* Journal of the American Chemical Society, 2000. **122**(34): p. 8303-8304.

80. Ostuni, E., et al., *Self-Assembled Monolayers That Resist the Adsorption of Proteins and the Adhesion of Bacterial and Mammalian Cells.* Langmuir, 2001. **17**(20): p. 6336-6343.

81. Wang, Z. and H. Zuilhof, *Antifouling Properties of Fluoropolymer Brushes toward Organic Polymers: The Influence of Composition, Thickness, Brush Architecture, and Annealing.* Langmuir : the ACS journal of surfaces and colloids, 2016. **32**(26): p. 6571-6581.

82. Halvey, A.K., et al., *Design of surfaces for controlling hard and soft fouling.* Philosophical Transactions of the Royal Society A: Mathematical, Physical and Engineering Sciences, 2019. **377**(2138): p. 20180266.

83. Jeon, S.I., et al., *Protein—surface interactions in the presence of polyethylene oxide: I. Simplified theory.* Journal of Colloid and Interface Science, 1991. **142**(1): p. 149-158.

84. Jeon, S.I. and J.D. Andrade, *Protein—surface interactions in the presence of polyethylene oxide: II. Effect of protein size.* Journal of Colloid and Interface Science, 1991. **142**(1): p. 159-166.

85. Binazadeh, M., M. Kabiri, and L.D. Unsworth, *Poly(ethylene glycol) and Poly(carboxy betaine) Based Nonfouling Architectures: Review and Current Efforts*, in *Proteins at Interfaces III State of the Art*. 2012, American Chemical Society. p. 621-643.

86. Shahkaramipour, N., et al., *Membranes with Surface-Enhanced Antifouling Properties for Water Purification.* Membranes, 2017. **7**(1).

87. Rau, D.C. and V.A. Parsegian, *Direct measurement of forces between linear polysaccharides xanthan and schizophyllan.* Science, 1990. **249**(4974): p. 1278.

88. Luk, Y.-Y., M. Kato, and M. Mrksich, *Self-Assembled Monolayers of Alkanethiolates Presenting Mannitol Groups Are Inert to Protein Adsorption and Cell Attachment.* Langmuir, 2000. **16**(24): p. 9604-9608.

89. Hook, A.L., et al., *Combinatorial discovery of polymers resistant to bacterial attachment.* Nat Biotechnol, 2012. **30**(9): p. 868-75.

90. Rosenhahn, A., et al., *The role of "inert" surface chemistry in marine biofouling prevention.* Physical Chemistry Chemical Physics, 2010. **12**(17): p. 4275-4286.

91. Alexander, M.R. and P. Williams, *Water contact angle is not a good predictor of biological responses to materials.* Biointerphases, 2017. **12**(2).

92. An, Y.H. and R.J. Friedman, *Concise review of mechanisms of bacterial adhesion to biomaterial surfaces.* J Biomed Mater Res, 1998. **43**(3): p. 338-48.

93. Zita, A. and M. Hermansson, *Effects of ionic strength on bacterial adhesion and stability of flocs in a wastewater activated sludge system.* Appl Environ Microbiol, 1994. **60**(9): p. 3041-8.

94. Otto, K., H. Elwing, and M. Hermansson, *Effect of ionic strength on initial interactions of Escherichia coli with surfaces, studied on-line by a novel quartz crystal microbalance technique.* J Bacteriol, 1999. **181**(17): p. 5210-8.

95. Jucker, B.A., A.J.B. Zehnder, and H. Harms, *Quantification of Polymer Interactions in Bacterial Adhesion.* Environmental Science & Technology, 1998. **32**(19): p. 2909-2915.

96. Salerno, M.B., B.E. Logan, and D. Velegol, *Importance of molecular details in predicting bacterial adhesion to hydrophobic surfaces.* Langmuir, 2004. **20**(24): p. 10625-9.

97. Lindhout, T., et al., *Truncation in the core oligosaccharide of lipopolysaccharide affects flagella-mediated motility in Pseudomonas aeruginosa PAO1 via modulation of cell surface attachment.* Microbiology-Sgm, 2009. **155**: p. 3449-3460.

98. Kearns, D.B., *A field guide to bacterial swarming motility.* Nat Rev Microbiol, 2010. **8**(9): p. 634-44.

99. Maier, B. and G.C.L. Wong, *How Bacteria Use Type IV Pili Machinery on Surfaces.* Trends in Microbiology, 2015. **23**(12): p. 775-788.

100. Tolker-Nielsen, T., et al., *Development and dynamics of Pseudomonas sp biofilms.* Journal of Bacteriology, 2000. **182**(22): p. 6482-6489.

101. Jain, R. and B.I. Kazmierczak, *Should I Stay or Should I Go? Pseudomonas Just Can't Decide.* Cell Host & Microbe, 2019. **25**(1): p. 5-7.

102. Conrad, J.C., et al., *Flagella and Pili-Mediated Near-Surface Single-Cell Motility Mechanisms in P. aeruginosa.* Biophysical Journal, 2011. **100**(7): p. 1608-1616.

103. O'May, C. and N. Tufenkji, *The Swarming Motility of Pseudomonas aeruginosa Is Blocked by Cranberry Proanthocyanidins and Other Tannin-Containing Materials.* Applied and Environmental Microbiology, 2011. **77**(9): p. 3061-3067.

104. Ellison, C.K., et al., *Obstruction of pilus retraction stimulates bacterial surface sensing.* Science, 2017. **358**(6362): p. 535-538.

105. Wang, R.J., et al., *The Second Messenger c-di-GMP Adjusts Motility and Promotes Surface Aggregation of Bacteria.* Biophysical Journal, 2018. **115**(11): p. 2242-2249.

106. Berne, C., et al., *Bacterial adhesion at the single-cell level.* Nature Reviews Microbiology, 2018. **16**(10): p. 616-627.

107. Buijssen, K.J.D.A., et al., *Influence of surface roughness on silicone rubber voice prostheses on in vitro biofilm formation and clinical lifetime in laryngectomised patients.* Clinical Otolaryngology, 2017. **42**(6): p. 1235-1240.

108. Glauser, S., et al., *Bacterial colonization of resin composite cements: influence of material composition and surface roughness.* European Journal of Oral Sciences, 2017. **125**(4): p. 294-302.

109. Lieberzeit, P.A., et al., *Softlithography in Chemical Sensing – Analytes from Molecules to Cells.* Sensors (Basel, Switzerland), 2005. **5**(12): p. 509-518.

110. Ammar, Y., et al., *Influence of surface roughness on the initial formation of biofilm.* Surface & Coatings Technology, 2015. **284**: p. 410-416.

111. Tang, H., et al., *Influence of silicone surface roughness and hydrophobicity on adhesion and colonization of Staphylococcus epidermidis.* J Biomed Mater Res A, 2009. **88**(2): p. 454-63.

112. Vadillo-Rodriguez, V., et al., *Bacterial response to spatially organized microtopographic surface patterns with nanometer scale roughness.* Colloids and Surfaces B-Biointerfaces, 2018. **169**: p. 340-347.

113. Song, F., et al., *How Bacteria Respond to Material Stiffness during Attachment: A Role of Escherichia coil Flagellar Motility.* Acs Applied Materials & Interfaces, 2017. **9**(27): p. 22176-22184.

114. Kolewe, K.W., S.R. Peyton, and J.D. Schiffman, *Fewer Bacteria Adhere to Softer Hydrogels.* Acs Applied Materials & Interfaces, 2015. **7**(35): p. 19562-19569.

115. Yoda, I., et al., *Effect of surface roughness of biomaterials on Staphylococcus epidermidis adhesion.* BMC Microbiology, 2014. **14**(1): p. 1-7.

116. Andreotti, A.M., et al., *In vitro evaluation of microbial adhesion on the different surface roughness of acrylic resin specific for ocular prosthesis.* Eur J Dent, 2018. **12**(2): p. 176-183.

117. Yang, J., et al., *Probing the Structural Dependence of Carbon Space Lengths of Poly(N-hydroxyalkyl acrylamide)-Based Brushes on Antifouling Performance.* Biomacromolecules, 2014. **15**(8): p. 2982-2991.

118. van der Westen, R., et al., *Floating and Tether-Coupled Adhesion of Bacteria to Hydrophobic and Hydrophilic Surfaces.* Langmuir, 2018. **34**(17): p. 4937-4944.

119. Straub, H., et al., *Bacterial Adhesion on Soft Materials: Passive Physicochemical Interactions or Active Bacterial Mechanosensing?* Advanced Healthcare Materials, 2019. **8**(8).

120. Cheng, Y.F. and C.I. Moraru, *Long-range interactions keep bacterial cells from liquid-solid interfaces: Evidence of a bacteria exclusion zone near Nafion surfaces and possible implications for bacterial attachment.* Colloids and Surfaces B-Biointerfaces, 2018. **162**: p. 16-24.

121. Bioscience, L. *RPMI 1640 Medium without L-Glutamine*. 2019 [cited 2019 September]; Available from: https://bioscience.lonza.com/lonza_bs/LU/en/Culture-Media-and-Reagents/p/000000000000183913/RPMI-1640-Medium-without-L-Glutamine#accept.

122. Sanni, O., et al., *Bacterial attachment to polymeric materials correlates with molecular flexibility and hydrophilicity.* Adv Healthc Mater, 2015. **4**(5): p. 695-701.

123. Parreira, P., et al., *Effect of surface chemistry on bacterial adhesion, viability, and morphology.* J Biomed Mater Res A, 2011. **99**(3): p. 344-53.

124. Carniello, V., et al., *Physico-chemistry from initial bacterial adhesion to surface-programmed biofilm growth.* Advances in Colloid and Interface Science, 2018. **261**: p. 1-14.

125. Römling, U., M.Y. Galperin, and M. Gomelsky, *Cyclic di-GMP: the first 25 years of a universal bacterial second messenger.* Microbiology and molecular biology reviews : MMBR, 2013. **77**(1): p. 1-52.

126. Lin, T.-Y. and D.B. Weibel, *Organization and function of anionic phospholipids in bacteria.* Applied Microbiology and Biotechnology, 2016. **100**(10): p. 4255-4267.

127. Franklin, M., et al., *Biosynthesis of the Pseudomonas aeruginosa Extracellular Polysaccharides, Alginate, Pel, and Psl.* Frontiers in Microbiology, 2011. **2**(167).

128. Tsuneda, S., et al., *Extracellular polymeric substances responsible for bacterial adhesion onto solid surface.* FEMS Microbiology Letters, 2003. **223**(2): p. 287-292.

129. Zhao, W., et al., *Bacterial cell surface properties: Role of loosely bound extracellular polymeric substances (LB-EPS).* Colloids and Surfaces B: Biointerfaces, 2015. **128**: p. 600-607.

130. Strathmann, M., J. Wingender, and H.-C. Flemming, *Application of fluorescently labelled lectins for the visualization and biochemical characterization of polysaccharides in biofilms of Pseudomonas aeruginosa.* Journal of Microbiological Methods, 2002. **50**(3): p. 237-248.

131. Friedman, M., *Applications of the ninhydrin reaction for analysis of amino acids, peptides, and proteins to agricultural and biomedical sciences.* Journal of Agricultural and Food Chemistry, 2004. **52**(3): p. 385-406.

132. Yang, L., et al., *Distinct roles of extracellular polymeric substances in Pseudomonas aeruginosa biofilm development.* Environmental Microbiology, 2011. **13**(7): p. 1705-1717.

133. Toyofuku, M., et al., *Identification of Proteins Associated with the Pseudomonas aeruginosa Biofilm Extracellular Matrix.* Journal of Proteome Research, 2012. **11**(10): p. 4906-4915.

134. Wingender, J., T.R. Neu, and H.-C. Flemming, *What are Bacterial Extracellular Polymeric Substances?*, in *Microbial Extracellular Polymeric Substances: Characterization, Structure and Function*, J. Wingender, T.R. Neu, and H.-C. Flemming, Editors. 1999, Springer Berlin Heidelberg: Berlin, Heidelberg. p. 1-19.

135. Flemming, H.C. and J. Wingender, *Relevance of microbial extracellular polymeric substances (EPSs) - Part I: Structural and ecological aspects.* Water Science and Technology, 2001. **43**(6): p. 1-8.

136. Zeng, G.H., R. Ogaki, and R.L. Meyer, *Non-proteinaceous bacterial adhesins challenge the antifouling properties of polymer brush coatings.* Acta Biomaterialia, 2015. **24**: p. 64-73.

137. Rodriguez-Martinez, J.M. and A. Pascual, *Antimicrobial resistance in bacterial biofilms.* Reviews in Medical Microbiology, 2006. **17**(3): p. 65-75.

138. Stone, J.H., M.M. Gabriel, and D.G. Ahearn, *Adherence of Pseudomonas aeruginosa to inanimate polymers including biomaterials.* J Ind Microbiol Biotechnol, 1999. **23**(1): p. 713-7.

139. Stewart, P.S. and J.W. Costerton, *Antibiotic resistance of bacteria in biofilms.* Lancet, 2001. **358**(9276): p. 135-8.

140. Li, X., et al., *Synergistic in vitro effects of indocyanine green and ethylenediamine tetraacetate-mediated antimicrobial photodynamic therapy combined with antibiotics for resistant bacterial biofilms in diabetic foot infection.* Photodiagnosis Photodyn Ther, 2019. **25**: p. 300-308.

141. Kochkodan, V. and N. Hilal, *A comprehensive review on surface modified polymer membranes for biofouling mitigation.* Desalination, 2015. **356**: p. 187-207.

142. Bordi, C. and S. de Bentzmann, *Hacking into bacterial biofilms: a new therapeutic challenge.* Annals of Intensive Care, 2011. **1**.

143. Von Eiff, C., et al., *Modern strategies in the prevention of implant-associated infections.* International Journal of Artificial Organs, 2005. **28**(11): p. 1146-1156.

144. Chen, X., et al., *Structural identification of a bacterial quorum-sensing signal containing boron.* Nature, 2002. **415**(6871): p. 545-549.

145. Reading, N.C. and V. Sperandio, *Quorum sensing: the many languages of bacteria.* FEMS Microbiology Letters, 2006. **254**(1): p. 1-11.

146. Diggle, S.P., et al., *Cooperation and conflict in quorum-sensing bacterial populations.* Nature, 2007. **450**(7168): p. 411-414.

147. Hawver, L.A., S.A. Jung, and W.-L. Ng, *Specificity and complexity in bacterial quorum-sensing systems.* FEMS Microbiology Reviews, 2016. **40**(5): p. 738-752.

148. Smith, R.S. and B.H. Iglewski, *P. aeruginosa quorum-sensing systems and virulence.* Current Opinion in Microbiology, 2003. **6**(1): p. 56-60.

149. Papenfort, K. and B.L. Bassler, *Quorum sensing signal–response systems in Gram-negative bacteria.* Nature Reviews Microbiology, 2016. **14**(9): p. 576-588.

150. Williams, P. and M. Cámara, *Quorum sensing and environmental adaptation in Pseudomonas aeruginosa: a tale of regulatory networks and multifunctional signal molecules.* Current Opinion in Microbiology, 2009. **12**(2): p. 182-191.

151. McKnight, S.L., B.H. Iglewski, and E.C. Pesci, *The Pseudomonas Quinolone Signal Regulates rhl Quorum Sensing in Pseudomonas aeruginosa</em&gt.* Journal of Bacteriology, 2000. **182**(10): p. 2702.

152. De Kievit, T.R., *Quorum sensing in Pseudomonas aeruginosa biofilms.* Environmental Microbiology, 2009. **11**(2): p. 279-288.

153. Waters, C.M. and B.L. Bassler, *Quorum sensing: cell-to-cell communication in bacteria.* Annual review of cell and developmental biology, 2005. **21**: p. 319-346.

154. Yarwood, J.M., et al., *Quorum Sensing in Staphylococcus aureus Biofilms.* Journal of Bacteriology, 2004. **186**(6): p. 1838.

155. Yarwood, J.M. and P.M. Schlievert, *Quorum sensing in Staphylococcus infections.* The Journal of Clinical Investigation, 2003. **112**(11): p. 1620-1625.

156. Rutherford, S.T. and B.L. Bassler, *Bacterial quorum sensing: its role in virulence and possibilities for its control.* Cold Spring Harbor perspectives in medicine, 2012. **2**(11): p. a012427.

157. Pollitt, E.J.G., et al., *Cooperation, Quorum Sensing, and Evolution of Virulence in <span class="named-content genus-species" id="named-content-1">Staphylococcus aureus</span&gt.* Infection and Immunity, 2014. **82**(3): p. 1045.

158. Cardo, D., et al., *National Nosocomial Infections Surveillance (NNIS) System Report, data summary from January 1992 through June 2004, issued October 2004.* American Journal of Infection Control, 2004. **32**(8): p. 470-485.

159. Mandakhalikar, K.D., R.R. Chua, and P.A. Tambyah, *New Technologies for Prevention of Catheter Associated Urinary Tract Infection.* Current Treatment Options in Infectious Diseases, 2016. **8**(1): p. 24-41.

160. Warren, J.W., *Catheter-associated urinary tract infections.* Int J Antimicrob Agents, 2001. **17**(4): p. 299-303.

161. Zhu, Z.L., et al., *Antimicrobial strategies for urinary catheters.* Journal of Biomedical Materials Research Part A, 2019. **107**(2): p. 445-467.

162. Lam, T.B.L., et al., *Types of indwelling urethral catheters for short-term catheterisation in hospitalised adults.* Cochrane Database of Systematic Reviews, 2014(9).

163. Feneley, R.C., I.B. Hopley, and P.N. Wells, *Urinary catheters: history, current status, adverse events and research agenda.* J Med Eng Technol, 2015. **39**(8): p. 459-70.

164. JF Falconer, D.G., *Metallic, Ceramic, and Polymeric Biomaterials*. Elsevier. Vol. 1. 2017, United Kingdom: Oliver Walter. 13.

165. Neoh, K.G., et al., *Surface modification strategies for combating catheter-related complications: recent advances and challenges.* Journal of Materials Chemistry B, 2017. **5**(11): p. 2045-2067.

166. Roy, A., et al., *Green synthesis of silver nanoparticles: biomolecule-nanoparticle organizations targeting antimicrobial activity.* RSC Advances, 2019. **9**(5): p. 2673-2702.

167. Ogilvie, A.T., et al., *In vitro evaluation of the impact of silver coating on Escherichia coli adherence to urinary catheters.* Can Vet J, 2015. **56**(5): p. 490-4.

168. Wang, R., et al., *Antifouling coating with controllable and sustained silver release for long-term inhibition of infection and encrustation in urinary catheters.* J Biomed Mater Res B Appl Biomater, 2015. **103**(3): p. 519-28.

169. *Prevention of Catheter-Associated Urinary Tract Infections Using Silver Impregnated Catheters: Does Silver Matter?* American Journal of Infection Control, 2009. **37**(5): p. E51-E52.

170. Grainger, D.W., et al., *Critical factors in the translation of improved antimicrobial strategies for medical implants and devices.* Biomaterials, 2013. **34**(37): p. 9237-9243.

171. AshaRani, P.V., et al., *Cytotoxicity and Genotoxicity of Silver Nanoparticles in Human Cells.* ACS Nano, 2009. **3**(2): p. 279-290.

172. Desai, D.G., et al., *Silver or nitrofurazone impregnation of urinary catheters has a minimal effect on uropathogen adherence.* J Urol, 2010. **184**(6): p. 2565-71.

173. Fisher, L.E., et al., *Biomaterial modification of urinary catheters with antimicrobials to give long-term broadspectrum antibiofilm activity.* J Control Release, 2015. **202**: p. 57-64.

174. Martinez, J.L. and F. Baquero, *Interactions among strategies associated with bacterial infection: Pathogenicity, epidemicity, and antibiotic resistance.* Clinical Microbiology Reviews, 2002. **15**(4): p. 647-+.

175. Chen, M., Q.S. Yu, and H.M. Sun, *Novel Strategies for the Prevention and Treatment of Biofilm Related Infections.* International Journal of Molecular Sciences, 2013. **14**(9): p. 18488-18501.

176. Zander, Z.K., et al., *Post-fabrication QAC-functionalized thermoplastic polyurethane for contact-killing catheter applications.* Biomaterials, 2018. **178**: p. 339-350.

177. Huang, J., et al., *Antibacterial polypropylene via surface-initiated atom transfer radical polymerization.* Biomacromolecules, 2007. **8**(5): p. 1396-9.

178. Knetsch, M.L.W. and L.H. Koole, *New Strategies in the Development of Antimicrobial Coatings: The Example of Increasing Usage of Silver and Silver Nanoparticles.* Polymers, 2011. **3**(1).

179. Wang, S., et al., *Do quaternary ammonium monomers induce drug resistance in cariogenic, endodontic and periodontal bacterial species?* Dental Materials, 2017. **33**(10): p. 1127-1138.

180. Ioannou, C.J., G.W. Hanlon, and S.P. Denyer, *Action of disinfectant quaternary ammonium compounds against Staphylococcus aureus.* Antimicrobial Agents and Chemotherapy, 2007. **51**(1): p. 296-306.

181. Li, P., et al., *A polycationic antimicrobial and biocompatible hydrogel with microbe membrane suctioning ability.* Nature Materials, 2011. **10**(2): p. 149-156.

182. Han, H., et al., *Immobilization of amphiphilic polycations by catechol functionality for antimicrobial coatings.* Langmuir, 2011. **27**(7): p. 4010-9.

183. Cen, L., K.G. Neoh, and E.T. Kang, *Surface Functionalization Technique for Conferring Antibacterial Properties to Polymeric and Cellulosic Surfaces.* Langmuir, 2003. **19**(24): p. 10295-10303.

184. Yu, K., et al., *Anti-adhesive antimicrobial peptide coating prevents catheter associated infection in a mouse urinary infection model.* Biomaterials, 2017. **116**: p. 69-81.

185. Irwin, N.J., C.P. McCoy, and J.L. Trotter, *Hydrogel Coatings for Medical Device Applications.* Hydrogels: Design, Synthesis and Application in Drug Delivery and Regenerative Medicine, 2018: p. 89.

186. Chirife, J., et al., *In vitro antibacterial activity of concentrated polyethylene glycol 400 solutions.* Antimicrob Agents Chemother, 1983. **24**(3): p. 409-12.

187. Nie, F.Q., et al., *Acrylonitrile-based copolymer membranes containing reactive groups: Surface modification by the immobilization of poly(ethylene glycol) for improving antifouling property and biocompatibility.* Langmuir, 2003. **19**(23): p. 9889-9895.

188. Dong, B.Y., et al., *Generation of antifouling layers on stainless steel surfaces by plasma-enhanced crosslinking of polyethylene glycol.* Journal of Applied Polymer Science, 2005. **97**(2): p. 485-497.

189. Cheng, G., et al., *Inhibition of bacterial adhesion and biofilm formation on zwitterionic surfaces.* Biomaterials, 2007. **28**(29): p. 4192-4199.

190. Robinson, K.J., et al., *Comparison between polyethylene glycol and zwitterionic polymers as antifouling coatings on wearable devices for selective antigen capture from biological tissue.* Biointerphases, 2015. **10**(4).

191. Wichterle, O. and D. LÍM, *Hydrophilic Gels for Biological Use.* Nature, 1960. **185**(4706): p. 117-118.

192. Wheeler, J.C., et al., *Evolution of hydrogel polymers as contact lenses, surface coatings, dressings, and drug delivery systems.* Journal of long-term effects of medical implants, 1996. **6**(3-4): p. 207-217.

193. Roberts, J.J. and P.J. Martens, *9 - Engineering biosynthetic cell encapsulation systems*, in *Biosynthetic Polymers for Medical Applications*, L. Poole-Warren, P. Martens, and R. Green, Editors. 2016, Woodhead Publishing. p. 205-239.

194. Griesser, H.J. and P.A. Kambouris, *Biocompatible Hydrogels*, in *Encyclopedia of Materials: Science and Technology*, K.H.J. Buschow, et al., Editors. 2001, Elsevier: Oxford. p. 548-550.

195. Nogueira, N., et al., *Characterization of poly(2-hydroxyethyl methacrylate) (PHEMA) contact lens using the Langmuir monolayer technique.* Journal of Colloid and Interface Science, 2012. **385**(1): p. 202-210.

196. Hook, A.L., et al., *Discovery of novel materials with broad resistance to bacterial attachment using combinatorial polymer microarrays.* Adv Mater, 2013. **25**(18): p. 2542-7.

197. Chen, S., et al., *Surface hydration: Principles and applications toward low-fouling/nonfouling biomaterials.* Polymer, 2010. **51**(23): p. 5283-5293.

198. Bose, R.K. and K.K.S. Lau, *Mechanical Properties of Ultrahigh Molecular Weight PHEMA Hydrogels Synthesized Using Initiated Chemical Vapor Deposition.* Biomacromolecules, 2010. **11**(8): p. 2116-2122.

199. Park, S., S.H. Nam, and W.-G. Koh, *Preparation of collagen-immobilized poly(ethylene glycol)/poly(2-hydroxyethyl methacrylate) interpenetrating network hydrogels for potential application of artificial cornea.* Journal of Applied Polymer Science, 2012. **123**(2): p. 637-645.

200. Yang, W., et al., *Film Thickness Dependence of Protein Adsorption from Blood Serum and Plasma onto Poly(sulfobetaine)-Grafted Surfaces.* Langmuir, 2008. **24**(17): p. 9211-9214.

201. Chang, Y., et al., *Highly protein-resistant coatings from well-defined diblock copolymers containing sulfobetaines.* Langmuir, 2006. **22**(5): p. 2222-6.

202. Smith, R.S., et al., *Vascular catheters with a nonleaching poly-sulfobetaine surface modification reduce thrombus formation and microbial attachment.* Sci Transl Med, 2012. **4**(153): p. 153ra132.

203. Szymanski, P., M. Markowicz, and E. Mikiciuk-Olasik, *Adaptation of High-Throughput Screening in Drug Discovery-Toxicological Screening Tests.* International Journal of Molecular Sciences, 2012. **13**(1): p. 427-452.

204. Celiz, A.D., et al., *Discovery of a Novel Polymer for Human Pluripotent Stem Cell Expansion and Multilineage Differentiation.* Adv Mater, 2015. **27**(27): p. 4006-12.

205. Algahtani, M.S., et al., *High throughput screening for biomaterials discovery.* J Control Release, 2014. **190**: p. 115-26.

206. Howbrook, D.N., et al., *Developments in microarray technologies.* Drug Discovery Today, 2003. **8**(14): p. 642-651.

207. Hook, A.L., H. Thissen, and N.H. Voelcker, *Advanced substrate fabrication for cell microarrays.* Biomacromolecules, 2009. **10**(3): p. 573-9.

208. Gupta, N., et al., *A versatile approach to high-throughput microarrays using thiol-ene chemistry (vol 2, pg 138, 2010).* Nature Chemistry, 2012. **4**(5): p. 424-424.

209. Anderson, D.G., S. Levenberg, and R. Langer, *Nanoliter-scale synthesis of arrayed biomaterials and application to human embryonic stem cells.* Nat Biotechnol, 2004. **22**(7): p. 863-6.

210. Thanu, D.P.R., et al., *Chapter 8 - Fundamentals and Applications of Plasma Cleaning*, in *Developments in Surface Contamination and Cleaning: Applications of Cleaning Techniques*, R. Kohli and K.L. Mittal, Editors. 2019, Elsevier. p. 289-353.

211. Tyler, B.J., et al., *Development and characterization of a stable adhesive bond between a poly(dimethylsiloxane) catheter material and a bacterial biofilm resistant acrylate polymer coating.* Biointerphases, 2017. **12**(2): p. 02C412-02C412.

212. Barbulovic-Nad, I., et al., *Bio-Microarray Fabrication Techniques—A Review*. Critical Reviews in Biotechnology, 2006. **26**(4): p. 237-259.

213. Coyle, R., J. Jia, and Y. Mei, *Polymer microarray technology for stem cell engineering.* Acta Biomater, 2016. **34**: p. 60-72.

214. Stears, R.L., T. Martinsky, and M. Schena, *Trends in microarray analysis.* Nature Medicine, 2003. **9**(1): p. 140-145.

215. Belu, A.M., D.J. Graham, and D.G. Castner, *Time-of-flight secondary ion mass spectrometry: techniques and applications for the characterization of biomaterial surfaces.* Biomaterials, 2003. **24**(21): p. 3635-3653.

216. Sodhi, R.N.S., *Time-of-flight secondary ion mass spectrometry (TOF-SIMS):—versatility in chemical and imaging surface analysis.* Analyst, 2004. **129**(6): p. 483-487.

217. Alnajeebi, A.M., J.C. Vickerman, and N.P. Lockyer, *Matrix effects in biological SIMS using cluster ion beams of different chemical composition.* Biointerphases, 2016. **11**(2): p. 02A317.

218. Benninghoven, A., *Chemical-Analysis of Inorganic and Organic-Surfaces and Thin-Films by Static Time-of-Flight Secondary-Ion Mass-Spectrometry (Tof-Sims).* Angewandte Chemie-International Edition in English, 1994. **33**(10): p. 1023-1043.

219. Gulin, A.A., et al., *Applicability of TOF-SIMS for the assessment of lipid composition of cell membrane structures.* Biochemistry (Moscow), Supplement Series A: Membrane and Cell Biology, 2017. **11**(2): p. 144-150.

220. Ista, L.K., S. Mendez†, and G.P. Lopez, *Attachment and detachment of bacteria on surfaces with tunable and switchable wettability.* Biofouling, 2010. **26**(1): p. 111-118.

221. *Introduction*, in *Surface Analysis – The Principal Techniques*. p. 1-8.

222. *Electron Spectroscopy: Some Basic Concepts*, in *An Introduction to Surface Analysis by XPS and AES*. p. 1-15.

223. Haasch, R.T., *X-Ray Photoelectron Spectroscopy (XPS) and Auger Electron Spectroscopy (AES)*, in *Practical Materials Characterization*, M. Sardela, Editor. 2014, Springer New York: New York, NY. p. 93-132.

224. Taylor, M., et al., *Partial least squares regression as a powerful tool for investigating large combinatorial polymer libraries.* Surface and Interface Analysis, 2009. **41**(2): p. 127-135.

225. Bhattacharjee, S., *DLS and zeta potential – What they are and what they are not?* Journal of Controlled Release, 2016. **235**: p. 337-351.

226. Thomas, T.E., et al., *Laser Doppler Electrophoresis and electro-osmotic flow mapping: A novel methodology for the determination of membrane surface zeta potential.* Journal of Membrane Science, 2017. **523**: p. 524-532.

227. Thomas, T.E., et al., *Laser Doppler Electrophoresis and electro-osmotic flow mapping: A novel methodology for the determination of membrane surface zeta potential.* Journal of Membrane Science, 2017. **523**: p. 524-532.

228. Corbett, J.C.W., et al., *Measuring surface zeta potential using phase analysis light scattering in a simple dip cell arrangement.* Colloids and Surfaces A: Physicochemical and Engineering Aspects, 2012. **396**: p. 169-176.

229. Mateos, H., et al., *Measurement of the zeta-potential of solid surfaces through Laser Doppler Electrophoresis of colloid tracer in a dip-cell: Survey of the effect of ionic strength, pH, tracer chemical nature and size.* Colloids and Surfaces A: Physicochemical and Engineering Aspects, 2019. **576**: p. 82-90.

230. Andrzejewska, E., *Chapter 2 - Free Radical Photopolymerization of Multifunctional Monomers*, in *Three-Dimensional Microfabrication Using Two-photon Polymerization*, T. Baldacchini, Editor. 2016, William Andrew Publishing: Oxford. p. 62-81.

231. Borman Christopher David, I.D.J., *Production of vinylic polymers;* , in *International Patent*. 2000.

232. Adlington, K., et al., *Enhanced 'in situ' catalysis via microwave selective heating: catalytic chain transfer polymerisation.* RSC Advances, 2014. **4**(31): p. 16172-16180.

233. Smeets, N.M.B., *Amphiphilic hyperbranched polymers from the copolymerization of a vinyl and divinyl monomer: The potential of catalytic chain transfer polymerization.* European Polymer Journal, 2013. **49**(9): p. 2528-2544.

234. Dundas, A.A., et al., *Validating a Predictive Structure–Property Relationship by Discovery of Novel Polymers which Reduce Bacterial Biofilm Formation.* Advanced Materials, 2019. **31**(49): p. 1903513.

235. Merritt, J.H., D.E. Kadouri, and G.A. O'Toole, *Growing and analyzing static biofilms.* Current protocols in microbiology, 2005. **Chapter 1**: p. Unit-1B.1.

236. Hüsler, A., et al., *Effect of surfactant on Pseudomonas aeruginosa colonization of polymer microparticles and flat films.* RSC Advances, 2018. **8**(28): p. 15352-15357.

237. Kurmoo, Y., et al., *Real time monitoring of biofilm formation on coated medical devices for the reduction and interception of bacterial infections.* Biomaterials Science, 2020.

238. Magennis, E.P., et al., *Making Silicone Rubber Highly Resistant to Bacterial Attachment Using Thiol-ene Grafting.* ACS Applied Materials & Interfaces, 2016. **8**(45): p. 30780-30787.

239. Monod, J., *THE GROWTH OF BACTERIAL CULTURES.* Annual Review of Microbiology, 1949. **3**(1): p. 371-394.

240. Fellers, T.J. and M.W. Davidson. *Introduction to Confocal Microscopy*. [cited 2019 September]; Available from: https://www.olympus-lifescience.com/en/microscope-resource/primer/techniques/confocal/confocalintro/.

241. Database, J.S.E., *Ultraviolet-Visible (UV-Vis) Spectroscopy.* JoVE, 2019.

242. Heinz-Helmut, P., *UV-VIS Spectroscopy and Its Applications*. 1992, Springer-Verlag, Heidelberg.

243. Celiz, A.D., et al., *Materials for stem cell factories of the future.* Nature Materials, 2014. **13**: p. 570.

244. Rahmati, M. and M. Mozafari, *Protein adsorption on polymers.* Materials Today Communications, 2018. **17**: p. 527-540.

245. Hindié, M., et al., *Effects of fibronectin coating on bacterial and osteoblast progenitor cells adherence in a co-culture assay*, in *Advances in Microbiology, Infectious Diseases and Public Health*. 2016, Springer. p. 17-30.

246. Baumgartner, J.N. and S.L. Cooper, *Influence of thrombus components in mediating Staphylococcus aureus adhesion to polyurethane surfaces.* Journal of Biomedical Materials Research: An Official Journal of The Society for Biomaterials, The Japanese Society for Biomaterials, and the Australian Society for Biomaterials, 1998. **40**(4): p. 660-670.

247. *Acid Hydrolysates of Casein to Replace Peptone in the Preparation of Bacteriological Media.* The Journal of Immunology, 1941. **40**(1): p. 33.

248. Nolan, R.A., *Amino Acids and Growth Factors in Vitamin-Free Casamino Acids.* Mycologia, 1971. **63**(6): p. 1231-1234.

249. Allen, S.J., G. McKay, and J.F. Porter, *Adsorption isotherm models for basic dye adsorption by peat in single and binary component systems.* Journal of Colloid and Interface Science, 2004. **280**(2): p. 322-333.

250. Foo, K.Y. and B.H. Hameed, *Insights into the modeling of adsorption isotherm systems.* Chemical Engineering Journal, 2010. **156**(1): p. 2-10.

251. Watts, J.F. and J.E. Castle, *The determination of adsorption isotherms by XPS and ToF-SIMS: their role in adhesion science.* International Journal of Adhesion and Adhesives, 1999. **19**(6): p. 435-443.

252. Ray, S. and A.G. Shard, *Quantitative Analysis of Adsorbed Proteins by X-ray Photoelectron Spectroscopy.* Analytical Chemistry, 2011. **83**(22): p. 8659-8666.

253. ASTM, *Standard Guide for Measurement of Electrophoretic Mobility and Zeta Potential of Nanosized Biological Materials.* ASTM International, 2018.

254. Mei, Y., et al., *Combinatorial development of biomaterials for clonal growth of human pluripotent stem cells.* Nat Mater, 2010. **9**(9): p. 768-78.

255. Kawecki, M. and L. Bernard, *Database of proteinogenic amino acid reference spectra for Bismuth-cluster ToF-SIMS. II. Positive polarity.* Surface Science Spectra, 2018. **25**(1): p. 015002.

256. Tao, P., R. Wang, and L. Lai, *Calculating Partition Coefficients of Peptides by the Addition Method.* Molecular modeling annual, 1999. **5**(10): p. 189-195.

257. Naef, R., *A Generally Applicable Computer Algorithm Based on the Group Additivity Method for the Calculation of Seven Molecular Descriptors: Heat of Combustion, LogPO/W, LogS, Refractivity, Polarizability, Toxicity and LogBB of Organic Compounds; Scope and Limits of Applicability.* Molecules, 2015. **20**(10): p. 18279-18351.

258. Ranu, B.C. and T. Mandal, *Water-Promoted Highly Selective Anti-Markovnikov Addition of Thiols to Unactivated Alkenes.* Synlett, 2007. **2007**(06): p. 0925-0928.

259. Skinner, E.K., F.M. Whiffin, and G.J. Price, *Room temperature sonochemical initiation of thiol-ene reactions.* Chemical Communications, 2012. **48**(54): p. 6800-6802.

260. Sinha, A.K. and D. Equbal, *Thiol−Ene Reaction: Synthetic Aspects and Mechanistic Studies of an Anti-Markovnikov-Selective Hydrothiolation of Olefins.* Asian Journal of Organic Chemistry, 2019. **8**(1): p. 32-47.

261. Vieira, J.C., L.C. Soares, and R.E.S. Froes-Silva, *Comparing chemometric and Langmuir isotherm for determination of maximum capacity adsorption of arsenic by a biosorbent.* Microchemical Journal, 2018. **137**: p. 324-328.

262. Cohn, E.J., *The Chemistry of the Proteins and Amino Acids.* Annual Review of Biochemistry, 1935. **4**(1): p. 93-148.

263. Pauling, L., R.B. Corey, and R. Hayward, *The Structure of Protein Molecules.* Scientific American, 1954. **191**(1): p. 51-59.

264. Ederer, J., et al., *Determination of amino groups on functionalized graphene oxide for polyurethane nanomaterials: XPS quantitation vs. functional speciation.* RSC Advances, 2017. **7**(21): p. 12464-12473.

265. Bhattacharjee, S., *DLS and zeta potential - What they are and what they are not?* Journal of Controlled Release, 2016. **235**: p. 337-351.

266. Jefferson, K.K., *What drives bacteria to produce a biofilm?* Fems Microbiology Letters, 2004. **236**(2): p. 163-173.

267. Patriquin, G.M., et al., *Influence of quorum sensing and iron on twitching motility and biofilm formation in Pseudomonas aeruginosa.* Journal of bacteriology, 2008. **190**(2): p. 662-671.

268. Parsek, M.R. and T. Tolker-Nielsen, *Pattern formation in Pseudomonas aeruginosa biofilms.* Current Opinion in Microbiology, 2008. **11**(6): p. 560-566.

269. Miller, R.M., et al., *Pseudomonas aeruginosa Twitching Motility-Mediated Chemotaxis towards Phospholipids and Fatty Acids: Specificity and Metabolic Requirements.* Journal of Bacteriology, 2008. **190**(11): p. 4038.

270. Oliveira, N.M., K.R. Foster, and W.M. Durham, *Single-cell twitching chemotaxis in developing biofilms.* Proceedings of the National Academy of Sciences, 2016. **113**(23): p. 6532.

271. Ni, L., et al., *Bacteria differently deploy type-IV pili on surfaces to adapt to nutrient availability.* Npj Biofilms And Microbiomes, 2016. **2**: p. 15029.

272. Carabelli, A.M., *Exploring Bacteria-Surface Interactions*, in *Pharmacy*. 2019, University of Nottingham eTheses.

273. Urquhart, A.J., et al., *High Throughput Surface Characterisation of a Combinatorial Material Library.* Advanced Materials, 2007. **19**(18): p. 2486-2491.

274. Seracu, D.I., *The Study of Uv and Vis Absorption-Spectra of the Complexes of Amino-Acids with Ninhydrin.* Analytical Letters, 1987. **20**(9): p. 1417-1428.

275. Wimalasena, R., K.L. Audus, and J.F. Stobaugh, *Rapid optimization of the post-column fluorogenic ninhydrin reaction for the HPLC-based determination of bradykinin and related fragments.* Biomed Chromatogr, 2003. **17**(2-3): p. 165-71.

276. Kobus, H.J., M. Stoilovic, and R.N. Warrener, *A simple luminescent post-ninhydrin treatment for the improved visualisation of fingerprints on documents in cases where ninhydrin alone gives poor results.* Forensic Science International, 1983. **22**(2): p. 161-170.

277. Hook, A.L., et al., *Polymer microarrays for high throughput discovery of biomaterials.* J Vis Exp, 2012(59): p. e3636.

278. Azizi, N. and M.R. Saidi, *Highly Chemoselective Addition of Amines to Epoxides in Water.* Organic Letters, 2005. **7**(17): p. 3649-3651.

279. Dyker, G., A. Thöne, and G. Henkel, *Reactions of glycidyl derivatives with ambident nucleophiles; part 2: amino acid derivatives.* Beilstein journal of organic chemistry, 2007. **3**: p. 28-28.

280. Kamble, V.T. and N.S. Joshi, *Synthesis of β-amino alcohols by ring opening of epoxides with amines catalyzed by cyanuric chloride under mild and solvent-free conditions.* Green Chemistry Letters and Reviews, 2010. **3**(4): p. 275-281.

281. Philippe, C., et al., *Non Lewis acid catalysed epoxide ring opening with amino acid esters.* Organic & Biomolecular Chemistry, 2009. **7**(10): p. 2026-2028.

282. Soliman, M., et al., *Multicomponent Synthetic Polymers with Viral-Mimetic Chemistry for Nucleic Acid Delivery.* Molecular Pharmaceutics, 2012. **9**(1): p. 1-13.

283. Shechter, L., J. Wynstra, and R.P. Kurkjy, *Glycidyl Ether Reactions with Amines.* Industrial & Engineering Chemistry, 1956. **48**(1): p. 94-97.

284. Li, Y., F. Xiao, and C.P. Wong, *Novel, environmentally friendly crosslinking system of an epoxy using an amino acid: Tryptophan-cured diglycidyl ether of bisphenol A epoxy.* Journal of Polymer Science Part A: Polymer Chemistry, 2007. **45**(2): p. 181-190.

285. Ripin, D. and D. Evans, *pKa's of Inorganic and Oxo-Acids.* The Evans, 2005.

286. Tsibouklis, J., et al., *Fluoropolymer coatings with inherent resistance to biofouling.* Surface Coatings International Part B: Coatings Transactions, 2002. **85**(4): p. 301-308.

287. Gross, U., S. Rüdiger, and H. Reichelt, *Perfluorocarbons: chemically inert but biologically active?* Journal of Fluorine Chemistry, 1991. **53**(2): p. 155-161.

288. Brady, R.F., S.J. Bonafede, and D.L. Schmidt, *Self-assembled water-borne fluoropolymer coatings for marine fouling resistance.* Surface Coatings International, 1999. **82**(12): p. 582-585.

289. Tyers, M. and G.D. Wright, *Drug combinations: a strategy to extend the life of antibiotics in the 21 st century.* Nature Reviews Microbiology, 2019. **17**(3): p. 141-155.

290. Mikulskis, P., et al., *Prediction of Broad-Spectrum Pathogen Attachment to Coating Materials for Biomedical Devices.* ACS Applied Materials & Interfaces, 2018. **10**(1): p. 139-149.

291. Kohn, J., *New approaches to biomaterials design.* Nature Materials, 2004. **3**(11): p. 745-747.

292. Patel, A.K., et al., *High throughput screening for discovery of materials that control stem cell fate.* Current Opinion in Solid State and Materials Science, 2016. **20**(4): p. 202-211.

293. Tourniaire, G., et al., *Polymer microarrays for cellular adhesion.* Chemical Communications, 2006(20): p. 2118.

294. Epa, V.C., et al., *Modelling and Prediction of Bacterial Attachment to Polymers.* Advanced Functional Materials, 2014. **24**(14): p. 2085-2093.

295. Vasilevich, A.S., et al., *How Not To Drown in Data: A Guide for Biomaterial Engineers.* Trends in Biotechnology, 2017. **35**(8): p. 743-755.

296. Lin, S., et al., *Predictive modelling-based design and experiments for synthesis and spinning of bioinspired silk fibres.* Nature Communications, 2015. **6**: p. 6892.

297. Brooks, T. and C.W. Keevil, *A simple artificial urine for the growth of urinary pathogens.* Letters in Applied Microbiology, 1997. **24**(3): p. 203-206.

298. Veber, D.F., et al., *Molecular Properties That Influence the Oral Bioavailability of Drug Candidates.* Journal of Medicinal Chemistry, 2002. **45**(12): p. 2615-2623.

299. Hook, A.L., et al., *Analysis and prediction of defects in UV photo-initiated polymer microarrays.* J Mater Chem B Mater Biol Med, 2013. **1**(7): p. 1035-1043.

300. Hook, A.L., et al., *Polymers with hydro-responsive topography identified using high throughput AFM of an acrylate microarray.* Soft Matter, 2011. **7**(16): p. 7194-7197.

301. Urquhart, A.J., et al., *TOF-SIMS analysis of a 576 micropatterned copolymer array to reveal surface moieties that control wettability.* Anal Chem, 2008. **80**(1): p. 135-42.

302. Terent'eva, N.A., G.I. Cherednichenko, and Y.G. Nikulichev, *Interfacial tension of some SF at the hydrocarbon-water interface.* Chemistry and Technology of Fuels and Oils, 1989. **25**(8): p. 404-406.

303. Shi, G., et al., *Unexpectedly Enhanced Solubility of Aromatic Amino Acids and Peptides in an Aqueous Solution of Divalent Transition-Metal Cations.* Physical Review Letters, 2016. **117**(23): p. 238102.

304. Donlan, R.M. and J.W. Costerton, *Biofilms: Survival Mechanisms of Clinically Relevant Microorganisms.* Clinical Microbiology Reviews, 2002. **15**(2): p. 167-193.

305. Römling, U. and C. Balsalobre, *Biofilm infections, their resilience to therapy and innovative treatment strategies.* Journal of Internal Medicine, 2012. **272**(6): p. 541-561.

306. Jenal, U. and J. Malone, *Mechanisms of cyclic-di-GMP signaling in bacteria.* Annual review of genetics, 2006. **40**: p. 385-407.

307. Römling, U. and D. Amikam, *Cyclic di-GMP as a second messenger.* Current opinion in microbiology, 2006. **9**(2): p. 218-228.

308. Vasseur, P., et al., *The pel genes of the Pseudomonas aeruginosa PAK strain are involved at early and late stages of biofilm formation.* Microbiology (Reading, England), 2005. **151**(Pt 3): p. 985-997.

309. Ryan, R.P., et al., *Cyclic Di-GMP Signaling in Bacteria: Recent Advances and New Puzzles.* Journal of Bacteriology, 2006. **188**(24): p. 8327.

310. Matsuo, H., et al., *Deterioration of polymethyl methacrylate dentures in the oral cavity.* Dental Materials Journal, 2015. **34**(2): p. 234-239.

311. Bean, T.A., et al., *Effect of esterase on methacrylates and methacrylate polymers in an enzyme simulator for biodurability and biocompatibility testing.* J Biomed Mater Res, 1994. **28**(1): p. 59-63.

312. Adlington, K., et al., *Application of Targeted Molecular and Material Property Optimization to Bacterial Attachment-Resistant (Meth)acrylate Polymers.* Biomacromolecules, 2016. **17**(9): p. 2830-2838.

313. Banerjee, S., *Solubility of Organic Mixtures in Water.* Environmental Science & Technology, 1984. **18**(8): p. 587-591.

314. Gershanik, J., et al., *The gasping syndrome and benzyl alcohol poisoning.* N Engl J Med, 1982. **307**(22): p. 1384-8.

315. Meyer, B.K., et al., *Antimicrobial preservative use in parenteral products: Past and present.* Journal of Pharmaceutical Sciences, 2007. **96**(12): p. 3155-3167.

316. Lucchini, J.J., J. Corre, and A. Cremieux, *Antibacterial activity of phenolic compounds and aromatic alcohols.* Res Microbiol, 1990. **141**(4): p. 499-510.

317. Simm, R., et al., *Benzyl alcohol induces a reversible fragmentation of the Golgi apparatus and inhibits membrane trafficking between endosomes and the trans-Golgi network.* Exp Cell Res, 2017.

318. Gratzl, G., et al., *Antimicrobial activity of poly(acrylic acid) block copolymers.* Mater Sci Eng C Mater Biol Appl, 2014. **38**: p. 94-100.

319. Mattenheimer, H. and U. Burchardt, *Origin of Enzymes in Urine*, in *Urinary Enzymes: in Clinical and Experimental Medicine*, K. Jung, H. Mattenheimer, and U. Burchardt, Editors. 1992, Springer Berlin Heidelberg: Berlin, Heidelberg. p. 3-7.

320. Mattenheimer, H., *Enzymes in the Urine.* Medical Clinics of North America, 1971. **55**(6): p. 1493-1508.

321. Li, C.Y., L.T. Yam, and K.W. Lam, *ESTERASES IN HUMAN LEUKOCYTES.* Journal of Histochemistry & Cytochemistry, 1973. **21**(1): p. 1-12.

322. Williams, F.M., *Clinical Significance of Esterases in Man.* Clinical Pharmacokinetics, 1985. **10**(5): p. 392-403.

323. Wilhelm, S., et al., *The autotransporter esterase EstA of Pseudomonas aeruginosa is required for rhamnolipid production, cell motility, and biofilm formation.* Journal of Bacteriology, 2007. **189**(18): p. 6695-6703.

324. Tielen, P., et al., *Extracellular enzymes affect biofilm formation of mucoid Pseudomonas aeruginosa.* Microbiology, 2010. **156**(7): p. 2239-2252.

325. Pesaresi, A., et al., *Isolation, Characterization, and Heterologous Expression of a Carboxylesterase of Pseudomonas aeruginosa PAO1.* Current Microbiology, 2005. **50**(2): p. 102-109.

326. van den Berg, B., *Crystal Structure of a Full-Length Autotransporter.* Journal of Molecular Biology, 2010. **396**(3): p. 627-633.

327. Teale, F.W. and G. Weber, *Ultraviolet fluorescence of the aromatic amino acids.* Biochem J, 1957. **65**(3): p. 476-82.

328. Jiang, L., L. He, and M. Fountoulakis, *Comparison of protein precipitation methods for sample preparation prior to proteomic analysis.* J Chromatogr A, 2004. **1023**(2): p. 317-20.

329. Cockram, A.A., et al., *Effect of Monomer Solubility on the Evolution of Copolymer Morphology during Polymerization-Induced Self-Assembly in Aqueous Solution.* Macromolecules, 2017. **50**(3): p. 796-802.

330. Jeffery, N., et al., *A new bacterial resistant polymer catheter coating to reduce catheter associated urinary tract infection (CAUTI): A first-in-man pilot study.* European Urology Supplements, 2019. **18**(1): p. e377.